Durham E-Theses

Organisation and dynamics of well-defined graft copolymers at the air-water interface

Miller, Aline Fiona

How to cite:

Miller, Aline Fiona (2000) *Organisation and dynamics of well-defined graft copolymers at the air-water interface*, Durham theses, Durham University. Available at Durham E-Theses Online: http://etheses.dur.ac.uk/4226/

Use policy

The full-text may be used and/or reproduced, and given to third parties in any format or medium, without prior permission or charge, for personal research or study, educational, or not-for-profit purposes provided that:

- a full bibliographic reference is made to the original source
- a link is made to the metadata record in Durham E-Theses
- the full-text is not changed in any way

The full-text must not be sold in any format or medium without the formal permission of the copyright holders.

Please consult the full Durham E-Theses policy for further details.

Organisation and Dynamics of Well-Defined Graft Copolymers at the Air-Water Interface

September 2000

Aline Fiona Miller

Graduate Society
University of Durham

A thesis submitted to the University of Durham in partial fulfillment of the regulations for the Degree of Doctor of Philosophy.

Thesis
2000/
MIL

Declaration

The work reported in this thesis has been carried out at the Interdisciplinary Research Centre in Polymer Science and Technology, Department of Chemistry, Durham University and at the Rutherford Appleton Laboratory in Oxfordshire between October 1997 and September 2000. This work has not been submitted for any other degree in Durham or elsewhere and, unless stated otherwise, is the original work of the author.

Statement of Copyright

Organisation and Dynamics of Well-Defined Graft Copolymers at the Air-Water Interface

Abstract

Novel amphiphilic graft copolymers with a backbone of poly(norbornene) (PNB) with poly(ethylene oxide) (PEO) grafts have been synthesised by a combination of ring opening metathesis and anionic polymerisation methods. The polymer has been prepared with hydrogenous and deuterated grafts and with grafts of different degrees of polymerisation. These graft copolymers spread at the air-water and air-PEO solution interface forming thin films and their organisation and dynamic behaviour is discussed.

Monolayer behaviour was characterised from surface pressure isotherms and it was demonstrated that the shape of the isotherm is dependent on graft length and on the concentration of PEO in the subphase. Using neutron reflectometry the organisation of such spread films at the air-water interface have been obtained over a range of surface concentrations for each length of PEO graft. Data were analysed by both exact calculation methods and the partial kinematic approximation and the models adopted were verified by applying the model independent Bayesian analysis. All yield the same description i.e. the hydrophobic backbone remains at the uppermost surface while the PEO grafts penetrate the subphase. The PEO layer increases in thickness with increased surface concentration and graft length. In each case the rate of increase with surface concentration was initially rapid but above a critical concentration, a slower rate was observed. In this latter regime the variation of the tethered layer height scales with surface density (σ) and degree of polymerisation of the graft (N) as, $\Gamma_s \approx N^{1.06} \sigma^{0.33}$, which agrees well with scaling and self consistent field theory of polymer brushes.

The dynamic behaviour of each copolymer film spread on water has been studied using surface quasi-elastic light scattering. A resonance between the capillary and dilational waves is observed at identical surface concentrations for each copolymer film. The viscoelastic behaviour of the dilational mode is reminiscent of Kramers-Kronig relations. The phenomenon of resistive mode mixing was observed in frequency dependency studies.

Acknowledgements

I am deeply indebted to a number of people who all played their part the production of this thesis. Firstly, many thanks go to Randal who has been an inspirational guide over the past three years. His guidance and support have proved invaluable.

Many thanks are also due to Ezat Khosravi and Lian Hutchings for passing on their ROMPing experience and for remaining calm at every 'oops' muttered from my end of the bench. Thanks also to Andrew Bozanko and Doug Carswell for running my GPC and DSC samples, and to Alan Kenwright for his guidance with NMR. In addition I am grateful to Mark Wilson and Melanie Cook for the Monte Carlo simulation work and for allowing me to direct my first movie!

The SQELS experiments reported here could not have been carried out without the help of Andrew Milling and Marcella Alexander. Likewise the neutron reflectometry work relied heavily on the expertise of the instrument scientists, Jeff Penfold, John Webster, and Michele Sferrazza, and lets not forget the coffee machine! A big thank you also goes to Andrew 'splitter' Brown not only for his experimental assistance but also his enthusiasm for exploring the pubs of south Oxfordshire and for his enviable patience when being bombarded with an endless list of questions.

I would like to collectively thank everyone, past and present, who has worked in CG156 for making it such a diverse and enjoyable place to work. Special thanks must go to everyone who made it to Dublin to play 'bunnies', Mark for keeping my inbox full, to Stu, well, for being Stu and to Helen who constantly reminds me that any crisis can be solved by having a good gossip and some chocolate. Thanks to Anja and the rowing crew for reminding me that the sun rises way too early in the morning and also Annette, Nic and Shona for the girlie weekends.

Finally, I would like to thank my parents whose endless patience, support and encouragement have been second to none. I would not have made it without you.

Preface: Units and Symbols

Abbreviations

PEO	poly(ethylene oxide)
PNB	poly(norbornene)
dPEO	perdeuterated poly(ethylene oxide)
ROMP	ring opening metathesis polymerisation
NR	neutron reflectometry
SQELS	surface quasi-elastic light scattering

where i is present as a subscript the quantity may be expressed explicitly in terms of component i

i	Component
EO	PEO
NB	PNB
W	Water

Greek Symbols

α	expansion coefficient
β	phase shift on traversing the layer
γ_{sub}	surface tension of subphase
γ_{oST}	surface tension of film covered subphase
γ	shear tension modulus
γ_o	SQELS surface tension
γ'	transverse shear viscosity
Γ	wave damping
Γ_s	surface concentration in mg m^{-2}
Γ^*	surface concentration at the onset of the semi dilute regime
Γ_{si}	surface concentration of component i

Γ^*_{brush} surface concentration at the onset of brush type behaviour, from scaling laws

Γ_{sLIM} maximum surface concentration without subphase penetration, from area considerations

$\Delta\rho$ difference in the scattering length density of air and the subphase,

$$\Delta\rho = \rho_{-\infty} - \rho_{\infty}$$

δ separation of number density distributions along the z axis

$\delta\theta$ scattering angle, from SQELS

$\epsilon_{\Sigma T}$ static dilational modulus

ϵ_o dilational modulus

ϵ' dilational viscosity

η viscosity

θ glancing incident angle for the neutron beam, or the incident angle measured normal to the interface during SQELS

κ Coupling coefficient for dilational and transverse surface modes in SQELS.

λ the wavelength of the neutron beam, or capillary wavelength in SQELS

ν critical scaling exponent

ξ 'blob' dimensions

$\xi(x,t)$ displacement

Π surface pressure, $\gamma_{sub} - \gamma_{oST}$

π osmotic pressure

ρ_i in the context of neutrons, scattering length density of layer, or component i.

ρ in the context of SQELS, density of the subphase

Ω_i frequency of the free, uncoupled, oscillator

σ full width of Gaussian at n_i/e

τ_r relaxation for Rouse movement

ϕ_i volume fraction of component i

χ_D displacement transfer function

χ_V velocity transfer function

χ interaction parameter

ω capillary wave frequency

ω_o wave frequency

Roman Symbols

a   statistical step length of a monomer unit

A_2 second virial coefficient

A_{22} two dimensional second virial coefficient

b_i the scattering length of species i

$D(\omega)$ dispersion equation

d_i thickness of the layer occupied by component i

d_m dimensionality of the system

c   solution concentration

c*   solution concentration at the onset of semi dilute regime

d   layer thickness

d_i thickness of layer i

$G^*(\omega)$ complex dynamic modulus

$G'(\omega)$ storage modulus

$G''(\omega)$ loss modulus

$g(\tau)$ correlation function

$h_{ii}(Q)$ self partial structure factor

$h_{ij}(Q)$ cross partial structure factor

I_o neutron incident intensity

I_r neutron reflected intensity

I_r SQELS incident intensity

I_s SQELS scattered intensity

K   SQELS scattering vector

k_B Boltzmann's constant

k_i incident wave vector

k_f reflected wave vector

M_i	molecular weight of component i
M_j	matrix for layer j
M_{ij}	element ij of the matrix M
M_n	number average molecular weight
M_w	weight average molecular weight
m	represents the degree of polymerisation of the backbone of the graft copolymer
m	coupling coefficient
N	number of segments, i.e. degree of polymerisation
N	the atomic number density in neutron theory
N_A	Avogadro's Number
n	represents the number of ethylene oxide monomers in each graft
n	neutron refractive index
n_i	number density of species i
n_{w0}	number density of bulk water
nrw	null reflecting water
P_v	velocity power response
P_D	velocity power response
$P(\omega)$	power spectrum of scattered light
Q	scattering vector
q	wavenumber
R	Rydberg constant
R_g	radius of gyration
R_{go}	unpeturbed radius of gyration
r_{ij}	Fresnel coefficient between layers i and j
R(Q)	reflectivity
$R_s(Q)$	reflectivity of a sharp interface
R_{exp}	experimental reflectivity
R_f	Fresnel reflectivity
T	absolute temperature
T*	oscillatory strain modulus
T_g	glass transition temperature

w_i weight fraction of component i

X_j represents the four surface parameters

Contents

Chapter One

Introduction

Section 1.1   Polymers at Interfaces

Polymer molecules exhibit unique and intriguing properties when present at surfaces and interfaces and have been investigated extensively over recent years[1,2]. As we move into the new century the research in this field continues to grow, motivated by the need for greater understanding to allow controlled manipulation and optimisation of properties. The characteristics of a host of different systems have been studied, including polymers at air-liquid, liquid-liquid, air-solid and polymer-polymer interfaces. One aspect that is at the forefront of experimental and theoretical research is the phenomenology of the air-water interface and the research presented here focuses on the organisation and dynamic properties of a polymer with novel topology when spread at such an interface.

In addition to the scientific curiosity evoked by such systems, polymers at interfaces have practical applications including stabilising the flocculation in colloidal dispersions[3,4], controlling adhesion[5,6], lubrication[7,8] or wetting properties of surfaces[9,10], inhibiting the adsorption of proteins onto surfaces or cells[11,12], drug delivery[13,14] and bio-compatibility[15]. All applications rely on having a prior knowledge of the interfacial structure-property relationships.

A common goal in polymer science and technology involves the development of novel polymeric materials, many of which have complicated architectures, for example graft[16] or star[17] copolymers, hyperbranched[18] or dendritic[19] materials. Amphiphilic copolymer molecules, where one polymer is hydrophilic and the other hydrophobic, are well known for forming monolayers at the air-water interface and have previously exhibited unique, 'dual' properties. Of particular interest are tethered polymers where one chain end is fixed at the interface by either chemical grafting or adsorption[20,21]. Much experimental and theoretical work is in progress towards understanding the structure - property relationship of such systems but the majority of these studies have concentrated on amphiphilic diblock copolymers[22-25]. The more unusual topology of a graft copolymer is adopted in this study to examine the influence of the different architecture on the balance of enthalpic and entropic contributions to the free energy and on the long wavelength dynamics of the spread film.

The air-liquid interface is an ideal medium for the study of such interfacial phenomenon and is often viewed as a model system for the more complex behaviour of

for example polymers in colloidal dispersions[3]. The water surface is naturally flat and smooth in nature as it only experiences a roughness of circa 2 Å due to perturbation by thermal fluctuations. When a polymer film is spread on a water surface the behaviour and interfacial properties are inherent to the spread material and can be modified easily by altering the polymer or in the case of a copolymer its architecture or composition. Understanding the properties of an air-water interface is industrially important, for example in the preparation of electronic devices[26], as these are formed by spreading a monolayer at the air-water interface and is subsequently transferred onto a solid substrate. Repetition of this technique allows substrates with multiple layers to be formed, which can be tailored to individual needs. It follows that, by understanding the physical characteristics of each layer at the air-water interface, the properties of the final products can be predetermined.

The concept of spreading monolayers on fluid surfaces is not a new one. The first reports of using such phenomenon date back to the eighteenth century BC where Babylonians practised divinity by observing oil spread on water[27]. Scientific interest however was not shown until 1774 when Benjamin Franklin reported that one teaspoon of oil spread 'with surprising swiftness' to cover over half an acre of the surface of a pond in Clapham Common[28]. Agnes Pockels reported the first study where the film was contained in a trough and was the first to realise the significance of surface cleanliness[29]. More recently however Irwin Langmuir investigated the relationship between surface pressure and monolayer concentrations[30] and Katherine Blodgett developed the technique of transferring monolayers on to solid substrates enabling multilayer formation[31] as described above.

There are two methods available to populate an air-water interface with polymer molecules. The first involves a surface active polymer dissolved in the subphase, for example poly(ethylene oxide) (PEO)[32], and since PEO reduces the surface tension of water a surface excess layer forms, i.e. the concentration of polymer at the near surface is greater than the bulk concentration. The monolayer is however in a dynamic equilibrium with the bulk as molecules continuously adsorb and desorb from the near surface. The second method involves spreading an insoluble polymer on the liquid surface, usually from a solution of polymer in a volatile solvent. Amphiphilic molecules are ideal for such studies as their hydrophobic/hydrophilic balance prevents them from

becoming dispersed in the aqueous phase. In both cases the monolayer characteristics can be manipulated by varying the subphase quality, temperature, and composition.

Numerous experimental techniques have been applied to study the characteristic behaviour of polymer monolayers at the air-liquid interface including surface pressure isotherms, fluorescent microscopy, brewster angle microscopy, ellipsometry, Fourier transform infra-red spectroscopy, X-ray reflectivity, neutron reflectivity and surface quasi-elastic light scattering. These techniques are discussed below, with emphasis being placed on the methods used in this work.

The simplest characterisation method involves recording surface pressure isotherms, where changes in surface pressure are monitored as a function of molecular area, or conventionally for polymer films, monolayer concentration. The isotherms obtained for polymeric materials are relatively featureless in comparison to low molecular weight molecules, and their behaviour is usually classified into one of two categories depending on their orientation: liquid expanded or liquid condensed[27]. This method therefore enables qualitative information regarding the arrangement of molecules at the surface to be obtained from which details of film structure can be inferred.

Scaling law descriptions of polymer properties in concentrated solution were introduced by de Gennes[33], later developed by des Cloizeaux[34] and Daoud and Jannink[35], have been applied successfully to surface pressure isotherm data for spread polymer films. This approach allows the extraction of quantitative physical information from the characteristic isotherm, including the surface concentration of phase transitions, Gibbs elasticity and information regarding the thermodynamic interactions between the polymer monolayer and the subphase. Extensive experimental work has been published on polymers at the air-water interface and are covered in a comprehensive review by Kawaguchi[36]. This work is complemented by various computer simulations[37-39].

Measuring surface pressure isotherms provides a qualitative insight into molecular orientation and is extremely versatile as numerous factors can be easily varied experimentally, such as the surface density, subphase composition, quality and temperature. However only small alterations in monolayer behaviour can be detected and isotherms do not provide a detailed description of film orientation or dynamics. This method can be beneficial in elucidating structures however, if used in tandem with

other techniques, thus allowing behaviour to be correlated to provide a greater insight into surface properties[22].

Numerous microscopy methods have been designed for the application to air-water interfaces. One example is fluorescence microscopy[40] and can be applied to systems where a fluorophore is either naturally present on the polymer or is doped into the monolayer. The fluorescence spectrum is recorded across the surface film and any in-plane inhomogenieties are detected. The pattern of the emission spectra obtained is directly correlated to the molecular structure and it can distinguish between condensed or expanded areas[41] for example. This method works well if the polymer already contains a fluorophore, but when fluorescence is artificially introduced there is always the uncertainty whether the monolayer behaviour has been modified.

A technique that has evolved from fluorescence microscopy is Brewster angle microscopy, which has the advantage of being able to determine the in-plane structure of films without the addition of foreign species[42]. This method capitalises on resolving plane polarised light into two components, one parallel (p-component) to and one perpendicular (s-component) to the surface. When the p-component is incident on a clean, sharp surface at 53.1 ° (referred to as the Brewster angle) no light is reflected. If however a polymer film was introduced to the surface the light would be reflected, and can provide an image of the surface. This image is directly related to the position and concentration of the in-plane inhomogenieties of dimensions greater than 1 μm. There are however many molecules in such an area, therefore the polymer morphology on the molecular level cannot be identified. This method was only developed over the past decade but has already proved successful in elucidating not only the general morphology of monolayers but also the chain tilt, interfacial line tension and film thickness. Much of this work has recently been reviewed by Möbius[33].

Ellipsometry has been applied to a variety of interfaces[44] and exploits the changes in ellipticity of plane polarised light on reflection from a surface. The refractive index of the surface determines the extent of reflection of the light, which is coupled to both the film thickness and composition, hence neither parameter can be resolved in a single experiment. Film thicknesses can be obtained however by monitoring differences between a clean water surface and when a polymer monolayer is present but structural information can only be obtained on length scales of circa 100 nm.

Various infrared (IR) spectroscopy techniques have been applied to the study of interfaces ranging from attenuated total reflection[45] and modulation polarisation spectroscopy[46] to conventional Fourier transform IR[47]. The former method has successfully been used to study the 'real time' kinetics of polymer adsorption onto a pre-formed layer[48] and in contrast the latter two methods have been used to measure the orientation of chains normal to the interface[49]. The results obtained from such experiments only provide an average picture of composition variation over the film that may be as much as 1μm from the surface.

The spectroscopy techniques outlined above can provide invaluable structural information, but detail is limited since information on a molecular level cannot be extracted due to the low resolution of the experimental methods. In contrast X-ray and neutron scattering methods provide molecular information normal to the interface giving a detailed picture of the surface structure. Both techniques rely on the monolayer scattering the probing radiation to differing extents, where changes in the intensity of the reflected beam are related to interfacial composition. X-rays have the advantage of a high flux, but cannot provide the detail accessible to neutron reflectometry where the possibility of modifying the refractive index profile of the interface through isotopic labelling provides a particularly powerful and selective technique[50-52].

The reflection of neutrons was first observed in 1946 by Fermi[53] and co-workers but the method has only been adopted and developed to study polymeric systems at wet interfaces over the past two decades. Recent advancements in instrumentation, for example the implementation of CRISP[54] and more recently SURF[55] reflectometers at the Rutherford Appleton Laboratory, have led to optimised conditions and increased experimental opportunities. The reflectivity profiles obtained from neutron experiments are however not simple to analyse, but by using appropriate isotopic labelling detailed structural information with resolutions down to circa 2 Å can be extracted. Various analysis methods can be adopted and have been extensively reviewed[5]. Initial experiments in the early 1980's elucidated the organisation of surfactant layers[57,58] by exploiting isotopic substitution and a trial and error method where an interfacial model was predicted, its reflectivity profile simulated and the model subsequently modified as required. This method is still applied, but is usually complemented with the Kinematic Approximation. This latter method was applied to polymer layers by Crowley and co-workers[59] and the application of isotopic labelling was introduced by Thomas and co-

workers[60]. In principle this approach allows the distribution of individual components and their separation to be determined, provided each component can be labelled. This is not, however, always possible but a partial analysis can be adopted and used in tandem with other techniques[61]. More recently Sivia developed a model independent analysis method using Bayesian probability theory[62]. This method both justifies the application of other conventional analysis methods and provides a free-form fitting method that can provide a natural extension for complicated systems[63].

Neutron reflection has been adopted to investigate the structure of numerous systems at the air-water interface including surfactants[64], polymers[65] and proteins[66] and there are a number of reviews available[67]. Much of the early work on polymer systems was focussed on PEO and PMMA polymers, initially as homopolymers[68-71] and more recently as copolymers, where their architecture increased in complexity from linear diblock[72] to graft copolymers[73]. Further studies have involved analysing surface excess layers[74], and surprisingly it was found that the molecular arrangement of a surface excess layer of PEO differs from a chemically equivalent spread layer. From this work numerous factors have been discovered that influence the organisation of spread films such as the tacticity of the spread polymer[68,69] and the nature of the subphase, i.e. the pH[75] and presence of surfactant[76], polymer[77] or electrolyte[78]. This field of research is continually expanding and most recently has involved the study of films spread at liquid-liquid interfaces where pioneering experiments have involved a triblock copolymer of poly(ethylene oxide)- poly(propylene oxide)- poly(ethylene oxide) spread on water with a superphase of n-hexane[79].

The presence of an amphiphilic polymer spread at the air-water interface can have a profound effect on the long-wavelength dynamics of the interface, i.e. the capillary surface waves[1]. This behaviour is, to some extent, identifiable with the nature of the polymer and by implication the manner in which the polymer organises at the interface. Ideally to obtain a complete understanding of the properties of an interfacial system the surface organisation should be investigated in parallel with the surface dynamics and the observed behaviour correlated.

Quantifying such dynamic behaviour relies on the relatively new technique of surface quasi-elastic light scattering (SQELS). This method is similar to an experimental set-up developed by Hård[80], but was recently modified by Earnshaw[81]. SQELS is dependent on the scattering of light by capillary waves and these are

influenced by the surface tension of the system. The properties of the surface waves are also modified when a spread film (or surface excess layer) is present. All parameters that are characteristic of the surface dynamics namely, surface tension, transverse shear viscosity, dilational modulus and dilational viscosity, can, in principle, be obtained using SQELS. This method is non-perturbative and also allows the surface behaviour to be probed as a function of both surface concentration and frequency.

There are several groups that use SQELS to study the dynamic behaviour but unfortunately there is no consensus in analysis methods. One set of published results is the work of Yu and co-workers[82-88]. They have investigated the characteristics of numerous polymer films at the air-water interface including poly(vinyl acetate)[82], poly(vinyl stearate)[83], a poly(ethylene oxide)-polystyrene block copolymer[84], poly(n-butyl methacrylate)[85], PEO[86], and linear[87] and branched[88] poly(dimethylsiloxane)s. There is much debate concerning the validity of such studies as the analysis method they adopt involves unsupported assumptions where the surface tension assumes its zero frequency value and that the transverse shear viscosity is zero. More fundamentally they extract the propagating characteristics of the capillary waves by fitting the experimental data with a true, rather than a skewed, Lorentzian curve.

An improved analysis method was pioneered by Earnshaw and McLaughlin[89], which allows all four parameters to be determined without any a priori assumptions. Such methods have led to the investigation of a variety of systems, including surfactants[90,91] and polymers[92-95]. The application of SQELS to polymeric surfaces is relatively new, but significant progress has already been made. The dynamic properties including PMMA, PEO homopolymers[92] and also as diblock[93] and graft[94] copolymers and linear diblock copolymer of poly(methyl methacrylate) and poly-4-vinyl pyridine quaternised with ethyl bromide[95], have been examined. One surprising observation made was that one viscoelastic parameter, namely the dilational viscosity, could explore negative values, which appears at first sight to be unphysical. Such negative viscosity values have been interpreted as effective parameters and are thought to arise due to inadequacies of the dispersion equation. This prompted a theoretical reanalysis of the dispersion equation where the model is specific to polymer monolayers.

The new dispersion equation derived by Buzza[96] and co-workers includes two new viscoelastic parameters, the coupling and the bending modulus and also equates the transverse shear viscosity to zero. This new approach has recently been applied to a

polymer film of polysilylene-poly(ethylene oxide) multi block copolymer[97], however negative viscosities were still observed, suggesting that the dispersion equation remains incomplete.

Section 1.2   Objectives

The aim of this project was to investigate the organisation and long-wavelength dynamics of a series of amphiphilic copolymers at the air-water interface. This project was stimulated by earlier work on random graft copolymers, which exhibited novel surface visco-elastic phenomenon as a function of concentration of spread film[94]. Due to the ill-defined nature of the materials used it left the question whether the observed properties were due to the amount of PEO present or the grafting frequency at the surface. In attempt to answer such questions well-defined graft copolymers were synthesised, by combining anionic and ring opening metathesis polymerisations, where such materials have a hydrophobic hydrocarbon backbone and hydrophilic poly(ethylene oxide) grafts. Three copolymers have been prepared where the backbone length was kept constant at 50 norbornene repeat units, while the degree of polymerisation of the graft was varied to contain 15, 25 and 50 ethylene oxide units.

Following the copolymer synthesis the surface organisation of a monolayer of each material spread at an air-water interface was elucidated as a function of surface concentration and graft length using a combination of surface pressure isotherms and neutron reflectometry. The results obtained were subsequently compared to data simulated using Monte Carlo calculations. The surface dynamics and viscoelasticity of the monolayers were measured using surface quasi-elastic light scattering and where appropriate, their behaviour correlated to the molecular organisation. In addition this work was extended to analyse the organisation of one copolymer when spread on an aqueous subphase containing mobile homoPEO. Ultimately the properties inherent of the graft copolymers studied here are compared to the homopolymer analogue and to diblock and graft copolymers containing PEO in attempt to provide a model that accounts for the differences in the characteristic behaviour.

Section 1.3   References

1)   Jones, R. A. L.; Richards, R. W. *Polymers at Surfaces and Interfaces,* Cambridge University Press, **1999**.

2)   Richards, R. W. (ed.); Peace, S. K. (ed.) *Polymers at Interfaces III,* John Wiley and Sons, **1999**.

3)   Napper, D. H.; *Polymeric Stabilisation of Colloidal Dispersions,* Academic Press, New York, **1983**.

4)   Fleer, G. J.; Cohen Stuart, M. A.; Scheutjens, J. M. H. M.; Cosgrove, T.; Vincent, B. *Polymers at Interfaces,*Chapman and Hall, London, **1993**.

5)   Lèger, L.; Raphael, E.; Hervert, H. *Adv. Poly. Sci.* **1999**, *138*, 185.

6)   Kim, J. B.; Yun, H. J.; Kwon, Y. G. *Polymer,* **2000**, *41*, 8035.

7)   Klein, J. *J. of Physics-Cond. Matt.,* **2000**, *28*, A19.

8)   Zhang, Z. Z.; Xue, Q. J.; Liu, W. M.; Shen, W. C. *J. of Appl. Polym. Sci.,* **2000**, *8*, 1240.

9)   Reiter, G.; Auroy, P.; Auvray, L. *Macromolecules,* **1996**, *29,* 2150.

10)   Kim, J. S.; Friend, R. H.; Cacialli, F. *Synthetic Met 111,* **2000**, *1*, 369.

11)   Halperin, A. *Langmuir,* **1999**, *15*, 2525.

12)   Kenausis, G. L.; Voros, J.; Elbert, D. L.; Huang, N. P.; Hofer, R.; Ruiz-Taylor, L.; Textor, M.; Hubbell, J. A.; Spencer, N. D. *J. of Phys. Chem. B,* **2000**, *14*, 3298.

13)   Breitenbach, A.; Pistel, K. F.; Kissel, T. *Polymer,* **2000**, *13*, 4781.

14)   Malzert, A.; Boury, F.; Saulnier, P.; Benoit, J. P.; Proust, J. E. *Langmuir,* **2000**, *4*, 1861.

15)   Clarke, S.; Davies, M. C.; Roberts, C. J.; Tendler, S. J. B.; Williams, P. M.; O'Byrne, V.; Lewis, A. L.; Russel, J. *Langmuir,* **2000**, *11*, 5116.

16)   Feng, Y.; Zhao, J. R.; Wang, Q.; Li, M.; Chen, X. F. *J. of Appl. Poly. Sci.,* **2000**, *475*, 75.

17)   Matyjaszewski, K.; Miller, P. J.; Pyun, J.; Kickelbick, G.; Diamanti, S. *Macromolecules,* **1999**, *32*, 6526.

18)   Kim, Y. H. *J. of Poly. Sci. A,* **1998**, *11*, 1685.

19)   Sferrazza, M.; Jones, R. A. L.; Penfold, J.; Bucknall, D. B.; Webster, J. R. P. *J. of Materials Chemistry,* **2000**, *10,* 127.

20) Halperin, A.; Tirrell, M.; Lodge, T. P. *Adv. Polym. Sci.,* **1992**, *100*, 31.

21) Szleifer, I.; Carignano, M. A. *Adv. in Chem. Phys.*, **1996**, *44*, 165.

22) Kent, M. S. *Macromol. Rapid Commun.,***2000**, *21*, 243.

23) Currie, E. P. K.; Leermakers, F. A. M.; Stuart, M. A. C.; Fleer, G. J. *Macrmolecules,* **1999**, *32*, 487.

24) Cox, J. K.; Yu, K.; Constantine, B.; Eisenberg, A.; Lennox, R. B. *Langmuir,* **1999**, *15*, 7714.

25) Senshu, K.; Kobayashi, M.; Ikawa, N.; Yamashita, S.; Hirao, A.; Nakahama, S. *Langmuir*, **1999**, *15*, 1763.

26) Dabke, R. B.; Dhanabalan, A.; Major, S.; Talwar, S. S.; Lal, R.; Contractor, A. Q. *Thin Solid Films*, **1998**, *335*, 208.

27) Adamson, A. W. *Physical Chemistry of Surfaces, Fourth Edition*, **1982**, 124, Wiley, New York.

28) Franklin, B. *Phil. Trans. Roy. Soc.,* **1774**, *64*, 445.

29) Pockels, A. *Nature*, **1891**, *43*, 437.

30) Langmuir, I. *J. Am. Chem. Soc.,* **1917**, *39*, 1848.

31) Blodgett, K. B. *Phys. Rev.* **1939**, *55*, 391.

32) Glass, J. E. *J. Phys. Chem., 1968, 72, 4459.*

33) de Gennes, P. G. *Scaling Concepts in Polymer Physics*, **1991**, Cornell University, New York.

34) des Cloizeaux, J. *J. Phys. (Paris),* **1976**, *41*, L-151.

35) Daoud, M.; Jannink, G. *J. Phys. (Paris)*, **1976**, *37*, 973.

36) Kawaguchi, M. *Progress in Polymer Sci.*, **1993**, *18,* 341.

37) Aguie-Beghin, V.; Leclerc, E.; Dauod, M.; Douillard, R. **1999**, *214*, 143.

38) Vilanove, R.; Poupinet, D.; Rondelez, F. *Macromolecules*, **1989**, *22*, 2491.

39) Kremer, K.; Lyklema, J. W. *Phys. Rev. Lett.*, **1985**, *54*, 267.

40) Bhawalkar, J. D.; Swiatkiewicz, J.; Samaranadu, J. K.; Liou, W. S.; He, G. S.; Berezney, R.; Cheng, P. C.; Prasad, P. N. *Scanning*, **1996**, *18*, 562.

41) Caruso, F.; Gruiser, F.; Thistlewaite, P. J.; Furlong, D. N.; *Macromolecules*, **1994**, *27*, 77.

42) Webster, J. R. P.; Langridge, S. *Curr. Opin. in Coll. and Inter. Sci.,* **1999**, *4*, 186.

43) Möbius, D. *Curr. Opin. in Coll. and Inter. Sci.*, **1998**, *3,* 137.

44)   Asnacios, A.; Klitzing, R.; Langevin, D. *Colloid Surface A*, **2000**, *167*, 189.

45)   Brinkhuis, R. H.; Schouten, A. J. *Macromolecules*, **1991**, *24*, 1496.

46)   Fauré, M. C.; Bassereau, P.; Desbat, B. *Euro. Phys. J. E*, **2000**, *2* 151.

47)   Dluhy, R. A.; Cornell, D. G.; *J. Phys. Chem.*, **1985**, *89*, 3195.

48)   Hishikawa, Y.; Togawa, E.; Kataoka, Y.; Kondo, T. *Polymer*, **1999**, *40*, 7117.

49)   Kim, K. J.; Hsu, S. L. *Polymer*, **1994**, *35*, 3612.

50)   Higgins, J. S.; Benoit, H. C. *Polymers and Neutron Scattering*, Oxford University Press, **1994**.

51)   Thomas, R. K. *Scattering Methods in Polymer Science*, **1995**, *Chapter 4*, Ed. Richards, R. W. Ellis Horwood.

52)   Russel, T. P. *Mat. Sci. Rep. 5*, **1990**, 171.

53)   Fermi, E.; Marshall, L. *Phys. Rev.*, **1947**, *71*, 666.

54)   Penfold, J.; Ward, R. C.; Williams, W. G.; *J. Phys. E: Sci. Instrum.*, **1987**, *20*, 1411.

55)   Penfold, J.; Richardson, R. M.; Zarbakhsh, A.; Webster, J. R. P.; Bucknall, D. G.; Rennie, A. R.; Jones, R. A. L.; Cosgrove, T.; Thomas, R. K.; Higgins, J. S.; Fletcher, P. D. I.; Dickinson, E.; Roser, S. J.; McLure, I. A.; Hillman, A. R.; Richards, R. W.; Staples, E. J.; Burgess, A. N.; Simister, E. A.; White, J. W. *J. Chem. Soc. Faraday Trans.*,**1997**, *93*, 3899.

56)   Lovell, M. R.; Richardson, R. M. *Current Opinion in Coll. and Inter. Sci.*,**1999**, *4*, 197.

57)   Lee, E. M.; Thomas, R. K. *J. Phys. Chem.*, **1989**, *93*, 381.

58)   Penfold, J.; Lee, E. M.; Thomas, R. K. **1989**, *68*, 33.

59)   Crowley, T. L.; Lee, E. M.; Simister, E. A.; Thomas, R. K.; Penfold, J.; Rennie, A. R. *Colloids and Surfaces*, **1990**, *52*, 85.

60)   Crowley, T. L.; Lee, E. M.; Simister, E. A.; Thomas, R. K. *Physica B*, **1991**, *174*, 143.

61)   Cooke, D. J.; Lu, J. R.; Lee, E. M.; Thomas, R. K.; Pitt, A. R.; Simister, E. A.; Penfold, J. *J. Phys. Chem.* **1996**, *100*, 10298.

62)   Sivia, D. S.; Webster, J. R. P. *Physica B: Condensed Matter*, **1998**, *248*, 327.

63)   Sivia, D. S. *Data Analysis: A Bayesian Tutorial*, Oxford University Press, Oxford, **1996**.

64)   Lu, J. R.; Hromadova, M.; Simister, E. A.; Thomas, R. K.; Lu, J. R. *Macromolecules*, **1993**, *26*, 4591.

65)   Reynolds, I.; Richards, R. W.; Webster, J. R. P. *Macromolecules*, **1995**, *28*, 7845.

66)   Atkinson, P. J.; Dickinson, E.; Horne, D. S.; Richardson, R. M. *J. Chem. Soc., Faraday Trans,* **1995**, *91*, 2847.

67)   Rutherford Appleton Laboratory Website.

68)   Gissing, S. K.; Richards, R. W.; Rochford, B. R. *Colloids and Surfaces A:Physiochem. Eng. Asp.*, **1994**, *86*, 171.

69)   Henderson, J. A.; Richards. R. W.; Penfold, J.; Shackleton, C.; Thomas, R. K. *Polymer*, **1991**, *32, 3284.*

70)   Henderson, J. A.; Richards. R. W.; Penfold, J.; Thomas, R. K. *Macromolecules*, **1993**, *26*, 65.

71)   Henderson, J. A.; Richards. R. W.; Penfold, J.; Thomas, R. K.; Lu, J. R.; *Macromolecules*, **1993**, *26*, 4591.

72)   Richards, R. W.; Rochford, B. R.; Webster, J. R. P. *J. Chem. Soc. Farad. Discuss.* **1994**, *98*, 263.

73)   Peace, S. K.; Richards, R. W.; Taylor, M. R.; Webster, J. R. P.; Williams, N. *Macromolecules*, **1998**, *31*, 1261.

74)   Peace, S. K.; Richards, R. W.; Kiff, T.; Penfold, J.; Williams, N. *Polymer*, **1999**, *40*, 207.

75)   An, S. W.; Thomas, R. K.; Baines, F. L.; Billingham, N. C.; Armes, S. P.; Penfold, J. *J. Phys. Chem. B.,* **1998**, *102*, 5120.

76)   Penfold, J.; Staples, E.; Thompson, L.; Tucker, I.; Hines, J.; Thomas, R. K.; Lu, J. R. *Langmuir,* **1995**, *11,* 496.

77)   Peace, S. K.; Richards, R. W. *Langmuir,* **1997**, *14*, 667.

78)   Brown, A. S. *Ph.D. Thesis,* Durham University, **1999**.

79)   Cosgrove, T.; Phipps, J. S.; Richardson, R. M. *Langmuir,* **1994**, *9*, 3530.

80)   Hård, S.; Hammerius, Y.; Nilsson, O. *J. App. Phys.* **1976**, *47*, 2433.

81)   Hughes, C. J.; Earnshaw, J. C. *J. Phys. E.: Rev. Sci. Instrum.,* **1993**, *64*, 2789.

82)   Kawaguchi, M.; Sano, M.; Chen, Y. L.; Zografi, G.; Yu, H. *Macrmolecules*, **1986**, *19*, 2606.

83)   Chen, Y. L.; Kawaguchi, M.; Yu, H.; Zografi, G. *Langmuir*, **1987**, *3*, 31.

84) Sauer, B. B.; Yu, H.; Tien, C. F.; Hager, D. F. *Macromolecules*, **1987**, *20*, 393.

85) Sauer, B. B.; Kawaguchi, M.; Yu, H. *Macromolecules*, **1987**, *20*, 2732.

86) Yoo, K. H.; Yu, H. *Macrmolecules*, **1989**, *22*, 4019.

87) Runge, F. E.; Yu, H. *Langmuir*, **1993**, *9*, 3191.

88) Runge, F. E.; Yu, H.; Woermann, D. *Ber. Bunsenges. Phys. Chem.*, **1994**, *98*, 1046.

89) Earnshaw, J. C.; McGivern, R. C.; McLaughlin, A. C.; Winch, P. J. *Langmuir*, **1990**, *6*, 650.

90) Earnshaw, J. C.; McCoo, E. *Langmuir*, **1995**, *11*, 1087.

91) Earnshaw, J. C.; Nugent, C. P.; Lunkenheimer, K. *Langmuir*, **1997**, *13*, 1368.

92) Richards, R. W.; Taylor, M. R. *J. Chem. Soc., Faraday Trans.*, **1996**, *92*, 601.

93) Richards, R. W.; Rochford, B. R.; Taylor, M. R. *Macromolecules*, **1996**, *29*, 1980.

94) Peace, S. K.; Richards, R. W. *Langmuir*, **1998**, *14*, 667.

95) Brown, A. S.; Richards, R. W.; Buzza, D. M. A.; McLeish, T. C. B. *Faraday Discuss.*, **1999**, *112*, 1.

96) Buzza, D. M. A.; Jones, J. L.; McLeish, T. C. B.; Richards, R. W.; *J. Chem. Phys.*, **1998**, *109*, 5008.

97) Milling, A. J.; Richards, R. W.; Hiorns, R. C.; Jones, R. G. *Macromolecules*, **2000**, *33*, 2651.

Chapter Two

Theory

Section 2.1   Synthetic Background

2.1.1   Introduction

All molecules with molecular masses ranging from several thousand to several million are commonly referred to as polymer molecules or macromolecules. Such substances are giant molecules, which consist of many simple chemical units (monomers) covalently linked together in numerous patterns via a polymerisation reaction. This methodology has been studied extensively over the last 100 years[1, 2] and has culminated in the production of various commercially viable materials. Polymeric materials are commonplace in everyday life, for example polyamides as nylons plastics, poly (tetrafluoro ethylene) (commonly known as teflon) as non-stick material for cooking utensils, various polyether compounds as adhesives and polybutadiene used in rubber.

Manipulation of polymerisation reaction conditions first began in the 1930's in an attempt to control the architecture (molecular weight (M.Wt.), polydispersity and tacticity of polymer molecules. Such molecular design enabled the control and optimisation of the physical properties of the materials prepared. Initially, macromolecules were prepared using a single monomer species hence the product was classified as a homopolymer, or more simply, a polymer. Modifications of macromolecular properties can be obtained by the simultaneous polymerisation of two or more monomers to form copolymers. Examples of the various architectures that have been prepared (random, alternating, block or graft copolymers.) are given in figure 2.1.1. The physical properties of such systems for example the degree of crystallinity, viscoelasticity, glass transition and melt temperature were discovered to be dependent on both the architecture and the percentage composition of the copolymer.

The commercial interest for novel polymeric materials with unique topologies that exhibit ever-improved properties continues to grow. The demand therefore to design and gain control of the synthesis of well-defined polymeric materials is increasing and is an area of great academic[4] and industrial[5] interest.

ABABABABABABABABA

Alternating copolymer

AABABBAABABBABAAB

Random copolymer

AAAAAAAAAAAAAABBBBBBBBBBBBBB

Block copolymer

AAAAAAAAAAAAAAAAAAAAAAAAAAAAAA
B   B   B   B   B   B
B   B   B   B   B   B
B   B   B   B   B   B
B   B   B   B   B   B
B   B   B   B   B   B

Graft copolymer

A monomers forming the main chain or backbone

B monomers forming the side chain or grafts
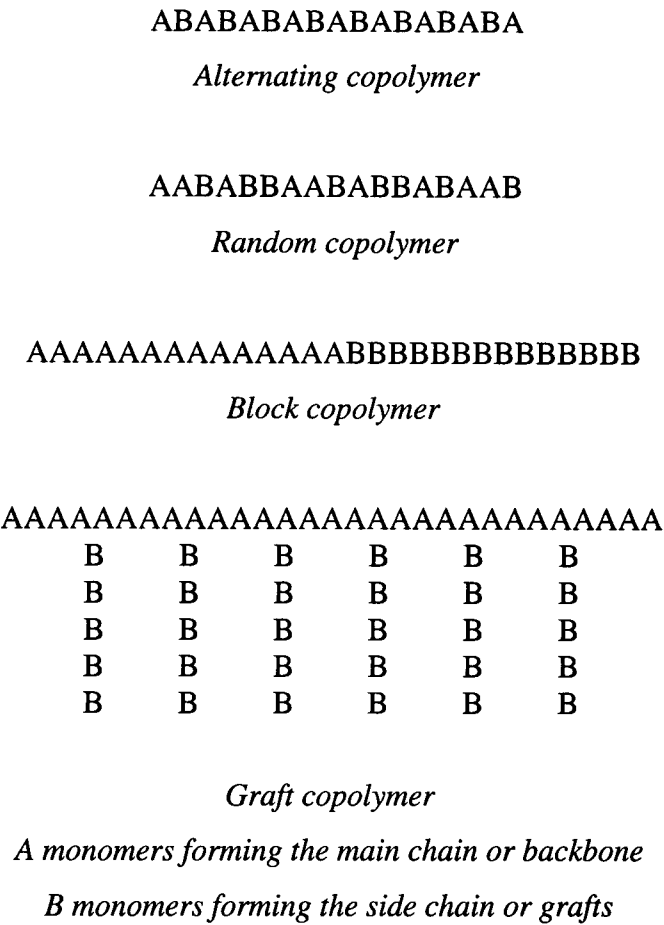
Figure 2.1.1. Monomer distribution in copolymers.

2.1.2 Polymerisation Reactions

Polymeric materials have been divided into two classes depending on their method of preparation[6]. The first group is condensation polymers where the step-wise incorporation of a monomer repeat unit involves the loss of a small molecule, such as water or hydrochloric acid in an esterification reaction. This contrasts with the second group, addition polymers. In a typical addition polymerisation an active site (anion, cation or radical) initiates the sequential addition of monomer units and has the advantage of forming no by-product. One important category of addition reactions occurs when the active site on the growing polymer chain is indefinitely available for

further propagation. Such reactions are known as living polymerisations and are employed where precise M.Wt. and narrow polydispersities are required.

The living polymerisation method allows complete conversion of all monomer species to polymeric material regardless of the propagation rate provided the system is free from impurities, as these cause termination of the propagating chain or initiation of chain transfer reactions. When the initiation step (preparation of first active site) is fast in comparison to the propagation step (sequential addition of monomer to active site), all polymer chains grow at identical rates, thus preparing monodisperse material (i.e. $1.0 < M_w / M_n < 1.1$). This provides control over the M.Wt. of the polymer simply by altering the monomer to initiator ratio.

Copolymers are ideally prepared under living conditions for example block copolymers since addition of a second monomer to a living homopolymer leads to continued propagation. Polybutadiene-polystyrene has been successfully prepared using this methodology where the styrene monomer was added to living homo polybutadiene[7]. More recently living radical polymerisation reactions have produced well-defined topologies for example polystyrene-poly (methyl methacrylate) was synthesised according to atom transfer radical polymerisations[8].

2.1.2.1 Anionic Polymerisations

Anionic polymerisation is one class of living polymerisation where the active propagating site is a carbanion[9]. Monomers that contain electron-withdrawing substituents connected to double bonded carbons form stable carbanions and are therefore susceptible to anionic polymerisation in the presence of a suitable initiator. Initial formation of a carbanionic species usually occurs through initiation of one monomer species. Typically monomers are dienes, styrenes or methacrylates, initiated using organo-metallic compounds and the resulting carbanion is stabilised through a combination of mesomorphic and inductive effects. The initiation step, as shown schematically in figure 2.1.2, usually occurs through addition of a basic ion, which opens the double bond in the monomer, leaving an anionic active site ready to attack another monomer unit.
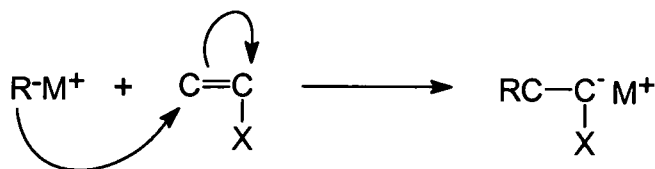
Figure 2.1.2. Initiation of anionic polymerisation using an organo-metallic reagent.

Alkali metal alkyl compounds for example Grignard reagents (RMg^+ Cl^-), n-butyl lithium, sec-butyl lithium are often used as initiators. Bulkier compounds, for example tert-butyl lithium, are employed when greater stereochemical control is desired. Electron transfer reagents such as metallic sodium or sodium- napthalene have also been employed to initiate polymerisation reactions where the radical anion generated after electron transfer rapidly dimerises resulting in a propagating di-anion. This process is outlined in figure 2.1.3.
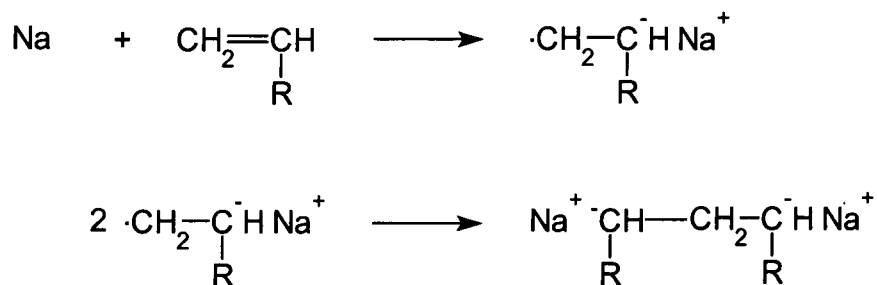
Figure 2.1.3. Preparation of propagating dianion using metallic sodium as an electron transferring agent.

In order to prepare monodisperse polymer it is essential to ensure the initiation of monomer is faster than the propagation reaction. Various factors can effect this balance including the nature of the initiator and the quality of the solvent. A good solvent for enhanced rate of reaction is one that solvates the cation of the initiating species, thus maximising the nucleophilicity of the anion and also discouraging aggregation of the initiating species.

As previously stated the propagating chain end in an anionic process remains active until an impurity, or specific terminating compound, is added to stop propagation. When the terminating agent contains functional groups then this final step is often

referred to as the 'end-capping' of the polymer chain. The active chain ends are, however, sensitive to traces of water or other protic impurities as these species react causing premature termination of the living polymer. Care needs to be taken therefore to eliminate such impurities before and during the reaction. Typically all glassware used needs to be thoroughly cleaned, reagents purified and reactions carried out under a nitrogen atmosphere, otherwise unfunctionalised, polydisperse polymer of low molecular weight is produced.

Living anionic polymerisations are generally well understood[10] and are employed in many industrial processes, for example the synthesis of stereo regular polyisoprene (synthetic natural rubber), where butyl lithium is used as the initiator.

2.1.2.2 Graft Copolymers

Graft copolymers are one group of polymers that have unique properties and can be prepared using living polymerisation methods[11]. Initially two alternative synthetic strategies were employed to prepare such topologies: the 'grafting onto' and the 'grafting from' methods.

The "grafting onto" route involves the preparation of two functionalised polymers, usually via living anionic polymerisation where one polymer is end functionalised, while the other contains functional sites at regular intervals throughout the chain. The graft copolymer is then prepared by coupling the end functionalised material to the fully functionalised polymer. It is difficult to achieve quantitative grafting using this method, as it requires an excess of the side chain polymer, which increases the quantity of homopolymer prepared. Such by-products can be removed however along with any unreacted polymer by employing fractionation techniques.

Alternatively, the "grafting from" route requires two separate polymerisation steps. Initially a functionalised monomer is polymerised to form a homopolymer, which will ultimately form the main chain of the graft copolymer. Ideally the functional sites on this polymer will be easily activated and will act as initiator for a second polymerisation reaction to allow the growth of pendant chains. Such graft copolymers have been successfully synthesised using radical[12], anionic[13] or cationic[14] polymerisation techniques. The advantage of the "grafting from" method is that the

quantity of homopolymers formed is reduced, however no control over the grafting density can be obtained.

The most common synthetic route to prepare graft copolymers to date involves the polymerisation of a macromonomer. The first step towards the target copolymer involves the preparation of an end functionalised macromonomer through living anionic polymerisation. Thereafter the functional groups present are linked together to form the main chain of copolymer via free radical polymerisation. A wide range of macromonomer species have recently become available by endcapping a monodisperse homopolymer with an unsaturated reactant. For example styryl or methacryloyl functionality acts as an endcapping reagent and is suitable to undergo free radical polymerisation with a different monomer. For example homo poly(ethylene oxide) (PEO) was prepared via living anionic polymerisation and endcapped with a methacryl chloride. The double bond of the functional group was subsequently free radically polymerised with methyl methacrylate (MMA) monomer to prepare PMMA-*g*-PEO[16]. Although this route was successful in the preparation of graft copolymers the structure of the materials obtained by the radical processes were ill-defined.

The general problem to synthesise well-defined graft copolymers using a macromonomer is the lack of a living polymerisation technique to polymerise the unsaturated end-group. One solution to this problem was shown by Feast and co-workers[17] as they combined two established living polymerisation techniques: anionic and ring opening metathesis polymerisation (ROMP) to prepare polynorbornene-*g*-polystyrene (PNB-*g*-PS). Initially polystyrene was anionically polymerised and endcapped with norbornene. The highly ring strained norbornene group was ring opened in a step-wise fashion in the presence of the Schrock initiator (a molybdenum base complex, see figure 2.1.7). Combination of these two living processes produced a well-defined graft copolymer consisting of a PNB main chain with pendant PS chains. The living nature of each step provided control over the molecular weight, molecular weight distribution and grafting density of both the main and graft chains.

2.1.2.3 Ring Opening Metathesis Polymerisation

Olefin metathesis is a catalytically induced bond reorganisation process and involves exchange of carbon to carbon double bonds. For an acyclic olefin this leads to exchange of alkylidene units. The first report such a process was given by Calderon[18, 19] where he published his results from the polymerisation of cyclo-octene and cyclo-1,5,-diene in ethanol, using tungsten hexa-chloride and dichloro ethyl aluminium as co-catalytic system.

One class of olefinic metathesis reactions that has developed from this initial experiment is ring opening metathesis polymerisation (ROMP), which is now an established route to various commercially viable products. For example poly(p-phenylenevinylene) exhibits emissive electroluminescence and is implemented as an emissive material in diodes[20]. Polyacetylene is another example as it is produced as flexible semi-conducting films that can be made highly conducting by either oxidation or reduction[21].
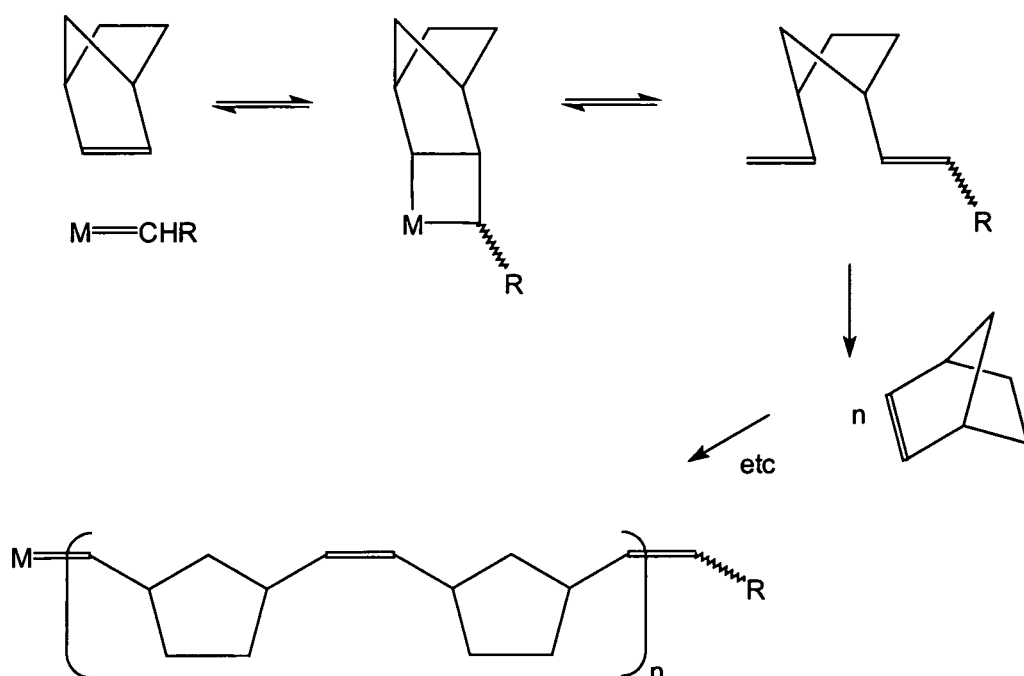

Figure 2.1.4. Proposed mechanistic steps for ring opening metathesis polymerisation of norbornene.

It was initially proposed that the mechanism for ROMP involved the overlap of orbitals from the transition metal with the p-orbitals from the monomer double bonds. This theoretically would allow the formation of a weak cyclobutane type complex[22]. This idea was superseded however with the postulation that a metal carbene forms and acts as the propagating species[23]. Such a process involves a reversible [2+2] cycloaddition of the olefinic carbon-carbon double bond to a metal carbene species. This forms a metallocyclobutane, which then ring opens either degenerately to regenerate the original starting materials, or productively to form a new olefin and a new metal carbene. Repetition of the productive cycle results in the formation of an unsaturated polymer chain. This mechanism is outlined in figure 2.1.4 where M represents the metal in the initiating complex, M=CHR is the propagating species and the monomer is bicyclo[2.2.1]heptene, commonly referred to as norbornene. The propagating complex remains active until a transfer or termination reaction occurs, resulting in regeneration of the metal complex.

The ROMP process is living, hence monodisperse material can be prepared with desired M.Wt. The living character of these polymerisation reactions lends itself to the preparation of well-defined block[24] or graft[25] copolymers.

The driving force for the ROMP of functionalised cyclic monomers is predominantly ring strain. For small rings (with three, four or five carbons) the deformation of the bond angles during ring opening is thermodynamically favourable. Alternatively for rings with seven or more carbons, torsional or transannular effects are the driving forces. For example the ROMP of the monomer species norbornene is favoured despite there being no enthalpic change in the reaction (no net bond making or breaking), due to high ring strain of the bi-cyclic compound[26].

The stereochemistry of the final product depends on the respective orientation of the propagating species and monomer during propagation. There are four stereochemically different polymers that could result from a symmetrical olefinic monomer and these are shown for norbornene in figure 2.1.5. The backbone double bonds can either be cis or trans to each other and also every monomer possesses two chiral carbons each giving rise to varying tacticities. Further stereochemical complexity is quickly introduced when unsymmetrical monomers are polymerised as alternating head/tail monomer addition ensues. These differences in microstructure can be detected by careful examination of their ^{13}C NMR spectra[27]. Stereochemical control of the

ROMPed product can be attained however by meticulously designing the initiating metal complex[28].
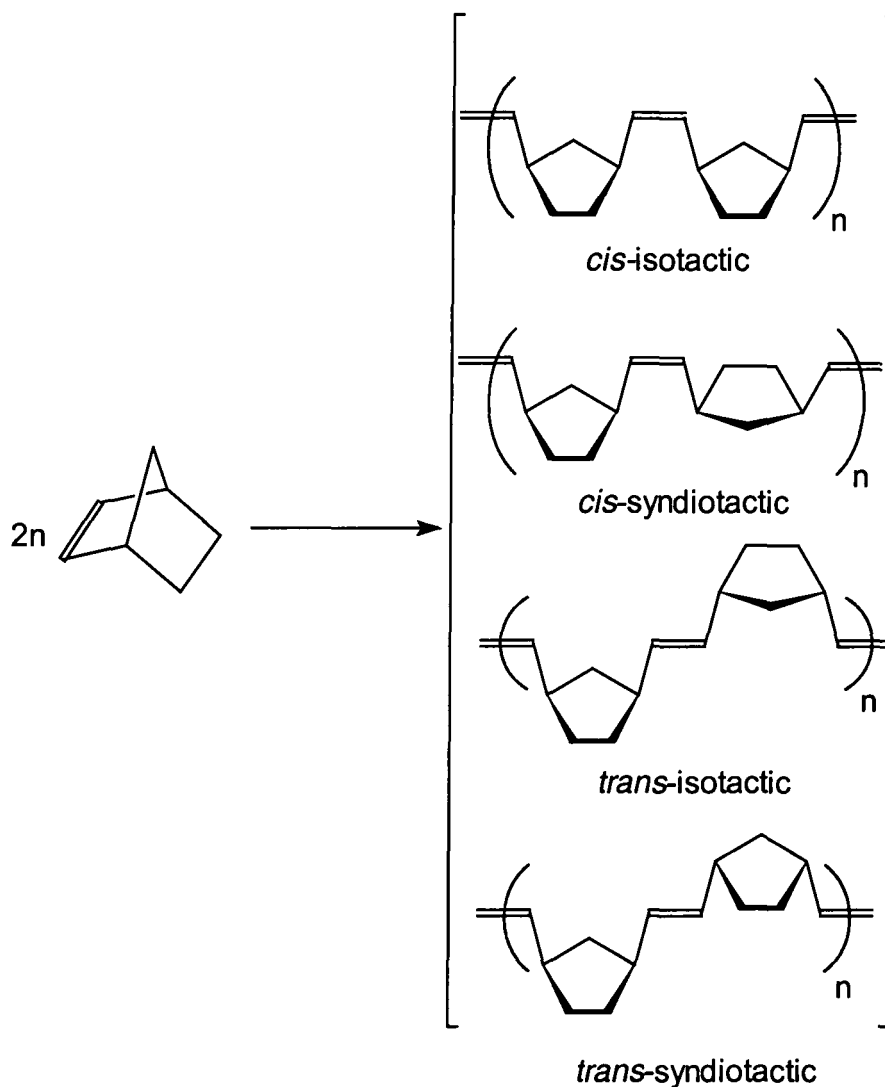
Figure 2.1.5. The four possible assembly modes of ring-opened norbornene monomers.

2.1.2.4 Initiating Species for Ring Opening Metathesis Polymerisation

The transition metal complexes used to initiate ROMP have developed over the past 15 years providing more robust reaction conditions, an extension of monomer functionalities tolerated and increased efficiency. In the early days of ROMP the initiating species (now referred to as the classical catalysts) were easily prepared but

were intolerant to many functional groups present on the monomer. A dual-component formulation of a transition metal halide and a main group co-catalyst for example WCl$_6$ with Ph$_4$Sn, was often used to initiate the polymerisation of compounds such as phenyl alkynes[29]. The initial formation of the alkylidene complexes was slow, occurred in low yield and many of the complexes formed decomposed during a typical polymerisation reaction. All these factors contributed to the final product having an ill-defined architecture with a broad molecular weight distribution.

In 1986 Grubbs and co-workers reported that two titanacyclobutane complexes, shown in figure 2.1.6, initiated the polymerisation of cycloalkene monomers to give well-defined materials[30, 31]. This strategy was developed and each metal complex led to the successful preparation of diblock and triblock copolymers of norbornene[32, 33] and substituted norbornene[34] compounds.
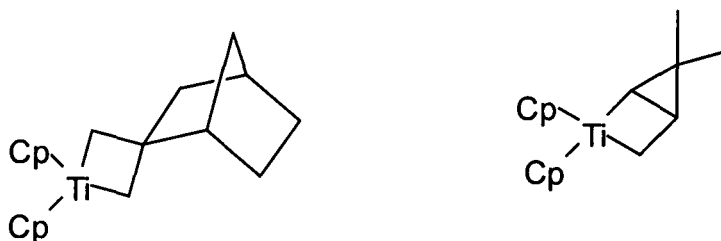
Figure 2.1.6. First reported ring opening metathesis initiators for the polymerisations of a cycloalkene compound.

The drawback of polymerisation reactions involving the titanium complexes was that they were only successful at elevated temperatures (> 50 °C) and deactivation was common in the presence of any functional group. Such problems were overcome with the development of new transition metal complexes[35] with tungsten, molybdenum and more recently ruthenium at the core. Each of these compounds possesses a metal-carbene bond and has various bulky substituents in attempt to gain thermodynamic and kinetic control. Examples of two such complexes with tungsten and molybdenum at the core are given in figure 2.1.7. These tetrahedral complexes have been meticulously designed to provide sufficient space for small molecules to attack the central metal atom, and formation of the tetrahedral transition complex predicted in figure 2.1.4. The bulky nature of the ligands helps prevent decomposition or ligand scrambling reactions of the intermediate compound and their presence also enhances the stereoregularity of

the polymer produced by influencing the orientation of the approaching monomer. The ligands can also be designed to control the activity of the metal by altering the degree of Lewis activity[36], for example the reactivity towards ordinary olefins is enhanced when a *t*-butoxide ligand is replaced with the more electron withdrawing ligand hexafluoro-*t*-butoxide. The electrophilicity of the ligand is thought to influence the first step of the mechanism, since any change will alter the activity of the metal core, which will in turn effect the rate of electrophilic attack of the olefin by the metal core. The less reactive complex with the *t*-butoxy ligand is still useful for polymerisation of for example functionalised norbornene, as it reduces the possibility of undesired backbiting reactions.

Ar = 2,6-C_6H_{3i}-Pr$_2$

R = CMe$_3$

R' = CMe$_2$Ph
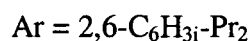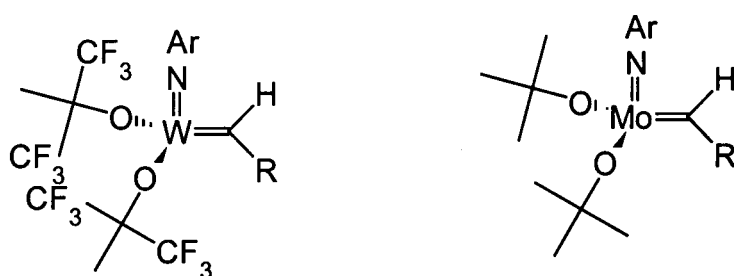
Figure 2.1.7. Example of molybdenum and tungsten initiating complexes for the ROMP reaction.

Tungsten complexes are more reactive than their molybdenum counterparts consequently they are less tolerant and deactivate in the presence of many functionalised groups. Molybdenum complexes have the advantage of being stable in the presence of such groups including acetyl, cyano, epoxy and ester functionalities and fluorinated side groups. Both initiating species however decompose in the presence of oxygen, moisture or other protic impurities and to avoid unwanted deactivation the polymerisation reactions are carried out in inert atmospheres.

The initiating complex developed by Grubbs and co-workers[37] is shown in figure 2.1.8 and consists of a ruthenium core with bulky ligands in a tetrahedral

environment. Such complexes are highly versatile as they tolerate functionalities such as ketones, amines, alcohols and acids, and can even be used in aqueous media[38]. The activity of the catalyst can be manipulated by alternating the substituents on the phosphine ligands, for example a tri-phenyl phosphine substituted complex allows ring opening of highly strained electron ring olefins. Alternatively a tri-cyclohexyl phosphine ligand is more reactive towards monomers containing functional groups, for example monomers with acyclic groups. In each case the ruthenium initiator produces polymeric material with a well-defined structure.
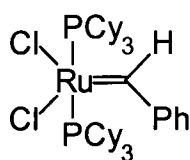
Figure 2.1.8. Ruthenium complex known as the Grubbs initiator.

Section 2.2   Monolayer Behaviour

2.2.1   Spread Films

The surface tension, γ, of an air-liquid interface is defined as the quantity of work required, dW, to increase the area of the liquid surface isothermally and reversibly by unit area, dA.

$$\gamma = \frac{dW}{dA}$$ **Equation 2.2.1.**

When an insoluble or surface active material forms a thin film on such a liquid surface, the surface tension is reduced since the film increases the thermodynamic stability at the surface[39]. The two dimensional surface pressure exerted by the film, π, is defined as this reduction in surface tension;

$$\pi = \gamma_0 - \gamma$$ **Equation 2.2.2.**

where γ_0 and γ are the surface tensions of pure liquid and that of the film covered surface respectively. By monitoring changes in the surface pressure as a function of surface concentration a qualitative insight into the molecular organisation of the film at the interface can be obtained. The necessary data is obtained using a Langmuir trough with movable barriers that allow the surface concentration to be easily varied by compressing and expanding the film, while changes in the surface pressure are continuously monitored using a Wilhelmy plate (see Chapter Three for further details). These variations in surface pressure are plotted as a function of surface concentration thus providing a surface pressure isotherm. An example of an ideal isotherm for low molecular weight materials, for example stearic acid, is given in figure 2.2.1. This diagram highlights the three individual orientation states that simple molecules classically exhibit: the gaseous (G); liquid expanded (LE) and the liquid condensed (LC).
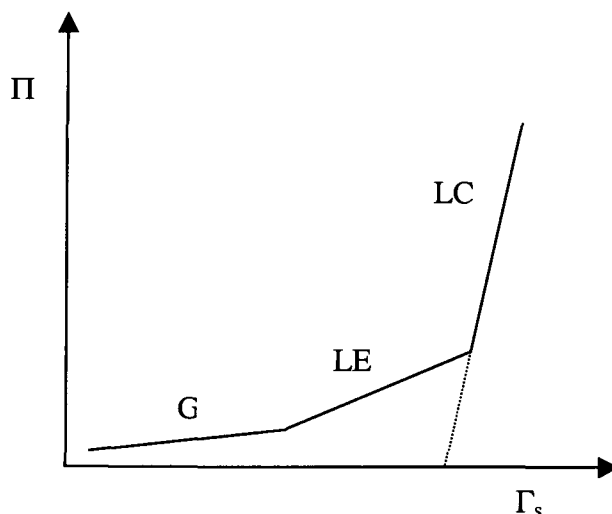
Figure 2.2.1. A typical surface pressure isotherm for low molecular weight material representing the three different monolayer states: gaseous (G), liquid expanded (LE) and liquid condensed (LC) for low molecular weight materials.

The gaseous state occurs when the surface concentration of molecules is low, hence the area per molecule is large in comparison to molecular area. The individual components have freedom to move independently over the surface and they obey the two-dimensional equation of state of a perfect gas, $\pi A = RT$, where R is the gas constant and T is the temperature of the system. In contrast the liquid condensed state occurs when the surface concentration is high forcing the molecules to pack closely and orientate steeply towards the surface. In the intermediate (liquid expanded) state the molecules still have freedom to move on the surface but they begin to overlap and interact with each other.

Generally polymeric films do not undergo distinct changes in state, hence their surface pressure isotherms are relatively featureless[40]. When a polymer film is compressed the surface pressure tends to increase in a uniform manner and the molecules move gradually from a liquid expanded state into a liquid condensed phase. If the region of sharpest increase in the isotherm is extrapolated to zero surface pressure (dotted line in figure 2.2.1), the minimum area per molecule can easily be calculated. This value is valid for small molecules but can be applied to polymers to provide a qualitative insight into surface organisation. Care needs be taken however when interpreting this value for polymeric material as chain segments may be coiled or desorbed at the surface thus rendering it difficult to discuss the precise organisation of

polymer monolayers. However, by analysing the shape of each isotherm a qualitative picture of molecular orientation as a function of surface concentration can be drawn.

2.2.2 Equations of State

To expand on the speculative monolayer characteristics extracted directly from surface pressure isotherms mathematical models, equations of state, have been introduced. These models are fitted to the experimental data using parameters that provide a physical interpretation of the monolayer behaviour. Singer[41] introduced the first models by developing Huggins theory of polymer solutions[42] to relate changes in the surface pressure to the degree of polymerisation and surface area. Frisch[43] expanded this work to account for the looping of chains, and subsequently Motomura[44] included cohesive forces.

Attempts to quantify monolayer behaviour initially involved the introduction of the mean field description by Scheutjens and Fleer[45, 46]. This theory however, overestimated stretching and excluded volume interactions of polymer in good solvent conditions (see section 2.3.1). More recently Daoud and Jannink[47] developed the theory to describe homopolymers in three dimensions and these mathematical relationships have been manipulated to include the dimensionality of the system as a variable, thus enabling application of the laws to two-dimensional monolayers. This theory has been applied to spread polymer layers and the results have been discussed in a qualitative manner[48]. Much of this work has been summarised by Kawaguchi[49].

2.2.3 Scaling Theory

de Gennes extended the theory outlined above and developed scaling theory[50] where he uses mathematical power laws to express the dynamic and thermodynamic properties of polymer molecules immersed in a good solvent, as a function of their molecular weight and concentration. From such analysis he predicted that polymers when surrounded by a good solvent can adopt one of three different conformations depending on the solution concentration: dilute; semi-dilute and concentrated. This

treatment was extended to describe monolayer behaviour where the three states (dilute, onset of semi-dilute and semi-dilute) describe two-dimensional solutions. These different regimes, represented schematically in figure 2.2.2, relate to the number of entanglements of the individual polymer chains. They range from the dilute solution where the polymer molecules exist as separate entities, to the semi-dilute case where the molecules interact to a significant extent. When the polymeric chains first begin to overlap they behave as hard spheres and this conformation is known as the onset of semi-dilute conditions.

Dilute   **Onset of semi-dilute**   **Semi-Dilute**
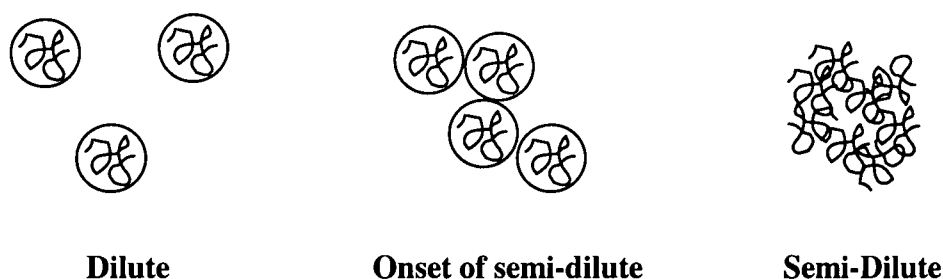
Figure 2.2.2. Representation of dilute, onset of semi-dilute and the semi-dilute regime.

A summary of the fundamental points of the scaling laws for each conformation and their application to two-dimensional systems is given here[47].

2.2.3.1 Dilute Regime

At low polymer concentrations molecules exist as single entities, therefore only intrachain interactions are important. In a good solvent, repulsion between separate polymer segments leads to the swelling of the polymer molecule. It is postulated that individual polymer coils occupy a sphere of radius equivalent to the radius of gyration (R_g). The radius of gyration is dependent on the number of monomer units, N, present in the polymer and the excluded volume exponent, υ.

$$R_g = N^\upsilon$$
                                           Equation 2.2.3.

The excluded volume exponent, for a good solvent, is related to the dimensionality of the system, d_m, via Florys general expression;

$$\upsilon = \frac{3}{d_m + 2}$$

Equation 2.2.4.

By modelling the polymer coils as impenetrable spheres and applying the pseudo gas law, the osmotic pressure of the system, π, is expressed in terms of solution concentration, c,

$$\frac{\pi}{T} = \frac{c^2}{N} + A_2 c^2$$

Equation 2.2.5.

where T is the temperature and A_2 is the second virial coefficient. The value of A_2 depends on the nature of the polymer-solvent interactions and generally increases numerically as interactions improve. des Cloizeaux[51], Daoud and Jannink[47] incorporated the dimensionality of the system into equation 2.2.5, thus allowing the two-dimensional osmotic pressure for a monolayer to be expressed as;

$$\frac{\pi}{RT} = \frac{\Gamma_s}{M_n} + \Gamma_s^2 A_{22}$$

Equation 2.2.6.

where Γ_s is the surface concentration, M_n, is the molecular mass and A_{22} is the two-dimensional second virial coefficient.

2.2.3.2 Onset of Semi-Dilute Regime

The onset of semi-dilute conditions is basically a diffuse intermediate stage that occurs at a critical threshold concentration, c^*, where polymer chains just begin to touch each other, and interact. It has been predicted that c^* is identical to the local concentration of an individual polymer coil and can be expressed as a function of its radius of gyration;

$$c^* = \frac{N}{R_g^{\ 3}} = a^{-3}N^{(1-3\upsilon)} = a^{-3}N^{-\frac{4}{5}}$$ **Equation 2.2.7.**

where a is the length of a monomer unit. The equivalent threshold value for the volume

fraction ϕ, is $\phi^* \leq N^{-\frac{4}{5}}$.

2.2.3.3 The Semi-Dilute Regime

When the concentration of polymer in solution exceeds the critical concentration the distance between each sphere becomes less than the radius of gyration and the polymer chains begin to overlap. In this case both intramolecular and intermolecular interactions are important, therefore the polymer chains can no longer be pictured as single spheres. This led to the development of 'blob' theory, where the overlapping molecules are divided into sequential segments of size ξ, which is referred to as the screening, or correlation length. When the distance between the overlapping coils is higher than ξ only intrachain interactions occur hence polymer behaviour is akin to a single chain with excluded volume. Conversely when the distance between the polymer chains is less than ξ, the material is classified as being in the semi dilute regime and the thermodynamic properties are no longer dependant on the degree of polymerisation, but on the concentration as predicted by the scaling law for osmotic pressure;

$$\frac{\pi}{T} \approx \frac{c^*}{m} \approx k.\left(c^*\right)^m$$ **Equation 2.2.8.**

where $m = \dfrac{\upsilon d_m}{\left(\upsilon d_m - 1\right)}$ and k is a constant.

The dimensionality, d_m, of the system was again manipulated to allow treatment to a monolayer, where the surface coverage was above the threshold value, Γ_s^*;

$$\pi = \Gamma_s^y \qquad\qquad \textbf{Equation 2.2.9.}$$

where $y = \dfrac{2\upsilon}{2\upsilon - 1}$.

For good solvent conditions mean field theory predicts ν to be 0.75^{52}, and generally this values has been observed experimentally[48] and predicted from Monte Carlo simulations[53, 54] and matrix transfer methods[55]. In theta solvent conditions a wide range of values have been offered[56] ranging from 0.50 (the ideal random walk value) to $\frac{2}{3}$ (the mean field value when only ternary interactions are considered), but currently 0.55 is the recognised value.

Section 2.3 Brush Theory

It is known that the properties of interfaces can be modified by the presence of polymer molecules[57]. The surface energy is lowered for example and the interfacial fracture toughness is improved between two immiscible polymers when a diblock copolymer is present at the interface (with blocks similar in structure to each bulk polymer)[58]. Tethered species are polymeric chains that are attached by one end to a surface or interface, either by adsorption or chemical grafting. These materials also exhibit similar stabilising behaviour and have numerous practical applications such as the stabilisation of colloidal particles[59], adhesion technology[60] and also have significant biological importance for example inhibiting the adsorption of proteins or cells onto surfaces[61]. The architecture, conformation and concentration of such polymer materials have a profound influence on the interfacial behaviour of the system. Theoretical models for such behaviour are outlined in the following section.

2.3.1   Free Polymer Chains

When an isolated polymer molecule (of specific degree of polymerisation) is mixed and dispersed in a suitable solvent, then the size of the polymer coil depends on the thermodynamic quality of the solvent[57]. In a good solvent (where the interaction between the two species is attractive) the polymer coil expands from its unperturbed dimensions, as individual segments seek to maximise contact with the solvent. This is driven by the repulsive excluded volume interactions between the segments (positive excluded volume). In a poor solvent (where the interaction between polymer segment and solvent species is repulsive) there are few polymer/solvent interactions and the coil collapses in on itself since the interaction between polymer segments is attractive (negative excluded volume).

The conformation of a polymer coil in solution also depends on the temperature of the system[57]. As the temperature increases for any given polymer/solvent system, the thermodynamic quality of solvent also improves. The transition from the poor to good regime occurs at a specific temperature known as the theta temperature. In this state the

excluded volume effects are eliminated and the polymer coil is in its unperturbed dimensions.

2.3.2 Tethered Polymers in Pure Solvent

The conformation and molecular interactions exhibited by tethered polymers (at a surface or interface) are qualitatively different in comparison to free chain molecules in solution[62],[63]. Such variation is due to the limitation of configurational space in the case of tethered chains, since one end of the molecule is fixed to a point (for a solid-solvent interface) or fixed in a two-dimensional plane (for a fluid-fluid interface). If for example a monodisperse material is considered, which is chemically grafted on a macroscopically flat surface and is surrounded by a thermodynamically good solvent, then two different behavioural regimes are possible. Classification of these regimes depends on two parameters: the number of grafts in an unit area (square of a segment size), which is a dimensional parameter referred to as the grafting density, σ, and also on the radius of gyration, R_g. The first case occurs when the radius of gyration of the polymer coil is less than the distance between grafting points, hence there is no interaction between polymer chains. In this regime two conformations are possible. The first occurs when the individual molecules are swollen and form a series of *mushrooms* (figure 2.3.1(a)). The second conformation transpires when the tethered molecules preferentially adsorb at the interface (i.e. they reduce the surface tension of the liquid surface) where the polymers lie flat at the interface as *pancakes* (figure 2.3.1(b)) but still do not interact. The second behavioural regime occurs when the distance between tethered ends is less than R_g, thus forcing the polymer coils to overlap and interact. Excluded volume interactions between neighbouring chains cause the tethered polymers to stretch normal to the interface, hence minimising monomer/monomer contact while the maximising the enthalpically favourable monomer/solvent interactions. This lowering of the interaction energy per polymer chain is counterbalanced by an increase in the elastic free energy, since each chain is being stretched from its random walk configurations. It is the balance between these two forces that controls the extent of stretching of the polymer chains, which are commonly referred to as polymer *brushes* (figure 2.3.1(c)).
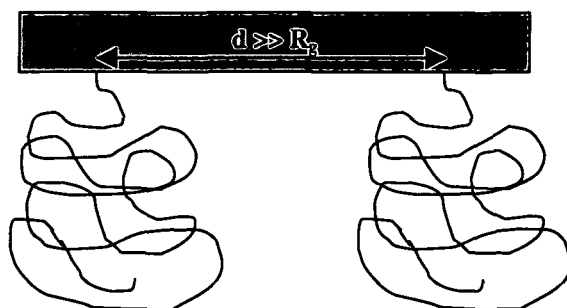
a) Mushrooms
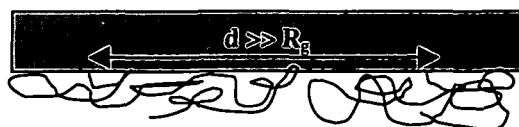
b) Pancakes
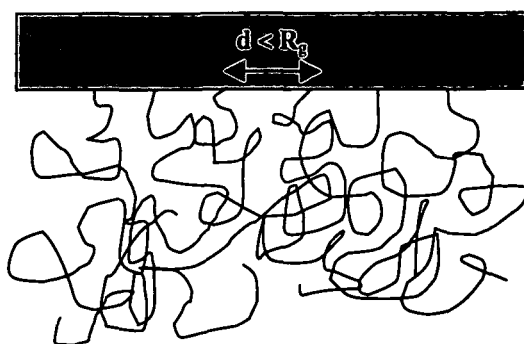
c) Polymer brushes

Figure 2.3.1. Schematic illustration of : a) mushrooms, b) pancakes and c) polymer brushes

The brush height (h, the distance from the tethered end of the polymer to the point where the volume fraction falls to zero) depends not only on the grafting density, but also on the thermodynamic quality of the solvent. If the solvent is good then the brush height is up to several times the unpeturbed radius of gyration. When the solvent quality reduces however, the brushes tend to collapse as the segments attempt to reduce their enthalpically unfavourable interactions with solvent molecules.

The volume fraction profile of the distribution of tethered polymer chains from the interface has been the subject of numerous theoretical models. The relevant models for grafted chains to this study will be discussed here. These include tethered chains in good solvent conditions where the solvent molecule is small in comparison to the polymer, and also when the polymer is immersed in a solution of mobile polymer.

2.3.2.1 Tethered Polymers Immersed in a Good Solvent

Alexander[64] pioneered theoretical predictions of the conformation and stretching of solvated, tethered polymers. He predicted that the brush extended from the interface with a uniform profile and using scaling arguments expresses brush height, h, as;

$$h \sim Na\sigma^{1/3} \qquad\qquad \textbf{Equation 2.3.1.}$$

where N is the degree of polymerisation of the chain, a is the Kuhn step length of the repeat unit and σ is the grafting density (number of grafts per unit area). In this study where the organisation of a graft copolymer is compared to the behaviour of polymer brushes the grafting density was calculated by;

$$\sigma = \frac{\Gamma_s N_A X}{M_n} \times 10^{-23} \text{ chains per Å}^{-2} \qquad\qquad \textbf{Equation 2.3.2.}$$

where Γ_s is the surface concentration, M_n is the average mass of one repeat unit, N_A is Avogadros number and X is the number of grafts on each molecule.

de Gennes[65] developed the scaling arguments using an energy balance to characterise brush behaviour which is valid when the conditions within the brush become concentrated, for example at higher grafting densities. The relationship he proposed is given in equation 2.3.3 and incorporates the significance of excluded volume per statistical step length, υ, on the extent of brush stretching,

$$h \sim N(\upsilon\sigma)^{\frac{1}{3}}$$ **Equation 2.3.3.**

The models proposed by Alexander and de Gennes both suggest that the brush height exhibits a linear dependence on the degree of polymerisation of the graft chain, and on the cube root of the grafting density. Each model assumes that the polymer volume fraction is constant throughout the brush, i.e. a uniform distribution, and that all the free ends of the brush are located at the outer extremity. This assumption is however not very realistic but is useful as a first approximation.

Milner, Witten and Cates[66] developed theoretical predictions for the statistics of a grafted polymer brush using a self-consistent field method (SCF), which is valid for weak excluded volume interactions and for moderately high surface coverage. Their model system consisted of a set of monodisperse polymer chains in a thermodynamically good solvent, but contrasting both Alexander and de Gennes, Milner and co-workers made no assumption regarding the monomer distribution normal to the interface (except that one end was tethered to the interface).

The solution from the SCF equations postulate that the height of the brush scales as;

$$h = \left(\frac{12}{\pi^2}\right)^{\frac{1}{3}} N(\sigma\upsilon)^{\frac{1}{3}}$$ **Equation 2.3.4.**

This relation reveals that the height of the brush in SCF theory is again linearly dependent on the number of repeat units and the cube root of the grafting density, identical to the prediction of scaling theory. Differences between the theories are apparent when the number density distributions are compared. The volume fraction profile from the SCF calculations predicts a parabolic decay from the surface,

contrasting the step-function of scaling arguments. Moreover the free polymer chain ends are distributed throughout the entire height of the brush rather than unrealistically confined to the brush tip. This theory has been extended by Shim and Cates[67] as they consider finite extensibility of the chain at high surface coverage's ($\sigma > 0.05$). They found that the density profile was a little flatter than a pure parabolic distribution but still scales according to equation 2.3.4 for the majority of surface coverage. Deviation was only found when the volume fraction throughout the entire polymer layer approached unity where the penetration depth scales exactly with grafting density. Comparing the volume fraction profiles predicted highlights the differences in polymer distribution between the two theories (figure 2.3.2).

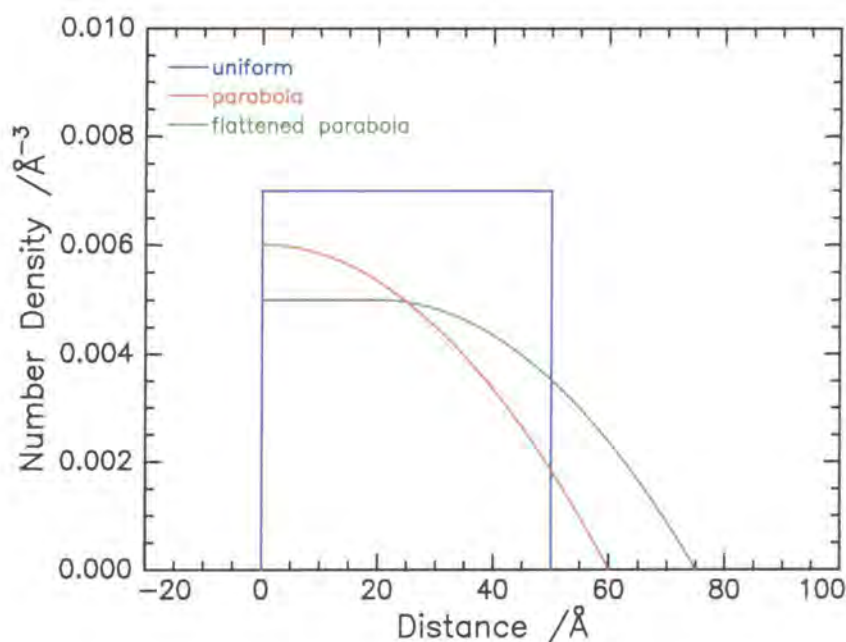**Figure 2.3.2.** Schematic illustration of a uniform (blue) and parabolic (red) number density distribution as a function of distance form the grafting surface, z, from the interface.

2.3.2.2 Tethered Polymers in Mobile Polymer Solution

The theoretical predictions for the conformation of grafted chains in good solvent has been extended to the structure of tethered chains in polymer melts and in

polymer solutions. This theory is valid for a three component system where the tethered chains are immersed in a semi-dilute solution of free homopolymer chains, which are chemically identical to the grafted material.

Scaling theory[65] and self-consistent field theory[68, 69] have both been applied and both show that the layer thicknesses are dependent on the degree of polymerisation of both grafted and mobile chains; the concentration of both typical chains and also on the grafting density of the tethered chain. Both theories envisage three cases for strongly stretched chains when the number of repeat units in the tethered chain, N, is less than that for the free polymer, P. In the first regime the free polymer plays no role in the organisation of the grafted layer i.e $\phi_N > \phi_P$, where ϕ_N is the volume fraction of the grafted layer and ϕ_P is the volume fraction of the mobile polymer. Such an organisation and scaling relationship is identical to that of the tethered chains in pure solvent: $h \sim N a \sigma^{1/3}$. As the free polymer concentration increases such that $\phi_P > \phi_N$, significant contraction of the tethered layer is anticipated. This layer shrinkage can occur via two different routes depending on the osmotic pressure inside the grafted layer. The first occurs when the system reaches equilibrium with minimal penetration of the free polymer (second regime), or alternatively with significant penetration of mobile material (third regime). The polymer brushes in these two regimes are often referred to as unmixed and mixed respectively. The latter scenario leads to screening of excluded volume interaction between monomer species within the tethered layer. The scaling predictions for both regimes are given in equations 2.3.5 and 2.3.6 for the unmixed and mixed regimes respectively.

$$L = \sigma N \varphi_N^{-1}$$

Equation 2.3.5.

$$L = \sigma^{1/3} N P^{-1/3} \varphi_N^{-5/12}$$

Equation 2.3.6.

There has been no theory published to date for the case where the free chains are large in comparison to the tethered chains (i.e. $P \gg N$). This scenario has only been alluded to[68] in passing where it has been suggested that the third region completely disappears and is replaced by the expanded second regime where the grafted and mobile chains are separated.

Section 2.4   Neutron Reflectometry

Neutron reflectometry is a well-established technique for investigating the structural properties of polymer materials at surfaces and interfaces[70]. This approach is attractive as it allows the study of 'buried' interfaces, is non-evasive and has a high spatial resolution. When a beam of neutrons is incident on such a surface it generally behaves in an analogous manner to light (or X-rays), since the beam is reflected to an extent depending on the refractive index of the sample. The significant difference between the two techniques is the interaction that occurs between the probing radiation and the interface, since X-rays are scattered by electrons and neutrons are scattered by nuclei.

When a beam of neutrons is incident on a surface four different processes occur including specular reflection, transmission, bulk scattering and non-specular reflection, as outlined in figure 2.4.1 as processes 1, 2, 3 and 4 respectively.
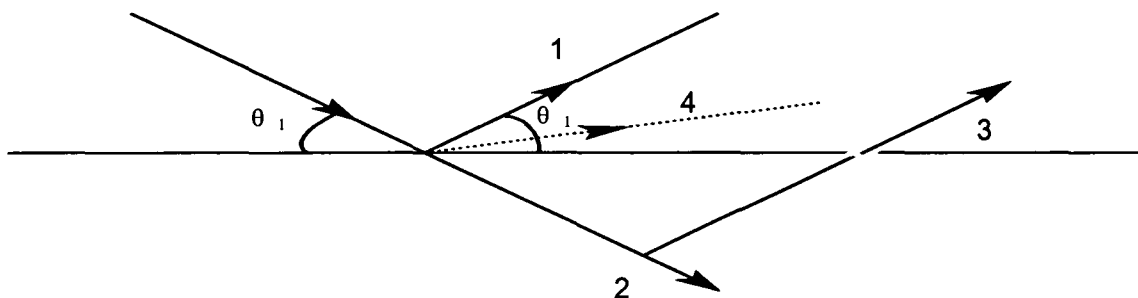
Figure 2.4.1. Processes that occur when a neutron beam hits a surface: 1 - specular reflection; 2- transmission; 3- scattering from the bulk and 4 - non-specular reflection.

Specular reflection (1) from a surface occurs when the angle of incidence equals that of reflection. Non-specular reflection (4) occurs when the surface under study has been roughened by, for example, thermal fluctuations, but the intensity of reflection from these processes is less than the background signal, if the experimental system is mounted on an anti-vibration table. Specular reflection also occurs from the bulk subphase (3) (if a scattering species is present), which contributes to the background signal. If the beam is not reflected to any extent then it is completely transmitted into the subphase (2). Experimentally the reflectivity from a surface is monitored by taking

the ratio of the intensity of the specularly reflected beam to that of the incident beam, and basically changes in the reflectivity collected as a function of depth normal to the interface are related to variations in the molecular organisation.

As previously stated the reflective properties of neutrons are analogous to those of light hence the basic rules of geometric optics can be applied to neutron reflectometry with minimal alterations. When discussing the reflection of neutrons the terms wavevector and scattering length densities replace the conventional optical terms of scattering angle and refractive index. The neutron refractive index at the boundary between two media determines the extent to which the neutrons are reflected from a surface. If a macroscopically smooth surface is considered then the neutron refractive index, n, can be expressed as;

$$n = 1 - \frac{\lambda^2 Nb}{2\pi}$$ **Equation 2.4.1.**

where λ is the wavelength of the neutron beam, N is the atomic number density and b is the coherent scattering length of the atom. In contrast to X-ray reflectivity the scattering length is a nuclear property, therefore the values vary randomly across the periodic table. Values for nuclei pertinent to this study are given in table 2.4.1.

Nucleus	b / scattering length x 10^{-4} Å
C	0.67
O	0.58
^{1}H	-0.37
^{2}H	0.68

Table 2.4.1. Scattering length values for various nuclei pertinent to this study.

The magnitude and sign of the scattering length influences the amplitude of the reflected wave. A high positive scattering length, for example deuterium (see table 2.4.1), enhances the amplitude of the neutron beam, thus coherently reflecting the neutrons strongly. Contrasting this behaviour is the coherent scattering of its isotope, which is weak and the reflected signal merely contributes to the incoherent background.

Such characteristics are due to the magnitude of the scattering length being small, and also the negative sign causes the incident beam to undergo a phase change following interaction with a hydrogenous nucleus, which effectively reduces the reflected intensity. This difference in scattering power between these two isotopes is fundamental to the neutron reflectometry work undertaken in this study on spread polymer monolayers at fluid interfaces.

The scattering length density, ρ, depends on the number density, n_i, and scattering length, b, of species i at the surface.

$$\rho = \sum_i n_i b_i \qquad \textbf{Equation 2.4.2.}$$

By combining equation 2.4.1 and 2.4.2 it is evident that the surface refractive index is dependent on the scattering length density and consequently the atomic composition normal to the surface. It is fortuitous therefore that hydrogen and deuterium have vastly differing scattering lengths, as changing the isotopic composition of the material at the interface permits the superphase or subphase to provide contrast in otherwise physically identical experimental systems without perturbing the original organisation. Such contrast variation allows the number density distribution of all components to be identified normal to the interface. The orientation of molecules on a microscopic scale is unfortunately not attainable as the experiment is restricted by the low resolution of the technique, hence isotopic labelling is confined to whole segments or blocks of atoms.

Values for the scattering length and scattering length densities for components relevant to this study are given in table 2.4.2. The opposing signs of light (H_2O) and heavy (D_2O) water allow the preparation of a subphase with a scattering length density of zero, simply by combining the components in an appropriate ratio. This mixture is referred to as null reflecting water (nrw) and does not contribute to the coherent scattering of neutrons.

Unit	$\Sigma b_i / 10^{-4}\,\text{Å}$	$\rho / 10^{-6}\,\text{Å}^{-2}$
H_2O	-1.68	-0.56
D_2O	1.92	6.35
air	0	0
ethylene oxide	0.41	0.56
deuterated ethylene oxide	4.58	6.33
norbornene	1.78	0.89

Table 2.4.2.   Scattering length and scattering length densities for materials used in this study.

The fundamental variable in a neutron reflectometry experiment is the scattering vector, Q;

$$Q = \frac{4\pi}{\lambda}\sin\theta$$

Equation 2.4.3.

Q is the magnitude of the vector between the transmitted beam and the specularly reflected beam, as illustrated in figure 2.4.2, where k_i and k_r are the wavevectors of the incident and reflected beam respectively.

The organisation of materials can be probed at various depths normal to the interface simply by monitoring the reflectivity over a range of Q values by altering either the wavelength of the incoming neutron beam, λ, or the grazing angle of incidence, θ.
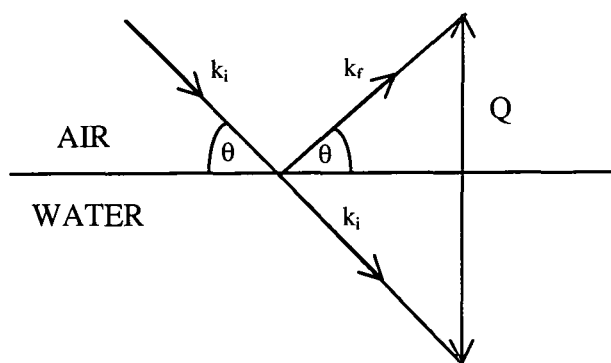
Figure 2.4.2. Wavevector diagram.

A complete description of the theory behind this technique has been summarised by several authors[70-73]. Only a brief outline of the fundamental points are outlined here.

2.4.1 Specular Reflection

When a neutron beam impinges a macroscopically smooth surface, specular reflection of all incident neutrons occurs at a critical angle θ_c. From Snells law, $n_1\cos\theta_1 = n_2\cos\theta_2$, where n_1 and n_2 are the refractive index of layer 1 and 2 respectively, total specular reflection will occur at the upper surface when equation 2.4.4 is obeyed.

$$\cos\theta_c = \frac{n_2}{n_1}$$

Equation 2.4.4.

The air-water interface for example has a very small critical glancing angle since the refractive index of both the upper and lower media are approximately one. The value for the critical angle can be calculated by combining equations 2.4.1, 2.4.2 and 2.4.3 and using a cosine expansion to give the following;

$$\theta_c = \lambda\sqrt{\frac{\rho_d}{\pi}}$$

Equation 2.4.5.

where ρ_d is the scattering length density of the subphase.

For an air-D_2O interface the critical angle occurs at a critical momentum transfer (Q_c) of 0.0179 Å^{-1}. The lowest Q value obtained experimentally in this study was circa 0.025 Å^{-1}, therefore the critical angle is not encountered during experimental studies.
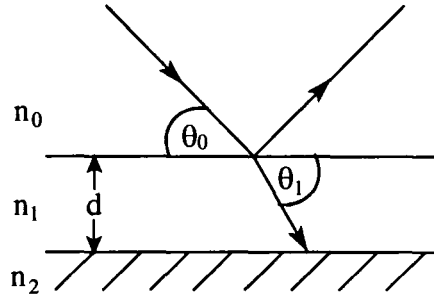
Figure 2.4.3. The specular reflection from a single film, n_1, at an interface between two media n_0 and n_2.

The organisation of a monolayer, 1, when spread at an interface between two media, 0 and 2, (indicated in figure 2.4.3) can be probed using neutron reflectometry. The reflectivity, R, of such a system is analysed as a function of scattering vector and can be expressed according to Fresnel as in equation 2.4.6.

$$R = \left| \frac{r_{01} + r_{12}\exp(2i\beta)}{1 + r_{01}r_{12}\exp(2i\beta)} \right|^2 \qquad \textbf{Equation 2.4.6.}$$

The reflected and transmitted amplitudes of the beam at each interface (between 0 and 1, and 1 and 2) are represented by the Fresnel coefficients r_{01} and r_{12} respectively, and β is the phase shift of the beam which can be calculated as the neutrons transverse each layer, i, calculated using equation 2.4.7;

$$\beta = \left(\frac{2\pi}{\lambda} \right) d\sin\theta_i \qquad \textbf{Equation 2.4.7.}$$

where d is the thickness of the monolayer. In general for an i-j interface the Fresnel coefficients are defined as;

$$r_{ij} = \frac{n_i\sin\theta_i - n_j\sin\theta_j}{n_i\sin\theta_i + n_j\sin\theta_j} \qquad \textbf{Equation 2.4.8.}$$

This relationship allows the expansion of equation 2.4.6 to give the expression below for the overall reflectivity of the spread monolayer;

$$R = \frac{r_{01}^2 + r_{12}^2 + 2r_{01}r_{12}\cos2\beta}{1 + r_{01}^2 r_{12}^2 + 2r_{01}r_{12}\cos2\beta}$$

Equation 2.4.9.

Equation 2.4.9 reveals that a maxima and minima in the reflectivity occurs when $\cos2\beta = \pm1$. When Q is greater than the critical value (0.0179 Å^{-1}) and the equation for the phase shift (2.4.7) is substituted into the expression for overall reflectivity, it is clear that the separation of the maxima is dependent on the layer thickness and Q_c of the specific system. Since Q has previously exhibited a dependence on the scattering angle and therefore on the scattering length density and the phase shift through equations 2.4.5 and 2.4.7, then it should now be clear that in principle a complete description (including the composition and depth of the layers) of the near surface can be extracted from a reflectivity profile. In practice data are unable to be Fourier transformed directly to give the composition distribution since phase information is lost from the data and the Q range is limited due to the high incoherent background signal. Interpretation of experimental data therefore frequently relies on comparing data to simulated data from model systems.

Three approaches have been employed in this study to extract structural information from experimental data. The first is an exact method where the experimental data is fitted with theoretical models[74]. The second is the kinematic approximation where the contribution from individual species to R(Q) can be extracted. Finally the third is Bayesian analysis method developed by Sivia[75]. Each method is outlined in the following sections.

2.4.2   The Optical Matrix Method

The optical matrix approach involves simulating a reflectivity curve based on a theoretical model where the surface depth profile is described as a series of lamellae of known thickness and number density as illustrated in figure 2.4.4.
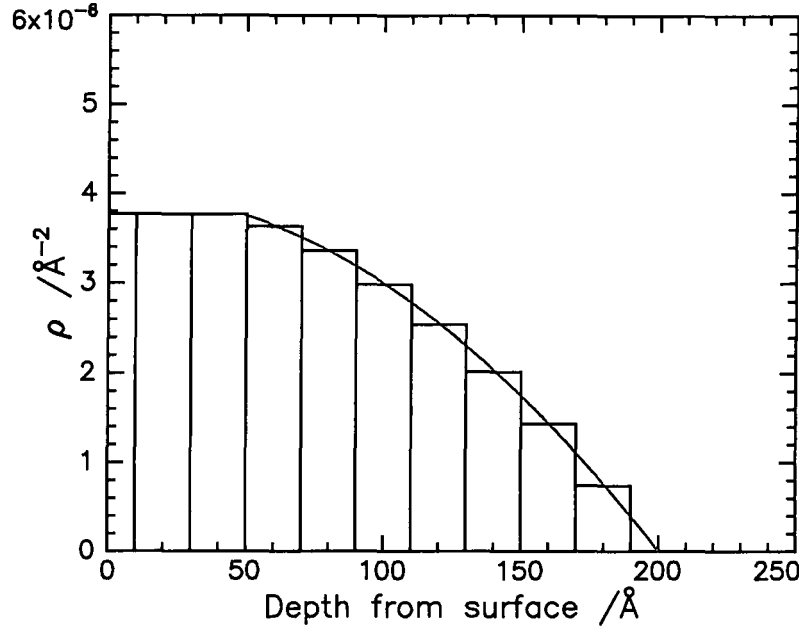
Figure 2.4.4. The gradual change in the scattering length density (red line) and its approximation as a series of discrete lamellae.

The reflectivity curves for the chosen model can be calculated using standard optical methods as outlined in equation 2.4.6. This expression describes a single layer at an i, j interface. Theoretically this approach can be extended to incorporate numerous layers, but in reality the computation becomes exponentially complex. A general solution that overcomes this problem is the characteristic matrix formalism of Born and Wolf[76] where they represent the reflection properties of each stratified layer that models the composition distribution within a characteristic matrix. For example for a single layer, j, the characteristic matrix is given in equation 2.4.10.

$$M_j = \begin{bmatrix} \cos\beta_j & -\left(i/_\kappa\right)\sin\beta_j \\ -i\kappa_i\sin\beta_i & \cos\beta_j \end{bmatrix}$$ **Equation 2.4.10.**

where $\kappa_i = n_i\sin\theta_i$. When a model consists of multiple layers then the product of all the individual matrices provides a resultant 2x2 matrix;

$$M = [M_1][M_2][M_3]\ldots\ldots[M_n] = \begin{bmatrix} M_{11} & M_{12} \\ M_{21} & M_{22} \end{bmatrix}$$ **Equation 2.4.11.**

and the individual elements of the resultant matrix combine to give the overall reflectivity,

$$R = \left| \frac{(M_{11} + M_{12}\kappa_s)\kappa_a - (M_{21} + M_{22})\kappa_s}{(M_{11} + M_{12}\kappa_s)\kappa_a + (M_{21} + M_{22})\kappa_s} \right|$$ **Equation 2.4.12.**

where the subscripts a and s refer to the upper and the lower phase respectively.

The interface under study is however never perfectly smooth. When the surface is rough or the interface diffuse the intensity of the reflectivity signal is reduced[77]. Such effects can be accounted for by introducing a Debye-Waller-like factor of the form;

$$I = I_0 \exp\left(-Q^2 \langle \sigma_r \rangle^2\right)$$ **Equation 2.4.13.**

where I and I_0 are the reflected intensity of the beam with and without surface roughness, and σ_r is the root mean square roughness.

This factor can be substituted directly into equation 2.4.10 but calculations quickly become complex when more than three or four layers are modelled. Abeles[78] provided a method that overcomes such problems by dividing the interface into additional layers that incorporate the roughness, $\langle \sigma_r \rangle^2$. This method, outlined by Heavens[79], defines each layer with a characteristic matrix in terms of Fresnel coefficients and phase factors.

$$M_j = \begin{bmatrix} \exp(i\beta_{j-1}) & r_j\exp(i\beta_{j-1}) \\ r_j\exp(-i\beta_{j-1}) & \exp(-i\beta_{j-1}) \end{bmatrix}$$ **Equation 2.4.14.**

For multiple layers the resultant matrix [M] is again calculated by multiplying the matrices for each layer i.e. [M] = [M$_1$][M$_2$].....[M$_n$] and the overall reflectivity is expressed in terms of the individual components of the resultant matrix,

$$R = \frac{M_{21}M_{21}^*}{M_{11}M_{11}^*}$$

Equation 2.4.15.

Analysis of experimental data using this approach necessitates the prediction of a model consisting of n layers, each of thickness d_n and scattering length density ρ_n. Computer codes simulate the reflectivity profile for the adopted model and the generated profiles are compared with the experimental data. The model parameters are subsequently varied in an iterative process until there is acceptable agreement between the experimental and simulated data. From the best-fit values, parameters describing the near surface organisation were obtained. Usually the initial model selected is simple, consisting of one uniform layer, and additional lamellae are introduced as necessary. The profiles of layers used in this study take on two forms: uniform and half-parabolic form.

The scattering length density for a uniform layer is the sum of the individual contributions,

$$\rho = \sum_i \rho_i \varphi_i = \sum_i n_i b_i$$

Equation 2.4.16.

where n_i is the number density and b_i the coherent scattering length of species i. From values of n_i the surface concentration, Γ_s can be calculated for each of the species in the layer.

$$\Gamma_s = \frac{n_i M_i d}{N_A} \times 10^{20} \, mg \, m^{-2}$$

Equation 2.4.17.

where M_i is the molecular weight of a monomer of species i, N_A is Avogadro's number d is in Å and n is in Å^{-3}. The equivalent expression for a decaying parabola is given in equations 2.4.18,

$$\Gamma_s = \left(\frac{4}{3} n_i \, \sigma\right) \frac{M_i}{N_A} \times 10^{20} \, mg \, m^{-2}$$

Equation 2.4.18.

where the real space distribution is $n_i(z) = n_i\left(1 - \dfrac{z^2}{\sigma^2}\right)$ and σ is the standard deviation of the half parabolic layer.

Although the optical matrix approach gives the exact reflectivity, ambiguities arise, as many models may fit the experimental data well and there is some difficulty determining which model is physically more realistic. To overcome any uncertainty about the uniqueness of the model used, reflectivity curves for different contrasts studied are fitted concurrently using the same model. Consistency of layer dimensions is used as a criterion for the validity of a model for the spread polymer organisation. Furthermore a model is only accepted if the surface concentration calculated from the fit parameters is in good agreement with the actual amount of copolymer spread. The errors are thus minimised, but there is still no guarantee of the uniqueness of any solution.

2.4.3 The Kinematic Approximation

Crowley and co-workers[80] developed the kinematic approximation to determine individual contributions of the system to the reflectivity profile from experimental neutron reflectivity data. This approach is also model dependent but the fitting procedure is quicker and it provides more subtle structural detail in comparison to the optical matrix method, therefore ambiguities are less inherent.

The kinematic approximation is only valid when the reflectivity is weak (generally $< 10^{-3}$) and $Q >> Q_c$ (Q_c being the critical value below which total reflection is observed). When these criterion are met the specular component of reflectivity, $R(Q)$, from a macroscopically flat surface can be written as;

$$R(Q) = \frac{16\pi^2}{Q^2} |\rho(Q)|^2$$

Equation 2.4.19.

where $\rho(Q)$ (given in equation 2.4.20) is the one dimensional Fourier transform of $\rho(z)$, the scattering length density distribution normal to the interface, ($\rho(z) = \sum_i b_i n_i(z)$) and $n_i(z)$ is the number density distribution of species i at a distance, z, normal to the interface.

$$\rho(Q) = \int_{-\infty}^{\infty} \exp(iQz)\rho(z)dz$$

Equation 2.4.20.

Alternatively equation 2.4.19 can be written in terms of the gradient of the refractive index profile, $\rho' = \frac{d\rho}{dz}$;

$$R(Q) = \frac{16\pi^2}{Q^4} |\rho'(Q)|^2$$

Equation 2.4.21.

where,

$$\rho'(Q) = \int_{-\infty}^{\infty} \exp(iQz)\left(\frac{d\rho}{dz}\right)dz$$

Equation 2.4.22.

When the scattering vector is zero equation 2.4.22 reduces to the scattering length density difference between the two bulk media, $\Delta\rho$.

$$\rho'(0) = \Delta\rho \qquad \textbf{Equation 2.4.23.}$$

and the reflectivity is now;

$$R(Q) = R_s(Q)h'(Q) \qquad \textbf{Equation 2.4.24.}$$

where,

$$R_s(Q) = \Delta\rho^2\left(\frac{16\pi^2}{Q^4}\right) \qquad \textbf{Equation 2.4.25.}$$

$R_s(Q)$ is the kinematic expression for the reflectivity of neutrons at a sharp interface, and $h'(Q)$ is the structure factor which modulates $R_s(Q)$ depending on the total scattering length density profile normal to the interface. $\Delta\rho$ is simply the difference in scattering length density between two components i.e. $\rho_2-\rho_1$. $R_s(Q)$ depends on the square of this term ($\Delta\rho$) therefore it can be difficult to exactly determine ρ_2 and ρ_1 with this method. One drawback with the kinematic approximation is the limited range of Q accessible experimentally: 0.0255 to 0.3 Å^{-1}. The lower limit is imposed due to the sensitivity of the system and data for Q values higher than 0.3 Å^{-1} are lost in the incoherent background. Despite these limitations however it is still possible however to determine the structure factor $h'(Q)$ allowing conclusions to be drawn concerning the number density distribution and separation of individual components at the interface.

Crowley and co-workers[81] have demonstrated that by exploiting isotopic substitution the individual contributions of components to the structure factor can be identified. The reflectivity can be expressed as in equation 2.4.25 by combining 2.4.2 and 2.4.21.

$$R(Q) = \frac{16\pi^2}{Q^2} \sum_i b_i b_j h_{ij}(Q)$$

Equation 2.4.26.

where h_{ij} is the partial structure factor.

When $i = j$ the self-partial structure factor term for species i, h_{ii}, is obtained. This describes the number density distribution of component i in the surface layer since;

$$h_{ii}(Q) = |n_i(Q)|^2$$

Equation 2.4.27.

Alternatively, when $i \neq j$ the cross-partial structure factor, $h_{ij}(Q)$, provides information on the separation of the two components (i and j) relative to each other.

$$h_{ij}(Q) = h_{ji}(Q) = \text{Re}\left|n_i(Q)n_j^*(Q)\right|$$

Equation 2.4.28.

By varying the isotopic composition of both the polymer sample and subphase the number density and distribution of all components in the system can be estimated.

The potential of the kinematic approximation to polymer systems is illustrated by considering a simple case where a copolymer (with constituent parts A and B) is spread at an air-water interface. The scattering length density can be written with respect to the copolymer system by expanding equation 2.4.2,

$$\rho = b_A n_A(z) + b_B n_B(z) + b_W n_W(z)$$

Equation 2.4.29.

where the labels A, B and W represent each segment of the copolymer and the water subphase respectively. The kinematic expression for the total reflectivity of the system is obtained by substituting this relationship into equation 2.4.26 to give equation 2.4.30.

$$R(Q) = \frac{16\pi^2}{Q^2}\left(b_A^2 h_{AA} + b_B^2 h_{BB} + b_W^2 h_{WW} + 2b_A b_B h_{AB} + 2b_A b_W h_{AW} + 2b_B b_W h_{BW}\right)$$

Equation 2.4.30.

To characterise fully the monolayer organisation regarding the position of each component relative to both the superphase and subphase a set of six experimental contrasts would be required to solve the simultaneous equations. These are available by interchanging hydrogen and deuterium on both the polymer and the subphase to obtain different values for b_A, b_B and b_W. Four different copolymers are required, the fully deuterated, fully hydrogenated versions and also two part-deuterated materials where each block is selectively labelled. Two different subphases are also used, D_2O and nrw ($b_W = 0$). It is obvious that six sets of experimental reflectivity profiles can be generated by varying the polymer/subphase isotopic combination as outlined in table 2.4.3, where H and D represent the hydrogenous and deuterated materials respectively.

Component A	Component B	Subphase
H	H	D_2O
H	D	D_2O
D	H	D_2O
H	D	nrw
D	H	nrw
D	D	nrw

Table 2.4.3. Combination of polymer and subphase to obtain six reflectivity profiles.

The raw data need to be corrected before analysis, otherwise the application of the kinematic approximation will be limited. For highly reflecting surfaces (D_2O) the experimental reflectivity, $R_{exp}(Q)$, must be corrected for multiple scattering. Crowley[82] introduced a correction factor (given in 2.4.31) that scales the experimental data by the reflectivity of a smooth surface, using the kinematic reflectivity $R_s(Q)$ and the Fresnel reflectivity R_f, which is calculated using exact methods.

$$R(Q) = \left[\frac{1 + \left(1 - \frac{Q_c^2}{Q^2}\right)}{2} \right] \frac{R_{exp} - R_f}{1 - R_f} + R_s(Q)$$

Equation 2.4.31.

It is this corrected reflectivity data that is subsequently used to extract the partial structure factors from equation 2.4.30.

Interpretation of the data in the partial structure form requires the adoption of model that predicts the component (polymer or subphase) distribution from the interface $n(z)$, which gives $n(Q)$ upon Fourier transformation. Numerous models including a uniform layer, half-gaussian, half-parabola distribution, a double uniform layer, a uniform layer with exponential decay and a uniform layer with parabolic decay have been applied to experimental data. As an example the simplest of these, the single uniform layer model, has a polymer distribution of,

$$n(z) = n_i \qquad \text{for } 0 < z < 1$$
$$n(z) = 0 \qquad \text{for all other } z$$

This gives the self-partial structure factor,

$$Q^2 h_{ii}(Q) = 4n_i^2 \sin^2\left(\frac{Qd}{2}\right)$$

Equation 2.4.32.

The models used in this study have been selected not only because they cover a wide range of possible conformations, but also their number density profile leads to a simple well-behaved function when Fourier transformed. Details of each model and their application to experimental profiles are given in Chapter Six.

The cross-partial structure factor provides information regarding the relative positions of two components and their distribution at the near surface. The cross-term between two distributions is expressed as,

$$h_{ij}(Q) = \text{Re}\{n_i(Q)n_j(Q)\exp(iQ\delta)\}$$

Equation 2.4.33.

where δ is the distance between the centre of the distribution of the two components.

If $n(z)$ is even about the centre (i.e. a symmetrical model for example a uniform distribution) then the Fourier transform is an even function. This is generally true for amphiphilic diblock molecules confined to the interface. Alternatively if $n(z)$ is odd (for example the subphase must be odd since its distribution will be assymetric) then the Fourier transform is imaginary. If it is assumed that $n_A(z)$ and $n_B(z)$ are exactly even and $n_W(z)$ is odd then the cross-term can be simplified for two even functions to,

$$h_{AB}(Q) = \pm(h_{AA}h_{BB})\sin Q\delta \qquad \textbf{Equation 2.4.34.}$$

and for one even and one odd function,

$$h_{AW}(Q) = \pm(h_{AA}h_{WW})\cos Q\delta \qquad \textbf{Equation 2.4.35.}$$

The $\pm$ represents the uncertainty in the phase.

This analysis therefore allows both the number density distribution of each component present and their separation to be determined. This enables the complete distribution and orientation of the copolymer with respect to its surrounding media.

If however a complete set of contrasts is not available to provide complete elucidation of the systems structure, as in this study, then a partial kinematic approximation is still valuable. This allows the distribution of certain species to be estimated and also can assess the uniqueness and resolution limitations of any assumed structural model.

2.4.4 Bayesian Analysis

The third method of analysis of the neutron reflectometry data involves the application of the basic principles of Bayesian probability theory. This method uses the ubiquitous least-squares apparatus of parameter estimation to question the distribution of the polymer in the subphase, and in doing so the prior assumptions regarding model selection tested. A general introduction to Bayesian analysis[83] and its application to the analysis of neutron reflectometry data[75] can be found elsewhere. Only an outline of the

free-form solution and application to a two component system spread at a liquid surface is given here.

Free-form solutions describe the depth profile, b(z), normal to the interface and arise by relaxing the assumptions made when specific models used to describe the distribution are considered. When considering a two-component system with scattering lengths B_1 and B_2, the volume fraction profile f(z) provides a greater insight than B(z). These two terms are related via,

$$\beta(z) = \beta_1 + f(z)[\beta_2 - \beta_1]$$

Equation 2.4.36.

To obtain a free form solution f(z) must be defined by a large set of parameters. Initial estimates of the key parameters of the final model are required to ensure stability (since instabilities arise as there are more variables than data). A probability density function (pdf) is used to least squares fit simulated data to experimental data and one that is appropriate for positive and additive distributions is,

$$\text{prob}(f|I) \propto \exp(\alpha S)$$

Equation 2.4.37.

where S is the entropy of the distribution f(z), α is a Lagrange multiplier[84], the vertical bar means *given* and the comma means *and*. The term I is always included in the right hand side in probability expression in his analysis as it represents information on the background and any assumptions made. This method gives a maximum entropy solution but there is still the unanswered question of uniqueness of fit. This is taken into account by considering the average values of f(z) over some region.

$$\Phi = \frac{1}{z_2 - z_1} \int_{z_1}^{z_2} f(z)dz = \Phi_0 \pm \sigma$$

Equation 2.4.38.

The error bars, σ, are monitored within the limits of integration. The uncertainty parameter, Φ, is large when z_2-z_1 is small and vice versa, suggesting that only the gross structural properties can be inferred from this analysis. In attempt to optimise the

simulated data, and perhaps bring the simulated data closer to reality the data is smoothed in accordance with marginalisation methods[83].

Suppose the sample under study consists of several distinct components, of scattering length b. Then the depth profile, $\beta(z)$ can be expressed as,

$$\beta(z) = b_A n_A(z) + b_B n_B(z)\ldots\ldots b_M n_M(z) \qquad \textbf{Equation 2.4.39.}$$

where $n_M(z)$ is the number density component for the Mth component and b is the scattering length. The number of parameters, μ, that infer structural detail are related to M, $\mu = M(M+1)/2$. Working with the kinematic approximation, where the different contributions from individual components can be extracted from the partial structure factors, which are linearly related to the raw data. By redefining these variables the problem can be expressed in the general form of a noisy set of simultaneous equations[75];

$$\sum_{i=1}^{\mu} B_{ji} X_i = D_j \pm \sigma_j \qquad \textbf{Equation 2.4.40.}$$

where $\{X_i\}$ are the number of parameters that contain structural information, and matrix B defines the experimental set-up for the number (υ) of measurements $\{D_j\}$. To obtain a unique solution for equation 2.4.39 $\upsilon = \mu$ different profiles are required where b is varied. This of course is achieved using isotopic substitution and each M value adds an extra line in the matrix B.

Information describing the distribution of components in the system is hidden within the data according to Bayes' theorem, and such information can be extracted using a least squares method using equation 2.4.41.

$$L = \log[\text{prob}(D|X,B,I)] = \text{Constant} - \frac{1}{2}\sum_{j=1}^{\nu}\frac{1}{\sigma_j^2}\left(D_j - \sum_{i=1}^{N} B_{ji} X_i\right)^2$$

$$\textbf{Equation 2.4.41.}$$

Equation 2.4.42 and 2.4.43 ensure that the probability, $\text{prob}(D|X,B,I)$, is a single multivariate Gaussian, whose properties (orientation and distribution from the maximum (ΔL, where $\Delta = \dfrac{\partial}{\partial x}$)) are governed by the eigen-characteristics of the second-derivative Hessian matrix,

$$\frac{\partial^2 L}{\partial X_i \partial X_{i'}} = -\sum_{j=1}^{v} \frac{B_{ji} B_{ji'}}{\sigma_j^2} \qquad \textbf{Equation 2.4.42.}$$

This equation implies that several different models can describe the distribution from the interface, but such ambiguities can be minimised by fitting all profiles obtained for the different contrasts using isotopic substitution.

Consider the experimental scenario where a two component system, for example a surfactant with dominant chain and negligible head group is spread on a liquid surface. By preparing both protonated and deuterated chains and by mixing light and heavy solvent, neutron data can be collected using various contrasts. There would be three structure factors (μ parameters) of interest, h_{cs}, h_{ss} and h_{cs} since $M = 2$, therefore data for three contrasts minimum would be collected in order to solve equation 2.4.39. This reduces the square root of the modulus of the determinant of the $\Delta\Delta L$ (left hand side of equation 2.4.42) matrix to $|\det(B)|$, where,

$$B \propto \begin{pmatrix} c_1^2 & s_1^2 & c_1 s_1 \\ c_2^2 & s_2^2 & c_2 s_2 \\ c_3^2 & s_3^2 & c_3 s_3 \end{pmatrix} \qquad \textbf{Equation 2.4.43.}$$

Four contrasts are experimentally available for this system using isotopic substitution: (H,H,H), (D,H,H), (D,D,H) and (D,D,D). Computer generated measurements determine the resultant maximum value of $|\det(B)|$ which provides the optimum distribution function. The assumption that $\sigma_j = \sigma$ is made throughout the analysis as the exact error values depend directly on the values of the partial structure factors that are trying to be determined. This assumption however will not effect the accuracy of the simulated data or generated distribution profiles.

Section 2.5   Surface Quasi-Elastic Light Scattering

Liquid surfaces are not uniformly flat but are continually perturbed by thermal fluctuations causing a roughening of the interface on a microscopic level. A pure water surface for example, typically has fluctuations with RMS amplitude of 2 Å. Such microscopic fluctuations are predominantly normal to the surface can be Fourier decomposed into a discrete set of transverse oscillations (referred to as capillary waves), where each set is characterised by the wavenumber, q. Despite the small amplitude of these surface waves they scatter light efficiently, which reflects the temporal evolution of the surface waves. The propagating waves are characteristic of the system under study as they are dependent on the physical properties including the surface tension (γ_o), density (ρ), viscosity (η) and the viscoelastic properties of any surface layer. It follows that the scattering properties of the capillary waves can be exploited to obtain information on such dynamical features of fluid interfaces, using the non-perturbative technique of surface quasi-elastic light scattering (SQELS).

The extent of vertical displacement, ξ, of the surface of a propagating capillary wave in the x-direction from its equilibrium position ξ_o, at time t is given by,

$$\xi(x,t) = \xi_o \exp(i(qx + \omega t))$$ **Equation 2.5.1.**

where ω is the propagating wave frequency, which is a complex quantity $\omega = \omega_o + i\Gamma$ where ω_o is the true frequency of the spatial fluctuation and Γ is the damping of these waves. The parameter q (in-plane momentum transfer) is the wavenumber and is defined as,

$$q = \frac{2\pi}{\lambda}$$ **Equation 2.5.2.**

where λ is the wavelength of the capillary wave.

The displacement on the surface caused by the capillary waves act as a weak phase grating, which causes the light incident on the surface to diffract. This process is outlined in figure 2.5.1a where k_o and k_r are the projections of the incident and reflected

wave vectors respectively. The angle of scatter $\delta\theta$, is related to q and the incident angle via $q = 2k_o \sin(\delta\theta/2)\cos\theta$ as illustrated in the resultant vector diagram in figure 2.5.1b.
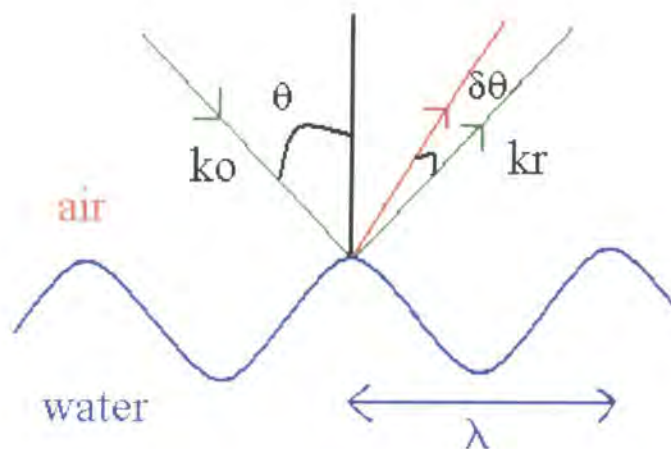
a) Scattering of light by a capillary wave

Figure 2.5.1. b) resultant vector diagram of the incident and scattered light.

When a monolayer is spread and supported by a liquid subphase the interfacial dynamic behaviour of the interface becomes increasingly complex. Lucussen[85, 86]

established that a longitudinal, or dilational mode (in plane motion) was present in addition to the transverse, or capillary mode (normal to the interface). Goodrich[87] later identified both of these waves as being two of the five modes of motion on the surf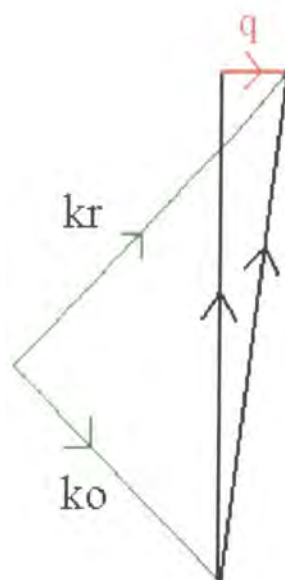ace, these being transverse shear, lateral compression (longitudinal mode), lateral shear, horizontal shear and vertical compression (transverse mode). Only the transverse and longitudinal hydrodynamic modes however are pertinent to this study, and their motion is illustrated in figure 4.5.2.
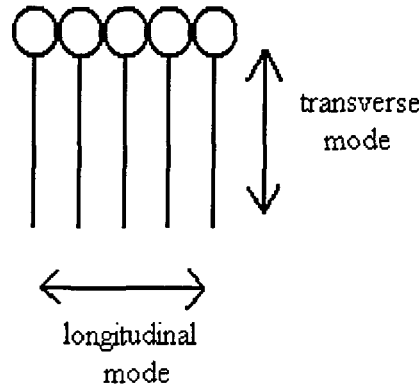
Figure 5.4.2. Schematic representation of the transverse and longitudinal modes.

The physical properties of the surface motion probed by SQELS is related to the specific wavenumber via the dispersion equation, D(ω), derived by Lucassen-Reynders and Lucassen[85, 86]. The general form for this expression for an air-water interface (i.e. the viscosity and density for the superphase are zero) is given in equation 2.5.3.

$$D(\omega) = \left[\epsilon q^2 + i\eta\,\omega(m+q) \right]\left[\gamma\,q^2 + i\eta\,\omega(m+q) - \omega^2\,\rho/q \right] + \left[\eta\omega(q-m) \right]^2 = 0$$

<div align="right">

Equation 2.5.3.

</div>

where the parameter m is defined as;

$$m = \text{Re}\left|\left(q^2 + i\omega\,q/\eta\right)\right|^{1/2}$$

<div align="right">

Equation 2.5.4.

</div>

and ρ and η are the density and viscosity of the water, and ε and γ are the moduli for the dilational and capillary waves respectively.

There are two physically realistic roots of the dispersion equation, one relating to the propagation characteristics of the capillary waves and the other to the dilational waves. To a first approximation the equations for each mode are given in the complex form ($\omega = \omega_0 + i\Gamma$) in equation 2.5.5 and 2.5.6 for capillary[88] and dilational[89] waves respectively.

Capillary mode $\qquad\qquad \omega = \sqrt{\dfrac{\gamma q^3}{\rho} + i\dfrac{2\eta q^2}{\rho}} \qquad\qquad$ **Equation 2.5.5.**

Dilational mode $\qquad\qquad \omega = \dfrac{1}{2}\left(\sqrt{3} + i\right)\left(\varepsilon^2 q^4 / \eta\rho\right)^{\frac{1}{3}} \qquad\qquad$ **Equation 2.5.6.**

The motion of the dilational mode is weakly coupled to the capillary mode to an extent depending upon the coupling coefficient[90], $\eta(q-m)$, (for an air-liquid interface). It is therefore technically incorrect to refer to the motion as consisting of purely translational or longitudinal waves, therefore the terms capillary and dilational modes are preferred. In the low frequency limit ($\omega \rightarrow 0$) the capillary waves are governed by the interfacial tension (γ) and the dilational waves by the dilational modulus (ε), where ε corresponds to the Gibbs static elasticity, $\varepsilon = \Gamma_s \left(\dfrac{d\pi}{d\Gamma_s}\right)$. Both moduli are complex quantities and are expanded as linear response functions to include dissipative effects.

$$\gamma = \gamma_0 + i\omega\gamma' \qquad\qquad \text{**Equation 2.5.7.**}$$

$$\varepsilon = \varepsilon_0 + i\omega\varepsilon' \qquad\qquad \text{**Equation 2.5.8.**}$$

γ_0 and ε_0 are the surface tension and dilational modulus obtained at the capillary wave frequency ω_0. Only the capillary waves scatter light but due to the coupling between the two modes information pertaining to the dilational wave can be extracted by carefully analysing the capillary wave scattering. The conditions giving the best opportunity of

observing dilational wave characteristics occurs when the two modes are resonating, i.e. the capillary and dilational waves are oscillating with identical frequencies. Classically resonance occurs when $\dfrac{\varepsilon_0}{\gamma_0} = 0.16$. The primed terms in equations 2.5.7 and 2.5.8 are the associated viscosities, transverse shear viscosity γ' and dilational viscosity ε', and account for energy dissipation. A recent theoretical study by Buzza[91] and co-workers has resulted in a modified interpretation of SQELS theory for a diblock copolymer forming a double brush layer at a fluid-fluid interface. This model was based on the Alexander[64]-de Gennes[65] model accounting for the curvature at the surface introduced by a capillary wave. Buzza[91] et. al. have predicted that four viscoelastic parameters surface tension (γ), dilational modulus (ε), coupling constant, (λ) and a bending modulus (κ) influence the properties of the film layer and more significantly they ascertained that γ' was non-existent (i.e. $\gamma' = 0$).

The additional coupling parameters included in the new theory, κ and λ, both have associated viscosities as given in equations 2.5.9 and 2.5.10,

$$\lambda = \lambda_0 + i\omega_0\lambda' \qquad\qquad \textbf{Equation 2.5.9.}$$

$$\kappa = \kappa_0 + i\omega_0\kappa' \qquad\qquad \textbf{Equation 2.5.10.}$$

The viscous (primed) terms account for the permeation of solvent through the polymer brush layer treated as a porous medium. The scaling relationships established from the theory for surface pressure, π, the dilational modulus, ε, dilational viscosity, ε', and the coupling constants, λ_0 and λ' are as follows,

$$\pi \approx \sigma^{11/6}b^{5/3}Nk_BT \qquad\qquad \textbf{Equation 2.5.11.}$$

$$\varepsilon_0 \approx \sigma^{11/6}b^{5/3}Nk_BT \qquad\qquad \textbf{Equation 2.5.12.}$$

$$\varepsilon' \approx \sigma^2 b^5 \eta N^3 \qquad\qquad \textbf{Equation 2.5.13.}$$

$$\lambda_0 \approx \sigma^{13/6}b^{10/3}N^2 k_BT \qquad\qquad \textbf{Equation 2.5.14.}$$

$$\lambda' \approx \sigma^{7/3}b^{20/3}\eta N^4 \qquad\qquad \textbf{Equation 2.5.15.}$$

where N is the degree of polymerisation where each repeat unit has a statistical step length b. The polymer is immersed in a subphase whose viscosity is η with grafting density σ.

In this study however neither κ nor λ contributes significantly to the surface properties. κ is only applicable to systems of extremely low surface tension (approximately zero) which is obviously not the case for a water subphase where γ_0 = 72 mN m^{-1}. The coupling constant is dependent on the capillary wavenumber and brush height (h_o) i.e. $\lambda = qh_o$, and since this value has to be circa 0.1 before λ contributes in any way, h_o has to be in this order of micrometers for the experimental q range used here. This height is circa three orders of magnitude higher than observed experimentally. In this work therefore the terms κ, λ and γ' were set to zero.

The spectrum of light scattered by the capillary waves reflects their frequency and is influenced by the viscoelastic properties of the monolayer. This power spectrum, $P(\omega)$, can be expressed in terms of the dispersion equation,

$$P(\omega) = \frac{-2k_B T}{\omega} \operatorname{Im}\left\{ \frac{i\eta\,\omega(q+m) + \varepsilon q^2}{D(\omega)} \right\}$$

Equation 2.5.16.

where k_B is Boltzman's constant and T is the absolute temperature. The power spectrum is a skewed Lorentzian with a maximum at frequency, ω, and a width of damping, Γ. Experimentally the Fourier transform of the power spectrum is collected,

$$g(\tau) = FT\left|P\!\left(\omega \middle| X_j\right)\right|$$

Equation 2.5.17.

where X_j represents all four viscoelastic terms, γ_0, ε_0, γ' and ε'. Experiments are limited to a q range of $100 < q < 2000$ cm^{-1} as the intensity of laser light falls off rapidly as q^{-2}. The shifts in frequency due to the scattering of light are small (approximately 10-100 kHz) therefore the necessitating a heterodyne detection technique. This involved mixing the scattered light of a particular q with a reference beam (with the frequency of the original light) at the detector, which is a photomultiplier tube. The photomultiplier detects the characteristic 'beating' of the combined waves and the output collected in

the temporal rather than the frequency domain to give $g(\tau)$. The experimental correlation function obtained, $g(\tau)$, is given in equation 2.5.18 and contains contributions from both heterodyning and homodyning.

$$g(\tau) = (I_s + I_r)^2 + I_s I_r g^1(\tau) + I_s^2 [g^2(\tau) - 1]$$

Equation 2.5.18.

where I_s and I_r are the intensity of the scattered and reference beams respectively, and τ is the delay time. $g^1(\tau)$ is the Fourier transform of the power spectrum referred to earlier and involves only the heterodyne contribution. To ensure that the homodyne contribution (I_s^2 term) is minimal the ratio of I_s / I_r must be greater than 10^{-3}. This can be achieved simply by attenuating the light beam using neutral density filters.

2.5.1   The Cosine Fit

To extract values for the propagating frequency and damping of the capillary waves the Fourier transform of the scattered data, at a discrete q, was fitted with the damped cosine function[90],

$$g(\tau) = B + A \times \cos(\omega_o \tau + \varphi) \times \exp\left(-\beta^2 \tau / 4^2\right) + C\exp(-\alpha\tau) + D\tau^2$$

Equation 2.5.19.

In equation 2.5.19 the phase term, φ, accounts for the deviation of the power spectrum from the true Lorentzian form. The Gaussian term, $\exp\left(-\beta^2\tau^2/4\right)$, takes into account the broad nature of the scattered intensity of light. This effect is due to the finite size of the incident beam sampling multiple capillary wave fluctuations. Fast relaxation processes and after pulsing effects in the photomultiplier tube, become apparent at short correlation channel widths (typically 2 μs) and are incorporated in the term $C\exp(-\alpha\tau)$. The term $(B-D\tau^2)$ corrects for the low frequency vibrations that generally arise form external sources (for example building vibrations), and are evident as they produce a

droop in the correlation functions at long times. Such external vibrations are minimised by mounting the surface under study on a vibration isolation unit on top of an optical table but they cannot be eliminated completely.

2.5.2 Spectral Fit

The cosine fit only provides information on the frequency and damping of the capillary waves. To extract the viscoelastic parameters γ_o, ε_o, and ε', a more complex fitting routine was required as all three parameters effect the spectrum of scattered light differently. Such a method was pioneered by Earnshaw[92], and is commonly referred to as the direct spectral fitting method. The equation developed for the fitting procedure is given in equation 2.5.20 and is similar to equation 2.5.3 except the cosine term has been replaced with the Fourier transform of the power spectrum.

$$\hat{g}(\tau) = B + A \times FT\left[P(\omega|X_j)\right] \times \exp\left(-\beta^2\tau^2/4\right) + C\exp(-\alpha\tau) + D\tau^2$$

Equation 2.5.20.

A model correlation function is generated from values estimated for the three variable viscoelastic parameters (γ_o, ε_o and ε', $\gamma' \equiv 0$). The fitting procedure initially involves generating a power spectrum, then the data is Fourier transformed to give $\hat{g}(\tau)$ which is subsequently non-linear least square fitted to the experimental data until F in equation 2.5.21 reaches a minimum.

$$F = \sum_{i=2}^{i=n} \left[g(\tau_i) - \hat{g}(\tau_i)\right]^2$$

Equation 2.5.21.

n is the total number of channels widths, excluding delay channels.

Section 2.6   References

1. Cowie, J. M. G. *Polymers: Chemistry and Physics of Modern Materials, 2nd Edition,* **1997**, *Chapter 1*, Blackie Academic and Professional, Glasgow.

2. Billmeyer, F. W. *Textbook of Polymer Science*, **1984**, John Wiley and Sons, Singapore.

3. Allen, G.; Bevington, J. C. *Comprehensive Polymer Science, Polymer Properties,* **1988**, *2*.

4. Feast, W. J.; Cacialli, F.; Diak, R.; Friend, R. H.; Herzog. E.; Heywood, B. R.; Hobson, L.; Megson, J. L.; Snowden, D. *Macromolecular Symposia,* **1999**, *143*, 81.

5. Meszena, Z. G.; Viczian, Z.; Gosden, R. G.; Mohsin, M. A.; Johnson, A.F. *Polymer Reaction Engineering,* **1999**, *7*, 71.

6. Odian, G. *Principles of Polymerisation, 3rd Edition,* **1991**, John Wiley and Sons, New York.

7. Tardi, M.; Sigwalt, P. *J. Eur. Polym.,* **1972**, *8*, 151.

8. Cheng, G. L.; Hu, C. P.; Ying, S. K. *Acta Polymerica Sinica,* **2000**, *2*, 210.

9. Szwarc, M.; Levy, M.; Milkovich, R. *J. Am. Chem. Soc.,* **1956**, *78*, 2656.

10. Hsieh, H. L.; Quirk, R. P. *Anionic Polymerisation, Principles and Practical Applications,* **1996**, Marcel Dekker, New York.

11. Dreyfuss, P.; Quirk, R. P.; *Encyclopaedia of Polymer Science and Enginerring*, Ed. Kroschwitz, J. I. **1977**, 551, John Wiley and Sons, New York.

12. Chen, R. Z.; Zhang, Y.; Pan, E. L.; Ou, Y. C.; Yu, Z. Z. *Acta Polymerica Sinica,* **2000**, *2*, 200.

13. Ruckenstein, E.; Zhang, H. M. *J. Poly. Sci. Part A. Polymer Chem.,* **2000**, *38*, 1195.

14. Lu, B.; Chung, T. C. *J. Poly. Sci. Part A. Polym. Chem.,* **2000**, *38*, 1337.

15. Plate, N. A.; Shibaev, V. P. *Comb Shaped Copolymers and Liquid Crystals,* **1987**, Plenum Press, New York and London.

16. Peace, S. K. *Ph.D. Thesis,* Durham University, **1996**.

17. Feast, W. J.; Gibson, V. C.; Johnson, A. F.; Khosravi, E.; Mohsin, M. A. *Polymer,* **1994**, *35*, 3542.

18. Calderon, N.; Ofstead, E. A.; Judy, W. A. *J. Poly. Sci. Part A. Polymer Chem.,* **1967**, *5*, 2209.

19. Calderon, N.; Chen, H. Y.; Scott, K. W. *Tetrahedron Lett.,* **1967**, *5*, 3327.

20. Burroughes, J. H.; Bradley, D. D. C.; Brown, A. R.; Marks, R. N.; Friend, R. H.; Burn, P. L.; Holms, A. B. *Nature,* **1990,** *347,* 539.

21. Bradshaw, C. P. C.; Howmann, E. J. *J. Catal.,* **1967,** *7,* 269.

22. Herrison, J. L.; Chauvin, Y. *Makromol. Chem., 1971, 141,* 161.

23. Shirakawa, H.; Ikeda, S. *Polymer,* **1971,** *2,* 231.

24. Khosravi, E.; AlHajaji, A. A. *Polymer,* **1998,** *39,* 5619.

25. Feast, W. J.; Gibson, V. C.; Johnson, A. F.; Khosravi, E.; Mohsin, M. A. *J. of Mol. Catalysis A: Chemical,* **1997,** *115,* 37.

26. Schrock, R. R. *Acc. of Chem. Research.,* **1990,** *23,* 158.

27. Hamilton, J. G. *Polymer,* **1998,** *8,* 1669.

28. McConville, D. H.; Wolf, J. R.; Schrock, R. R. *J. Am. Chem. Soc.,* **1993,** *115,* 4413.

29. Kress, J.; Osborn, J. A. *J. Am. Chem. Soc.,* **1987,** *108,* 733.

30. Grubbs, R. H.; Tumas, W. *Science,* **1989,** *243,* 907.

31. Cannizzo, L. F.; Grubbs, R. H. *Macromolecules,* **1988,** *21,* 1961.

32. Cannizzo, L. F.; Grubbs, R. H. *Macromolecules,* **1987,** *20,* 1488.

33. Schrock, R. R.; Depue, R. T.; Feldman, J.; Schaverien, C. J.; Dewan, J. C.; Liu, A. H. *J. Am. Chem. Soc.,* **1990,** *110,* 1423.

34. Schrock, R. R.; Murdzek, J. S.; Bazan, G. C.; Robbins, J.; DiMare, M.; O'Regan, M. *J. Am. Chem. Soc.,* **1990,** *112,* 3875.

35. Novak, B. M.; Risse, W.; Grubbs, R. H. *Ad. in Poly. Sci.,* **1992,** *102,* 47.

36. Schrock, R. R.; Feldman, J.; Grubbs, R. H.; Cannizzo, L. *Macromolecules,* **1987,** *20,* 1169.

37. Schwab, P.; Grubbs, R. H.; Ziller, J. W. *J. Am. Chem. Soc.,* **1996,** *118,* 100.

38. Wagaman, M. W.; Grubbs, R. H. *Macromolecules,* **1997,** *30,* 3978.

39. Shaw, D. J. *Colloid and Surface Chemistry, Fourth Edition,* **1996,** Butterworth-Heinemann.

40. Adamson, A. W. *Physical Chemistry of Surfaces, Fourth Edition,* **1982,** 124, Wiley, New York.

41. Singer, S. J. *J. Chem. Phys.,* **1948,** *16,* 872.

42. Huggins, M. L. *J. Phys. Chem.,* **1942,** *46,* 151.

43. Frisch, H. L.;.Simha, R. *J.Chem. Phys.,* **1957,** *27,* 22.

44. Motomura, K.; Matuura, R. *J. Coll. Sci.,* **1963,** *18,* 52.

45. Scheutjens, J. M. H. M.; Fleer, G. J. *J. of Phys.Chem.,* **1979,** *83,* 1619.

46. Scheutjens, J. M. H. M.; Fleer, G. J. *J. of Phys.Chem.*, **1980**, *84*, 178.

47. Daoud, M.; Jannink, G. *J. Phys. (Paris)*, **1976**, *37*, 973.

48. Vilanove, R.; Poupinet, D.; Rondelez, F. *Macromolecules*, **1988**, *21*, 2880.

49. Kawaguchi, M. *Progress in Polymer Sci.*, **1993**, *18*, 341.

50. de Gennes, P. G. *Scaling Concepts in Polymer Physics*, **1991**, Cornell University, New York.

51. des Cloizeaux, J. *J. Phys. (Paris)*, **1976**, *41*, L-151.

52. Flory, P. J. *Statistical Mechanics of Chain Molecules*, **1988**, *Chapter 2*, 30, Oxford University Press.

53. Havlin, S.; Ben Avraham, D. *Phys. Rev. A*, **1983**, *27*, 2759.

54. Pogorzelski, S. J. *Coll. and Surf. A: Phys. and Eng. Aspects*, **1996**, *114*, 297.

55. Derrida, B. *J. Phys. A: Math. Gen.*, **1981**, *14*, L-5.

56. Li, B.; Madras, N.; Sokal, A. D. *J. of Stat. Phys.*, **1995**, *80*, 661.

57. Jones, R. A. L.; Richards, R. W. *Polymers at Surfaces and Interfaces*, **1999**, Cambridge University Press.

58. Harrats, C.; Blacher, S; Fayt, R.; Jerome, R.; Teyssie, P. *J. of Polym. Sci. B: Polym. Phys.*, **1995**, *33*, 801.

59. Duchet, J.; Chapel, J. P.; Chabert, B.; Gerard, J. F. *Macromolecules*, **1998**, *31*, 8264.

60. Fleer, G. J.; Cohen Stuart, M. A.; Scheutjens, J. M. H. M.; Cosgrove, T.; Vincent, B. *Polymers at Interfaces*, **1993**, Chapman and Hall, London.

61. Halperin, A. *Langmuir*, **1999**, *15*, 2525.

62. Halperin, A.; Tirrell, M.; Lodge, T. P. *Adv. Polym. Sci.*, **1992**, *100*, 31.

63. Szleifer, I.; Carignano, M. A. *Adv. in Chem. Phys.*, **1996**, *44*, 165.

64. Alexander, S. *J. Phys.*, **1977**, *38*, 983.

65. de Gennes, P. D. *Macromolecules*, **1980**, *13*, 1069.

66. Milner, S. T.; Witten, T. A.; Cates, M.E. *Macromolecules*, **1988**, *21*, 2610.

67. Shim, D. F. K.; Cates, M. E. *J. Phys. France*, **1980**, *50*, 3535.

68. Zhulina, E. B.; Borisov, O. V. *Macromolecules*, **1991**, *24*, 4679.

69. Wijmans, C. M.; Zhulina, E. B.; Fleer, G. J. *Macromolecules*, **1994**, *27*, 3238.

70. Penfold, J.; Thomas, R. K. *J. Phys.: Condens. Matter*, **1990**, *2*, 1369.

71. Higgins, J. S.; Benoit, H. C. *Polymers and Neutron Scattering*, **1994**, Oxford University Press.

72. Thomas, R. K. *Scattering Methods in Polymer Science*, **1995**, *Chapter 4*, Ed. Richards, R. W. Ellis Horwood.

73. Majkrzak, C. F. *Acta Phys. Pol. A*, **1999**, *1*, 81.

74. Lovell, M. R.; Richarson, R. M. *Current Opinion in Coll. and Inter. Sci.,***1999**, *4*, 197.

75. Sivia, D. S.; Webster, J. R. P. *Physica B: Condensed Matter*, **1998**, *248*, 327.

76. Born, M.; Wolf, E. *Principles of Optics*, **1980**, Pergamon.

77. Nevot, L.; Croce, P. *Phys. Appl*, **1980**, *15*, 761.

78. Abeles, F. *Ann. de Physique,* **1948**, *3*, 504.

79. Heavens, O. S. *Optical Properties of Thin Films*, **1955**, Butterworths.

80. Crowley, T. L.; Lee, E. M.; Simister, E. A.; Thomas, R. K.; Penfold, J.; Rennies, A. R. *Colloids and Surfaces*, **1990**, *52*, 85.

81. Crowley, T. L.; Lee, E. M.; Simister, E. A.; Thomas, R. K. *Physica B*, **1991**, *174*, 143.

82. Crowley, T. L. *J. of Phys. Chem.*, **1962**, *66*, 1858.

83. Sivia, D. S. *Data Analysis: A Bayesian Tutorial*, **1996**, Oxford University Press, Oxford.

84. Skilling, J. *Maximum Entropy*, Ed. Buck, B.; MacCaulay, V. A., **1991**, Oxford University Press, Oxford.

85. Lucassen, J. *Trans. Faraday Soc.*, **1968**, *64*, 2221.

86. Lucassen-Reynders, E. H.; Lucassen, J. *Adv. Colloid Inter. Sci.* **1969**, *2*, 347.

87. Goodrich, F. C. *Proc. R. Soc.,* **1981**, *374*, 341.

88. Earnshaw, J. C.; McGivern, R. C. *J. of Colloid and Inter. Sci.,***1988**, *36*, 123.

89. Lamb, H. *Hydrodynamics*, **1945**, Dover.

90. Kramer, L. *J. Chem. Phys.,* **1971**, *55*, 2097.

91. Buzza, D. M. A.; Jones, J. L.; McLeish, T. C. B.; Richards, R. W. *J.of Chem. Phys.,* **1998**, *12,* 5008.

92. Earnshaw, J. C.; McGivern, R. C.; McLaughlin, A. C.; Winch, P. J. *Langmuir,* **1990**, *6*, 649.

Chapter Three

Experimental Techniques

Section 3.1   Surface Pressure Isotherms

All surface pressure data were collected using a circular Langmuir trough (NIMA technology, Coventry) as depicted in figure 3.1.1.
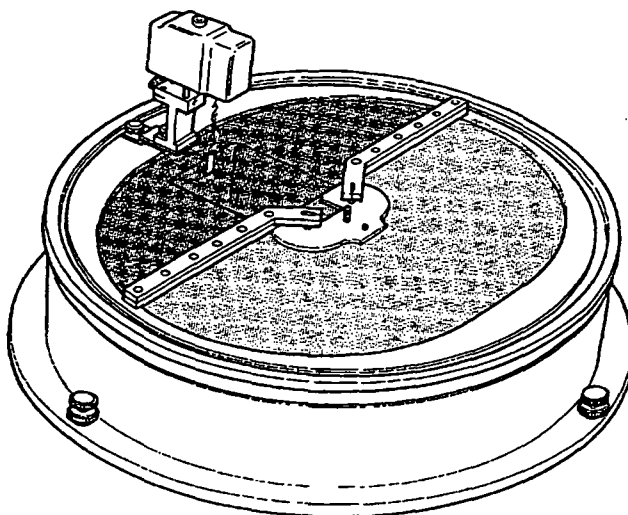

Figure 3.1.1. Circular NIMA trough (taken from NIMA laboratory manual).

The trough is fabricated from polytetrafluoroethylene (PTFE), as this material is inert and will not contaminate the subphase. A volume of circa 900 cm^3 of liquid was required to fill the trough until the level just brimmed over the top. The surface area was varied from 40 cm^2 to a maximum of 980 cm^2 by two motorised barriers that opened and closed symmetrically about the pressure sensor. The temperature of the subphase was regulated at 298 K by constantly circulating water underneath the teflon base using a Haake thermostat water circulator. External vibrations were minimised by mounting the trough on a heavy optical table.

3.1.1 Measurement of Surface Pressure

Surface pressure measurements were made using a Wilhelmy plate, which was connected to a displacement transducer. The Wilhelmy plate was a rectangular piece of high quality filter paper (Whatmans number 1) of dimensions 10 mm by 20 mm. When this paper was in contact with an air-liquid surface, it was pulled down into the bulk of the subphase by the surface tension of the surface. In this system additional forces have to be considered as gravity also acts downwards on the plate, and buoyancy acts upwards due to the displaced subphase molecules. An electromagnetic coil is attached to the Wilhelmy plate and determines the magnitude of the downward force. This is achieved by using an electromagnetic coil with a moving arm, which is illuminated by an infra-red diode. The shadow cast by the arm falls onto two infra-red detectors, and as the force on the arm changes, the voltage through the coil changes to ensure the shadow falling on each detector remains constant. The change in voltage passing through the coil is then converted directly into surface pressure. If the surface pressure was set to zero, for, say a clean air-water interface, then weight and upthrust can be eliminated and changes due to the presence of surface-active material could be directly measured.

The pressure sensor was calibrated by using a weighing pan, a 100 mg weight and an automatic calibration program included in the trough software package.

3.1.2 Sample Preparation

For all surface pressure isotherm measurements polymer solutions with a concentration of circa 1.0 mg m^{-2} in chloroform were prepared. Glassware, usually 10 ml volumetric flasks, was thoroughly cleaned by leaving permanganic acid (suphuric acid mixed with a few crystals of potassium permanganate) in the glassware to soak overnight. The vessels were then rinsed several times with ultra high quality (UHQ) water, and finally any residual water was driven off under vacuum at room temperature. The desired weight of polymer was dissolved in spectroscopic grade chloroform and left to stand overnight before use to ensure complete dissolution of polymer material.

3.1.3 Subphase Preparation

Ultra high quality (UHQ) water was obtained by passing doubly distilled water through an Elgastat UHQII water purification system (Elga Technology, High Wycombe, UK). The resulting pure water had a resistivity of 18.2 MΩ indicating the absence of any stray ions.

The aqueous solutions of PEO were prepared by dissolving appropriate quantities of PEO powder in UHQ water. The inhibitor present in the PEO (Aldrich), bis-(2-hydroxyethyl) terephthalate (BHT) was extracted by precipitation, using water and hexane as the solvent/non-solvent system. The molecular weight of the white PEO powder was determined to be 103 000 g mol^{-1} with a polydispersity of 1.21 by size exclusion chromatography. The PEO solutions were prepared several days prior to experiments to ensure complete dissolution.

3.1.4 Experimental Procedure

The Teflon base of the Langmuir trough was initially cleaned using dust free Kimwipes and chloroform. The trough was subsequently filled with the desired subphase until a high meniscus was obtained and the surface was aspirated to remove any lingering dust particles or surface impurities. To check the purity of the interface and the accuracy of the surface potentiometer the surface tension was measured and for a pure water surface a value of 72 mN m^{-1} was returned.

To spread a monolayer at the interface a known volume of the polymer solution was carefully deposited dropwise onto the subphase surface using a 50 or 100 µl gas-tight Hamilton syringe. A period of fifteen minutes elapsed to allow the chloroform solvent to evaporate and the molecules to equilibrate before the residual polymer monolayer was compressed by the barrier. The latter were controlled through the computer software package and were closed at a constant rate while surface pressure readings were taken continuously at 1 s intervals.

Surface pressure results were displayed initially as a function of surface area but were easily converted to surface concentration as the volume and concentration of deposited polymer solution was known.

3.1.5   Film Relaxation Studies

The relaxation of spread graft copolymer films was determined by compressing a monolayer to a desired surface concentration, and then setting the barrier speed to zero while surface pressure readings were taken every 3 s. Thus any variation in the surface pressure could be monitored as a function of time.

Section 3.2   Neutron Reflectivity

All neutron reflectivity experiments were carried out at the ISIS pulsed neutron source at the Rutherford Appleton Laboratory (RAL), Chilton, Oxfordshire. Two neutron reflectometers were used, CRISP and SURF.

The neutrons at ISIS are produced by spallation. This occurs when pulses (with frequency 50 Hz) of protons are accelerated towards a tantalum target resulting in the "boiling off", or spalling of neutrons. These neutrons are subsequently passed through a moderator where they continually bounce around loosing energy at every collision before they are guided to the individual instruments that surround the target. The wavelength range of the beam used on SURF and CRISP is circa 0.0255-0.7 Å.

3.2.1   Experimental Details

The basic principle behind all experimental measurements in this study was to quantify the reflectivity, R(Q), as a function of the scattering vector Q, defined by,

$$Q = \frac{4\pi}{\lambda}\sin\theta$$ **Equation 3.2.1.**

where θ is the grazing incidence angle of the neutron beam of wavelength λ, with respect to the horizontal. R(Q) was measured over a range of Q values simply by varying both the neutron wavelength and incident angle of the incoming beam.

SURF and CRISP are both variable wavelength instruments, therefore by collecting reflectivity data at two incident angles (0.8 ° and 1.5 °) a Q range of $0.0255 < Å^{-1} < 0.6$ on CRISP and $0.0255 < Å^{-1} < 0.7$ on SURF was accessible. The lower angle allowed Q values from 0.0255 to 0.06 $Å^{-1}$ to be explored, while the higher angle allowed data from 0.055 $Å^{-1}$ and above to be explored. The data from each incident angle were deliberately overlapped in Q range to minimise the error when the low and high angle data sets were combined.

3.2.2 Instrumental Details

The reflectometers used in this study (CRISP and SURF) use an identical set-up operation and experimental procedure. SURF is the newer of the two reflectometers at ISIS and is dedicated to the study of liquid surfaces. The main advantage of SURF is that it has an increased neutron flux allowing data collection in shorter time periods. Instrument details pertaining to CRISP are given here but are essentially analogous to those for SURF.

Neutrons incoming to the instrument have various energies, thus have a range of wavelengths varying from 0.5-6.5 Å which provides access to a full Q range when reflectivity data at two incident angles (0.8 ° and 1.5 °) is collected. A schematic representation of CRISP is given in figure 3.2.1.
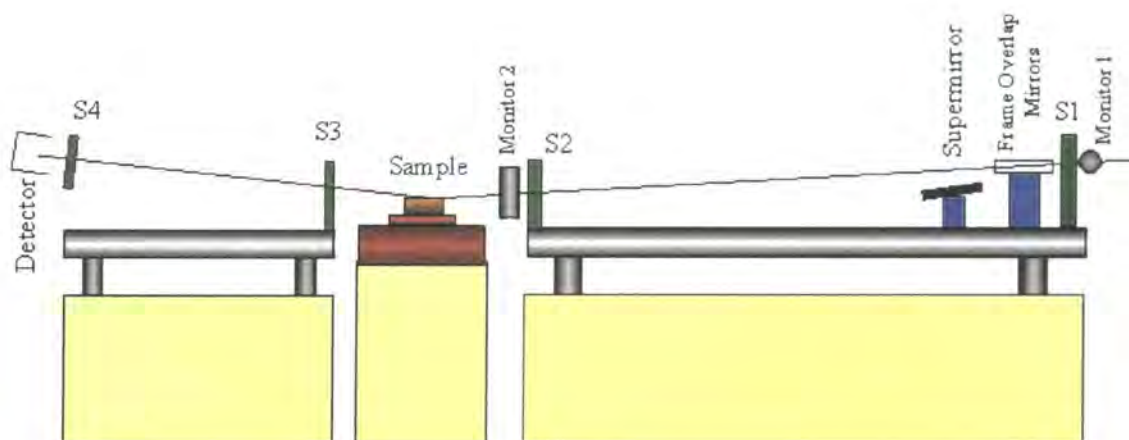

Figure 3.2.1. A schematic representation of CRISP reflectometer.

The incoming beam of neutrons contains a broad mixture of wavelength but the chopper selectively eliminates neutrons, allowing only those within the limits of the desired range through. The chopper is simply a disc with a narrow slit that rotates with an identical frequency (50 Hz) as the neutrons from the pulsed source. Hence only neutrons travelling at the correct velocity pass through the gap and travel through slit one (S). Occasionally neutrons with a long wavelength (referred to as slow neutrons) pass through the chopper

however. These are removed from the beam by the frame overlap mirrors. This nickel coated mirror has a large radius of curvature allowing it to reject slow neutrons selectively, permitting only neutrons of desired wavelength from each pulse to pass through. The super mirror controls the angle of the incoming neutron beam with respect to the horizontal.

The neutrons pass through the second slit (S2) before being incident on the sample interface. The reflected and scattered neutrons are channeled through two further slits before they finally fall on the time of flight detector. The four slits collimate the incident (S 1 and 2) and the reflected beam (S 3 and 4). The width of each slit varies depending on the incident angle and the experiment. In this study the widths for slits 1 to 4 were usually set to 1.5, 1, 4 and 4 mm respectively, for a neutron beam incident at $0.8\,^{\circ}$ to the horizontal and 3,2,2,3 mm for a $1.5\,^{\circ}$ angle.

The resultant reflectivity is defined as the ratio of the intensity of the incident beam (measured by the monitor) to the reflected beam (measured by the detector). The final reflectivity for each angle was calculated automatically using instrument software and by placing the data on an absolute scale and combining both data sets, a complete reflectivity curve was obtained.

3.2.3 Experimental Details

Polymer samples were prepared using an identical procedure as outlined in section 3.1.2. A rectangular trough (NIMA, Coventry) with two computer controlled, movable barriers was used. The teflon trough was cleaned with swatches of Kimwipes soaked in chloroform and the polymer monolayers spread on the subphase as described earlier (3.1.4). The experimental system was enclosed in a Perspex box with two quartz windows to allow passage of the neutron beam. This enclosed environment minimised surface contamination and hydrogen/deuterium exchange. The trough was placed on a vibration isolation unit on a mobile plinth allowing small adjustment of the height of the monolayer.

For each new experiment alignment of the neutron beam had to be optimised as the monolayer height would vary slightly depending on the volume of the subphase present. This was achieved using a laser that followed an identical trajectory as the neutron beam,

and the height of the monolayer was adjusted until the laser passed through all four slits, and focussed on the centre of the detector.

The data collection was instrument controlled through a command file that collected data for a pre-determined integrated incident neutron flux, and altered the geometry of the system when changing angle. Data collection times varied depending not only on the beam current but also on the polymer and the subphase under study. In general however times ranged from 30-60 minutes for low angle data to 2-4 hours for high angle data.

3.2.4 Data Analysis

The experimental system was calibrated by collecting reflectivity data for a pure D_2O subphase. Two scaling parameters were calculated from such data using the program MULF (available at RAL) to determine the factor required to express the reflectivity as a single reflectivity curve on an absolute scale. In general these factors were circa 0.05 and 0.02 for the high and low angle data respectively. These two scaling factors were then applied to all data sets to convert the profiles to an absolute reflectivity scale. The low and high angle sets were then combined to produce a single reflectivity profile with a Q range of 0.0255 to 0.65 $Å^{-1}$ for each polymer-subphase combination. The background for each profile was determined by taking the average reflectivity value when the reflectivity had reached a constant value, usually when Q is greater than approximately 0.4 $Å^{-1}$. This background signal was subtracted from the raw data and then two combined data files (one with and one without background subtracted) were saved as ASCII files for subsequent analysis.

Two different analysis procedures were subsequently applied in attempt to physically interpret the experimental results[1]. The data treatment for each analysis approach is outlined here.

3.2.4.1 Optical Matrix Analysis

The raw reflectivity profiles were fitted using the optical matrix analysis without further manipulation. The fitting program RWRDOC was used throughout and an outline of the general procedure is given here.

A single uniform layer model was applied initially and fitted to each contrast. Values for the layer thickness, d, and the scattering length density, ρ, of the model system were estimated and the calculated reflectivity non-linearly least squares fitted to the experimental data by adjusting d and ρ. From these best-fit values, parameters describing the near surface organisation were obtained. To overcome any uncertainty about the uniqueness of the model used to fit the data, reflectivity curves for all polymer-subphase contrasts used were fitted concurrently using the same model. A model was only accepted if it provided consistent layer dimensions for all contrasts and if the surface concentrations calculated from the fit parameters were in good agreement with the actual amount of copolymer spread. Additional layers were incorporated into the model as required.

3.2.4.2 Kinematic Approximation

Prior to the application of the kinematic approximation to determine the partial structure factors additional data reduction was required. The background signal was initially subtracted from all data files collected. The profiles where the subphase was D_2O were initially Crowley[2] corrected using the program CORRECT, which was available at RAL. Subsequently all profiles were converted into the form of $R(Q)Q^4$ versus Q using the program CONVERT (also available at RAL) and the treated data were finally saved in ASCII format.

Section 3.3   Surface Quasi-Elastic Light Scattering

All surface quasi-elastic light scattering (SQELS) measurements were collected using two similar sets of light scattering apparatus, both of which were constructed in Durham. One set used a 100 mW diode pumped YAG laser (λ = 532 nm) while the newer experimental setup used a 400 mW solid state diode pumped laser. Both sets of equipment produced similar experimental results but the more powerful laser enabled the study over a greater range of frequencies while reducing data collection time and the signal to noise ratio. The instrumental details and experimental procedure presented below are essentially independent of the laser used.

3.3.1   Instrumental Details

The basic principle of the SQELS experimental set-up is to reflect and focus the light emitted by the laser onto the liquid surface using a series of lenses and mirrors, and collect the scattered light for analysis. A general schematic representation of the apparatus is given in figure 3.3.1. The equipment in each case was mounted on a heavy optical table and enclosed with Perspex to minimise external vibrations and any variations in air current.

Initially, the laser light was reflected down the optical rail and through the half wave-plate (W) and polarisor (P) by mirrors 1 and 2 (M1 and M2). The wave-plate rotated the plane of polarised light and attenuated the power of the laser beam, while the polariser removed any remaining horizontal polarised light. The light then passed through the first lens (L 1) which focussed the beam in preparation to pass through the diffraction grating (DG). The diverging beams produced after diffraction were attenuated by the neutral density filter (ND) in order to reach optimum conditions for heterodyne correlation (when the ratio of scattered light intensity to reflected light intensity ranges from 10^{-3} to 10^{-5}). Various filters were used depending on the power of the light beam but for the majority of experiments a filter with a transmission of 1 % (optical density = 2) was used. The main beam and diffracted beams were subsequently re-converged by the second lens (L2) and

were reflected by mirrors 3 and 4 (M3 and M4) onto the liquid surface. M3 reflects the light by 90 ° so the beam is travelling vertically when it falls onto M4, where it is reflected onto the liquid surface.
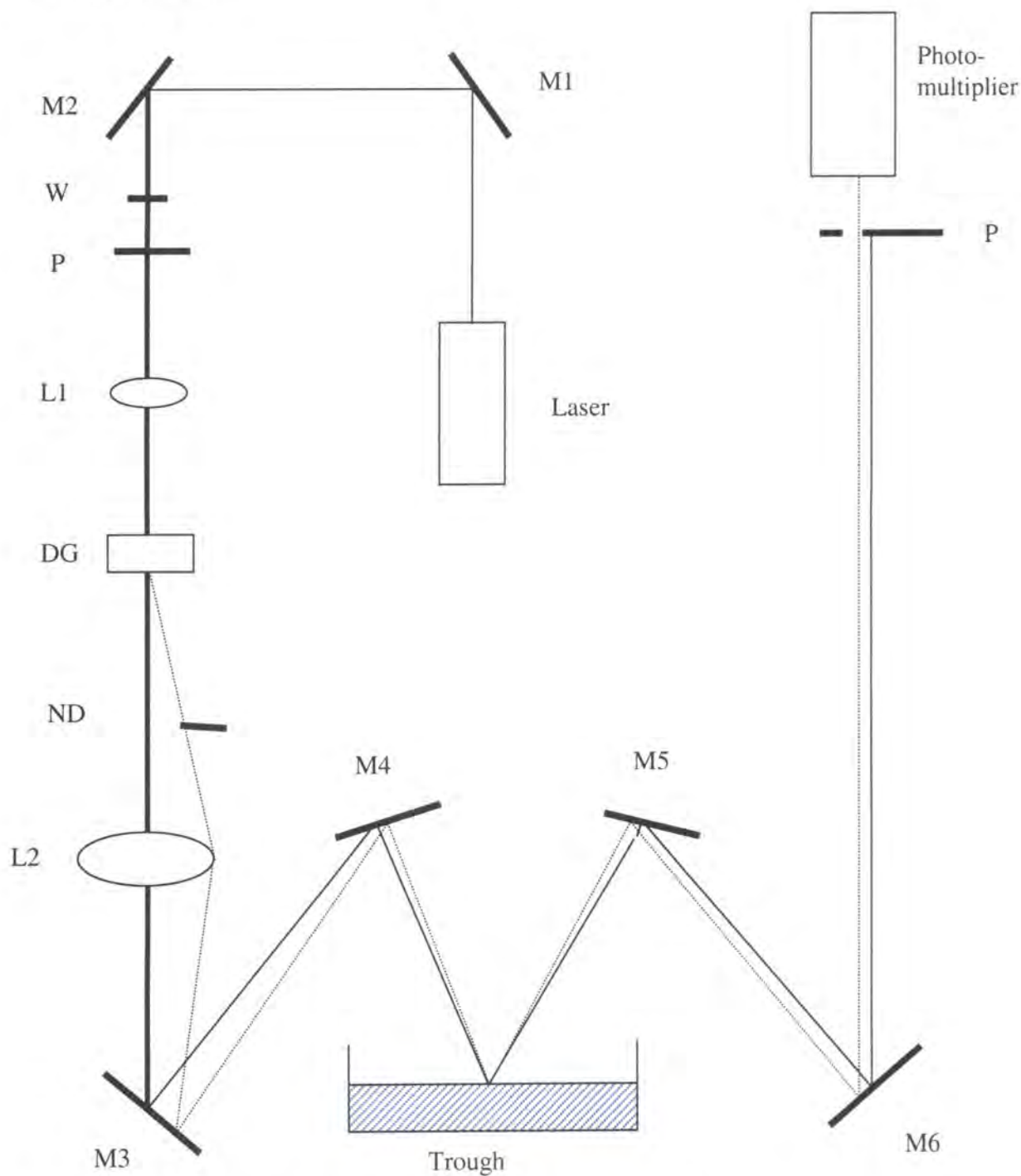

Figure 3.3.1. Schematic representation of the SQELS apparatus.

A rectangular Langmuir trough was used as the sample environment and was placed on a vibration isolation unit to minimise the impact of external vibrations. The subphase temperature was regulated using a Haake thermostat water circulator (only switched on between experimental runs). The coalesced light was reflected from the liquid surface and scattered to differing extents depending on the dynamical properties of the near surface. This light was subsequently reflected down by mirror 5 (M5) and through 90 $^\circ$ by mirror 6 (M6) so the path of the beam was once again parallel with the optical rail. As the beam travelled down the rail, it began to diverge, therefore when the beam arrived at the photomultiplier (PM) tube, it appeared as a horizontal array of spots. This array consisted of an intense spot, which was the un-diffracted main beam, and numerous adjacent spots with a rapidly decaying intensity. Each spot corresponds to a specularly reflected beam with different wavenumber and each consists of a mixture of the specularly reflected beam and light reflected by the main beam that fell at the same angle. Only the data from a single spot was collected at any one time hence only the desired spot was focussed down a pinhole (P) in front of the PM tube. This was achieved simply by manipulating the position of mirror 6, which was placed on a motor controlled mount, making fine adjustments possible.

The output from the Brookhaven PM tube was analysed by a correlator. The correlator was connected to a PC containing a 9000AT correlator card and Windows provided control through the Brookhaven program 9KDLSW. This correlator allowed the selection of a finite series of channel widths (for example 10 μs, 5 μs, 2 μs and 1 μs were commonly used), however this limited the number of channels. 256 channels were available at 10 μs, but only 128 channels at 5 μs, 80 at 2 μs and 40 at 1 μs.

3.3.2 Experimental Details

Three different types of experiments were undertaken using SQELS and each is outlined here. In all cases the trough was cleaned, and polymer samples prepared as previously outlined in section 3.1.2.

Prior to each experiment the apparatus was calibrated by determining the wavenumber, q, of each spot for the surface of pure UHQ water. Ten correlation functions were collected for every spot in turn, fitting each function using the damped cosine fit (see section 3.3.3.1 for further details), and then taking the average of the fitted capillary wave frequency and damping values. The physical parameters of the water subphase (surface tension, viscosity and density) for the experimental temperature were then entered into the program CANICE. This program solved the dispersion equation and calculated theoretical values of wave frequency and damping as a function of wavenumber. The experimental wavenumbers for each diffracted beam were subsequently determined by plotting the calculated wave frequency against q, then extracting the q value that corresponded to each experimentally obtained frequency value.

The first experiment undertaken examined the dependence of the surface properties on the surface concentration of the spread film. A single spot was selected, usually with a low q value (circa 350 cm^{-1}, spot 3), as correlation functions could be collected relatively quickly in approximately 30 seconds. Each film was spread (as outlined in section 3.1.4) and a period of 15 minutes elapsed to allow the evaporation of the solvent. The film was subsequently compressed to the desired surface concentration and a further period of 5 minutes elapsed to let the film equilibrate before ten correlation functions were recorded. This process was repeated for each surface concentration required.

In the second approach the frequency dependance of the film was investigated. Each film was compressed to a fixed surface concentration and ten correlation functions were collected at a series of wavenumbers. The wavenumber was simply varied by focussing each different diffracted spot on the pinhole of the PM tube. The range of wavenumbers accessible was dependent on the power of the laser used: 220-1300 cm^{-1} for the 100 mW laser and 220-1900 cm^{-1} for the 400 mW laser.

The final experiment was performed to explore the time dependency and stability of the film. Films were spread and compressed to a desired surface concentration in the usual manner, then one correlation function was taken every minute for a period of approximately ten hours. A fixed q value was used, usually spot 3 (wavenumber of circa 350 cm^{-1}). Each function was individually analysed and the values for wave frequency and damping were plotted as a function of time.

3.3.3 Data Analysis

All correlation functions were analysed using both the damped cosine analysis (to give frequency and damping) and the spectral fit[3] (to give surface viscoelastic parameters). The fundamental theory behind both fitting procedures has been outlined previously in Chapter Two, therefore only the operation of the individual programs will be presented here.

3.3.3.1 Damped Cosine Analysis

Values for frequency and damping of the capillary waves were obtained by fitting the experimental correlation functions using the program BRKFITS. Model correlation functions were generated from initial estimates of these two parameters, and the model was least squares fitted to the experimental, thus providing 'best-fit' values for the frequency and damping of the capillary waves.

The fitting procedure was extremely fast provided reasonable starting parameters were used. Different values were therefore used depending on the wavenumber of the diffraction spot under study. Each model correlation function was overlaid with experimental data and the quality of fit analysed. A typical example of a good quality fit is given in figure 3.3.2.

All accepted fits for each q value were averaged using the program FITSUM to give final values for frequency and damping.
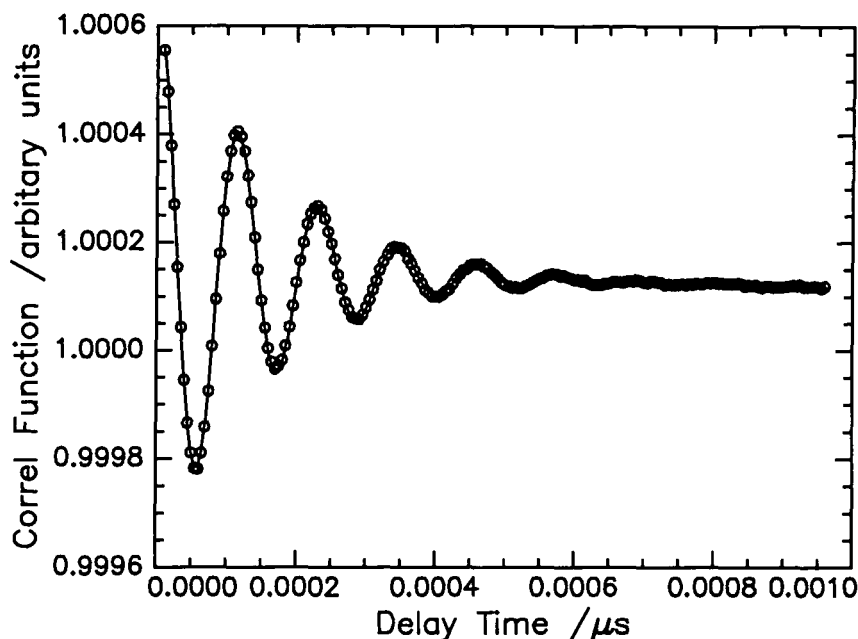
Figure 3.3.2. Experimental correlation function, circles, with damped cosine fit overlaid, solid line. The data is recorded for n25 at 0.3 mg m^{-2}, q = 330 cm^{-1}.

3.3.3.2 Spectral Fit

Extraction of the viscoelastic parameters required a more elaborate and time-consuming procedure than the damped cosine fitting procedure. Generally four surface visco-elastic parameters were estimated and the program BRKHERM generated a theoretical power spectrum of the scattered light, which gave a model correlation function when Fourier transformed. The generated correlation function was then compared to the experimental data and least squares fitted until the sum of squares was minimised. This procedure was again reliant on reasonable values being predicted for the starting parameters but it was relatively easy to estimate the surface tension (γ_o) and dilational modulus (ε_o) as the static values were known. These model parameters were then allowed to vary in the fitting procedure between 0-100 mN m^{-1}. The transverse shear viscosity was held constant at zero in accordance with current theory[4]. The value of the dilational viscosity was

unknown and a range of negative and positive starting parameters were tried and allowed to fluctuate between $-1e^{-3}$ and $1e^{-3}$ mN m^{-1}.

The fitting process was repeated several times, varying the initial values, depending on the quality of the returned fits. Final values were only accepted when the quality of fit was good and identical fits were obtained when the starting parameters were slightly above and below the returned values. The average values extracted were determined using the program HERMRES for each set of correlation functions.

Section 3.4   References

1.   Lovell, M.R.; Richardson, R.M. *Current Opinion in Colloid and Inter. Sci.,* **1999,** *4,* 197.

2.   Crowley, T.L. *Physica A,* **1993,** *195,* 354.

3.   SQELS data analysis software was originally made available by the late Professor John Earnshaw, Queens University Belfast and modified by Drs. A. Milling and R. W. Richards at Durham University.

4.   Buzza, D. M. A.; Jones, J. L.; McLeish, T. C. B.; Richards, R. W. *J. Chem. Phys.* **1998,** *109,* 5008.

Chapter Four

Synthesis and Characterisation of Graft Copolymers

Section 4.1   Introduction

This chapter discusses two aspects. Firstly the experimental procedure and synthetic strategy employed to prepare a series of well-defined amphiphilic graft copolymers are set out. Experimental details will be given in addition to a brief discussion of problems encountered. Secondly, an overview of the characterisation of all materials prepared will be presented before drawing conclusions as to their overall structure and composition.

The target copolymer material consisted of a hydrophobic hydrocarbon main chain with pendant hydrophilic grafts, schematically represented in figure 4.1.1. In this diagram the copolymer is forming a monolayer at the air-water interface with the grafts emanating from the backbone at regular intervals with a high grafting density (number of grafts per unit area). The hydrophilic grafts in this case are stretching into the subphase and behaving as stretched wet brushes.

Figure 4.1.1. Schematic representation of amphiphilic graft copolymer at an air-water interface.

The aim of this project was to examine the effect of varying the copolymer graft length on the organisation and dynamics of a thin film of the material at fluid interfaces. To this end three materials were prepared where the backbone length was kept constant while the degree of polymerisation of the grafts was varied. Ideally for neutron reflectometry studies four isotopically different copolymers are needed for each

copolymer in the homologous series; fully protonated version, fully deuterated and two where each homopolymer constituent was deuterium labelled.

Section 4.2   Synthetic Strategy

The target copolymer (given in figure 4.2.1) has a saturated backbone based on poly (norbornene) (PNB) with a poly (ethylene oxide) (PEO) graft on each backbone unit. Synthesis via three steps: living anionic polymerisation, ring opening metathesis polymerisation (ROMP) and a hydrogenation reaction was envisaged.
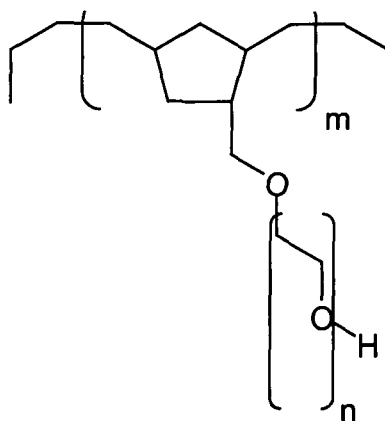

Figure 4.2.1. Graft copolymer with a poly (norbornene) based backbone and poly (ethylene oxide) grafts.

A bi-cyclic functionalised PEO macromonomer (macromer) was initially synthesised using anionic polymerisation, and the olefinic functional group subsequently ROMPed to prepare the polymacromer, a graft copolymer. In principle the living conditions of both polymerisation techniques would allow the architecture of the copolymer to be tailored as the molecular weight and the molecular weight distribution of both the macromer and the copolymer could in theory be controlled simply by varying the ratio of monomer to initiator species. The final step involved saturation of the backbone to eliminate the possibility of cross-linking reactions or photo-initiated degradation during a SQELS experiment, or over time. The added advantage of reducing the olefinic bonds was that it introduced the possibility of selectively deuterating the backbone.
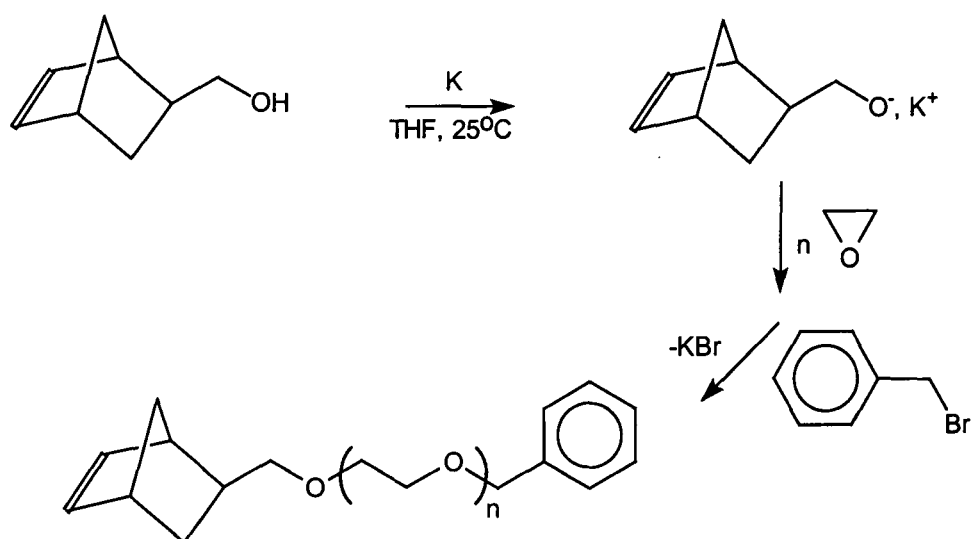
Figure 4.2.2. Preparation of norbornene functionalised poly (ethylene oxide) macromonomer.

The first step towards preparing the desired copolymer material (outlined in figure 4.2.2) was to synthesise norbornene functionalised PEO[1]. The starting material, norbornene methyl hydroxide, was deprotonated by passing it over a potassium mirror. The potassium alkoxide formed acted as initiator and attacked an ethylene oxide (EO) monomer to form an active carbanion. This active site acted as the propagating species for the stepwise addition of monomer units, and was terminated by adding benzyl bromide after all monomer was consumed.

The second step involved the ROMP of the functionalised PEO macromer[2] using the well-defined hexa-fluorinated Schrock or Grubbs initiating complexes (for further details see section 2.1) as outlined in figure 4.2.3. Each initiator has a metal core (molybdenum or ruthenium) with bulky ligands that control the approach and co-ordination of the reactive carbene bond to the double bond of the norbornene group on the macromer. The molybdenum catalyst has been proven to be stereospecific[3], but the ruthenium catalyst is tolerant to a wider range of functional groups including oxygen[4].
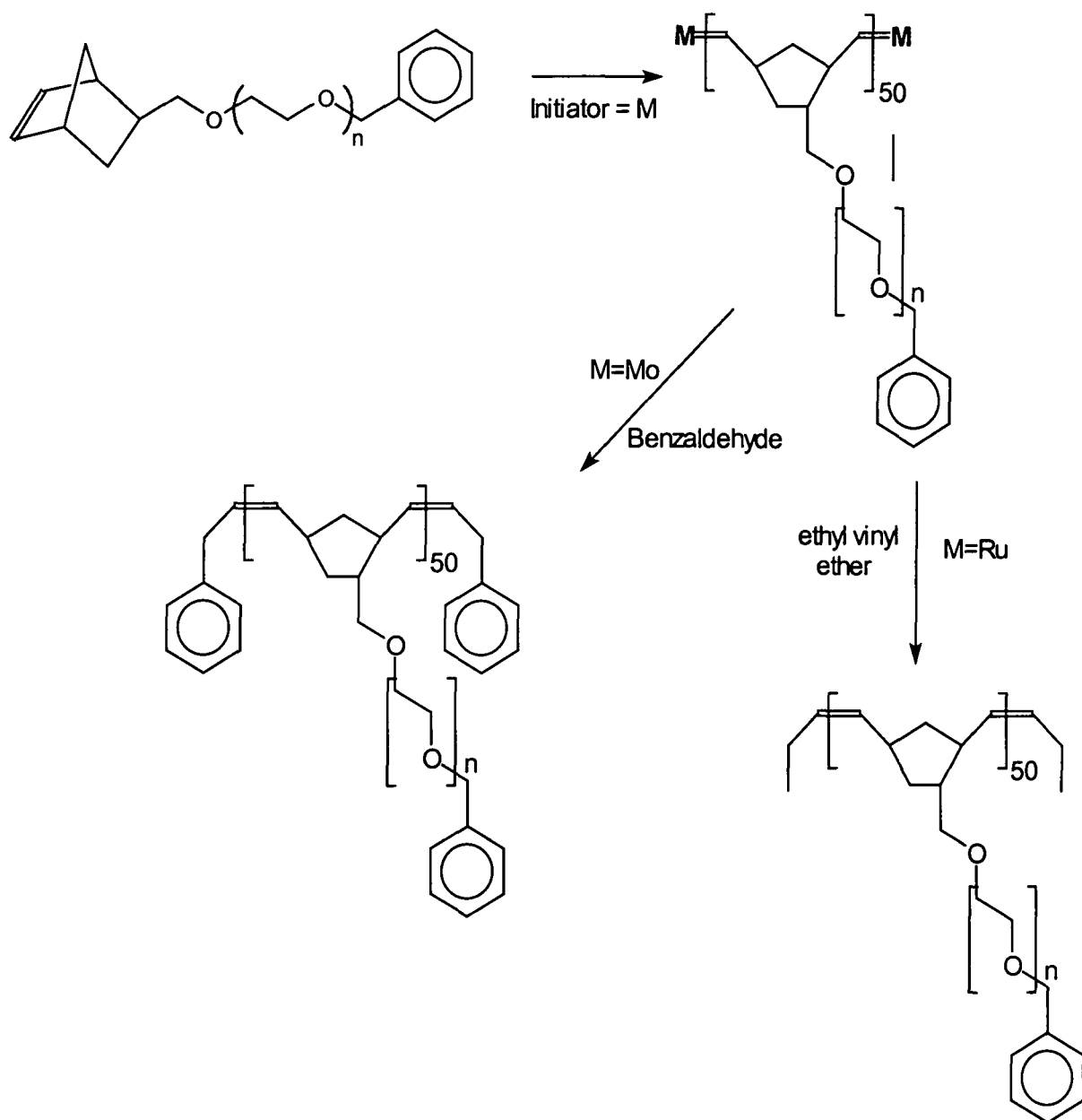
Figure 4.2.3. Ring opening metathesis polymerisation of PEO macromer.

Both metal complexes ring open the highly strained norbornene molecule to form the backbone of the copolymer. This process is a living polymerisation hence the backbone length, and consequently grafting density, can be controlled by manipulating the metal complex to macromer ratio[5]. The metal complex was cleaved from the propagating chain end by adding either an aldehyde, usually benzaldehyde (Schrock initiator), or ethyl vinyl ether (Grubbs initiator).

The final step was to reduce the backbone as shown schematically in figure 4.2.4, and two methods were attempted.
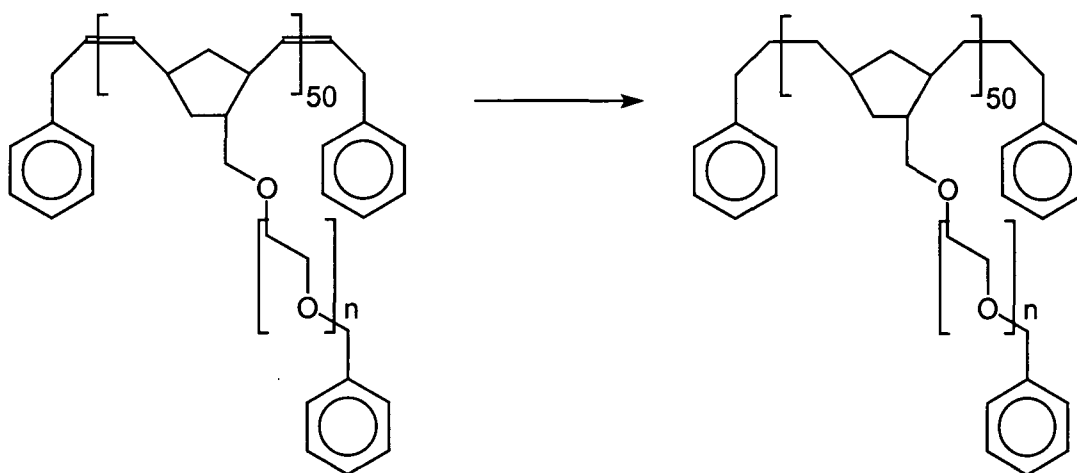

Figure 4.2.4. Reduction of the hydrophobic backbone.

The first was the high-pressure hydrogenation using a palladium catalyst supported by calcium carbonate (5 %)[6]. This heterogeneous reaction occurred when the olefinic double bonds came into contact with the palladium surface where hydrogen was exchanged in a cyclic mechanism, as depicted in figure 4.2.5.
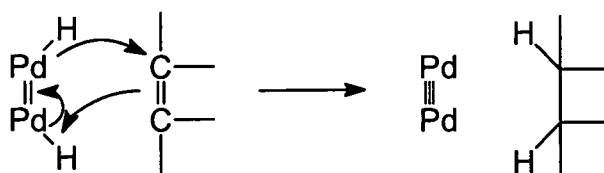

Figure 4.2.5. Mechanism for the reduction of the olefinic bond using a palladium supported catalyst.

The second method used a diimide prepared in-situ from a hydrazide salt[7]. In this homogeneous reaction the diimide reduces the olefinic bond via a similar cyclic mechanism as the catalytic hydrogenation.

Section 4.3   Experimental

4.3.1   General

All manipulations of air and moisture sensitive materials were performed using standard Schlenk and cannular transfer techniques under vacuum or nitrogen atmosphere, or in a glove box. NMR spectra were recorded using a Varian VXR400S (^{1}H at 399.95 MHz and ^{13}C at 100.58 MHz) using tetramethyl-silane (TMS) as internal standard. Size exclusion chromatography (SEC) data were obtained using chloroform solutions using a Knauer HPLC pump 64, a Waters R401 RI detector and three PL gel columns with pore size of 10^2, 10^3 and 10^5 Å (flow rate 1 cm^3 min^{-1}). Solutions were filtered through a Whatman WTP type 0.2 μm filter to remove particulates before injection. The columns were calibrated by PEO standards of molecular weight ranging from 400 to 2×10^6 g mol^{-1}. DSC measurements were recorded using a Perkin Elmer Pyris DSC at a rate of 10 K min^{-1}. Dilute solution viscometry data were collected using a Schott-Gerate automated viscometer system utilising a Schott-Gerate Ubbelohde viscometry tube (bore size 0.46 mm) immersed in a water bath at 298 K.

Materials

Ethylene oxide (EO - hydrogenous and deuterated) (Fluka) monomer was purified by stirring over sodium hydroxide (24 hrs), dried over calcium hydride (24 hrs) and then stirred with 20 % v/v of dibutyl magnesium before vacuum distilling immediately prior to use.   Hydroxy methyl-5-bicyclo [2,2,1] heptene, commonly referred to as norbornene methyl hydroxide (NBMeOH) (Aldrich) was fractionally distilled under reduced pressure (324 K, 0.8 mbar) from molecular sieves and used without further purification. The hexa fluorinated Schrock initiator for ROMP was Mo(NAr)(OC(CH$_3$)(CF$_3$)$_2$)$_2$(CHt-Bu) (Strem) and was used without purification. The Grubbs initiator also for the ROMP reaction was RuCl$_2$(=CHPh)(PCy$_3$)$_2$ and was prepared following the published method[8]. Benzyl bromide (Aldrich) was fractionally distilled under reduced pressure (337 K, 0.8 mbar) and stored over molecular sieves. Benzaldehyde and ethyl vinyl ether (both Aldrich) were used without further purification. Solvents used for polymerisation reactions were dried by prolonged reflux

over the appropriate drying agent (as indicated in parentheses below), freshly distilled then degassed prior to use: tetrahydrofuran (potassium benzophenone), benzene (calcium hydride) and chloroform (phosphorous pentoxide). Deuterated solvents were stirred over the appropriate drying agent and vacuum distilled prior to use.

4.3.2   Macromonomer Synthesis

The polymerisation was carried out in an evacuated reaction vessel (10^{-7} mbar) with a rubber seal. Washing the vessel with a living polystyrene solution in benzene eliminated any residual water or protic impurities remaining on the glass walls. The orange colour indicated the living carbanion and thus the absence of water. The vessel was subsequently washed with dry benzene, which was vacuum transferred into the reaction vessel from the side-arm containing the living polystyrene solution. This process was repeated several times until the benzene wash was clear. In a typical synthesis, 3.85 mmol of a 1 M stock solution of NBMeOH was added to 100 ml of dry, degassed tetrahydrofuran (THF) in the previously evacuated vessel. This clear solution was cannulated under positive dry nitrogen pressure on to a potassium mirror in an evacuated vessel and allowed to deprotonate for 24 hours. The solution was subsequently transferred through a silica filter to remove residual potassium metal before being cannulated back into the original vessel. The initiating solution (straw yellow in colour) was subjected to repeated freeze, evacuate, thaw cycles before the calculated quantity, 0.114 mol, of EO was vacuum distilled into the THF solution of the metallated NBMeOH. The solution was stirred continuously at room temperature for 3 days before terminating the living chain ends by adding excess benzyl bromide. After approximately one hour the potassium bromide by-product was removed by vacuum filtration through celite. The macromer was recovered by precipitation in a ten-fold excess of chilled hexane. After filtration and drying under vacuum at 298 K for three days, the white powder obtained (87 %) was analysed by elemental analysis, SEC, viscometry, ^{1}H and ^{13}C NMR. This macromer was used without further purification.

4.3.3 ROMP of Macromer

ROMP using the Schrock initiator was carried out in a nitrogen filled glove box to avoid deactivation of the metal complex, while reactions involving the more robust Grubbs catalyst were undertaken in the fume cupboard. This was essentially the only difference in experimental procedure for the two initiating complexes. Glassware for all polymerisations was pre-dried in the oven (448 K). In a typical NMR scale polymerisation, macromer (0.2 mmol, 50 equivalents) was dissolved in benzene-d_6 (600 μl) and added to a stirred solution of initiator (0.05 mmol) in the same solvent (400 μl). A low M.Wt. macromer was selected (1200 g mol^{-1}, 25 EO units) to ensure the ^{1}H NMR peaks due to the end groups could be identified. In a typical scaled-up ROMP using the Grubbs initiator a 5 ml solution of the ruthenium complex (47 μmol) in dry, degassed benzene was added to a 20 ml solution (2.3 mmol) of the prepared macromer (M_n = 1800 g mol^{-1}) dissolved in the same solvent. This was stirred vigorously for 4 days before the ruthenium complex was cleaved from the chain ends by adding excess ethyl vinyl ether. The copolymer was precipitated in a ten-fold excess of chilled diethyl ether, isolated and dried. Repeated dissolution and precipitation of the copolymer in the minimal volume of benzene removed residual catalyst and finally produced a white powder (78 %) after drying under vacuum at 298 K.

4.3.4 Hydrogenation

Method One

The palladium-supported catalyst (5 % calcium carbonate) was initially activated in a 2 L high pressure autoclave reactor by heating for four hours at 398 K under hydrogen gas (100 psi). Typically 2 grams of the graft copolymer was dissolved in 500 mls of ethanol and added to the contents of the autoclave, after it had returned to ambient temperature. The resulting heterogeneous mixture was heated to 368 K and stirred continuously under hydrogen (500 psi) for 18 hours. After reaction, the catalyst was removed by filtration through celite under a positive nitrogen pressure, then gravity filtered through Whatman WTP type 0.5 mm filter. Ethanol was evaporated and the

residual polymer was dissolved in minimal benzene, precipitated out in diethyl ether and dried under vacuum.

Method Two

Typically 0.02 g (1 µmol) of para-toluene sulfonhydrazide salt (CH$_3$C$_6$H$_4$SO$_2$NHNH$_2$) dissolved in chloroform (10 mls) was added to 1.00 g (10 µmol) of graft copolymer (M$_n$ = 1800 g mol^{-1}) in 140 mls of chloroform. The homogeneous solution was heated to reflux (373 K) where the onset of reaction was marked by the vigorous evolution of gas. Refluxing was maintained for three hours before the system equilibrated to room temperature.

The solvent was removed on the rotary evaporator before redissolving the copolymer in minimal benzene. The hydrazide salt was easily removed by vacuum filtration at this stage, as it was insoluble in benzene. The copolymer was recovered using a ten fold excess of chilled di-ethyl ether as non-solvent and subsequently dried in the vacuum oven (298 K) for three days.

Section 4.4   Results and Discussion

The first step towards preparing a graft copolymer involved the polymerisation of ethylene oxide (EO) to obtain the macromer. The deprotonation of norbornene methyl hydroxide (mixture of endo and exo forms in the ratio 4:6) was straightforward and fast as the colour of the solution switched immediately from clear to straw yellow, indicating the formation of the alkoxide. Residual potassium metal was removed from the reaction vessel to ensure that no unfunctionalised PEO macromers could be synthesised. The polymerisation solvent was THF, which is not only a good solvent for low molecular weight (M.Wt.) PEO, but it also enhances the degree of dis-aggregation of the metal alkoxide because the polar nature of the solvent helps the organo potassium to exist as a free species with strongly developed ionic character. It is important to have this conformation to ensure that the rate of the initiation (first ring opening of EO) is fast and occurs instantaneously for all alkoxide species, thus allowing all chains to grow at identical rates.

The rate of the polymerisation was slow in comparison to the preparation of the initiator as the viscosity of the reaction solution was observed to increase over a period of three days. The progress of the reaction for PEO with a target M.Wt. of 2300 (50 EO units) was analysed in detail by extracting samples from a reaction mixture periodically. The living chain ends in each aliquot were terminated, precipitated and analysed by size exclusion chromatography (SEC) in attempt to monitor the M.Wt. of the growing chain as a function of time. It is evident from the results from this study (figure 4.4.1) that the initial rate of polymerisation is fast as the M.Wt. increases rapidly over the first 36 hours. Thereafter the rate decreases and reaches a constant value after circa 44 hours. Such behaviour is probably due to the conversion of monomer into polymer, which will effectively reduce the concentration of monomer and also reduce the mobility of the active chain ends. This reaction was terminated after 72 hours and the macromer isolated, dried and analysed by SEC, viscometry and ^{1}H and ^{13}C NMR.
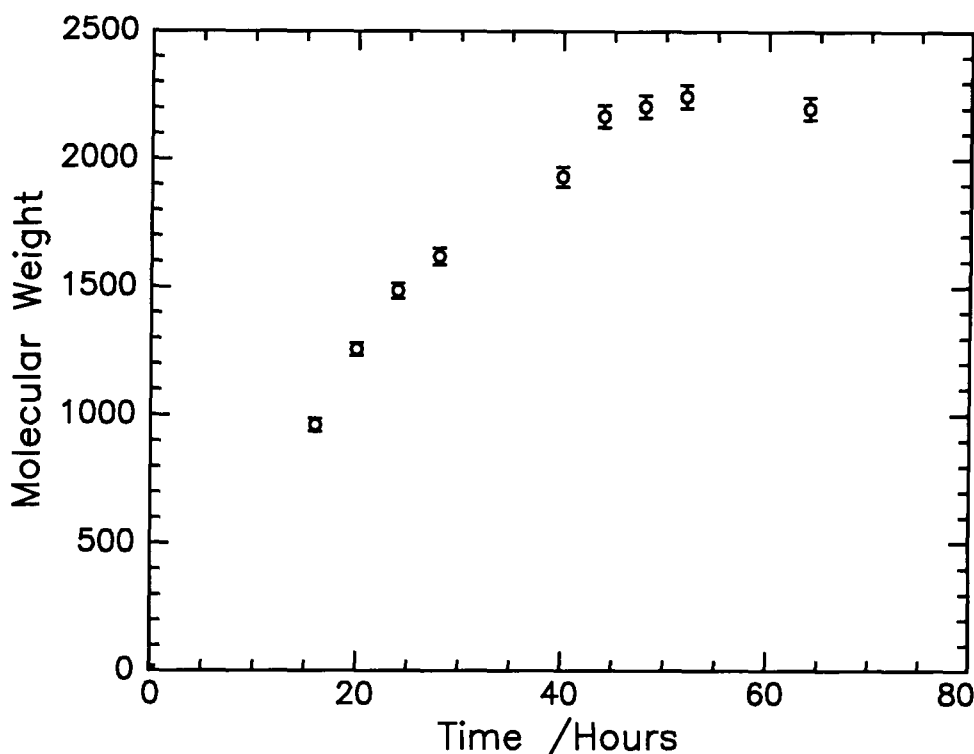
Figure 4.4.1. Graph of molecular weight versus time for the polymerisation of EO (target molecular weight of 2300).

A typical SEC trace for the macromers synthesised in this way is given in figure 4.4.2 and it is immediately obvious that the polymer is monodisperse and has been prepared via a living mechanism as the single peak observed is narrow with a polydispersity very close to one (1.04). The weight average M.Wt. is 2200 ± 40 (47 ± 1 EO units), which is extremely close to the target value. The degree of polymerisation of the macromer was also estimated from the proton NMR spectra (figure 4.4.3) by taking the ratio of the signal for the CH_2CH_2 protons from the EO group (δ 3.7-3.5 ppm) to twice that from the alkylidene protons (δ 6.1-5.9 ppm). The M.Wt. estimated using this analysis was 2280 (49 EO units), which is extremely close to the target value. The extent of functionalisation was also determined from NMR by dividing the integral value for the peak from the methylene protons next to the terminal benzylic group (δ 4.6 ppm) by the integral from the alkylidene peaks. This value was close to one (1.02) indicating that all macromer were initiated by norbornene methyl alkoxide.
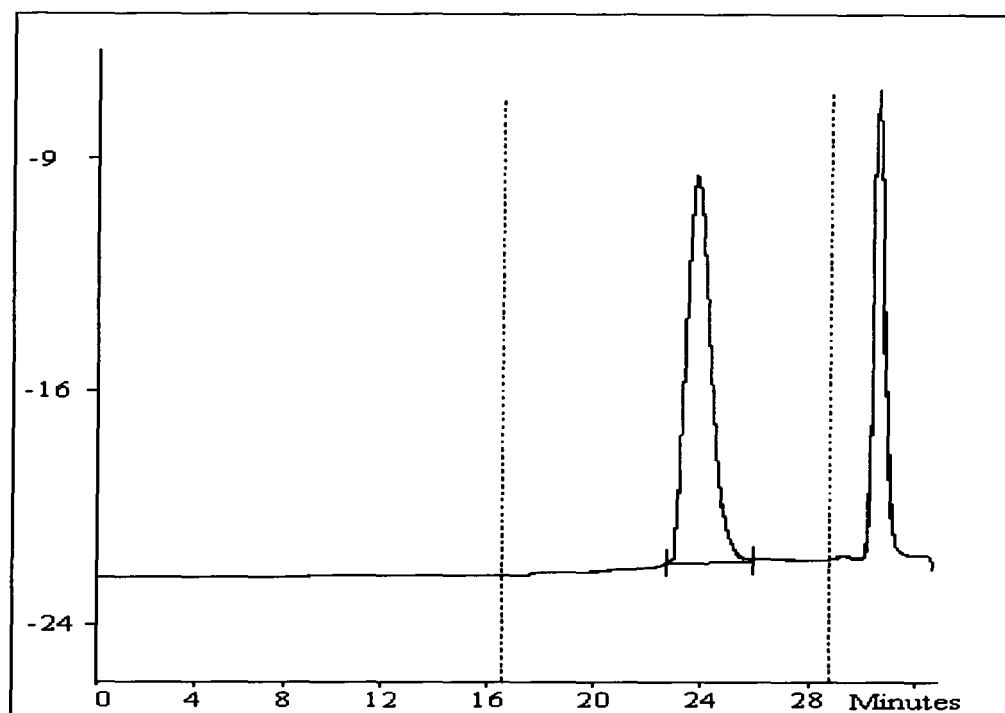
Molecular Weight Averages			
Mp=	2281	Mz=	2308
Mn=	2107	Mz +1=	2397
Mw=	2198	Mv=	2175
Polydispersity=	1.043	Peak Area=	138429

Figure 4.4.2. SEC trace obtained for macromonomer with a target degree of polymerisation of 50 EO units.

The rate study of the polymerisation of EO proved that the anionic polymerisation of EO using norbornene methyl alkoxide initiator was successful and that it should be left for at least three days to ensure consumption of all monomer. It also confirmed that manipulating the ratio of monomer to initiator species could control the degree of polymerisation. NMR studies revealed that there were no impurities present in the macromer sample therefore the materials were ROMPed without further purification. Macromers prepared with a M.Wt. below circa 1000 (and above circa 600) were all waxy solids and were fine white powders above this critical M.Wt. Full characterisation of the materials prepared is given in section 4.5.
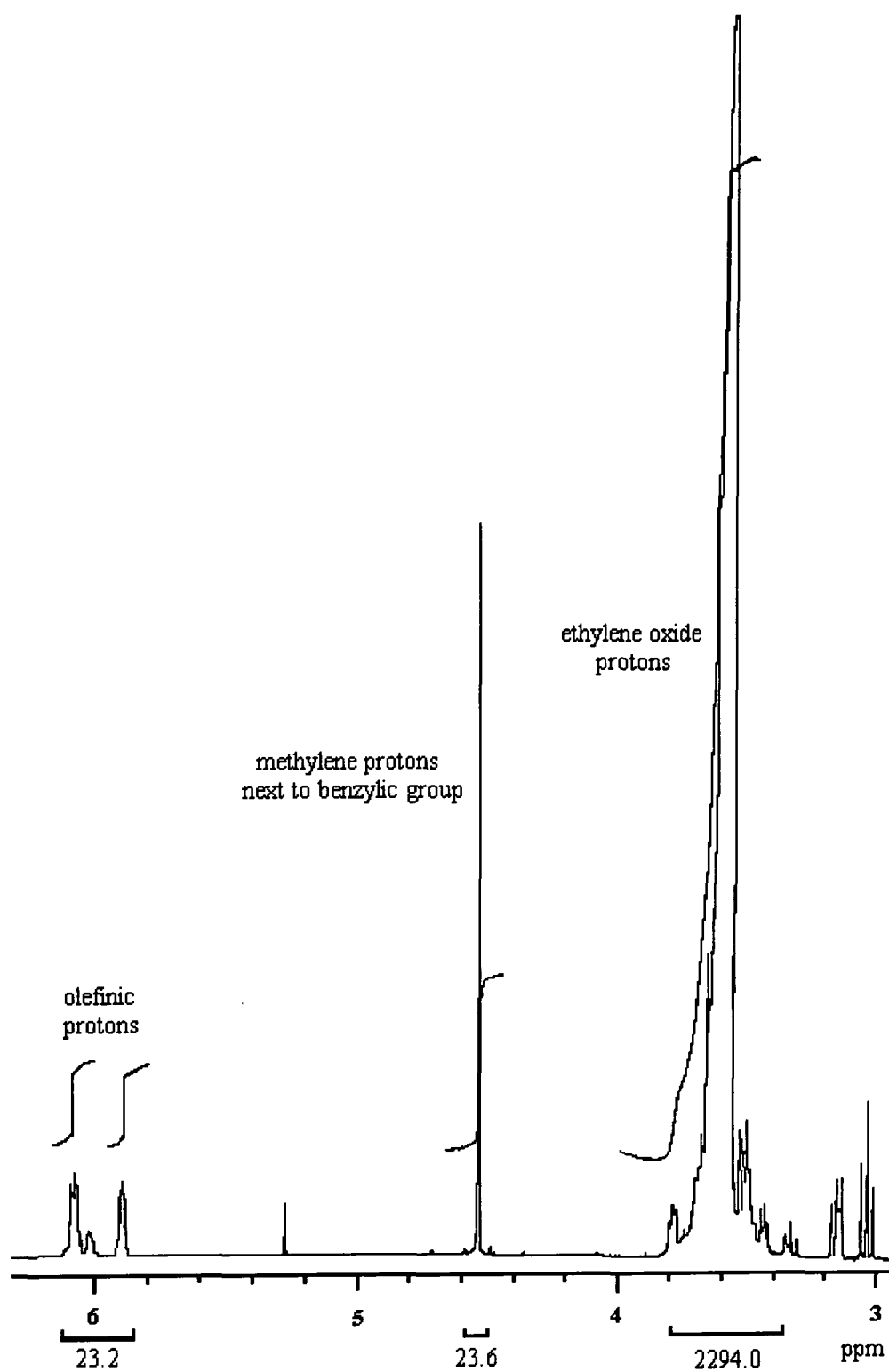
Figure 4.4.3. ^{1}H NMR obtained for the macromer with a target molecular weight of 2300 (50 EO units).

The well-defined macromers were ROMPed initially using the hexa fluorinated Schrock initiator, hence the copolymer was end-capped with benzaldehyde (see figure 4.2.3). The ROMP reaction was initially investigated on a NMR scale before the reaction was scaled up to obtain sufficient material for characterisation and property analysis. The NMR tube polymerisation allowed the living polymerisation system to be monitored by recording and analysing ^{1}H NMR spectra at various time intervals.

If the macromer was indeed initiated by the molybdenum initiator then the proton NMR spectra would have revealed two broad unresolved signals characteristic of the propagating alkylidene at circa 11.6 and 11.4 ppm[9]. If the initiating complex however was present in its uncomplexed state, then a single peak would have been observed at circa 11.3 ppm[9]. Unfortunately in this experiment no peaks were observed in this region suggesting that the molybdenum complex had instantly degraded. Several methods were attempted to overcome this problem including taking extra care to ensure both the solvent and glassware were dry and free from protic impurities; changing the reaction solvent to chloroform, dichloromethane and 1,2-diethoxyethane (chosen because it is chemically similar to EO); drying the macromer in the vacuum oven for several weeks at elevated temperatures (but below the melting point) and also less sterically hindered norbornene groups were added to try to at least start polymerisation. All attempts were however unsuccessful, thus it was concluded that heating the macromer under vacuum was an insufficient method of removing residual water from the extremely hydrophilic PEO grafts, and the water molecules that remained were immediately killing the catalyst.

An identical reaction was subsequently attempted where the molybdenum catalyst was replaced with the more robust ruthenium initiator. This reaction was more successful as the ^{1}H NMR spectra revealed two broad signals at δ18.9 and δ18.7 due to the propagating alkidenes as shown in figure 4.4.4. These signals could be due to head (PEO containing portion) or tail (remainder of norbornene group) insertion of macromer to the active site (a and b in figure 4.4.5) leading to head-tail, tail-head, tail-tail or head-head placements of repeat units in the polymer chain.
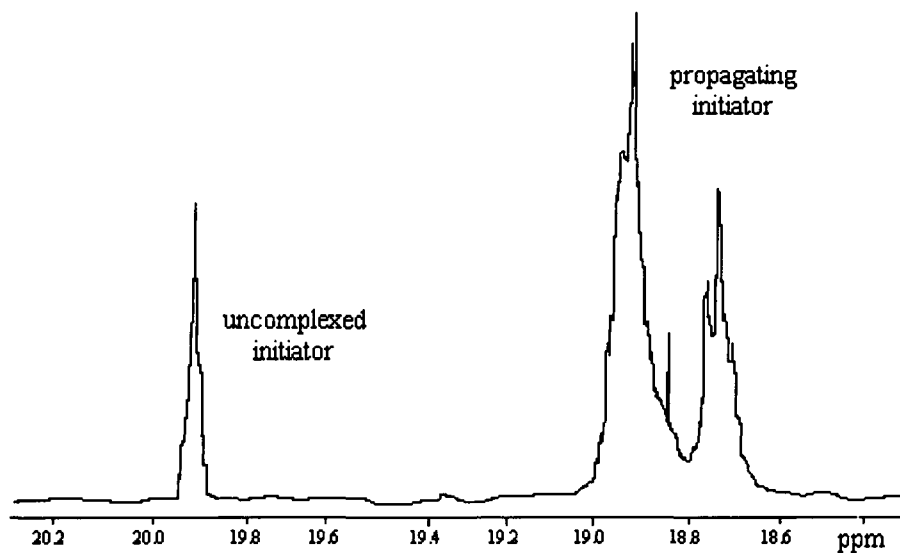
Figure 4.4.4. Alkylidene region of the ^{1}H NMR spectra for ROMP of macromer with 50 EO units after 15 minutes.
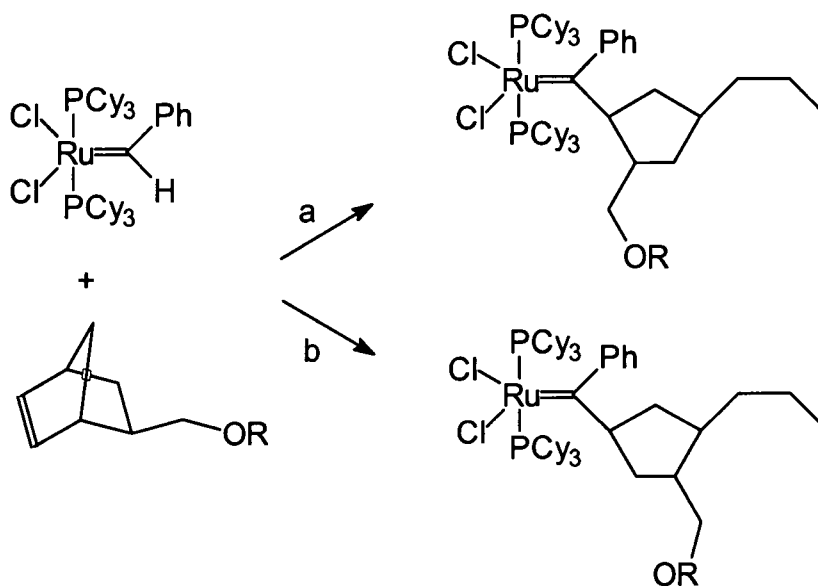

Figure 4.4.5. Head (a) and tail (b) insertion of macromers at the active site in the ROMP reaction.

The signals due to the propagating alkylidene protons are broad due to the complexity of the slightly differing environments of the nuclei. An additional single peak at 19.9ppm is observed in figure 4.4.4 due to uncomplexed ruthenium initiator. The intensity of this peak gradually diminishes as the polymerisation progresses indicating that the rate of initiation is slower than the rate of propagation. This observation agrees well with published work on norbornenes and mono-substituted norbornenes[10] and explains why final products have a relatively broad M.Wt. for a living polymerisation. The slow rate of initiation could be partly due to the metal complex remaining entrapped within the PEO chains as the electron rich oxygen's compete with the carbon-carbon double bonds for co-ordination to the vacant site of the transition metal catalyst. This hypothesis is probable as the polydispersities observed in this study (1.21-1.62) are slightly broader than those obtained for a similar ROMP reaction using the less electron donating polystyrene macromer (1.06-1.51)[9].
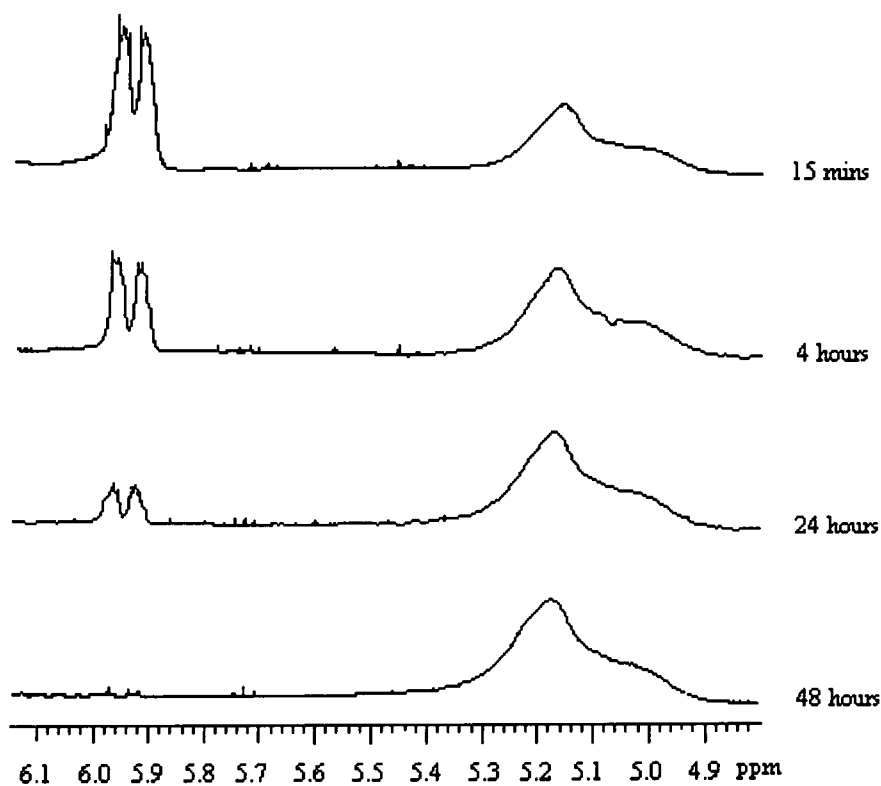

Figure 4.4.6. ^{1}H NMR study of the ROMP reaction as a function of time following the decrease in macromer (5.3–4.9ppm) and the increase of polymeric alkene (6.1–5.9ppm) protons.

The progress of the polymerisation reaction was studied by following the decrease of the macromer (6.1-5.9 ppm) and the increase of the polymeric alkene proton signals (5.3-4.9 ppm) over time. A selection of NMR spectra from such a study are given in figure 4.4.6 and it is evident that the rate of the initial propagation steps are fast as a peak for polymacromer is present after only 15 minutes. The remaining steps of the reaction are slow, probably due to the active site being sterically hindered, but the polymerisation eventually goes to completion after two days.

The living alkylidene ends of the copolymer were quenched and the product precipitated several times to remove residual catalyst (pink) trapped in the polymer chains. The SEC results of the pure copolymer (white), given in figure 4.4.7, reveal that the product was monomodal with a polydispersity of 1.32 and also that the product had a lower retention time, hence higher M.Wt. than the macromer indicating that ROMP was successful.

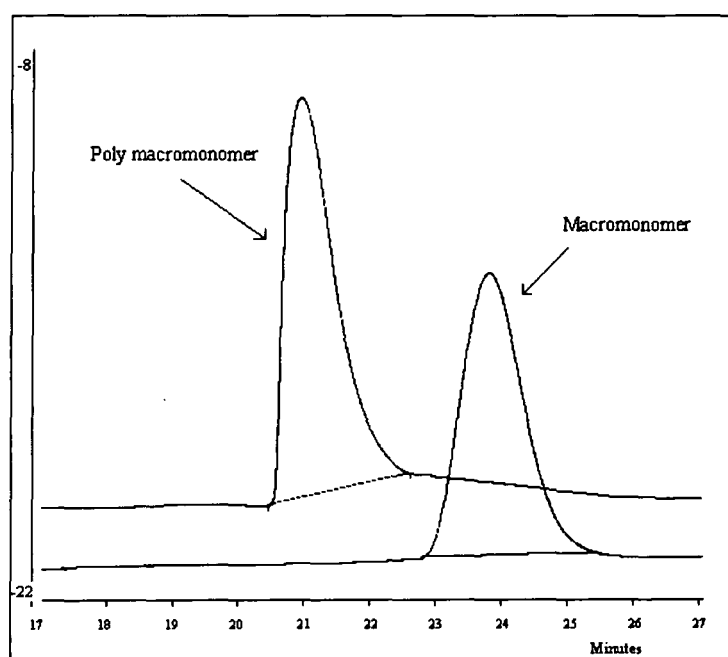**Figure 4.4.7.** SEC results for the polymacromer compared to the macromer where both graft and backbone have a target degree of polymerisation of 50 repeat units.

Accurate M.Wts. could not be extracted using this technique since the values were calculated with reference to the calibration material (PEO linear standards) and the hydrodynamic volume to M.Wt. relationship for the graft copolymers in this study is not

known. Despite this however, the NMR study provided sufficient evidence to conclude that the ROMP reaction was successful and took two days to obtain a copolymer with a backbone consisting of 50 graft chains, each with 50 EO units.

Typically in a preparative scale reaction, the appropriate quantity of catalyst in solution (5 mls) was added to 5 g of monomer dissolved in 20 ml. Initially very dilute solutions (circa 0.02 mol L^{-1}) were prepared and no reaction was observed but the proton NMR revealed the catalyst was present in a de-complexed form (single peak at 19.9 ppm). It is well documented however that ROMP reactions in general are highly dependent on the concentration of the reaction mixture[5] and this influences the entropy of the system and hence thus the Gibbs free energy (ΔG). ΔG must be ≤ 0 for polymerisation to proceed and is related to the enthalpy change (ΔH), the entropy change (ΔS) and the temperature, as in equation 4.4.1.

$$\Delta G = \Delta H - T\Delta S$$ **Equation 4.4.1.**

It is well known that the sign for a ROMP reaction ΔG is sensitive to a number of physical factors such as monomer concentration, temperature, pressure and to chemical factors for example the nature of substituents and their position on the ring. For example ΔG for an unsubstituted norbornene is only just negative and generally substituents have an unfavourable effect on the change in Gibbs energy in any ROMP reaction, either by making ΔG less negative or changing the sign from negative to positive[11]. For a polymerisation reaction ΔS is always negative since monomers combine to form macromolecules resulting in a reduction of their freedom. Therefore for a favourable reaction the enthalpy change must be greater than the T(ΔS) component. ΔH is dependent on ring strain and is negative for the highly strained bi-cyclic norbornene compound, however introducing a polymeric substituent onto the norbornene group (for example the PEO in this study) the balance between enthalpy and entropy becomes critical. Since the ROMP reaction failed at low solution concentrations it was thought that the change in entropy would become less negative hence more thermodynamically favourable for polymerisation if the reaction mixture was more concentrated. This strategy proved to be fortuitous as a (0.2 mol L^{-1}) macromonomer

solution ROMPed over a two day period. The copolymer prepared was recovered, purified and dried under vacuum before being fully characterised (see section 4.5).

Attempts were made to ROMP macromers with 75, 100 and 200 EO units using the same procedure but two peaks were invariably observed in the SEC trace for *n75* (see figure 4.4.8), and no reaction was detected at higher macromer lengths. In figure 4.4.8 the lower M.Wt. peak had an identical retention time as the macromonomer and was accompanied by a higher M.Wt. peak due to the copolymer.
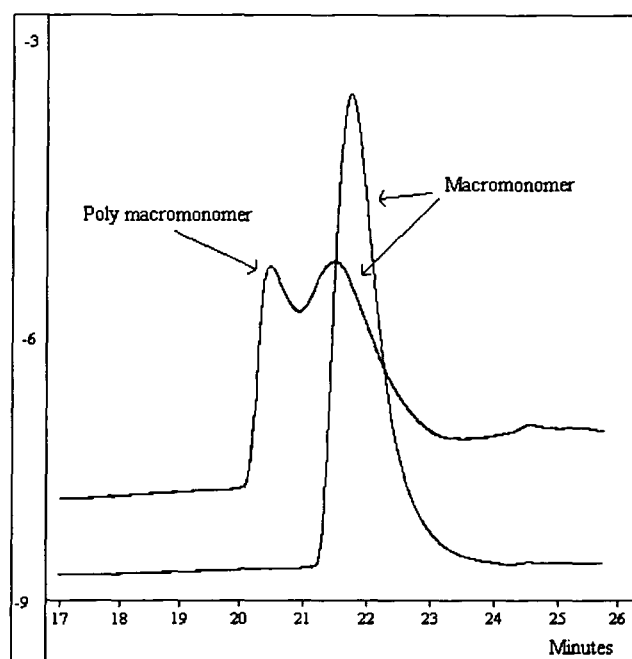

Figure 4.4.8. SEC trace for ROMPed material obtained from a macromer containing 75 units in comparison to the SEC trace for the macromer.

This phenomenon of incomplete polymerisation must be dependent on the M.Wt. of the macromer rather than the duration of reaction as the living chain ends of the polymer where n = 50 remained detectable by NMR for up to two weeks. Similar M.Wt. limitations have been reported by Feast and co-workers[12] when they ring opened 5-bicyclo[2.2.1]hept-5-ene-2,3-trans-bis(polystyrylcarboxylate). To confirm the predictions that the M.Wt. macromer was sterically hindering the propagating end a small, unsubstituted norbornene was added to the polymerisation mixture and left to react for two days. The SEC trace of the final product gave only one peak indicating

that all monomer (norbornene) and macromer had polymerised. This suggested that the small monomer was incorporated into the backbone chain and in doing so eliminated the steric hindrance of the active site hence enabling the unreacted macromer to participate in the polymerisation. This analogy is extended to account for the lack of reaction when macromer length exceeds 75 EO units as it is predicted that the norbornene double bonds are completely sterically hindered hence no initiation can occur. Furthermore the carbene bond of the ruthenium complex would be more susceptible to interact with the increased number of oxygen atoms of the longer length PEO chain.

The limitation in M.Wt. of the graft chain unfortunately restricted the number of copolymers that could be synthesised in the homologous series. Three copolymers were prepared however where the degree of polymerisation of the graft chain varied, n = 15, 25 and 50, and the macromer initiator ratio was kept constant at 50:1. For each copolymer in the series two isotopically different materials were prepared (one fully protonated and the other with the ethylene oxide grafts deuterated). A full discussion of the characterisation of each material is given in the following section.

Finally, two methods of hydrogenating the ROMPed materials were investigated. Initially attempts were made using the heterogeneous catalyst, $Pd/CaCO_4$, at high pressures. ^1H NMR spectra were taken before and after reaction and unfortunately no difference in the intensity of the olefinic protons was observed. One explanation could be that the amphiphilic copolymer does not dissolve in the reaction solvent (ethanol) but forms a micellar dispersion where norbornene and PEO form the core and the corona respectively. This structure would shield the olefin double bonds from the reactive palladium surface. Perhaps this reaction would have been more successful if better solvents were used for example benzene or chlorinated solvents, but unfortunately such solvents were not permitted to be used in the high pressure laboratory. An alternative explanation is that the electron rich oxygen atoms could irreversibly bind with the palladium thus deactivating and poisoning the catalysts hydrogenating surface. This argument is consistent with the observed difficulty of separating the catalyst from the polymer solution after reaction.

The second approach attempted involved the hydrogenation of the norbornene double bonds by a diimide (HN=NH) generated in situ from *p*-toluenesulphonylhydrazide (TSH). This route was chosen as TSH would selectively

reduce olefinic bonds[13] and has previously been applied to reduce ROMPed compounds[14]. A large excess of TSH was used because a substantial quantity of the diimide prepared disproportionates before it can attack the olefinic bond. The ^{1}H NMR spectra of the products were compared to the starting materials and no change was apparent as the intensity of the peaks due to the backbone double bonds (5.1-5.3 ppm) were identical. Various solvent combinations were attempted but they all gave similar results suggesting that the graft chains are coiled around the polymer backbone therefore sterically hindering attack of the diimide.

The failure of both hydrogenation methods unfortunately eliminates the possibility of selectively labelling the backbone with deuterium. This synthetic route has therefore only been successful in the preparation of two isotopically different copolymers, one fully protonated and the other with deuterated grafts.

Section 4.5   Characterisation

All copolymers prepared (and their precursor macromer) were characterised using elemental analysis, size exclusion chromatography (SEC), ^{1}H and ^{13}C NMR, dilute solution viscometry and ultra-violet (UV) spectroscopy. A brief outline of the results obtained from each technique is given here. Where possible the results for the series of materials will be compared and discussed.

4.5.1   Elemental Analysis

Elemental analysis was applied to determine the percentage of carbon, hydrogen and oxygen present in the protonated macromers only. The copolymer is simply a rearrangement of the components of the macromer precursor therefore the percentage composition would provide no additional information. By using the values obtained for the percentage of carbon in the material, %C, the degree of polymerisation, n, of the PEO macromer can be calculated using equation 4.5.1. The element carbon was chosen specifically to determine the length of the macromer since it is the predominant component and therefore should be less susceptible to background errors.

$$\%C = \frac{(15 \times 12) + (2 \times 12 \times n)}{214 + 44n} \times 100 \qquad \textbf{Equation 4.5.1.}$$

The results obtained are summarised in table 4.5.1 where the theoretical values are based on the target M.Wt. and an error was calculated by repeating measurements on an identical sample. From such results it is evident that the materials prepared are similar to the target molecules as the calculated and theoretical values for n compare favourably. The small error in the percentage of carbon corresponds however to a large error in n, for example the 0.24 % error in C % relates to a 41 % error for *n15*, which indicates that elemental analysis is not a reliable method for determining the degree of polymerisation of the PEO macromers. One explanation for such high error could be associated with the hydrophilic nature of the polymers. PEO is known to adsorb water readily and since each sample was exposed to air during preparation for different

periods of time it is possible that different quantities of water were adsorbed, thus influencing the results to different extents. It was concluded that this analysis method can be used as a first approximation but should be used in tandem with other techniques.

Theoretical				Experimental			
n	% C	% H	% O	n	% C	% H	% O
15	61.78	8.92	29.29	19 ± 7	60.57 ± 0.24	8.95 ± 0.04	30.48 ± 0.12
25	59.36	8.98	31.66	23 ± 7	59.63 ± 0.23	9.07 ± 0.04	31.30 ± 0.13
50	57.17	9.03	33.80	47 ± 7	57.32 ± 0.23	9.03 ± 0.04	33.65 ± 0.13

Table 4.5.1. Results from elemental analysis of the protonated macromers.

4.5.2 Size Exclusion Chromatography

All macromers prepared were submitted for SEC analysis to determine their molecular weight and polydispersity. Chloroform was used as the solvent in each case and the samples were left overnight to ensure complete dissolution. A typical SEC chromatogram for the macromer can be found in section 4.4, figure 4.4.2, and the results for the series are summarised in table 4.5.2. One advantage of this technique is that the protonated macromers can be compared directly to their isotopic counterparts. Unfortunately the hydrodynamic behaviour is not known for the graft copolymer system studied here hence no M.Wt. data can be extracted from the SEC traces. There have been numerous theoretical investigations to predict the number and weight average M.Wts. of graft copolymers[15] but to date these have been limited to simple cases of materials prepared via free radical polymerisations.

The macromer polydispersity values in table 4.5.2 are all very close to one indicating that all PEO chains in each sample have grown at similar rates and are of similar length. The target degree of polymerisation, n, is very close to the calculated

values confirming that the process is living, and that the structure of the macromer can be easily controlled simply by varying the monomer/initiator ratio. Additionally experimental values for the deuterated and protonated species match (within experimental error) indicating that the two isotopic species are physically identical.

Macromer[a]	$n_{theo.}$[b]	M_w[c]	M_n[d]	M_w/M_n[e]	$n_{calc.}$[f]
H	15	1052	946	1.11	17 ± 1
D	15	965	873	1.11	14 ± 1
H	25	1479	1351	1.10	26 ± 1
D	25	1586	1493	1.06	27 ± 1
H	50	2292	2197	1.04	47 ± 1
D	50	2702	2561	1.05	49 ± 1

a)   H and D represent the protonated and deuterated graft respectively.

b)   Target degree of polymerisation.

c)   Weight average molar mass.

d)   Number average molar mass.

e) M_w/M_n = Polydispersity

f)   Calculated degree of polymerisation from M_n.

Table 4.5.2.   SEC results for the protonated and deuterated macromers prepared.

4.5.3   Nuclear Magnetic Resonance

All macromers were characterised by both ^1H and ^{13}C NMR spectroscopy and a typical spectra are given in figures 4.5.1 and 4.5.2 respectively for a target macromer containing 25 EO units. Both spectra are dominated by the signal due to the EO repeat unit but fortunately the chains are sufficiently short and signals due to the end groups can still be detected. The characteristic peaks for norbornene are the doublet of doublets at circa 6.1 and 5.9 ppm due to the olefinic protons. For each peak there are two doublets in a 6:4 ratio since the norbornene starting materials contained a 6:4 mixture of exo/endo forms.
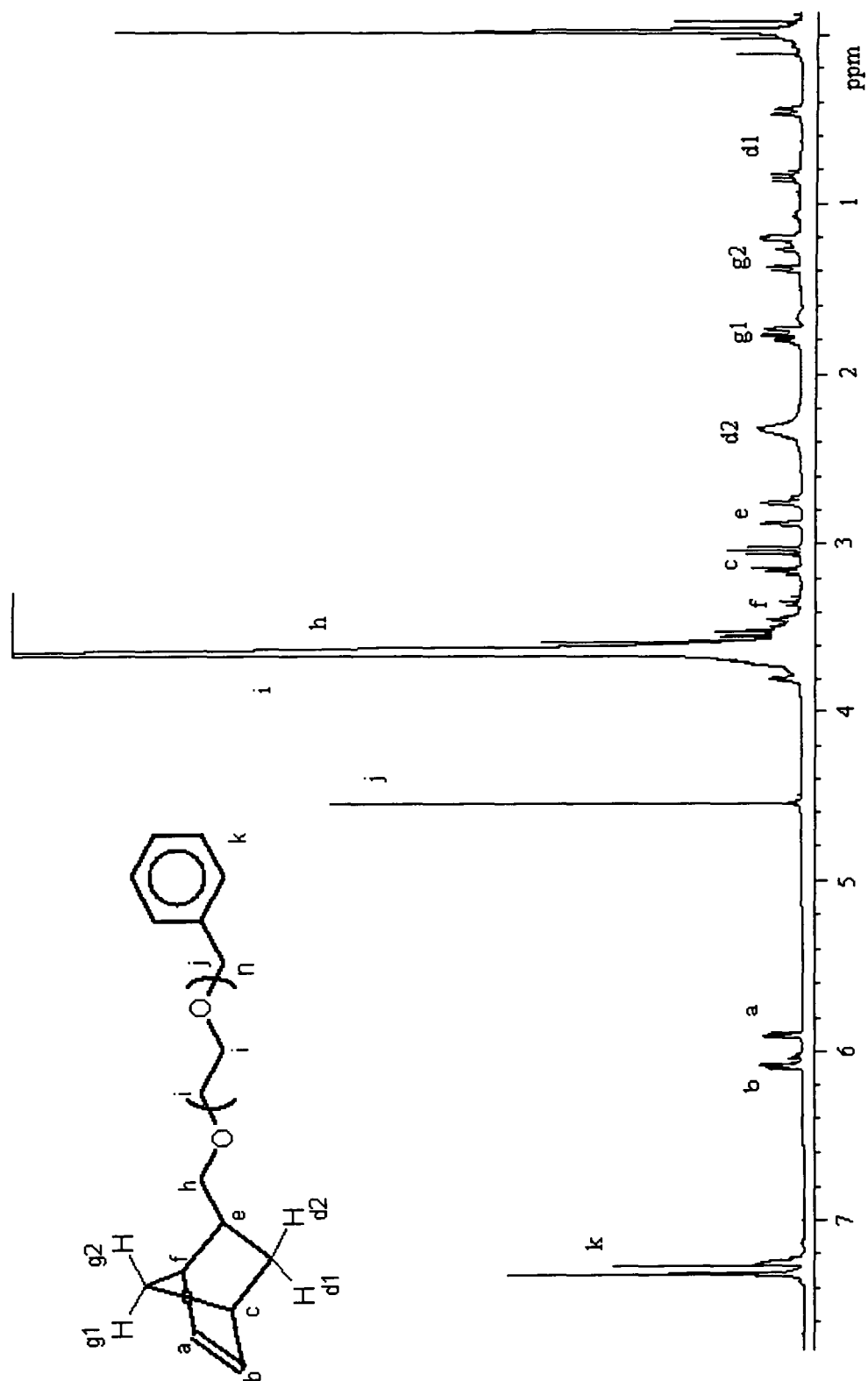
Figure 4.5.1. ^{1}H NMR spectra for the macromer with 25 EO units.
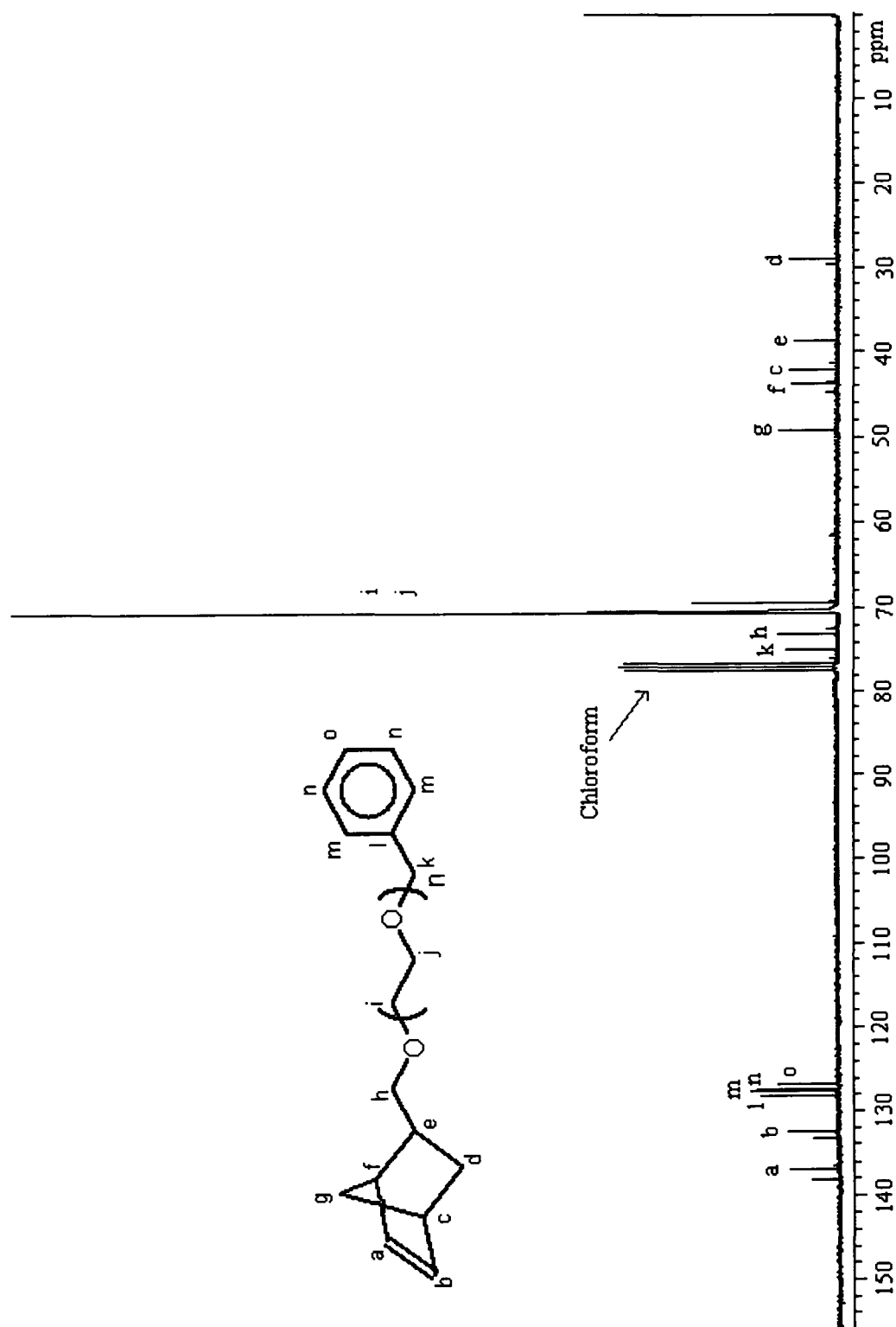
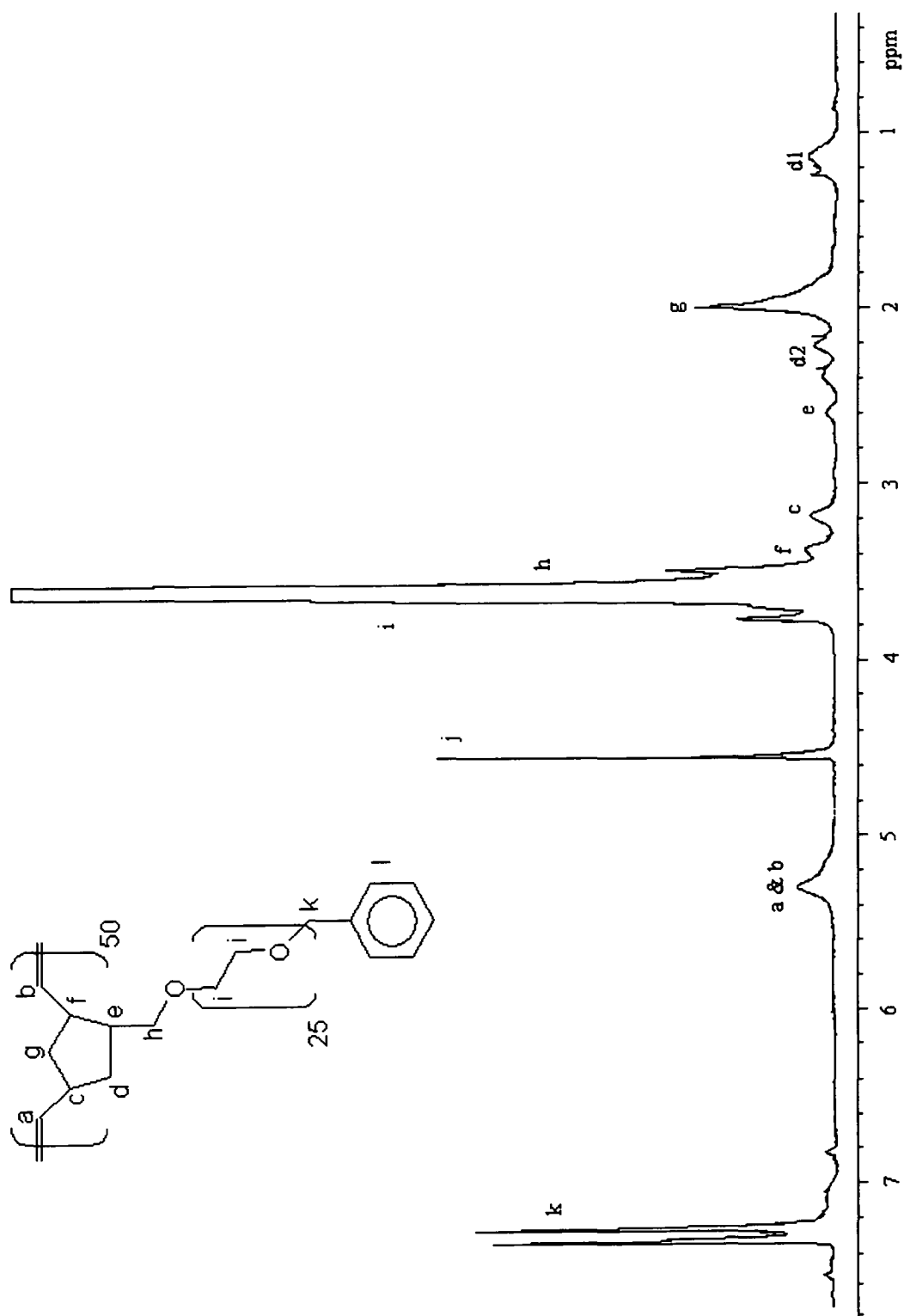**Figure 4.5.2.** ^{13}C NMR spectra for the macromer with 25 EO units.

Figure 4.5.3. ^{1}H NMR spectra for the graft copolymer with 25 EO units.
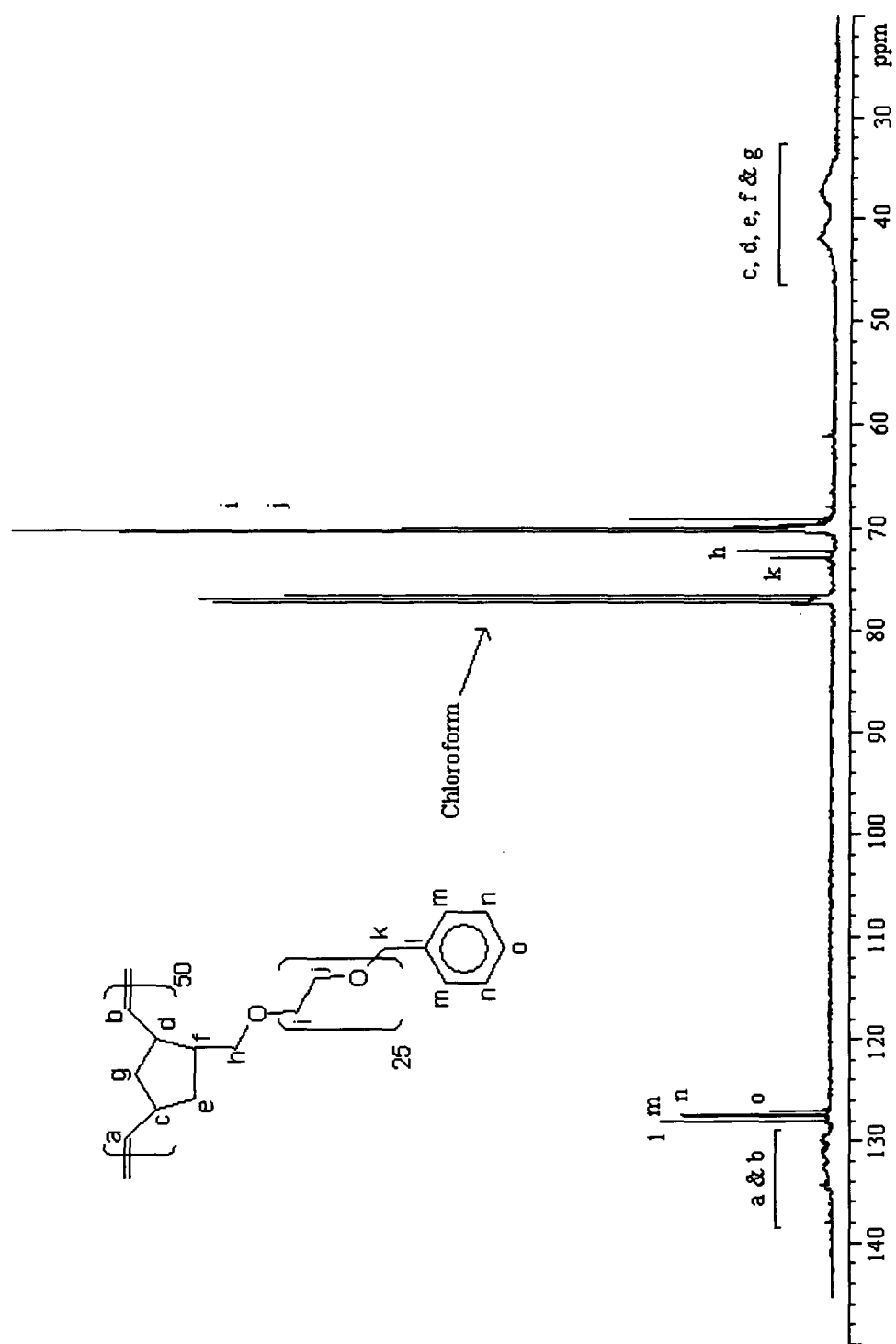
Figure 4.5.4. ^{1}C NMR spectra for the graft copolymer with 25 EO units.
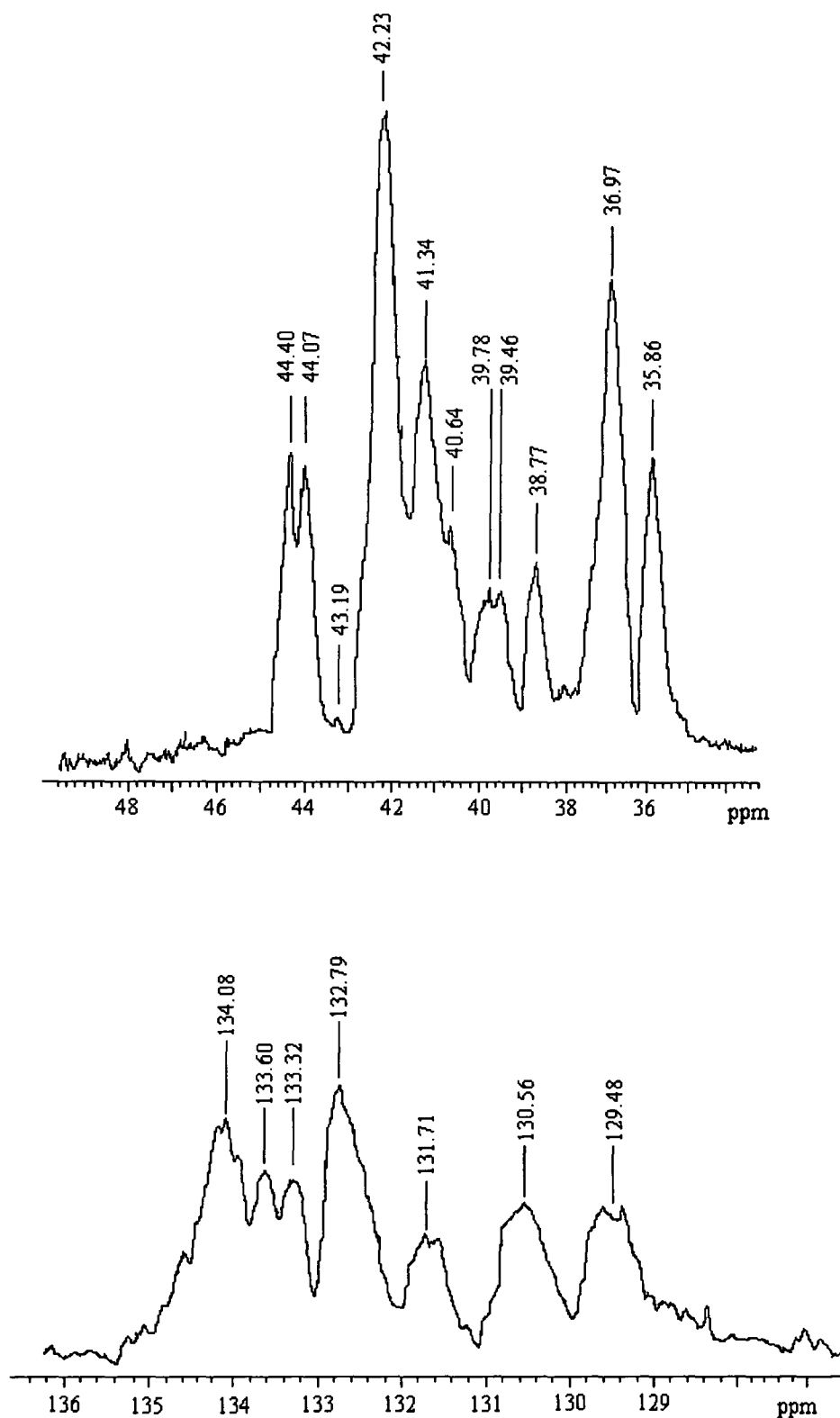
Figure 4.5.5. Expansion of norbornene regions for ^{13}C spectra for *hn25* graft copolymer.

By comparing the integral of the olefinic peaks with the integral of the methylene protons next to the benzylic group (4.6 ppm), the functionality can be estimated where complete functionalisation is of course one. Furthermore the degree of polymerisation can be estimated by taking the ratio of the olefinic integral with half the integral value due to the EO protons. The results from such studies are given in table 4.5.3 for all protonated species but only the functionality of the deuterated species could be determined.

Sample[a]	n_{theo}[b]	Functionality[c]	n_{calc}[d]
H	15	1.16	18 ± 2
D	15	1.12	-
H	25	1.09	27 ± 2
D	25	1.10	-
H	50	1.02	49 ± 2
D	50	1.05	-

a) H and D represent the protonated and deuterated graft respectively.
b) Target degree of polymerisation.
c) Ratio of norbornene end groups to benzene groups.
d) Calculated degree of polymerisation.

Table 4.5.3. NMR results for the protonated and deuterated macromers.

Typical NMR spectra obtained for the *hn25* graft copolymer are given in figure 4.5.3 and 4.5.4. Immediately it is evident from the complexity of such spectra that the microstructure of the copolymer is complicated, therefore variations in multiple bond stereochemistry and also tacticity needs to be considered[16].

The proton spectrum confirms that the ROMP reaction has been successful as the doublet of doublets due to the olefinic protons has shifted down field to 5.3 ppm and is broad in character. This broadening feature is present in all peaks in the spectra and is indicative of a successful polymerisation. In the ^{13}C NMR spectrum polynorbornene ring carbons are expected to appear in the region 30-50 ppm and the vinylic carbons of the backbone chain to appear between 130 and 140 ppm[17]. The signals in these regions are expanded in figure 4.5.5 and they provide evidence for the existence of both cis and

trans double bonds (see figure 4.5.6). The line positions and assignments for each peak are given in table 4.5.4 and the integral values were calculated by de-convoluting the peaks. Because the resonances for the doubly bonded carbons were close together and the signal to noise ratio was low, precise cis/trans content could not be calculated but were estimated to be 50 % cis, 50 % trans for the n15 material and 33 % cis, 67 % trans for both the n25 and n50 materials.

assignment	Position /ppm	
	cis	*trans*
C_a TH	134.08	133.60
C_a TT	133.32	132.79
C_b HH	130.56^b	131.71
C_b HT	130.56^b	129.48
C_c TH	36.97a	41.34
C_c TT	36.97a	40.64
C_d HH	38.77	44.40
C_d HT	38.77	44.07
C_e	36.97a	35.86
C_f	43.19	52.23
C_g	39.78	39.46

a) C_c *cis* and C_e *cis* are coincident.
b) C_e HT and C_e HH are coincident.

Table 4.5.4.   Line positions and assignments for *hn25* (figure 4.5.4 and 4.5.5). H and T represent head and tail addition of the incoming macromer respectively and the letter subscripts refer to the carbons labelled in figure 4.5.4.

The copolymers also contain a mixture of tacticities depending on the orientation of each macromer to the propagating species at the instant of polymerisation. If the PEO containing part of the macromer is arbitrarily labelled as the head (H), and the remainder as the tail (T), then the ratio of HH, HT, TH and TT additions were predicted by de-convoluting and comparing the area under the identified peaks (see

table 4.5.4). The distribution of percentages in table 4.5.5 indicates that all copolymers have similar tacticities. The tail-head addition was the most favoured conformation for cis double bonds and tail-tail addition for trans double bonds since such tacticities are predicted to be the least sterically hindered forms of addition. Differences between the molecular architecture of the copolymers is therefore only in the ratio of cis/trans double bonds.

Polymer	CIS /%				TRANS /%			
	HH	HT	TH	TT	HH	TH	HT	TT
n15m50	35		51	14	11	16	25	48
n25m50	39		51	9	7	15	26	52
n50m50	36		51	14	19	14	24	43

Table 4.5.5. Distribution of tacticities for each protonated copolymer material.
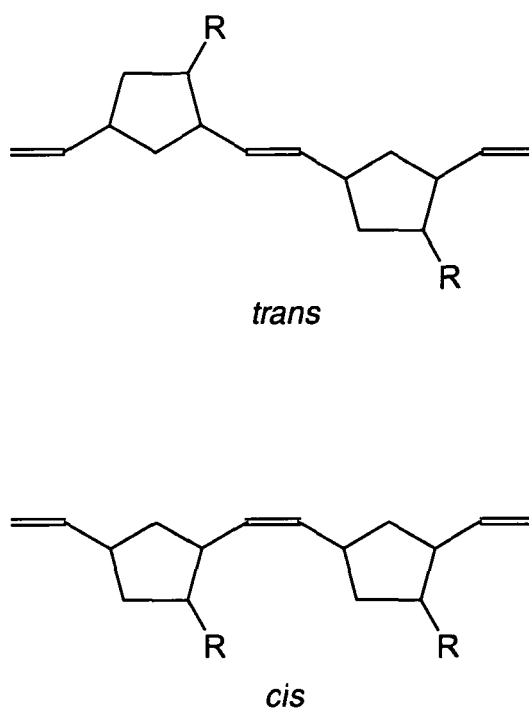

trans

cis

Figure 4.5.6. Examples of trans and cis tacticities for the olefinic bonds where R represents the PEO graft.

126

4.5.4 Differential Scanning Calorimetry

The melting point (T_m) is the phase transition from a solid to liquid and the glass transition (T_g) correspond to changes in the molecular motion thus the physical properties of the materials, and are used to characterise polymeric materials. Analysis of samples by DSC provides information on not only the T_g and T_m but also on the changes in enthalpy (ΔH) and entropy (ΔS) of the sample and any decomposition processes.

The value of T_g is dependent on the thermal history of the sample therefore fresh samples were always analysed and data were collected twice over the temperature range 198-548 K, by heating at a rate of 10 K min^{-1} and quench cooling at 400 K min^{-1}.

The results obtained for the macromer and copolymer are given in table 4.5.6. The temperatures quoted for the melting point are the extrapolated onset, whereas the temperatures for the second order transition are taken as the temperature at the mid-point of the observed peak[18]. The change in entropy has been calculated using the relationship, $T_m = \dfrac{\Delta H}{\Delta S}$.

	macromer				copolymer			
material	T_g /K	T_m /K	ΔH / J g^{-1}	ΔS / J g^{-1}K^{-1}	T_g /K	T_m /K	ΔH / J g^{-1}	ΔS / J g^{-1}K^{-1}
hn15	-	330	88	0.27	238	320	81	0.25
dn15	-	331	89	0.27	235	314	71	0.23
hn25	-	333	95	0.29	241	325	83	0.26
dn25	-	332	96	0.29	243	325	84	0.26
hn50	-	334	112	0.35	255	335	107	0.32
dn50	-	336	117	0.33	253	334	101	0.30

Table 4.5.6. Results from DSC for the macromer and copolymer.

No glass transition temperature was observed for any of the macromer samples. This behaviour has been previously observed by Read and co-workers for PEO of

molecular weight ranging between 200-4000 using broadline NMR[19]. They suggested that the behaviour they observed was due to the low M.Wt. PEO containing a high proportion of crystalline material (80 % for M.Wt. = 4000 g mol^{-1}), hence the glass transition is too small to detect or becomes lost within the melting peak. A typical DSC trace for *hn25* is shown in figure 4.5.7 and the T_g and T_m regions have been expanded in figure 4.5.8.

Only one T_g is observed for each graft copolymer suggesting that the poly norbornene and poly (ethylene oxide) segments do not undergo phase segregation. As the graft length increases the glass transition also increases. This dependence of T_g on M.Wt. has been predicted theoretically by Fox and Loshadek[20] to follow the relationship given in equation 4.5.2 where T_g^o is the limiting value of glass transition, K is a constant of value circa 10^5 and M is the M.Wt.

$$T_g(M) = T_g^o - \frac{K}{M}$$ **Equation 4.5.2.**

Addition polymers, for example polystyrene, comply with theoretical predictions as the T_g increases with M.Wt. and reaches a plateau value for high M.Wt.[21]. PEO exhibits very different behaviour however since the T_g for PEO increases and passes through a maximum of 280 K near 6000 g mol[-1][22,23].
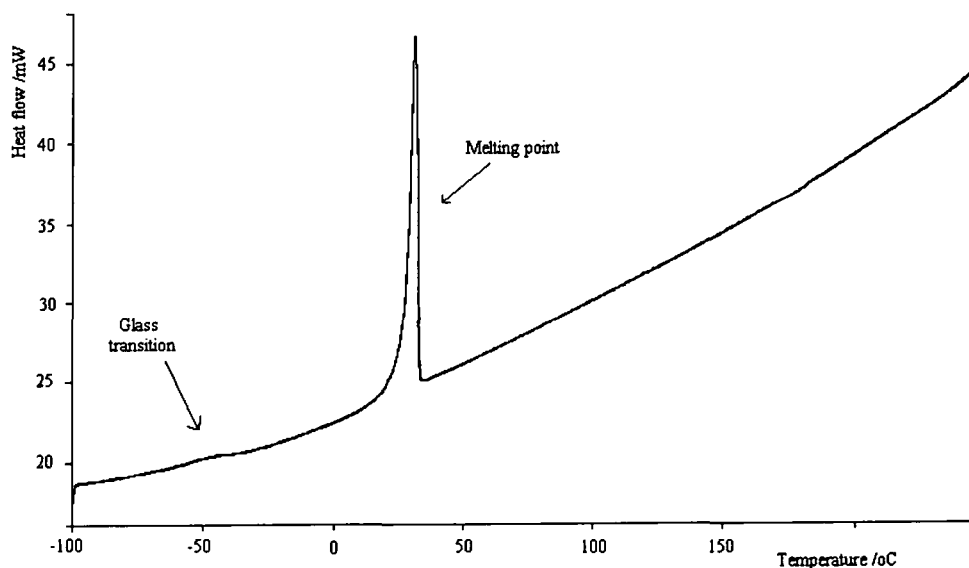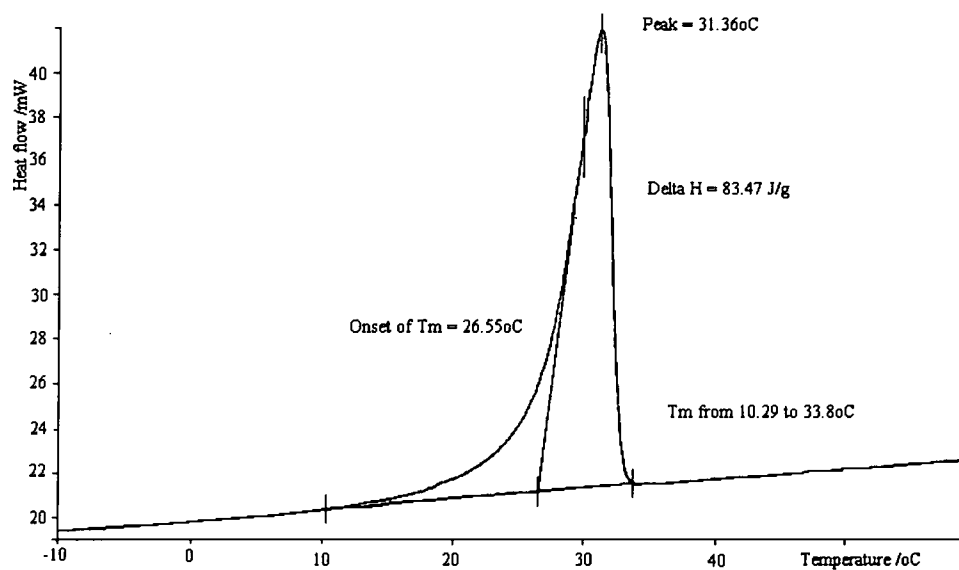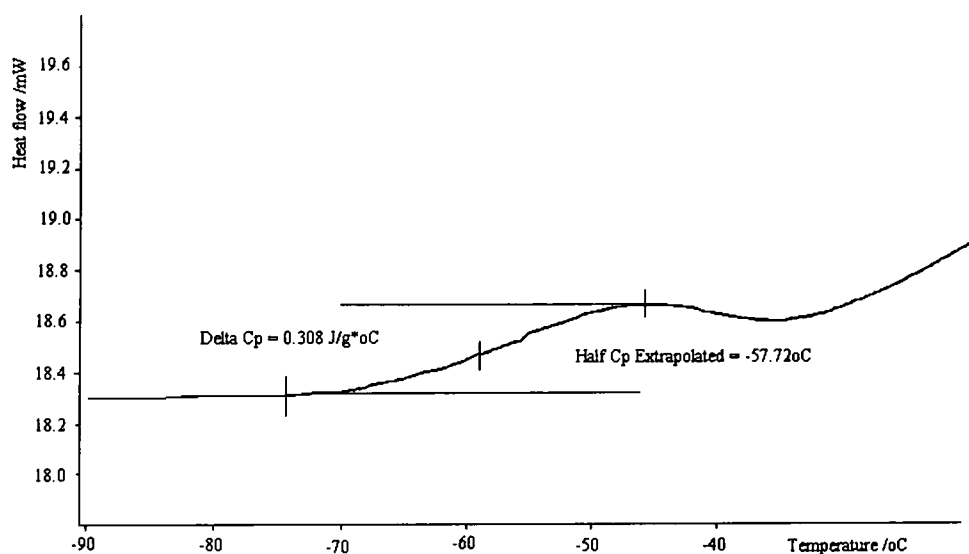

Figure 4.5.7. DSC trace for the copolymer with 25 EO units in each pendant chain.

a) melting point

b) glass transition

Figure 4.5.8. Expansion of DSC traces for *hn25* graft copolymer a) expansion of melting point region and b) expansion of glass transition region.

A similar trend is observed experimentally for the melting temperature of both the macromer and graft copolymer where T_m increases as the M.Wt. of PEO rises. This behaviour can easily be justified if the percentage of PEO chain ends is considered. When the chain length decreases the relative number of chain ends, hence chain mobility increases, therefore less energy is required to stimulate chain motion and the onset of the melting process. This suggestion is corroborated by the patterns of ΔH and ΔS. As the graft length decreases ΔH also decreases due to the reduction in energy required to initiate the phase change. The increase in the change of disorder of the system (ΔS) is attributed to the longer chains becoming more entangled and disorganised in the melt in comparison to the highly crystalline solid structure observed for all chains. Such a trend therefore suggests that the length of the graft is influencing the physical properties of the material.

When comparing the values for the T_m of the macromer and polymacromer a ten degree decrease is observed upon polymerisation. This is expected as it is well-known that introduction of a co-monomer will disturb the crystallisation and will lower the melting temperature of the corresponding homopolymer[24]. For each species the thermal characteristics for the protonated and deuterated materials are similar, verifying that copolymer compositions are similar and deuteration has no significant effect on the thermodynamic properties.

A number of empirical relationships have been proposed to relate the T_g of random copolymers and compatible blends to their composition. One simple approach for compatible systems that are not strongly polar has been developed by Fox[25] and is applied to this study. Fox proposed the relationship given in equation 4.5.3, where the T_g of the copolymer is expressed in terms of the weight fraction, w, of the individual components 1 and 2 and their respective glass transition temperatures for the homopolymers T_{g1} and T_{g2}.

$$\frac{1}{T_g} = \frac{w_1}{T_{g1}} + \frac{w_2}{T_{g2}}$$ **Equation 5.4.3.**

To calculate a theoretical T_g for each copolymer values for the weight fractions were based on the target molecule, and values for T_g were taken from the literature. T_g for the backbone is 333 K[11] but the value for PEO is M.Wt. dependent. Experimental

values for a range of PEO M.Wts. were taken from a study by Faucher and co-workers[23] and were plotted and T_g values extrapolated for the three PEO M.Wts. used in this study. They were found to be 257, 264 and 272 K for 15, 25 and 50 EO monomer units respectively.

Sample	Theoretical Tg /K	Experimental Tg /K
hn15	266	238
hn25	269	241
hn50	274	250

Table 4.5.7. Comparison of theoretical and experimental glass transition temperatures.

The calculated T_g values are compared in table 4.5.7 to the experimental values for the hydrogenated copolymers only, and it is noted that although the values are not equal, they follow a similar trend. This behaviour suggests that the composition of the series of synthesised materials changes as expected. The difference in magnitude of the values is probably due to the assumption in the derivation of equation 5.4.3 that the individual components of the copolymers are not affected by the presence of each other. This is highly unrealistic as the geometry of the backbone and main chain are being constrained due to the polymer architecture. Another contributing factor is that not all molecules will be identical as there will be a distribution of M.Wts. of both the graft and main chain lengths. Such imperfections will act to depress the T_g.

4.5.5   Viscometry

As a final test to ensure that the macromer had polymerised the viscometry characteristics of dilute solutions of all polymacromers and their precursors were determined using capillary viscometry.

The relative viscometry (η_r) is a measure of the viscosity of a polymer solution η, in relation to the viscosity of pure solvent (η_o) as described in equation 4.5.4.

$$\eta_r = \frac{\eta}{\eta_o}$$ **Equation 4.5.4.**

For infinitely dilute solutions the value of η_r approaches unity and it is useful to define the specific viscosity η_{sp} (equation 4.5.5) as it quantifies the increase in viscosity when polymer is added to the solvent.

$$\eta_{sp} = \eta_r - 1$$ **Equation 4.5.5.**

The reduced specific viscosity, η_{sp}/c, is often referred to as the reduced viscosity and when in infinite dilution it gives intrinsic viscosity, $[\eta]$, which is a measure of the influence of one polymer coil. This parameter can also be equated to the inherent viscosity, the ratio of $\ln \eta_r$ by c, at infinite dilution.

$$[\eta] = \left(\frac{\eta_{sp}}{c}\right)_{c \to 0} = \ln\left(\frac{\eta_r}{c}\right)_{c \to 0}$$ **Equation 4.5.6.**

Experimentally the relative viscosity is measured for a series of solutions of differing concentrations at 298 K, using an Ubbelohde viscometry tube connected to an automated viscometer[26]. Typically the initial polymer solution is 1 % polymer dissolved in dry, filtered chloroform. The intrinsic viscosity is subsequently determined by employing both the Huggins (equation 4.5.7) and the Kramer (equation 4.5.8) equations, hence a plot of both reduced and inherent viscosity versus concentration should be linear where both intercept values give $[\eta]$. A typical plot for *hn15* is given in figure 4.5.9.

$$\frac{\eta_{sp}}{c} = [\eta] + k'[\eta]^2 c$$ **Equation 4.5.7.**

$$\ln\frac{\eta_r}{c} = [\eta] + k''[\eta]^2 c$$ **Equation 4.5.8.**

The constant terms k' (Huggins coefficient) and k'' (Kramer coefficient) depend on a variety of factors but generally for polymers in a good solvent k' is circa 0.35 and k'' is approximately 0.15, and generally $k' + k'' = 0.5$. The values reported for [η] are the mutual intercept and are given for each material in table 4.5.8.

There is a definite increase in [η] when the macromer has been polymerised indicating there has been a significant increase in M.Wt. The results also reveal those as the graft length increases the polymer solutions become more viscous indicative of the increase of EO units. Similar trends have been observed for low M.Wt. homoPEO in benzene[27] and PS-g-PEO comb copolymers in THF[28] and in toluene/methanol (80/20)[29], but there is no data to date in the literature where the solvent was chloroform. The protonated and deuterated materials have returned similar viscosity behaviour, which substantiates earlier predictions that the copolymers are physically indistinguishable.
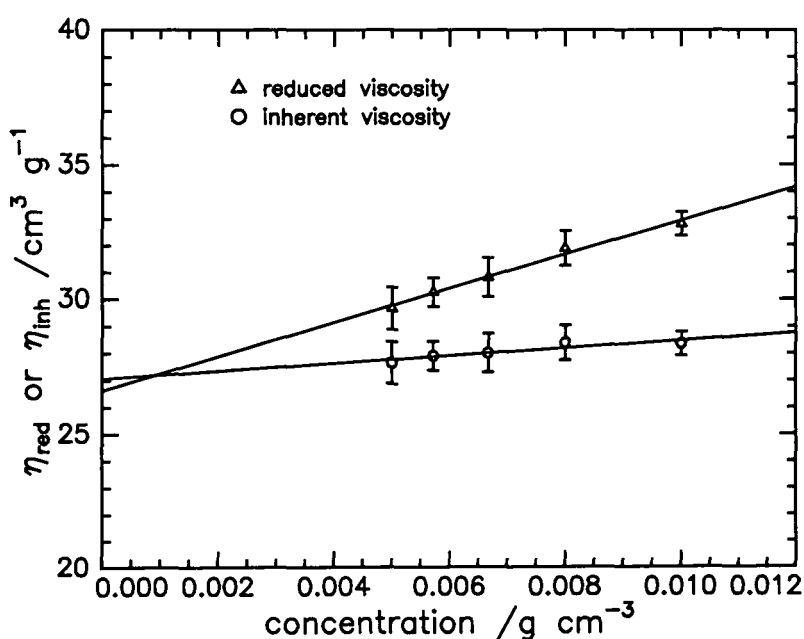

Figure 4.5.9. Data for the reduced and inherent viscosities plotted as a function of solution concentration for the copolymer with 15 EO units. The intercept point is the intrinsic viscosity value.

	Sample	intrinsic viscosity /$cm^3 g^{-1}$
Macromer	hn15	6.9
	hn25	8.7
	hn50	10.8
	dn50	11.0
Copolymer	hn15	26.8
	hn25	30.6
	hn50	34.3
	dn50	34.4

Table 4.5.8. Intrinsic viscosities for macromers and copolymers

Initially it was hoped that the M.Wt. (M) of the copolymer could be predicted by applying the Mark-Houwink[30] equation, $[\eta] = KM^a$, where K and a are constants for a given polymer, solvent and temperature. Values for the two constants are however not known for the novel copolymer/chloroform system but solution conformations can be inferred if a is extracted from a double logarithmic plot of $[\eta]$ versus target M. It is evident from such a plot (figure 4.5.9) that a is small (a = 0.216). Since a zero exponent is that of a rigid sphere system, and $0.5 \le a \le 0.8$ for flexible gaussian chains[30], the results indicate that each copolymer molecule has a densely filled flexible sphere like conformation. This value for a is indicative of highly branched material confirming that the co-polymerisation reaction was a success.
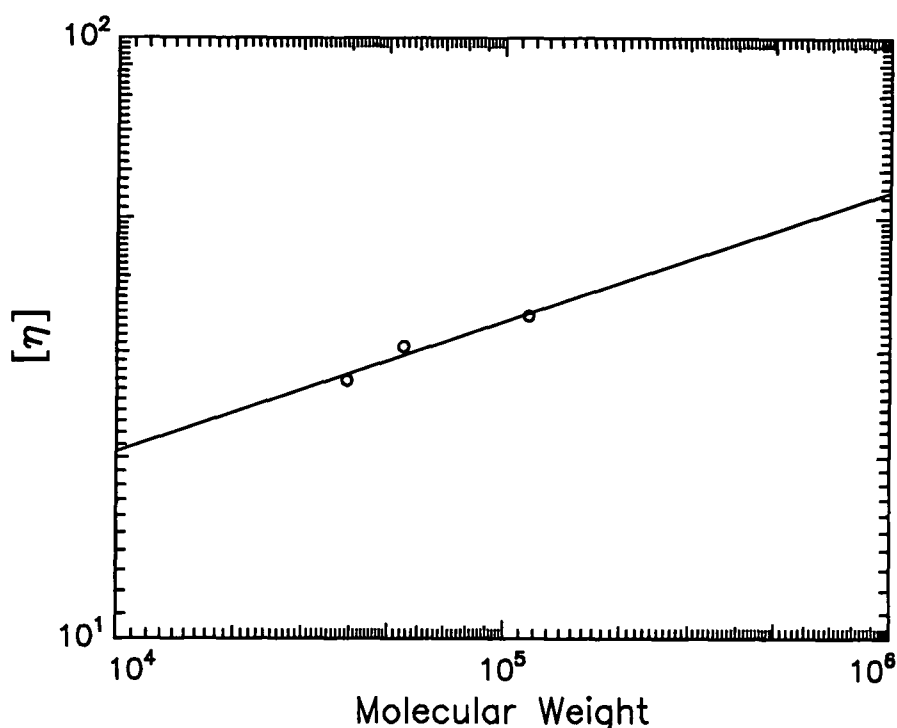
Figure 4.5.10. Mark-Houwink plot for series of graft copolymer.

4.5.6 Light Scattering

To elucidate accurate values for the weight average molar mass of each copolymer the measurement of scattered light intensity from dilute solutions was used.

Samples were prepared (2-10 mg ml^{-1} benzene solutions) and any erroneous particulates (for example dust) were removed by filtering through a membrane of pore size 0.2 μm. The refractive index increment (dn/dc) was measured at 298 K using a Brice-Phoenix differential refractometer and found to be -0.0126 ± 0.002 ml g^{-1} for *hn25*. This value was in good agreement with the value calculated (-0.0129 ± 0.0003 ml g^{-1}) based on the target composition and using values for the constituent homopolymers (PEO -0.016[21] and PNB 0.0559 ± 0.003 ml g^{-1} (determined experimentally)). This dn/dc value is small therefore changes in the intensity of the light scattered as a function of concentration will be modest. Nonetheless a conventional

135

procedure[31] according to the Zimm-Berry plot[32] was attempted to evaluate the weight-average M.Wt., M_w.

$$\left(\frac{K_c}{R_\theta}\right)^{1/2} = \left[\frac{1}{M_w}\left(1 + \frac{16\pi^2 n_o^2}{3\lambda_o^2}\langle s^2 \rangle \sin\left(\frac{\theta}{2}\right) + 2A_2 M_w c\right)\right]^{1/2}$$ **Equation 4.5.9.**

where,

$$K = \frac{4\pi^2 n_o^2}{N\lambda_o^4}\left(\frac{dn}{dc}\right)^2$$

R_θ is the Rayleigh ratio at the scattering angle of observation, which ranged from 30 to 150 $^\circ$, c is the concentration ranging over 2 to 10 mg ml^{-1}, λ is the wavelength of the incident light (488 nm), n_o the refractive index of the solvent, N Avogadro's number, $\langle s^2 \rangle$ the mean squared radius and A_2 the second virial coefficient.

Unfortunately a decrease in the intensity of the scattered light was detected as the sample concentration increased suggesting that the polymer molecules were absorbing the incident light. To confirm this prediction a UV-spectra was obtained for each copolymer using a 2 and 10 mg ml^{-1} chloroform solution and a 2 mg ml^{-1} chloroform solution of polynorbornene.

The results obtained are presented in figure 4.5.11 for *hn25* copolymer where the absorption, A, was determined by taking the log of the ratio of the incident to the transmitted light via Beers law,

$$A = \log\frac{I_0}{I} = \varepsilon l c$$ **Equation 4.5.10.**

where ε is the extinction coefficient, l the path length of the sample cell and c the concentration.
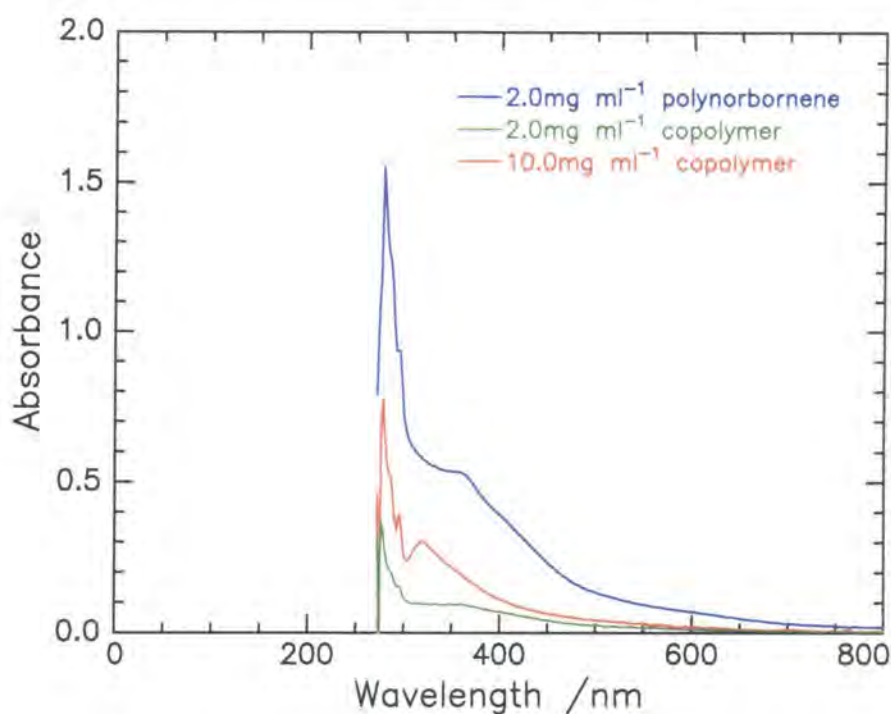
Figure 4.5.11. UV-Spectra obtained for *hn25* at 2 and 10 mg ml^{-1} concentration and a 2 mg ml^{-1} solution of polynorbornene in benzene.

It is obvious from the results that absorption occurred over a broad wavelength range that encompasses the wavelength of the two lasers available for light scattering studies, $\lambda = 488$ nm and $\lambda = 633$ nm. The absorption of light also increases with sample concentration, which agrees with Beers law, but also accounts for the increases in absorption of light with concentration in scattering studies. The peak observed in all uv-spectra (270 nm) is predicted to correspond to a π to $\pi*$ transition of electrons in the backbone double bond.

It was concluded from this study that light scattering could not be applied to determine the M.Wt. of the copolymer system.

Section 4.6   Conclusions

Three novel well-defined polynorbornene-*g*-poly (ethylene oxide) copolymers have been prepared by combining anionic and ring opening metathesis polymerisation techniques. Since both macromer and polymacromer synthesis involved living polymerisations the procedure provided control over the degree of polymerisation, molecular weight distribution of both the graft and main chain and also the grafting density.

Polymerisation of macromers of varying graft length indicate that beyond a threshold graft length value (circa 75 EO units) the polymerisation does not reach completion and at higher degrees of polymerisation no reaction was observed. It was concluded that such behaviour was due to steric hindrance of the active site.

Two isotopes of PEO graft were prepared for each architecture of copolymer using protonated and deuterated EO monomer. Two different hydrogenated reactions were attempted to reduce the double bonds of PNB but neither were successful, therefore it was not possible to selectively label the main chain with deuterium.

Characterisation of all materials revealed that both polymerisation reactions were successful and were of a living nature. The results from the macromer composition studies are summarised below in table 4.6.1 where n is the degree of polymerisation.

Target n[a]	method applied to estimate n			
	Elemental analysis	SEC	^{1}H NMR	average
h15	19 ± 7	17 ± 1	18 ± 2	18 ± 1
d15	-	14 ± 1	-	14 ± 1
h25	23 ± 7	26 ± 1	27 ± 2	25 ± 2
d25	-	27 +/- 1	-	27 ± 1
h50	47 ± 7	47 +/- 1	49 ± 2	48 ± 1
d50	-	49 +/- 1	-	49 ± 1

a)   H and D represent the protonated and deuterated macromers respectively.

Table 4.6.1.   Comparison of theoretical and calculated values for the target degree of polymerisation.

It is evident from these results that all target degrees of polymerisation are in good agreement with the experimental values, and also that the protonated and deuterated materials are structurally equivalent. NMR studies revealed that the microstructure of the copolymers is complex. The cis/trans ratio of the n15 copolymer is in a 2:1 ratio, whereas the n25 and n50 copolymer has a 1:1 ratio. This difference in structure could be an important factor in later organisation and dynamic studies. The thermal and viscometry studies observed that ROMP was successful as the characteristic behaviour of the copolymers are very different to their precursors. Differences were also noted within the copolymer homologous series indicating that molecular architecture, or more precisely the graft length, influences the material physical properties.

Section 4.7   References

1.   Eisenbach, C. D.; Peuscher, M.; Wegner, G. *Makromol. Chem.*, **1983**, *184*, 2313.

2.   Heroguez, V.; Breunig, S.; Gnanou, Y.; Fontanille, M. *Macromolecules*, **1996**, *29*, 4459.

3.   Bazan, G.; Schrock, R. R.; Khosravi, E.; Feast, W. J.; Gibson, V. C.; O'Regan, M. B.; Thomas, J. K.; Davis, W. M. *J. Am. Chem. Soc.*, **1990**, *112*, 8387.

4.   Novak, B. M.; Grubbs, R. H. *J. Am. Chem. Soc.*, **1998**, *110*, 7542.

5.   Grubbs, R. H.; Khosravi, E. *'ROMP and Related Processes' in Synthesis of Polymers- A Volume of Materials Science and Technology*, ed. Schluter, A. D.Wiley-VCH, **1998**, *Chapter 3*, 65.

6.   Bates, F.; Rosedale, J. H. *J. Am. Chem. Soc.*, **1988**, *110*, 3542.

7.   Sohn, S. H.; Gratt, J. A.; Lee, J. K.; Cohen, R. E. *J. App. Poly. Sci.*, **1995**, *58*, 1041.

8.   Schwab, P.; Grubbs, R. H.; Ziller, J. W. *J. Am. Chem. Soc.*, **1996**, *118*, 100.

9.   Rizmi, A. C. M. *Ph.D. Thesis*, Durham University, **1997**.

10.   Feast, W. J.; Khosravi, E. *New Methods in Polymer Science*, Vol. 2, ed. Ebdon, J. R.; Eastmond, G. C. Blackie Academic and Professional, **1995**.

11.   Ivan, K. J. *Olefin Metathesis*, Academic Press, London, **1993.**

12.   Feast, W. J.; Gibson, V. C.; Johnson, A. F.; Khosravi, E.; Mohsin, M. A. *Polymer*, **1994**, *35*, 3542.

13.   Miller, C. E. *J. Chem. Ed.* **1965**, *42*, 254.

14.   Megson, J. *Ph.D. Thesis*, Durham University, **1997**.

15.   Tobita, H. *Polymer*, **1999**, *40*, 3565.

16.   Hamilton, J. G. *Polymer*, **1997**, *39*, 1669.

17.   Ivan, K. J.; Lam, L. M.; Rooney, J. J. *Macromol. Chem. Phys.* **1994**, *195*, 1189.

18.   Gallagher, P. K. *Thermal Characterisation of Polymer Materials*, ed. Turi, E. A. Academic Press, **1997**, *Chapter 1*, 14.

19.   Connor, T. M.; Read, B. E.; Williams, G. *J. Appl. Chem.*, **1964**, *14*, 74.

20.   Fox, T. G.; Loshaek, S. *J. Poly. Sci.* **1955**, *15*, 371.

21.   Brandrup, J.; Immergut. *Polymer Handbook*, **1997**, Wiley Interscience.

22.   Read, B. E. *Polymer*, **1962**, *3*, 529.

23. Faucher, J. A.; Koleske, J. V.; Santee, E. R.; Stratte, J. J.; Wilson, C. W. *J. of App. Phys.* **1966**, *37*, 3962.

24. Mathot, V. B. F. *Calorimetry and Thermal Analysis of Polymers*, ed. Mathot, V. B. F. Hanser Publishers, **1994**, *Chapter 9*, 231.

25. Fox, T. G. *Bull. Am. Phys. Soc.*, **1952**, *1*, 123.

26. Boyd, R. H.; Phillips, P. J. *The Science of Polymer Molecules*, **1993**, Cambridge University Press.

27. Kawaguchi, S.; Imai, G.; Suzuki, J.; Miyahara, A.; Kitano, T.; Ito, K. *Polymer*, **1997**, *12*, 2885.

28. Ito, K.; Tomi, Y.; Kawaguchi, S. *Macromolecules*, **1992**, *25*, 1534.

29. Jannasch, P.; Wesslen, B. *J. of Poly. Sci. Part A: Polymer Chem.* **1993**, *31*, 1519.

30. Lovell, P. A. *Comprehensive Polymer Science, Volume 1 Polymer Characterisation,* ed. Booth, C.; Price, C. **1989**, *Chapter 9*, 173.

31. Ford, N. C. *Dynamic Light Scattering, Chapter 2*, ed. Pecora, R. **1985**, 7.

32. Berry, G. C. *J. Chem. Phys.* **1966**, *44*, 4550.

Chapter Five

Surface Pressure Isotherms

Section 5.1   Introduction

The characteristics of monolayer behaviour for the series of graft copolymers spread at air-fluid interfaces have been investigated using a Langmuir trough. The variation in surface pressure as a function of surface concentration has been monitored for each film spread initially at an air-water interface, and subsequently four different air-poly (ethylene oxide) (PEO) aqueous solution interfaces (0.1, 1, 2 and 5 %). The influence of the compression rate on the measured surface pressure was primarily determined and the optimum rate was selected and used for all subsequent experimental studies. The film stability, hysteresis and the behaviour of deuterated counterparts of such films have also been explored.

This chapter includes a brief overview of the apparatus and experimental procedure for obtaining surface pressure-surface concentration isotherms. Thereafter the chapter is split into three sections. The first outlines the compression rate dependance of experimental isotherms for copolymer films spread on a pure water subphase. The second reports and compares the individual isotherms obtained for homo PEO and each copolymer film (hydrogenous and deuterated) at the air-water interface. The thermodynamic properties of each monolayer have been determined by applying Scaling laws to the individual isotherms obtained and the results are discussed here. Finally the monolayer behaviour of films of *hn25* copolymer when spread on a range of concentrations of aqueous PEO solutions are compared and their thermodynamic properties are also discussed.

Section 5.2   Experimental

Surface pressure isotherms were obtained using a Langmuir trough (NIMA model 2001) and experimental detail has previously been outlined in Chapter Three

The experimental procedure to collect data for an aqueous PEO subphase was identical to that for a water subphase except a time period was allowed to lapse before spreading the film to allow the polymer-containing subphase to equilibrate. Additionally the surface tension of the subphase was determined prior to spreading the film using the Wilhelmy plate method. The pressure sensor was lowered allowing the plate to enter the subphase and the surface pressure was then zeroed before the plate was raised back out of solution. The resultant surface pressure gave the surface tension. This procedure was repeated ten times and the results averaged to give a value for the subphase surface tension. The polymer film was then spread as outlined in Chapter Three.

Section 5.3   Compression Rate Dependence

5.3.1   Introduction

To investigate the dependence of surface pressure on compression rate, films of the fully hydrogenous copolymer with 25 ethylene oxide (EO) units were spread onto a clean water surface and isotherms were obtained using several different barrier speeds. The polymer system with intermediate graft length was selected as it was presumed that the monolayer characteristics observed would be representative of the entire series of materials. Isotherms were obtained at 298 K using a range of barrier speeds: 10, 20, 30, 40 and 50 cm^2 min^{-1}.

5.3.2   Results

A summary of the results from this study is shown in figure 5.3.1 where the measured surface pressure at a surface concentration of 1.0 mg m^{-2} is given for each specific compression rate. Data for three different surface concentrations, 0.5, 1.0 and 1.5 mg m^{-2} were studied, and the results presented here are typical of the behaviour at each concentration. Each data point is an average of three consecutive isotherms.

It is evident from these results that the surface pressure measurements are dependent on the compression rate of the film. The slowest barrier speed consistently returns lower surface pressure values. There is less variation however, in surface pressures when higher compression speeds are used, 20-50 cm^{-2}, since the values obtained are all very similar within experimental error.
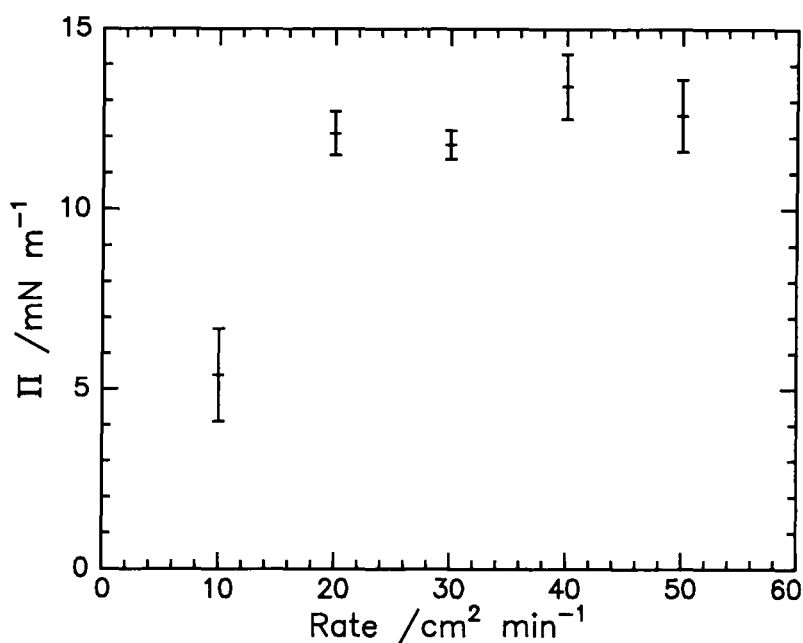
Figure 5.3.1. Surface pressure for a surface concentration of 1.0 mg m^{-2} as a function of compression rate for *n25*.

5.3.3 Discussion

The results provide conclusive evidence that the rate of compression of a monolayer effects the surface pressure and consequently the surface tension of the film under study.

When a slow compression rate is used (10 cm^2 min^{-1}) lower surface pressure values are obtained and this phenomenon is attributed to the ageing of the film. The slower the compression speed the longer the film has been on the surface before reaching a specific concentration and the longer it has to relax to the preferred concentration. It is also evident from figure 5.3.1 that there is no significant difference between the isotherms obtained when compression rate is varied between 20 and 50 cm^2 min^{-1}.

The aim of these experiments was to select the optimum compression rate for subsequent isotherm studies. In doing so various factors were considered including

relaxation processes, the time factor and the possibility of contamination. After considering such elements it was decided that a compression rate of 30 cm^2 min^{-1} would be ideal as this speed provides an excellent representation of surface behaviour and also would avoid lengthy time measurements, thus minimising the possibility of external film contamination. Isotherms obtained using this speed were highly reproducible, therefore any relaxation processes occurring during compression were also reproducible.

Section 5.4   Surface Pressure Isotherms at the Air/Water Interface

5.4.1   Homo poly (ethylene oxide)

It is well known that PEO is surface active in suitable media (for example water[1]) as it has a lower surface energy than water molecules therefore it reduces the surface tension. PEO is so surface active it even forms stable monolayers at the air-water interface[2] despite the fact that it is water soluble at room temperature. A typical surface pressure-surface concentration isotherm for a spread film of PEO homopolymer (with a molecular weight of 103 000 and a polydispersity of 1.21) is given in figure 5.4.1. The isotherm obtained was found to be highly reproducible, particularly at low surface concentrations.
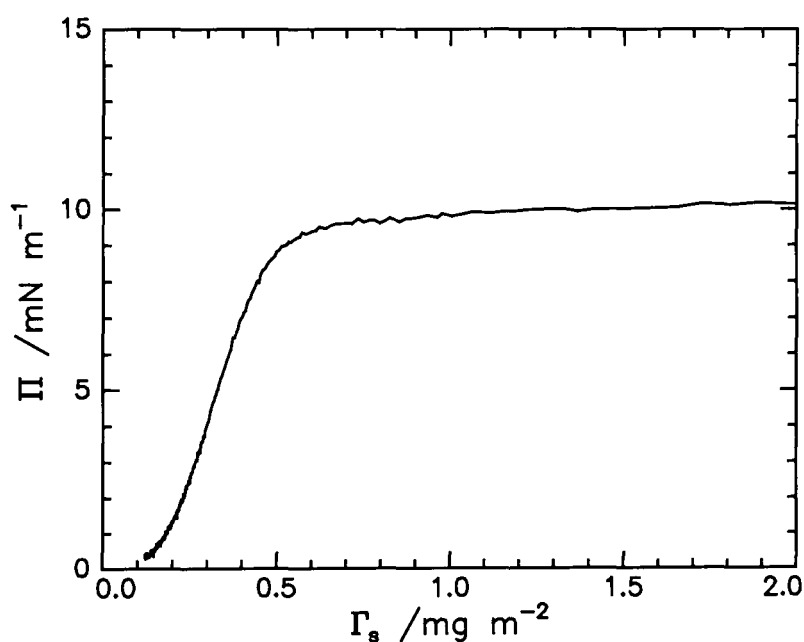

Figure 5.4.1. Surface pressure-surface concentration isotherm for homo (polyethylene oxide).

148

The experimental isotherm obtained agrees well with previous studies of spread PEO monolayers and has been divided into three characteristic regimes. The first of these occurs at minimum surface coverage (< 0.3 mg m^{-2}) where the surface pressure is low and constant. The second characteristic regime begins at circa 0.3 mg m^{-2} when the surface pressure begins to increase slowly, as the monolayer is compressed further the surface pressure passes through a point of inflection at 0.4 mN m^{-1}. Thereafter surface pressure rises rapidly as the surface concentration is increased to 0.7 mN m^{-1} where an equilibrium surface pressure of 10 mN m^{-1} is reached. The surface pressure then remains constant with further monolayer compression (third regime) and this equilibrium surface pressure is characteristic of pure homoPEO monolayer spread on water. If any impurities were present, for example excess terminating agent, they would be easily detected as the surface equilibrium value would be lowered.

Such qualitative observations have been confirmed by a study of the molecular monolayer organisation using neutron reflectometry[3]. The interpretations of isotherms presented in the literature indicate that the polymer sits on the uppermost layer of the surface and is highly diluted by the subphase at low surface concentrations (≤ 0.4 mg m^{-2}). This region corresponds to a dilute regime where the surface pressure is independent of chain length as the PEO molecules behave independently on the near surface. In the middle regime the rapid increase in surface pressure is predicted to be due to an increase in the two-dimensional density of the EO units on the surface. As the surface becomes saturated with EO molecules the surface pressure isotherm begins to plateau and this has tentatively been interpreted as the onset of penetration of the PEO chains into the subphase. Neutron studies have confirmed previous speculations as model behaviour revealed that the polymer chains start to extend into the subphase as loops and tails and distribute from the interface with a Gaussian profile. The chains stretch into the subphase to avoid unfavourable chain-chain interactions and to maximise the thermodynamically favourable EO-water interactions. As the chains extend further into the subphase, the number density of PEO segments in the layer closest to the interface remained constant throughout film compression.

5.4.2   Hydrogenous Copolymer

Typical surface pressure data obtained for the individual graft copolymers and that for poly (ethylene oxide) (PEO) are compared in figure 5.4.2. It is evident from this diagram that there are clear differences in the surface pressure isotherms for the graft copolymers and homopolymer. Furthermore, there are also marked differences between the isotherms for the different copolymers. This latter fact appears to be a direct result of the differing PEO graft lengths because the hydrocarbon backbone content of the copolymers are all very similar.
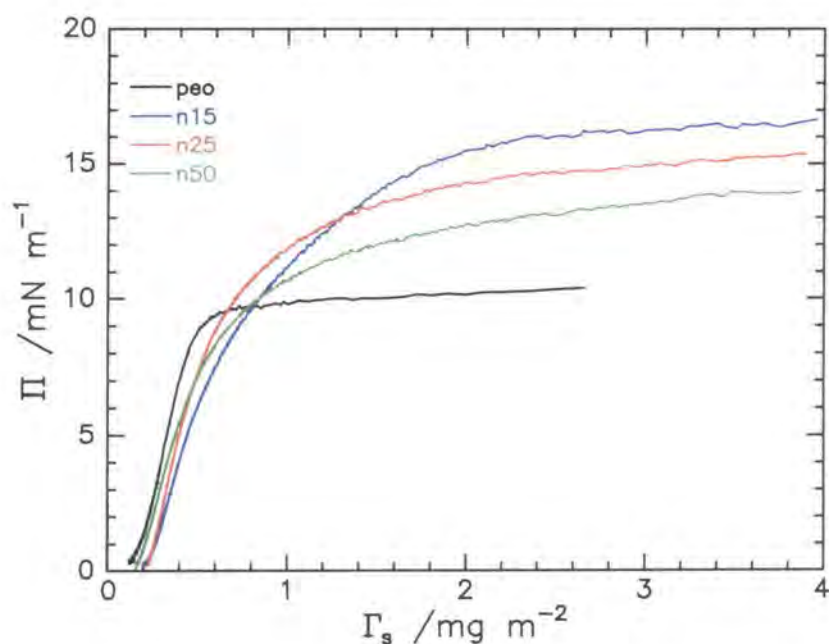

Figure 5.4.2.   Comparison of surface pressure surface concentration isotherms for all three graft copolymers.

In general, a steep rise in the surface pressure is observed over a narrow surface concentration range (0.2-0.7 mg m^{-2}), thereafter the increase in surface pressure is reduced and an asymptotic surface pressure is reached. It is evident from the similarities between the isotherm shape of all copolymer films and homo PEO at low surface coverage, that the

behaviour in this region is being dominated by the PEO present. Small distinctions between the isotherms however are apparent when the data is examined closely since the monolayer behaviour becomes increasingly like homo PEO as the percentage composition of EO in the copolymer materials increases. As the surface concentration surpasses the critical concentration of 0.7 mg m^{-2}, the isotherms begin to diverge and approach different equilibrium surface pressures. At high surface concentrations the behaviour of the graft copolymer again exhibits a dependency on graft length: as the EO content of the copolymer increases the equilibrium surface pressure value tends towards the value for homo PEO. The values decrease from circa 16.5 mN m^{-1} for *hn15*, to 15.3 mN m^{-1} for *hn25* and to 14.0 mN m^{-1} for *hn50*. All these values are significantly different to that for homoPEO (10 mN m^{-2}).

In general it is clear from the strong similarities between the monolayer behaviour for homo PEO and the graft copolymers that the behaviour of each film is predominantly influenced by the PEO. This is not surprising, as PEO constitutes the majority of the copolymer (89-96 %). However, the slight variations present suggest that the backbone contributes and influences monolayer organisation. When such differences between copolymers are analysed then it is obvious that monolayer organisation is correlated to the percentage of PEO in the copolymer i.e. the length of the graft chain. Therefore to aid interpretation of this influence on molecular organisation, the isotherms have been re-plotted (given in figure 5.4.3) in the form of surface pressure versus the surface concentration of PEO, Γ_{sPEO}.

When comparing this plot to the original isotherms (figure 5.4.2) subtle differences are apparent. For example, at low surface concentrations the isotherms for all copolymers now coincide with that for homo PEO. This suggests that in this surface concentration range the monolayer organisation is dominated by the PEO, and will possibly organise in a manner akin to the homo polymer. Consequently it can be tentatively suggested that the monolayer behaviour is independent of the hydrocarbon backbone at low surface coverage.
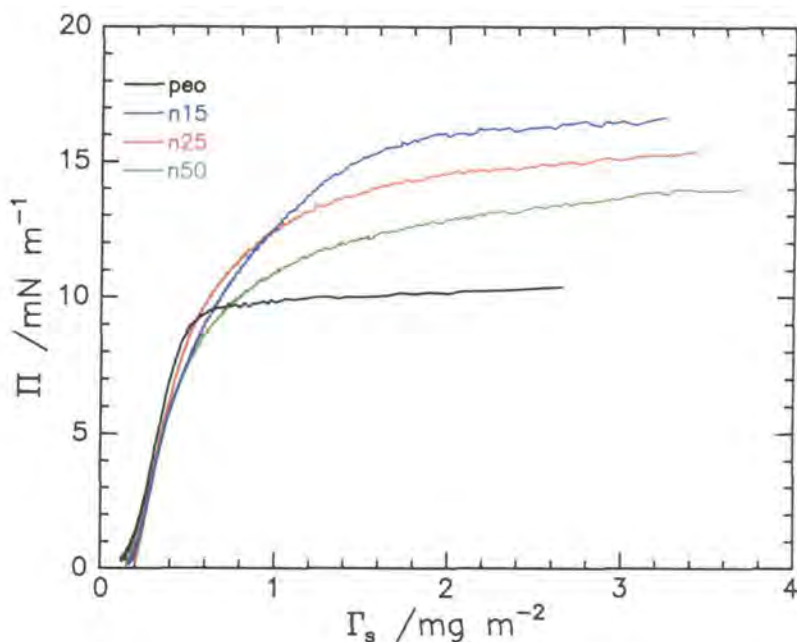
Figure 5.4.3. Surface pressure isotherms for all graft copolymers as a function of PEO concentration. The isotherm for homopolymer PEO is overlaid for comparison.

At monolayer concentrations greater than 0.7 mg m^{-2} the differences in characteristic behaviour are still evident, thus the organisation of the copolymer is influenced by both the backbone and the side chain length.

Returning to the original isotherms (figure 5.4.2) it is of particular interest to note the variation in the asymptotic surface pressure values with differing graft length. Surprisingly the experimental findings do not follow the anticipated trend since a decrease in the value for the equilibrium surface pressure (hence an increase in surface tension) is observed with increasing hydrophilic graft length. It was expected that as the graft length increased, the surface tension would decrease due to a greater number of surface active monomer units populating the near surface, thus the number of favourable PEO/subphase interactions would increase. The opposite behaviour however was experimentally observed possibly indicating that the surface is depleted of favourable PEO/subphase interactions as the graft length increases (at equivalent surface concentrations). One possible explanation could be connected to the tacticity of the polymer backbone. NMR studies (see Chapter

Four) provide evidence for the existence of both cis and trans double bonds in the main chain of the copolymer. At low surface concentrations the backbone and grafts are imagined to lie flat on the surface emanating from the backbone at all angles, therefore the different isomers have little, or no effect on monolayer organisation. If the PEO in the graft copolymer behaves in a similar manner to homoPEO the grafts will only penetrate the subphase at higher surface concentrations. By assuming this and presuming the system adopts a conformation of minimum energy then intuitively all the grafts must penetrate the subphase. At high surface concentrations the molecules within the film are tightly packed which forces the backbone to lift off the surface to enable grafts attached to trans configurations to curl over the backbone and enter the subphase. The buckling of the backbone would induce a depletion of polymer from the near surface that could reduce the number of favourable PEO/water interactions, thus leading to an increase in surface tension. It is possible that the buckling effect is more dominant in the higher graft lengths therefore enhancing surface depletion hence the surface tension increases accordingly. An alternative analogy could be associated with the hydrophilic and lipophilic balance of the PEO molecules as suggested by Cao and Kim[4, 5] for end functionalised PEO. It is envisaged that the PEO molecules become more hydrophobic in character as the surface concentration increases. This is due to a reduction in the number of the thermodynamically favourable EO/water interactions, which is a consequence of steric crowding of the near surface as EO monomer units replace water molecules. This increased hydrophobicity decreases the surface energy hence a reduction in surface tension is observed. As the molecular weight of the graft length increases the ends of the chain possibly have more mobility to explore the subphase and are not forced to pack as densely in the near surface. This increases the number of solvent molecules present which leads to an decrease in hydrophobicity at the near surface thus the surface tension increases and the surface pressure decreases.

To appreciate fully the behaviour of this system detailed structural information is required on a molecular level hence the non-perturbative technique of neutron reflectometry was employed.

For neutron reflectometry studies it was important to verify three properties: i) that monolayer behaviour was highly reproducible, ii) that the isotopically equivalent copolymers (with hydrogenated and deuterated grafts) behaved in a similar manner and iii)

that the films retained a stable conformation over the time required to collect reflectivity data. The procedure and results for the separate studies are discussed in the following three sections.

5.4.3 Reproducibility

The monolayer behaviour of each film was found to be highly reproducible, especially at low surface concentrations. For example two typical surface pressure isotherms obtained for separate spread films of *hn25* copolymer are given in figure 5.4.4.
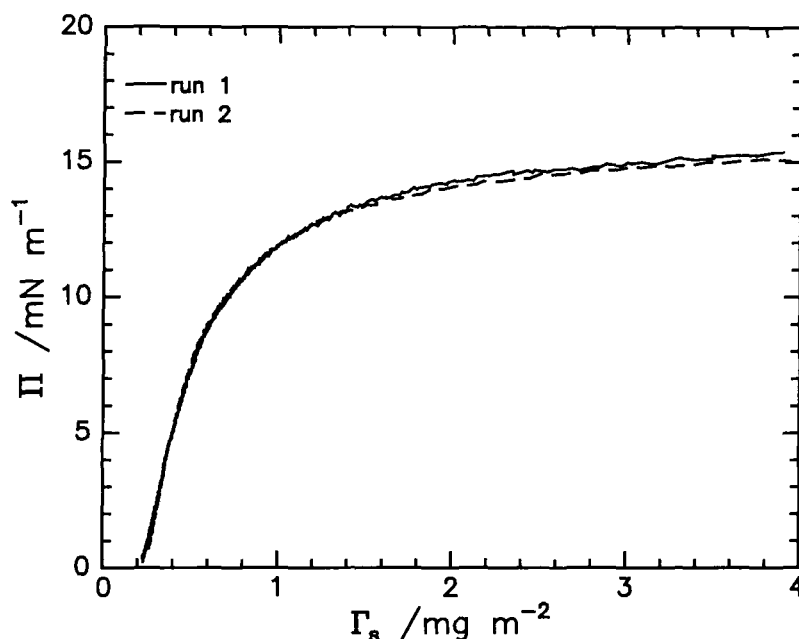

Figure 5.4.4. Typical examples for the reproducibility of surface pressure isotherms for two separate spread films of *hn25*.

It is noted that the two isotherm curves are indistinguishable within experimental error. This indicates that monolayer behaviour, and hence the near surface organisation, is highly reproducible. The slight discrepancies observed at high surface concentrations are within experimental errors. As the film becomes highly compressed it is more susceptible

to surface contamination from for example dust particles, which can lead to localised defects within the film, or even nucleate film collapse. Slight fluctuations in the temperature or chemical composition of the subphase or superphase is another possible source for the trivial inconstancies observed between the experimental data. Such possible sources of error can be minimised by regulating the subphase temperature and enclosing the system inside a Perspex box. Further experimental variations can arise at high surface concentrations due to the rigidity of the film, which causes displacement of the Wilhelmy plate from hanging vertically, hence the true surface pressure readings are distorted. Such deviations in the experimental results are minimised in practise by using a large circular trough with two barriers that close symmetrically, therefore exerting a symmetrical force on the Wilhelmy plate. Any deviations in highly compressed data however do not significantly influence the physical interpretations of the isotherms, as conclusions regarding monolayer behaviour are drawn from the highly reproducible, low surface concentration data.

5.4.4 Deuterated Copolymer

Isotopically equivalent graft copolymers have also been prepared where the EO grafts were selectively deuterated while the backbone remained hydrogenated. Chemical analysis outlined in (Chapter Four) has previously shown that the hydrogenated and deuterated counterparts are chemically equivalent. To assess the effect of isotopic substitution on monolayer organisation, or on thermodynamic polymer-water interactions, the surface pressure isotherms for the deuterated materials were obtained and compared to their hydrogenated counterparts. Experimental data for the deuterated materials were acquired using an identical procedure as previously described (in section 3.1.4). The isotherms obtained for *hn25* and *dn25* copolymers are compared in figure 5.4.5 and their behaviour is representative of the remaining copolymers in the series.

It is obvious by studying the results that the two isotherms are in good agreement (within experimental error) especially at minimal surface coverage. The slight differences present between the two curves are negligible and are within experimental error. Evidently

therefore isotopic substitution has no effect on the thermodynamic properties, nor on monolayer organisation between the hydrogenated and deuterated graft copolymers.
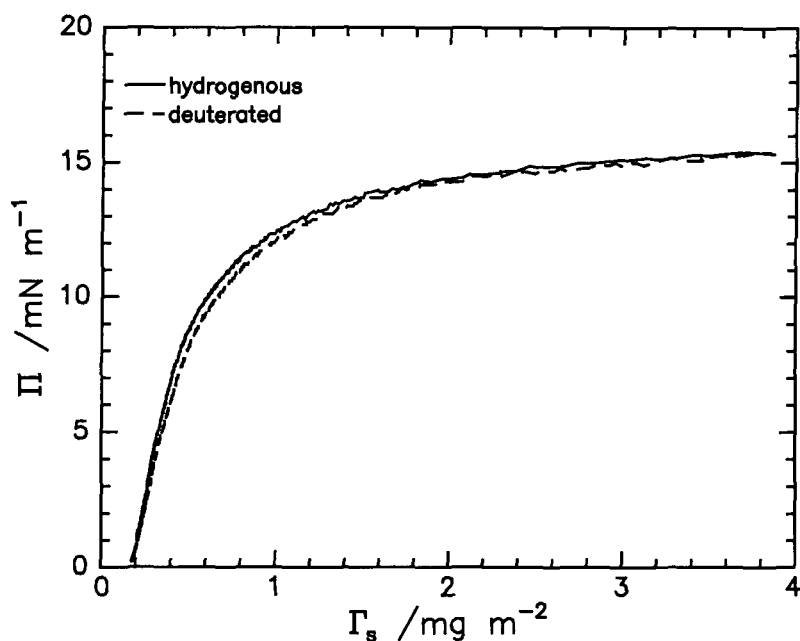

Figure 5.4.5. Comparison of surface pressure isotherms for hydrogenated and part deuterated graft copolymers containing 25 EO units

5.4.5 Film Stability

As previously mentioned it was pertinent for neutron reflectometry studies to ensure that the organisation of the spread films remained constant over the time required to collect reflectivity data (maximum four hours). To this end the surface pressure of freshly spread monolayers was continuously monitored for times in excess of four hours for each copolymer. Such stability measurements were taken at four separate surface concentrations: 0.4, 0.7, 2.0 and 4.0 mg m^{-2} and results are given in figure 5.4.6.
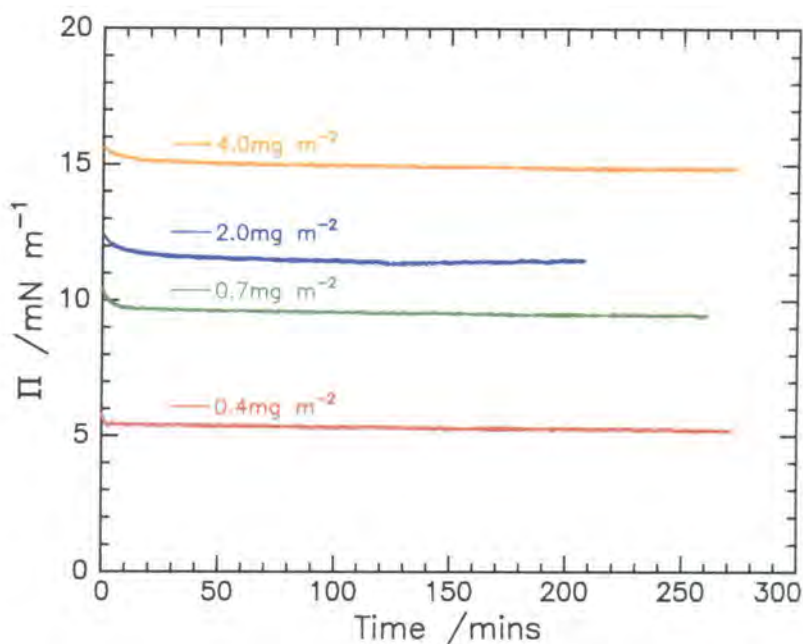
Figure 5.4.6. Typical examples of the surface pressure as function of time testing the stability of spread films of *hn25*.

Analysis of the surface pressure data as a function of time revealed the presence of a small relaxation in each film just after the initial compression to the desired surface concentration, thereafter the surface pressure remained constant with increased time. The relaxation time appeared to be dependent on the surface concentration spread as the time of the exponential decay increased with surface concentration. The maximum relaxation time observed however was only circa ten minutes. This result indicates that generally the surface organisation of the copolymer is constant with no dissolution into the subphase over the time range studied. Such behaviour is representative of the copolymer series, even those with 50 EO units. It was decided that experimental measurements would only be taken after a minimum of ten minutes elapsed, thus allowing sufficient time for the molecules to equilibrate.

5.4.6 Hysteresis

To investigate whether hysteresis occurred within this system a monolayer of *hn25* was steadily compressed to the maximum surface pressure, 15.8 mN m^{-1}. The barriers were then stopped and immediately opened at an identical speed (30 cm^2 min^{-1}) while the surface pressure was continuously monitored. The isotherm obtained for such an experimental cycle is shown in figure 5.4.7 and is again typical of the results gained for each copolymer.
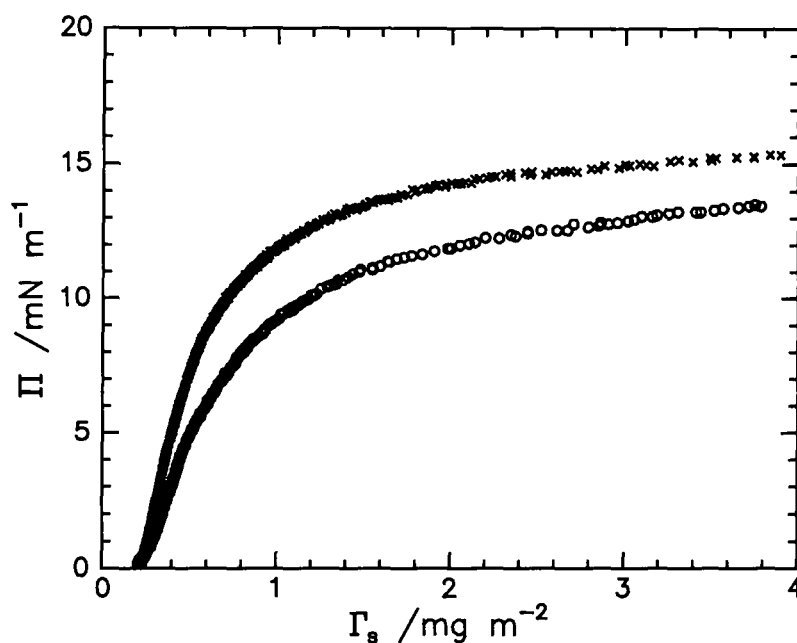

Figure 5.4.7. Surface pressure isotherm collected upon compression × and expansion (○) of a spread film of *hn25*.

It is evident from the results that the isotherm collected upon decompression does not follow the trajectory for film compression, i.e. there is hysteresis. This phenomenon is simply due to the polymer molecules having time to relax to an equilibrium state.

This compression/decompression cycle was repeated several times using the same film and all profiles were coincident. This behaviour implies that all copolymer remains at the near surface i.e. there is no dissolution into the subphase overtime.

5.4.7   Analysis of Isotherms

Scaling laws have been derived for spread films of homopolymers[6,7] and their application to the isotherm data has been previously outlined in Chapter Two. When such laws are extended to copolymer films the validity of the results obtained must be treated with caution due to additional interactions between separate entities of the copolymer, and each copolymer with the subphase possibly effecting the exact physical interpretation of the experimental data. Despite these limitations scaling laws have been applied to isotherms obtained in this study and have provided a first approximation of the thermodynamic behaviour of each copolymer, allowing at least a qualitative comparison of the materials.

5.4.7.1 Dilute Regime

In the dilute regime polymer chains exist as separate entities in a 2-dimensional monolayer i.e. they are non-interacting. Their behaviour can be expressed through the virial expansion,

$$\frac{\Pi}{\Gamma_s} = RT\left[\frac{1}{M_n} + A_{22}\Gamma_s\right]$$

Equation 5.4.1.

where R is the gas constant, T the temperature, M_n the number average molecular weight and A_{22} the second virial coefficient. By plotting $\dfrac{\Pi}{\Gamma_s}$ versus Γ_s the polymer molecular weight and A_{22} can be extracted from the experimental isotherm. Figure 5.4.8 shows such a plot for *hn25*, which is representative of the behaviour of all graft materials.

The data required to extract A_{22} and the molecular weight is at very low surface concentrations and it is clear from this diagram that the experimental data is particularly noisy in this region. This poor quality data is due to the lack of sensitivity of the pressure balance since only surface pressures of 0.2 mN m^{-1} could be accurately measured. The quality of the data is so poor that it did not justify fitting.

Very few studies have been reported where accurate surface pressures were experimentally detected at low surface concentrations. Vilanove and co-workers[8], have been working in this area and they have successfully extracted the characteristic parameters from the low surface concentration region. The apparatus they used was highly sensitive as readings as low as 1 μN m^{-1} were confidently measured, opposed to 200 μN m^{-1} limit of our equipment. Despite the limitation of apparatus in these experiments, a cross comparison of values of A_{22} through the series of homopolymers was possible by comparing the shapes and gradients of the different copolymers when plotted in the form of equation 5.4.1.
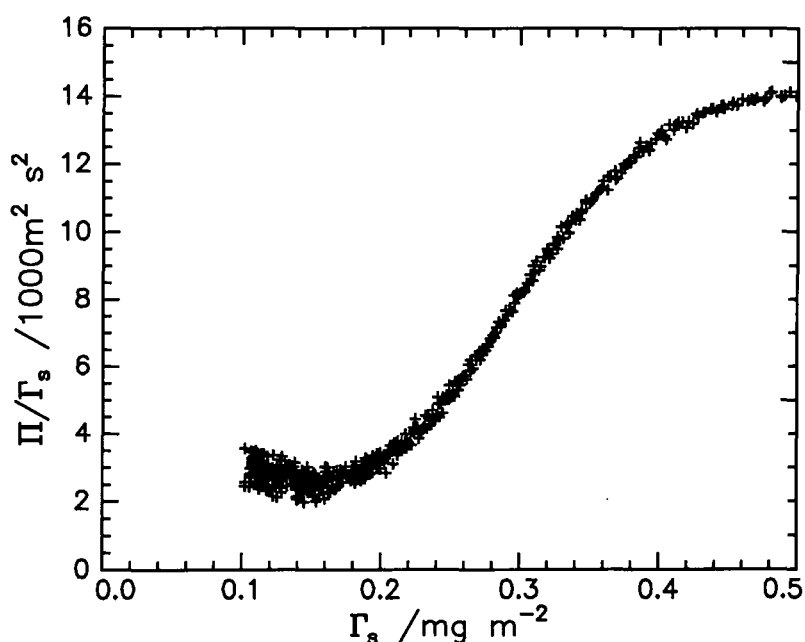

Figure 5.4.8. Surface pressure isotherm plotted in the form of equation 5.4.1 for a monolayer of *hn25*

All three copolymers exhibited similar behaviour at low surface concentrations as they all followed a similar trajectory. Interestingly all curves change gradient between 0.18-0.20 mg m^{-2}. Below this critical value the gradient of the curve is negative, therefore the

value for A_{22} will be negative. Since A_{22} quantifies the interactions between the polymer and subphase molecules it can be used to estimate the quality of the solvent, hence a negative value indicates the polymer molecule is in a coiled conformation, as if in a poor solvent. It is concluded therefore that these chains are subject to unfavourable chain-solvent interactions. It is noted that the slope for each copolymer becomes marginally less negative as the graft length increases, which indicates that the PEO graft interactions between the chains and the subphase becomes more favourable.

5.4.7.2 Semi-Dilute Regime

Polymer chains are described as being in the semi-dilute regime when they begin to overlap and interact, therefore both intramolecular and intermolecular interactions need to be taken into account. The nature of the thermodynamic interactions between polymer and subphase can be determined using the scaling relation between surface pressure and surface concentration,

$$\Pi = \Gamma_s{}^y \qquad \qquad \textbf{Equation 5.4.2.}$$

where $y = \dfrac{2\upsilon}{2\upsilon - 1}$ and υ is the critical scaling exponent. Values for y can be extracted by plotting $\log \Pi$ versus $\log \Gamma_s$ and calculating the scaling exponent. Such a double logarithmic plot for *hn25* is given in figure 5.4.9 and an example of the fitted linear section of the semi dilute regime is shown in figure 5.4.10. All isotherm data were subjected to this fitting procedure and the example presented is typical of the series of copolymers. The critical values extracted for the slope (y) and calculated for υ are given in table 5.4.1.

Polymer	y	$\upsilon_{calc.}$
homo PEO	2.88 ± 0.14	0.76 ± 0.01
n15	5.30 ± 0.27	0.62 ± 0.01
n25	4.70 ± 0.24	0.64 ± 0.01
n50	3.79 ± 0.19	0.68 ± 0.01

Table 5.4.1. Experimental v values calculated from double logarithmic plots of surface pressure isotherms.

The experimental value obtained for homo PEO, 0.76, is in close agreement with the reported value, 0.75, at room temperature in good solvent conditions[3]. The exponent values for each copolymer material are also close to that for homo PEO, indicating that the interactions between the copolymer grafts and the water subphase are thermodynamically favourable. As the PEO content of the copolymer increases, υ increases from 0.62 to 0.68, suggesting that the graft copolymer-water interactions become more favourable as the percentage of PEO in the copolymer increases.

It can be concluded from this information that the nature of the polymer-subphase interactions is dependent upon the composition of the copolymer.
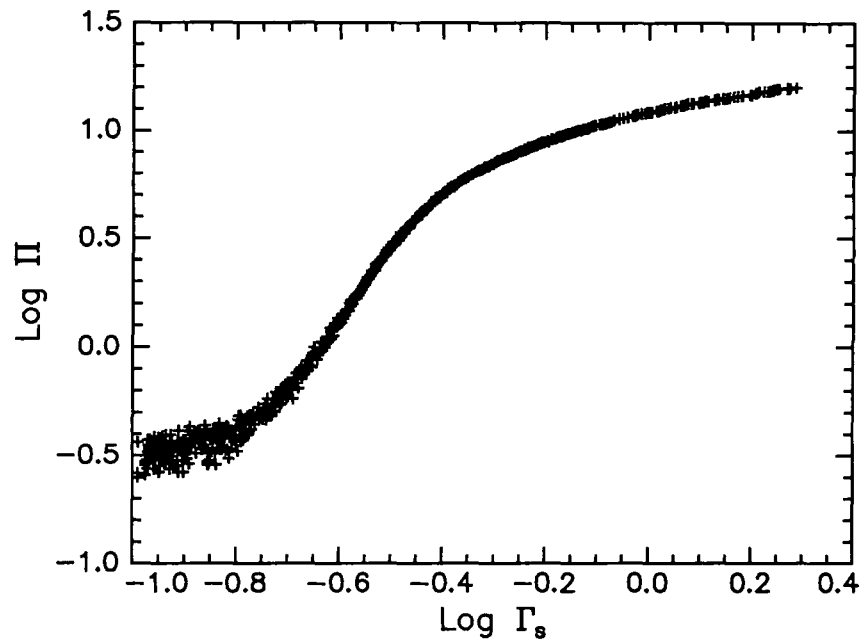
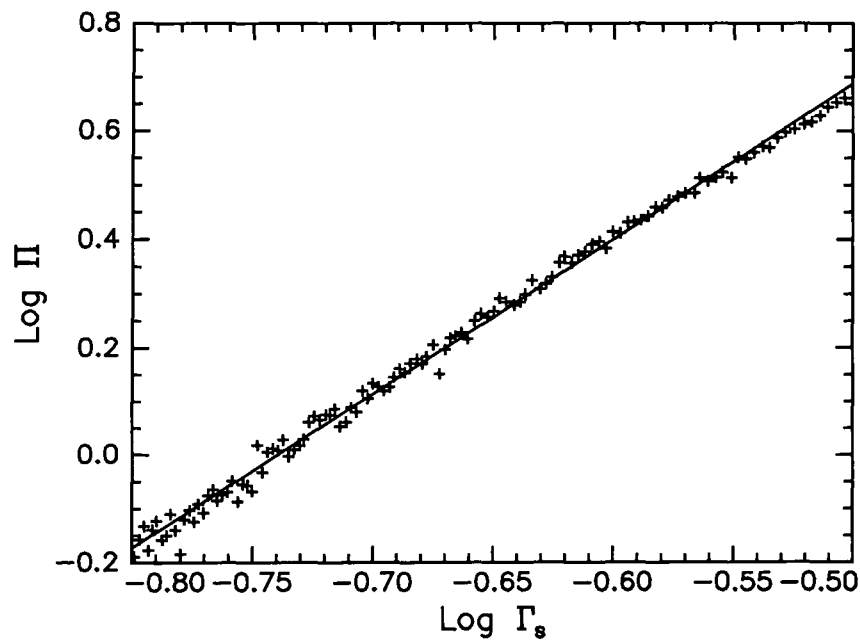**Figure 5.4.9.** Double logarithmic plot of Π versus Γ_s for *hn25* copolymer monolayer.

Figure 5.4.10. Typical example of a least squares fit of the linear portion of *hn25* isotherm (Figure 5.4.9) to extract y and υ.

5.4.7.3 Limiting Surface Area per Monomer Unit

Values for the limiting area have been determined by extrapolating the initial rise in surface pressure to zero surface pressure, then performing a simple calculation. A typical example of data fitted in this way is given in figure 5.4.11 and the data obtained for each copolymer is listed in table 5.4.2.
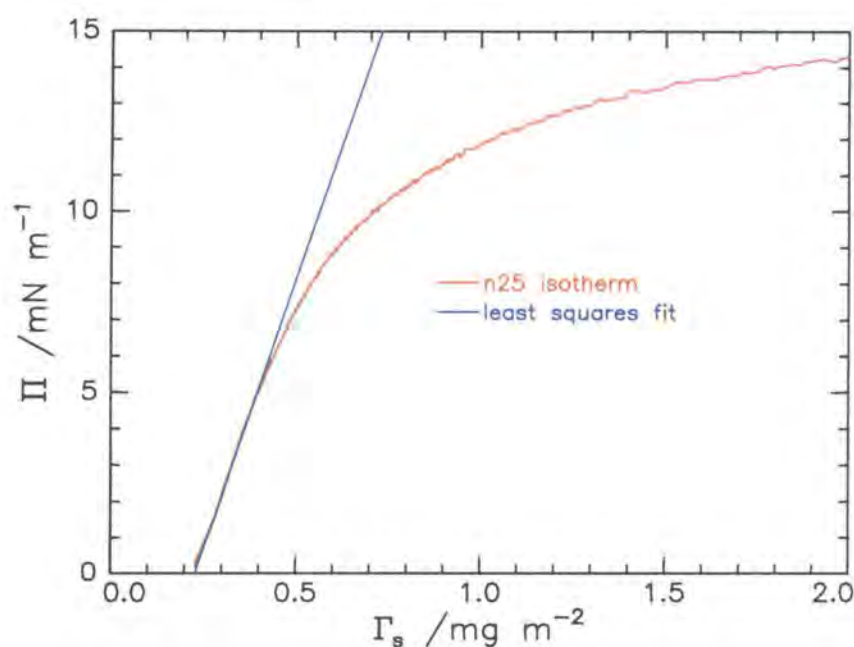

Figure 5.4.11. Typical example of least squares fit of linear portion of *hn25* isotherm to obtain the limiting surface concentration and the limiting area per monomer unit.

It is apparent from these results that as the PEO graft length increases the area occupied by one ethylene oxide monomer also expands. This difference in area could imply that the side chain undergoes a conformational change as the number of EO units alters. Such changes are possibly indicative of the grafts becoming more coiled, and adopting a less rod-like conformation as the graft length increases.

Polymer	$\Gamma_s$lim /mg m^{-2}	apmu$_{lim}$ /Å^2
n15	0.24	32.5
n25	0.23	33.9
n50	0.17	45.8

Table 5.4.2. Experimental values calculated for the limiting surface concentration ($\Gamma_s$lim) and the area per EO monomer unit (apmu$_{lim}$).

5.4.7.4 Phase Transitions

The points where the gradient changes on the double logarithmic plots of surface pressure versus surface concentration correspond to behavioural crossovers: the dilute to the semi-dilute, and from the semi-dilute to the concentrated regime. The critical concentrations, denoted by Γ_s^* and Γ_s^{**}, respectively can be extracted for each copolymer and the values obtained for each monolayer are listed in table 5.4.3.

Polymer	Γ_s^* /mg m^{-2}	Γ_s^{**} /mg m^{-2}
n15	0.22	1.59
n25	0.21	0.94
n50	0.17	0.79

Table 5.4.3. Surface concentrations of the phase transitions for polymer monolayers spread on water.

The values for Γ_s^* and Γ_s^{**} decrease as the PEO chain length increases in the copolymer. This trend suggests that the PEO grafts come into contact with each other as the monolayer is compressed. This is easily explained since the crowding of EO on the surface forces the grafts to compress and pack together, or in terms of brush theory form mushrooms on the surface which are packed more tightly, then stretch as wet brushes into the subphase as the surface coverage increases. The radius of gyration (R_g) is dependent on

the degree of polymerisation (N) of the graft, $R_g \sim aN^{3/5}$, (where a is the monomer step length) therefore the mushrooms will have a larger radius of gyration and the mushrooms begin to touch each other and overlap at lower surface coverage as the degree of polymerisation increases. The same reasoning can be applied to the transition from the semi-dilute to the concentrated regime as the increasing graft length induces further entanglements of the tethered chains and a transition to the stretched brush conformation at lower concentrations.

It proved difficult to classify the exact surface concentration of each phase transition as the change in conformation, i.e. from liquid expanded to a liquid condensed phase, is gradual in comparison to low molecular weight species. This behaviour is typical of polymer films.

Section 5.5   Surface Pressure Isotherms at the Air/Aqueous Poly(ethylene oxide) Interface

5.5.1   Introduction

Surface pressure-surface concentration isotherms were collected for *hn25* copolymer on four separate concentrations of aqueous homo PEO solutions, 0.1, 1.0, 2.0 and 5.0 % PEO using a procedure identical to the previous experiments on pure water subphases. PEO homopolymer was deliberately selected, as it is chemically identical to the copolymer graft, has a substantially higher molecular weight and is commercially available. The range of PEO solution concentrations were specifically chosen to allow the organisation of the spread copolymer to be analysed above and below the overlap concentration of the mobile PEO molecules, 0.7 % w/v.

5.5.2   Results

The surface tension of each clean subphase was initially measured several times using the procedure outlined in section 5.2. The results were averaged and are compared to pure water[9] in table 5.5.1.

% of PEO in subphase	Surface tension /mN m^{-1}
0.0	72.3
0.1	63.1 +/- 0.6
1.0	62.3 +/- 0.4
2.0	60.6 +/- 0.5
5.0	53.8 +/- 0.6

Table 5.5.1.   Experimental surface tension values for the different subphases.

The results from surface tension studies of the clean subphases reveal that there is a significant decrease in magnitude from the value for a water surface to that when PEO molecules are present. Furthermore a decrease in surface tension is observed with increasing concentration of free polymer. The reduction in surface tension from the pure water subphase when PEO molecules are present is expected as PEO molecules are adsorbed at the surface due to their surface energy being lower than water molecules. This conformation is preferred because lower energy molecules expend less energy maintaining a surface therefore they reduce the surface tension. The reduction in surface tension observed is circa 10 mN m^{-1} (the maximum reduction observed for a spread monolayer) for the two lowest concentrations of PEO solution, and increases thereafter to approximately 12 mN m^{-1} and 19 mN m^{-1} for 2 and 5 % subphases respectively. Cao and Kim[5] have observed the same values using a similar molecular weight PEO. At low solution concentrations the property of the adsorbed films are very similar to those of a spread monolayer of PEO[10]. The further decrease in surface tension at higher solution concentrations is predicted to be due to a reduction in the number of hydrogen bonds between the PEO and water molecules. This change in bonding increases the effective hydrophobicity of the PEO chains at the surface therefore the surface energy, and consequently the surface tension decreases.

The stability of the surface excess layer of PEO molecules was determined by monitoring the surface pressure as a function of time. It was observed that the initial surface pressure reading was perfectly maintained for times in excess of two hours indicating that the system had equilibrated. This result contradicts the early study by Glass[1] as he predicted that it took 2 hours for similar PEO solutions to equilibrate at 298 K, however the results presented here agree well with the more recent work reported by Lu and co-workers[11]. The discrepancies apparent in the work by Glass have been attributed to the polydispersity of the polymer samples used.
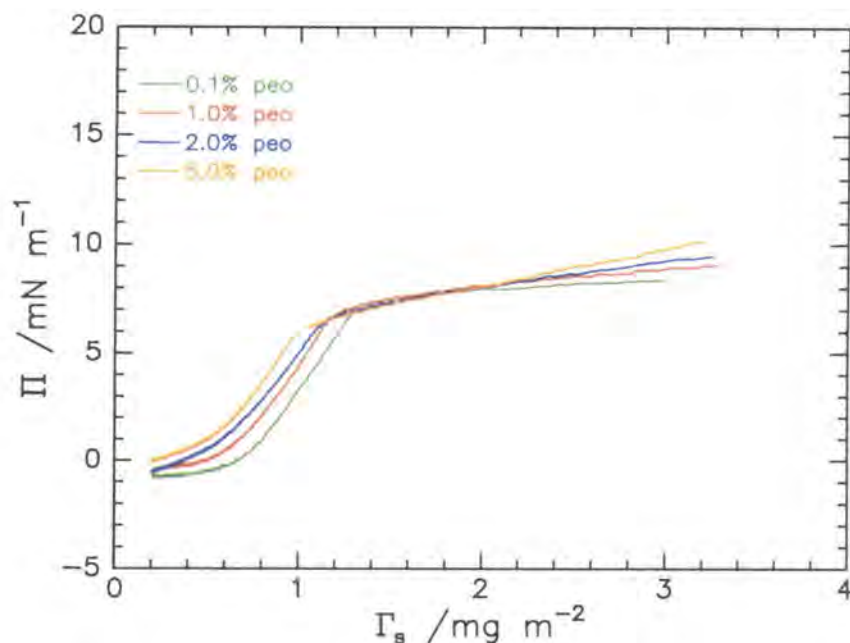
Figure 5.5.1. Surface pressure-surface concentration isotherm for *hn25* films spread on four different aqueous solution subphases.

The surface-pressure surface-concentration isotherms collected for *hn25* copolymer spread on each concentration of aqueous PEO solution are compared in figure 5.5.1. It is evident from this diagram that all four isotherms exhibit similar changes in surface pressure as a function of surface concentration as they have a similar shape. Although the isotherms follow a similar trajectory the values of surface pressure (at low surface concentrations 0.2-1.0 mg m^{-2}) exhibit a dependency on the subphase concentration. As the film is compressed above 1.0 mg m^{-2} the isotherms converge to an asymptotic surface pressure of circa 6 mN m^{-1}. Such characteristic behaviour implies that copolymer organisation is dependent on the percentage of mobile polymer at low surface concentrations, but as the surface coverage surpasses 1.0 mg m^{-2} the behaviour is similar at all subphase concentrations.

Closer examination of the isotherm suggests that the behaviour for each subphase can be split into three regions as with the water subphase. The first region is at very low surface coverage, 0.2-0.5 mg m^{-2}, where there is little variation in surface pressure with surface concentration. The values for surface pressure in this region are all negative, which

indicates that the number of thermodynamically favourable interactions at the surface are reduced in the presence of the copolymer film, i.e. there is a desorption of homoPEO from the near surface. Examination of all four isotherms reveals a correlation between the value of surface pressure and the percentage of PEO in the subphase i.e. the surface pressure becomes less negative as the subphase concentration increases. This trend implies that initially the lower PEO concentration subphases have a greater number of EO molecules displaced from the surface excess layer, which is a reasonable hypothesis as it is thought that the free PEO would be more mobile in the lower subphase concentrations. The middle characteristic regime occurs when the surface pressure rises from 0.5 to 1.0 mg m^{-2}. Again all four subphases return similar qualitative characteristics since the isotherm slopes are comparable, and a similar trend in the surface pressure values as a function of the quantity of mobile PEO is observed. The crossover between the second and third region corresponds to the onset of the equilibrium surface pressure and occurs at circa 1.0 mg m^{-2} for 5 % PEO, 1.2 mg m^{-2} for 1 and 2 % solutions and 1.3 mg m^{-2} for 0.1 % PEO. After this critical point the isotherm curves converge and behave in a similar manner, the surface pressure rising slowly and steadily as the film is compressed further. It was noted that differences in the points between regimes occur at increasing concentrations with increasing quantity of PEO in the subphase. One possible explanation for such a trend is that the two-dimensional, in-plane overlapping of molecules reaches its limit and hence forced to explore a third dimension at a lower surface coverage for higher concentration subphases. It has already been suggested from analysis of data at low surface concentrations that more mobile PEO molecules are present at the near surface as the subphase concentration increases. This crowding of the surface reduces the volume available for molecular compression, hence chain overlap occurs at lower surface concentration. This analogy assumes that the quantity of PEO in the near surface layer remains constant throughout the experiment.

All isotherms were highly reproducible over a surface concentration range of 0-2.0 mg m^{-2} since successive measurements provided isotherms that overlapped well. Above 2.0 mg m^{-2} however slight differences between isotherms were noticed and disagreements as high as 2 mN m^{-1} were recorded. Such an error is attributed to the stiffness of the spread film since the Wilhelmly plate noticeably tilted as the two barriers of the Langmuir trough compressed the film.

One approach to analyse and all data collected on PEO solutions and pure water involves using equation 5.5.1 and the experimental values for the surface tension of the clean subphases (γ_{sub}). This allows the variation in the surface tension of film covered subphase (γ_{ST}) to be monitored as a function of surface concentration, and moreover allows a comparison to be made between copolymers as the difference in subphase surface tension have been taken into account. It is assumed in such calculations that the surface excess layer of PEO present for the clean subphase remains constant when the monolayer is spread and as it is compressed, i.e. that the γ_{ST} value is constant throughout data collection. The data for all five isotherms were treated in such a manner and the results are compared in figure 5.5.2.

$$\pi = \gamma_{sub} - \gamma_{ST}$$ **Equation 5.5.1.**

It is evident that the experimental isotherm collected for the film spread on water is significantly different in comparison to the PEO containing subphases. This suggests that there are very different copolymer-subphase interactions when mobile PEO is present, hence the in-plane molecular structure is probably also different. All subphases containing PEO give isotherms of a similar shape, but in this plot the differences in surface pressure values are attenuated. Such behaviour implies that the copolymer-subphase interactions (hence monolayer organisation) are similar, but not identical. At low surface concentrations (less than circa 1.4 mg m^{-2}) the rate of decrease in surface tension is significantly different in the presence of PEO since the surface tension decreases rapidly for the monolayer on water, but decreases at a reduced rate and over an extended surface concentration range for PEO containing solutions.
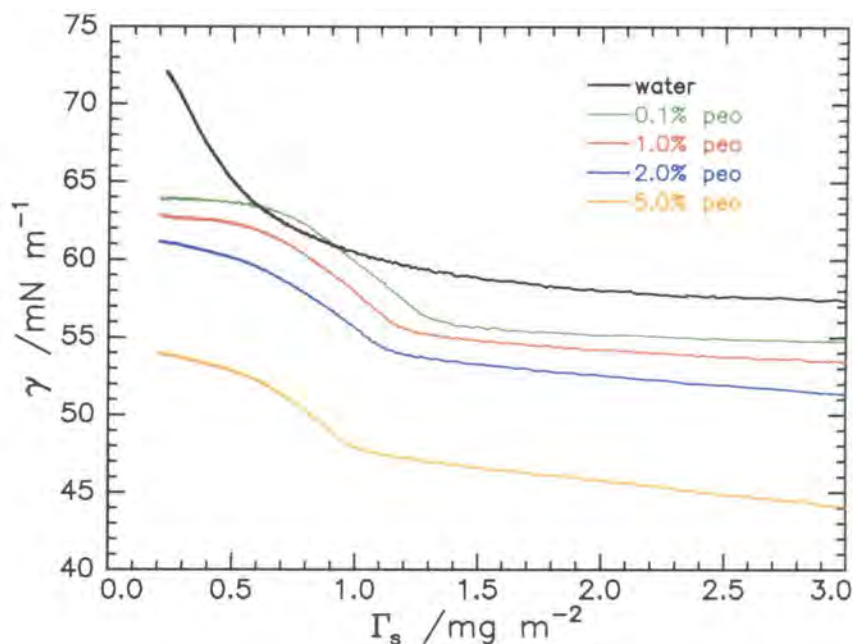
Figure 5.5.2. Surface tension-surface concentration isotherm for each aqueous PEO solution and pure water subphase.

This general behaviour on PEO solution, has been associated with the crowding of the near surface with both copolymer and homoPEO molecules. If this is the case, then molecules on a water subphase can easily expel small water molecules allowing the polymer chains to pack closer together hence allowing the surface tension to reduce rapidly. When there is already a layer of high molecular weight homopolymer present at the interface it becomes substantially more difficult for the copolymer film to compress and find a conformation of minimum energy due to an increase in the entanglements between copolymer and homoPEO. This analogy could explain why the rate of decrease in surface tension is comparatively slow as a function of surface concentration. At higher surface concentrations (greater than 1.4 mg m^{-2}) the rate of decrease in surface tension in all isotherms reduces and an asymptotic equilibrium surface tension is reached, the value of which varies linearly depending on the quantity of PEO in the subphase. As the percentage of mobile homopolymer increases the lower the equilibrium surface tension value becomes. Such behaviour can again be related to the increased crowding of PEO molecules at the

near surface, as this will increase the effective hydrophobicity of the layer hence the surface energy and surface tension will reduce.

5.5.3   Film Stability

It was pertinent for neutron reflectometry studies that the organisation of the spread films remained constant over a prolonged period of time. Surface pressure measurements were collected as a function of time (in excess of two hours) at various surface concentrations. The results obtained for three surface concentrations for a film of *hn25*spread on 2 % PEO solution are given in figure 5.5.3.

The results indicate that in general the monolayer relaxes over a period of 10-20 minutes thereafter the surface pressure values remain constant. There are however slight differences between film relaxation behaviour depending on the spread surface concentration. For low surface concentrations it is clear that there is minimal relaxation occurring, as the surface pressure values remain constant throughout the experiment. Initial measurements were taken approximately one minute after the film was spread. In contrast the films of higher surface concentration appear to relax to an equilibrium conformation after circa twenty minutes as the initial readings display a pseudo-exponential decrease for 1.0 mg m^{-2} and a slower rate of decrease 2.0 mg m^{-2} before a constant value is reached.
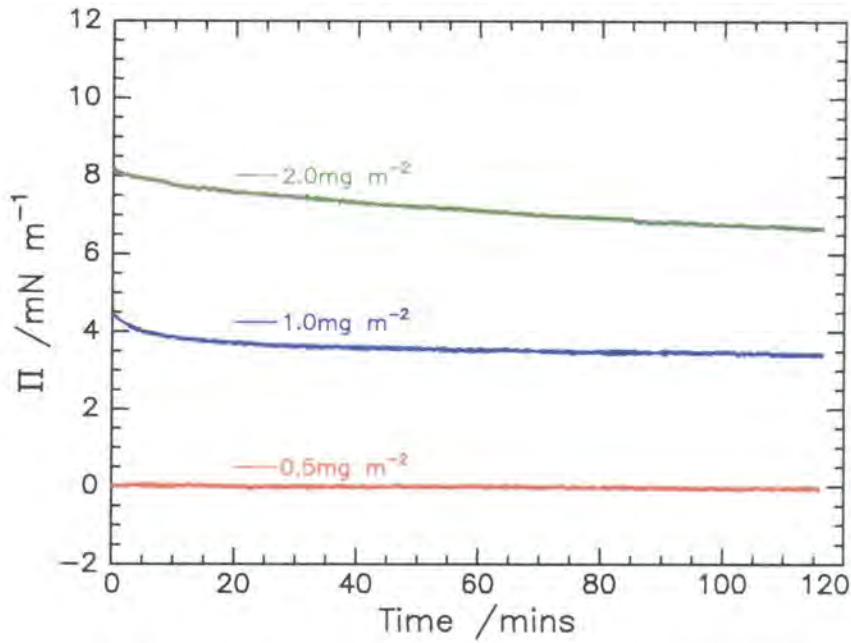
Figure 5.5.3. Relaxation in the surface pressure over time for *hn25* spread on 2 % PEO at three surface concentrations: 0.5, 1.0 and 2.0 mg m^{-2}.

5.5.4 Application of Scaling Laws

Scaling laws were applied to surface pressure data for *hn25* spread on each PEO solution using a similar approach as taken with the pure water subphase (section 5.4.7).

Analysis of the experimental data in the dilute regime theoretically allows the second virial coefficient, A_{22}, and the molecular weight of the copolymer to be extracted from a plot of π/Γ_s versus Γ_s (figure 5.5.2). Unfortunately as with the data for the air-water interface the insensitivity of the apparatus is apparent, as the noise levels at very low surface concentrations are so high the data cannot be reasonably fitted. A qualitative analysis is still possible however if the gradients of slopes are compared. As can be seen from the data for *hn25* on 1 % PEO (figure 5.5.3), the slope at low surface concentration is positive. This implies the value for A_{22} is positive, which implies that physically the polymer is highly solvated, as if swollen by a good solvent. This behaviour is opposite to

that observed for a water subphase as a negative value for A_{22} was observed. This suggests that the PEO grafts are highly stretched in the presence of mobile PEO as the chain-subphase interactions are more favourable. When a cross comparison of gradients is made over the different PEO subphases it is clear that all slopes are positive and the magnitude of the gradient decreases as the quantity of PEO increases. Such a trend can be interpreted to provide an insight into the quality of solvent: a decrease in the magnitude of A_{22} suggests that the chain-subphase interactions become less thermodynamically favourable therefore radius of gyration of the grafts becomes smaller. It was therefore concluded that the chain-subphase interactions increase significantly when homoPEO is introduced to the subphase. However, as the percentage of free polymer in the subphase increased the favorable interactions decrease and presumably the PEO penetration depth also decreases.
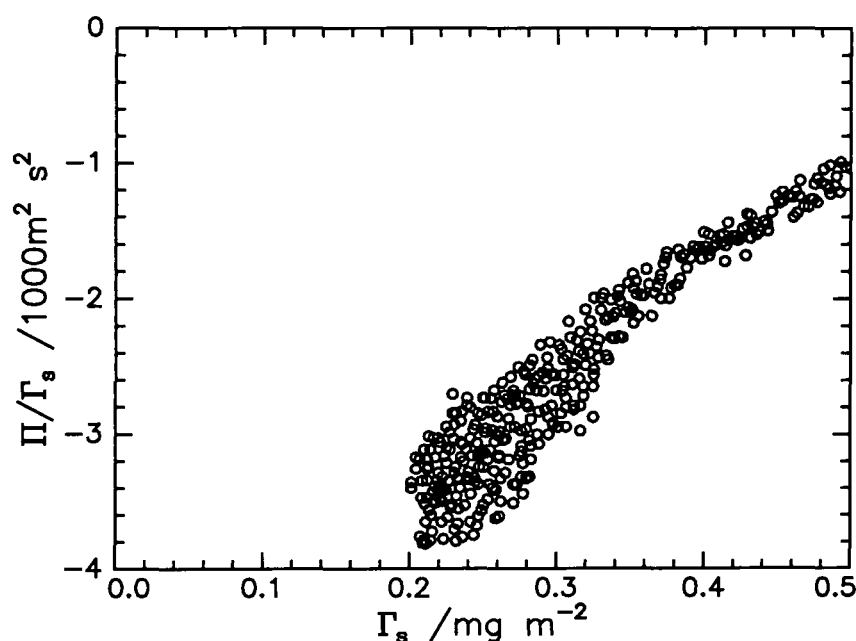

Figure 5.5.3. Plot of surface pressure isotherm in the form of equation 5.4.1 for a film of *hn25* spread on 1 % PEO subphase.

Application of the Scaling laws in the semi-dilute regime ($\pi = \Gamma_s{}^y$ where $y = \dfrac{2\upsilon}{2\upsilon - 1}$) allows the expansion coefficient, υ, to be estimated from a double logarithmic

175

plot of surface pressure versus surface concentration. Consider for example such a plot for *hn25* on 1 % PEO solution (figure 5.5.4), where the gradient of the linear increase of the plot (figure 5.5.5) gives y, from which υ can be simply calculated. The value for the slope and υ for this example are compared with those for the pure water subphase and the remaining PEO solution subphases in table 5.5.2.

% of PEO	y	υ
0	4.70 ± 0.24	0.64 ± 0.01
0.1	4.68 ± 0.23	0.64 ± 0.01
1.0	4.42 ± 0.22	0.64 ± 0.02
2.0	4.30 ± 0.21	0.66 ± 0.01
5.0	2.76 ± 0.14	0.78 ± 0.01

Table 5.5.2. Experimental υ values calculated from double logarithmic plots of surface pressure isotherms.
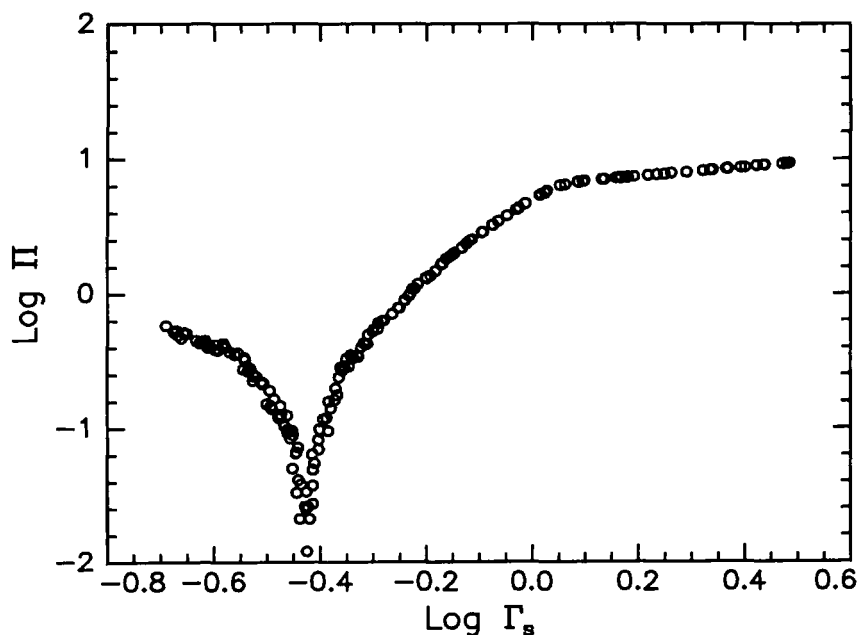

Figure 5.5.4. Double logarithmic plot of surface pressure against surface concentration or monolayer of *hn25* on 1.0 % PEO subphase.

From initial examination of these results it is evident that all values are close to that for homo PEO in good solvent (0.75), therefore the polymer appears to interact with all subphases thermodynamically favorably. Closer examination reveals that there is little or no variation in the values for the three lower concentrations of polymer subphases since all values are circa 0.64. There is however a significant jump in magnitude for the data collected on 5 % PEO (jumps from 0.64 to 0.78). There are two conceivable monolayer organisations that could account for this value being so close to the value for homo PEO. Either the PEO/water interactions are more enhanced for the graft chain due to further stretching of the graft into the subphase or more realistically that substantially more mobile PEO chains are populating and dominating the near surface. The latter suggestion agrees well with results from surface tension studies as the low value of surface tension observed indicated an excess of PEO at the surface for the 5 % solution. This result confirms earlier experimental findings since the surface tension values do not vary significantly either as the PEO concentration changes between 0.1 and 2.0 % PEO.
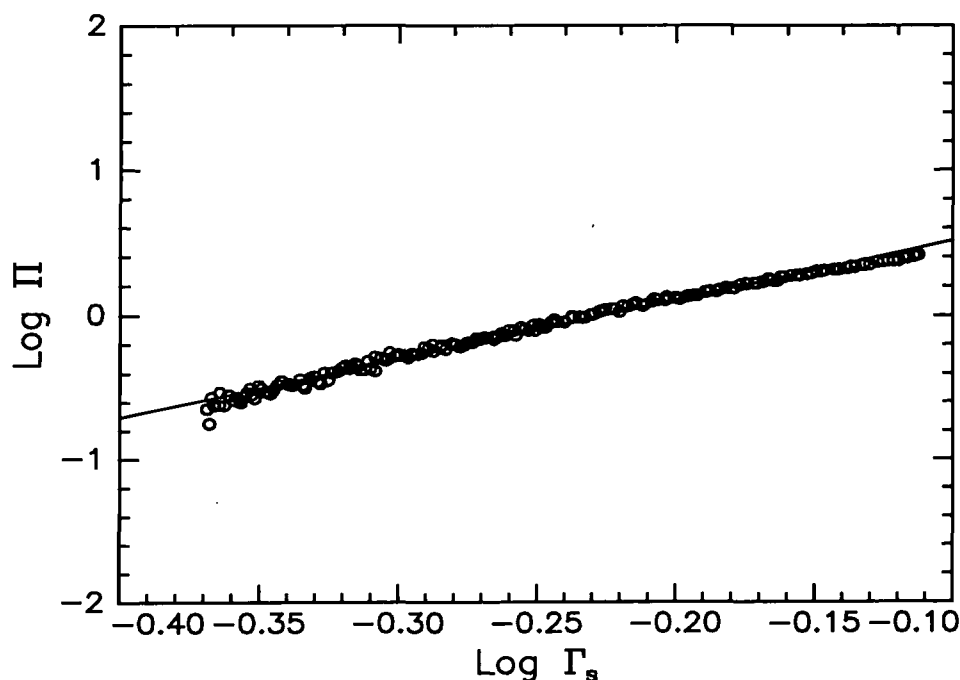

Figure 5.5.5. Typical example of a least squares fit to the increasing linear portion of the double logarithmic surface pressure isotherm for *hn25* to extract y and υ.

Section 5.6   Conclusions

Surface pressure isotherms have been measured for thin films of the series of graft copolymers prepared on water and four different concentrations of aqueous homoPEO solutions (0.1, 1.0, 2.0 and 5.0 %). The experimental data collected clearly indicate that monolayer behaviour is highly dependent on both the architecture of the spread copolymer and also on the chemical composition of the subphase.

When spread on water the monolayer characteristics of each graft copolymer are very similar to the behaviour of a film of homoPEO at low surface concentrations, but all isotherms begin to deviate at higher surface coverage's (> 0.7 mg m^{-2}). After analysing figure 5.4.3 it is predicted that organisation of the copolymer is independent of the backbone at low concentrations and that the film contains many characteristics associated with homoPEO. When the individual isotherms diverge the relative rate of change in surface pressure decreases and different equilibrium surface pressures are observed depending on the length of the PEO graft. As the degree of polymerisation of the graft increases the equilibrium surface pressure value decreases suggesting that the grafts of longer length adopt a more stretched conformation. Mathematical analysis of the isotherms consolidates such predictions as the PEO/water interactions are thermodynamically favourable and are enhanced as the graft length increases. Calculations of the expansion coefficient and the limiting area per monomer unit provides additional conformation as they reveal that the grafts become less coiled, hence are more solvated and expand as the number of EO monomers increases.

The surface tensions of the individual PEO solutions studied exhibit a dependance on the percentage of homopolymer present since the surface tension decreased exponentially as the quantity of homo PEO increased. The lowest surface tension detected was 53.8 +/- 0.6 mN m^{-1} which is lower than observed for spread films of PEO. This additional reduction is due to the increased hydrophobicity of the near surface layer due to more EO molecules being adsorbed in preference to water molecules, thus reducing the number of favourable EO/water interactions.

It is clear from surface pressure data collected (figure 5.5.2) as a function of surface concentration that monolayer behaviour is significantly influenced not only by the presence

of PEO in the subphase but also on the quantity of homopolymer dissolved. The data collected for the intermediate graft copolymer on each PEO subphase exhibits similar shapes hence the monolayers have similar behavioural characteristics. The magnitude of surface pressures measured is correlated to the volume fraction of PEO in the subphase since the surface pressure increases (decreasing surface tension) with increasing percentage of mobile polymer, which suggests that the quantity of PEO adsorbed on the surface increases. Isotherms reveal that PEO is desorbed from the near surface at low film concentrations and the quantity desorbed PEO is connected to the quantity of mobile PEO in the subphase. As the subphase concentration increases the homopolymer becomes less mobile as there are more chains and hence more polymer interactions at the surface, thus making it more difficult for the polymers to be displaced by copolymer and return to the bulk phase. Entanglements between homopolymers and homopolymer and graft copolymer reduce the mobility of the near surface layer and this rationalises the significant differences in the rates of increase of surface pressure with monolayer compression. The graft chains in the thin film when spread on water easily pack together and penetrate the subphase when compressed, but the rate of change of conformation decreases with increasing quantity of steric hindrance when homopolymer is present. It is postulated that the volume fraction of PEO in the near surface layer increases over the range of surface concentration studied as the mobile polymer concentration increases. This analogy accounts for the observed decrease in equilibrium surface tension values as a function of increasing mobile PEO as the hydrophobicity of the near surface layer increases as the density of PEO increases, leading to a reduction in the energy and therefore tension on the surface.

To conclude, it is clear that the length of the PEO graft chains have a significant influence on the surface pressure isotherms and therefore on the organisation and thermodynamic properties of the copolymer thin films when spread on a water subphase. The presence of free polymer in the subphase alters the characteristics of the spread film to an extent that depends on the percentage of homopolymer.

Section 5.7   References

1   Glass, J. E. *J. Phys. Chem.* **1968** , 4459.

2   Shuler, R. L.;Zisman, W.A. *J. Phys. Chem.* **1970,** *74*, 1523.

3   Henderson, J. A.; Richards, R. W.; Penfold, J.; Thomas, R. K.; Lu, J. R. *Macromolecules* **1993**, *26*, 4591.

4   Kim, M. W.; Cao, B. H. *Europhys. Lett.* **1993**, *24*, 229.

5   Kim, M. W.; Cao, B. H. *Faraday Discussions*, **1994**, *98,* 245.

6   Kawaguchi, M. *Progress in Polymer Science*, **1993**, *18*, 314.

7   Vilanove, R.; Rondelez, F. *Physical Review Letters,* **1980**, *45*, 1502.

8   Poupinet, D.; Vilanove, R.; Rondelez, F. *Macromolecules*, **1989**, *24*, 1496.

9   *Handbook for Chemistry and Physics* CRC Press Inc. **1988**.

10   Sauer, B. B.; Yu, H. *Macromolecules*, **1989**, *22*, 786.

11   Lu, J. R.; Su, T. J.; Thomas, R. K.; Penfold, J.; Richards, R. W. *Polymer*, **1996**, *37*, 109.

Chapter Six

Neutron Reflectometry

Section 6.1   Introduction

Neutron reflectometry has been applied to study the organisation normal to an air-water interface of spread monolayers of the graft copolymers. Additionally, the organisation of a monolayer of *n25* was determined when spread on the surface of an aqueous solution of poly(ethylene oxide). Eleven separate surface concentrations have been studied encompassing the full range of the surface pressure isotherms. The data collected were analysed using two different methods: the optical matrix analysis and the kinematic approximation. When used in conjunction with each other the fitting programs provide a full description of organisation at the air-water interface. A recently developed model independent method based on the Bayesian analysis has also been applied to a selection of the data, to consolidate the model dependent processes.

A brief outline of the experimental procedure is given followed by the results for the air-water interface. In the latter section an overview of the raw data is presented for the different surface concentrations and polymer-subphase contrasts investigated, followed by the results of each fitting procedure. The results are discussed to elucidate the influence of spread surface concentration and graft length.

Section 6.2   Experimental

Eleven different surface concentrations were selected (0.3, 0.4, 0.5, 0.7, 1.0, 1.5, 2.0, 2.5, 3.0, 3.5 and 4.0 mg m^{-2}) to obtain a detailed insight into the effect of monolayer compression on surface organisation when films are spread on a pure water surface. The surface concentrations selected correspond to constant surface pressures and encompass a full range of the surface pressure isotherm as indicated in figure 6.2.1.

Selective deuteration of the PEO graft allowed three sets of contrasts to be obtained for each surface concentration investigated: part deuterated copolymer on null reflecting water (nrw), part deuterated and fully protonated copolymer on D$_2$O. The backbone was unfortunately not available in a deuterated form therefore the six contrasts required for a full kinematic approximation were not available. Nonetheless a partial kinematic approximation was applied.
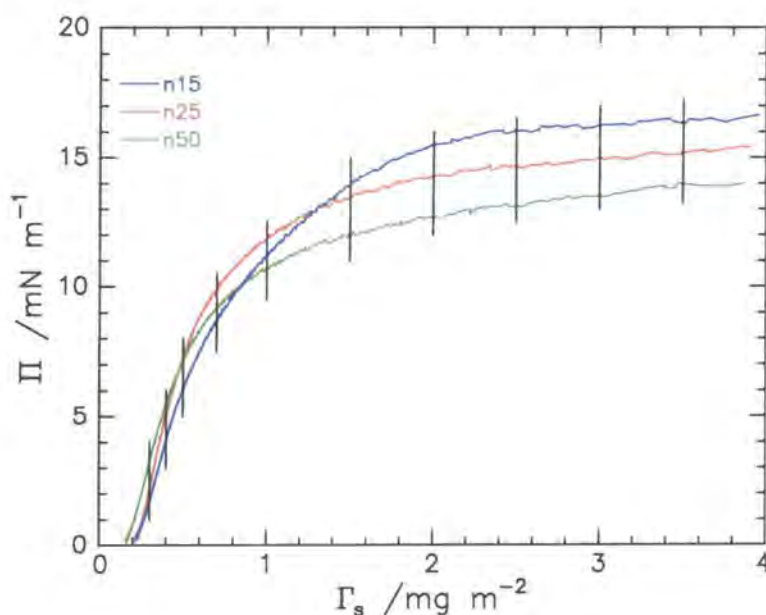

Figure 6.2.1. Surface pressure isotherms for all copolymers at the air-water. The lines on each plot represent the surface concentrations where neutron data was collected.

Section 6.3   Water Subphase

6.3.1   Reflectivity Data

Reflectivity profiles were obtained for the eleven separate surface concentrations for each graft copolymer as outlined in section 6.2. Rather than reproduce the reflectivity profiles for each of the systems studied, this section will concentrate on the results for the *n25* copolymer and the findings for *n15* and *n50* will be summarised subsequently. The *n25* copolymer/subphase system is representative of the general trends of the series of copolymers hence all remarks made here in reference to *n25* are applicable to all three materials. Results from each analysis method are presented separately where the fitting procedure and models adopted to describe the near surface distribution are outlined. The influence of monolayer compression and graft length on the molecular arrangement at the surface is discussed finally and the results are compared to recent theoretical predictions, but first, a general discussion of the characteristics pertinent to all reflectivity profiles is given.

6.3.1.1 Characteristics of Reflectivity Profiles

All profiles exhibit a rapid fall off in the coherently reflected signal with increasing scattering vector Q and the signal becomes coincident with the incoherent background at $Q \approx 0.2\text{-}0.25$ Å^{-1} for D_2O subphases, and $Q \approx 0.15\text{-}0.2$ Å^{-1} for the nrw subphase. Such behaviour is typical of neutron reflectometry work and is due to the dependence of the reflectivity (R(Q)) on Q, i.e. $R(Q) \propto Q^{-4}$. It was observed that the background signal is larger for the nrw subphase than that for D_2O, and in some cases circa three times greater. This large difference arises from the high incoherent scattering cross-section of the hydrogen nuclei present in nrw. It was also noted that the two reflectometers used to collect data in this study (CRISP and SURF) gave rise to different background reflectivity signals, CRISP being slightly higher as it has the poorer resolution. Therefore due to the

184

inconsistency of the background signal all profiles in the remainder of the discussion will have the background signal subtracted.

The surface concentration dependence on reflectivity for *n25* copolymer as a function of Q is exemplified in figures 6.3.1-6.3.3 for a selection of the part deuterated material on nrw, fully protonated and part deuterated on D_2O reflectivity profiles respectively. The reflectivity profile for a clean D_2O surface is overlaid when the subphase is D_2O for comparative purposes.

It is evident from the three plots that the reflectivity profiles are relatively featureless, i.e. there are no fringes, as the reflectivity falls off smoothly with Q until the signal reaches the incoherent background where the data become scattered. This behaviour suggests that there are no sudden changes or discontinuities in scattering length density. The reflectivity data for the part deuterated material spread on nrw increases with surface concentration due to the increased quantity of deuterated PEO in the near surface. The deuterated PEO is essentially the only source of reflectivity for this copolymer-subphase combination.
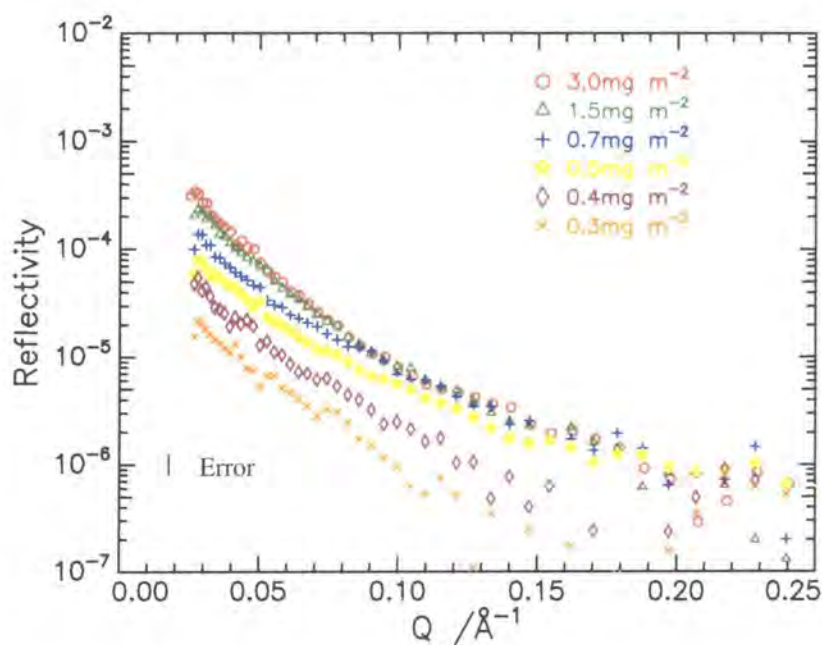

Figure 6.3.1. Reflectivity data for a range of surface concentrations for the part deuterated *n25* copolymer spread on nrw.
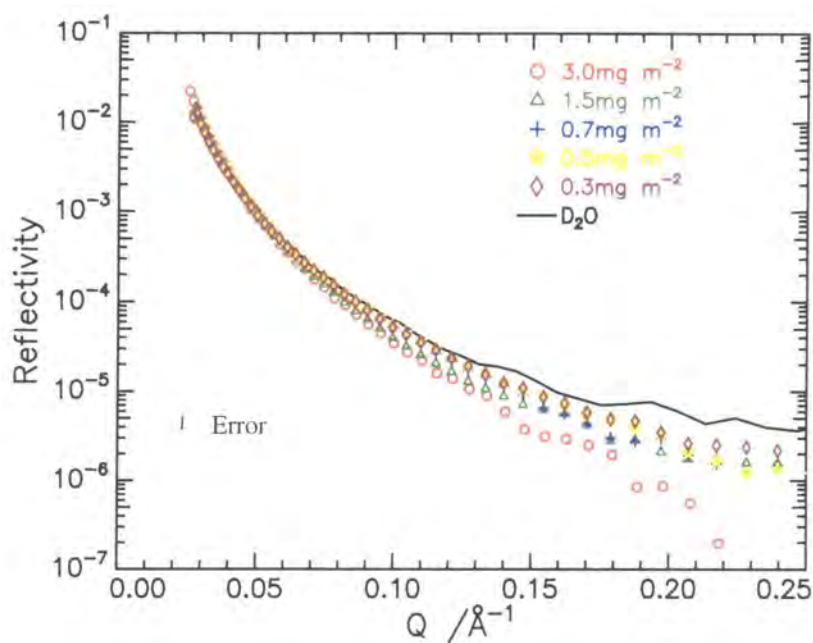
Figure 6.3.2. Reflectivity data for a range of surface concentrations for the fully protonated *n25* copolymer spread on D_2O.
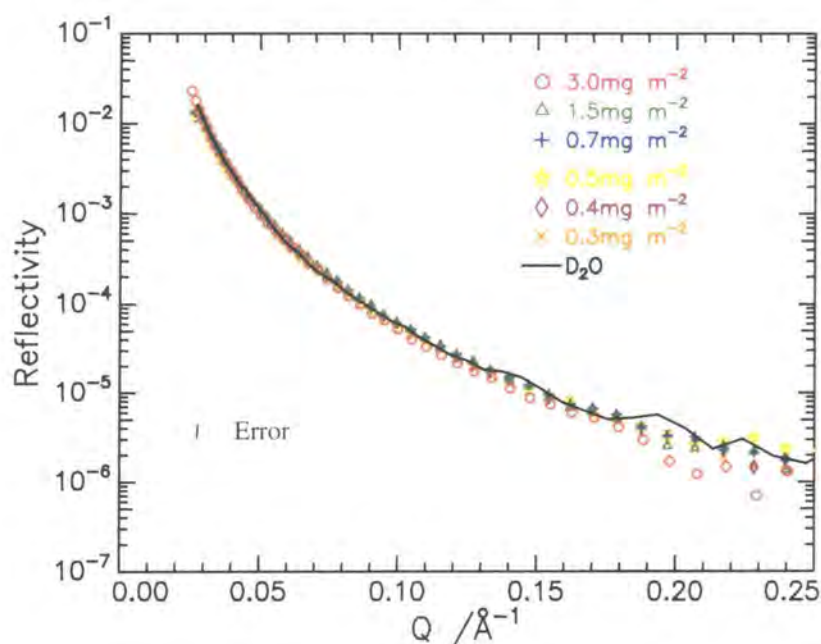

Figure 6.3.3. Reflectivity data for a range of surface concentrations for the part deuterated *n25* copolymer spread on D_2O.

For copolymers spread on D_2O, the subphase reflectivity is dominant and the changes due to the presence of a polymer film can be subtle. However, the reflectivity is slightly depressed when both graft copolymers (deuterated and fully hydrogenated) forms a monolayer over the Q range 0.1 Å^{-1} $< Q < 0.2$ Å^{-1} due to the presence of a greater number of weak reflecting protonated species. When the spread copolymer is fully protonated the reduction in the reflectivity compared to a pure D_2O subphase is distinct. Even though the effects of the spread layer are rather more subtle than when polymer is spread on nrw, differences are evident as the surface concentration changes. As the monolayer is compressed the greater the reduction in reflectivity from that of a clean D_2O surface, evidently the immediate surface layer contains increasingly more protonated polymer. This behaviour is apparent even at low surface concentration as depicted in figure 6.3.2. The reflectivity for the part deuterated/D_2O combination is very similar to that of the clean D_2O subphase (solid line in figure 6.3.3) because the small percentage of hydrogenous backbone present produces an almost negligible reduction in the reflectivity as it only scatters neutrons weakly (0.89×10^{-6} Å^{-2}). Furthermore the scattering length density of the deuterated graft (6.33×10^{-6} Å^{-2}) is extremely close to that of the bulk subphase 6.35×10^{-6} Å^{-2} hence these components are indistinguishable.

To determine whether the graft length has any influence on the near surface distribution the reflectivity profiles obtained for the part deuterated material on nrw (figure 6.3.4) and for the fully protonated material on D_2O (figure 6.3.5) for each copolymer are compared at a surface concentration of 2.0 mg m^{-2}. From the data collected on nrw it is evident that the reflectivity curve increases in intensity with graft length, behaviour indicative of the increasing quantity of deuterated material at the near surface as the number of deuterated EO monomer units rises from 15, to 25 and 50 (for material *n15*, *n25* and *n50* respectively). The reverse trend in reflectivity is observed for the protonated copolymer film as the signal is depressed with increasing graft length, as the near surface D_2O molecules with high scattering length density are displaced.
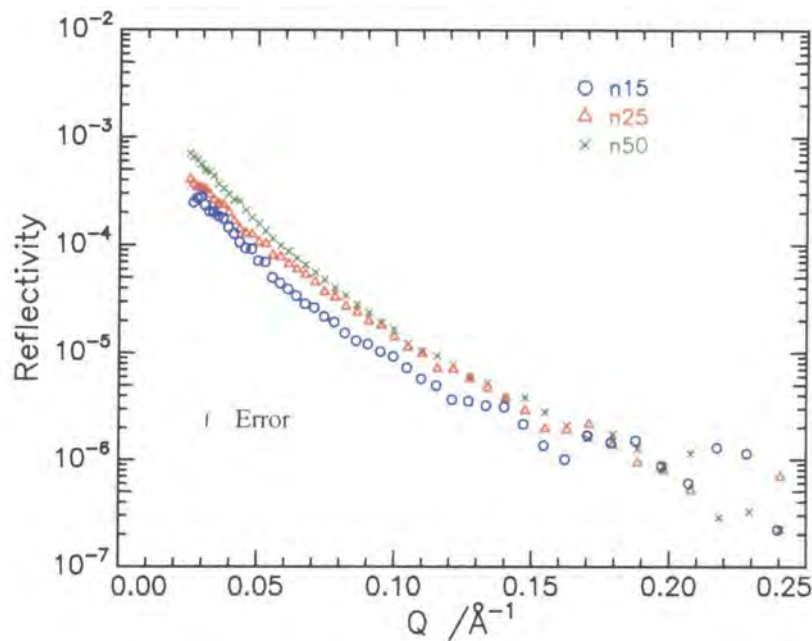
Figure 6.3.4. Influence of graft length for all part deuterated copolymers spread on nrw at 2.0 mg m^{-2}.
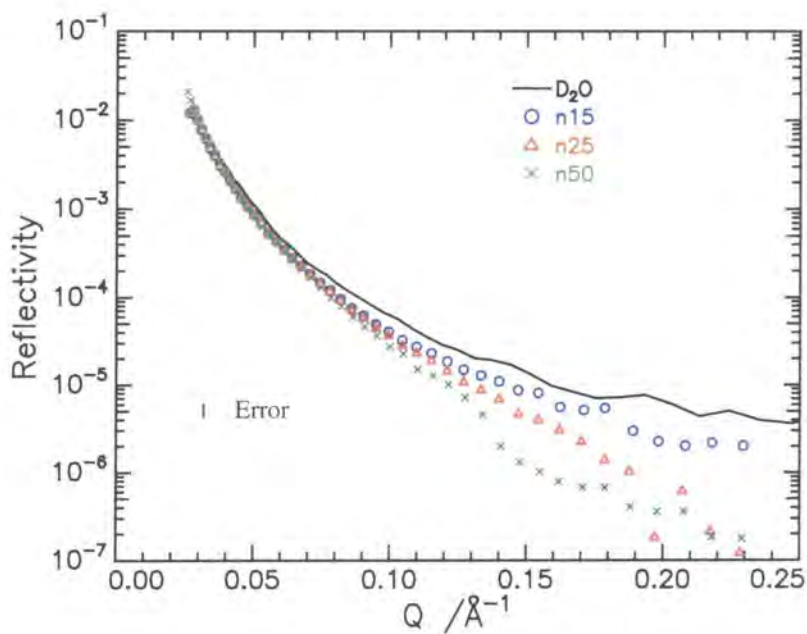

Figure 6.3.5. Influence of graft length for all fully protonated copolymers spread on D$_2$O at 2.0 mg m^{-2}.

6.3.1.2 Discussion

It was expected that the reduction in reflectivity would be proportional to the amount of protonated material present on the surface, however the dependence was not so straightforward. Initially at low surface concentrations the experimental reflectivity behaved as expected, i.e. the reflectivity decreased with increasing surface concentration, however the decrease was non-uniform. Moreover a higher surface concentrations the reflectivity remained roughly constant and a minima was observed at circa 0.2 Å^{-1}. In order to obtain an understanding of this behaviour the reflectivity was expressed using the kinematic approximation (equation 6.3.1) where the difference between the scattering length densities of the clean surface and polymer covered surface can be identified.

$$R(Q) = \frac{16\pi^2}{Q^4}\left(\Delta\rho - 4\rho_d(\Delta\rho - \rho_d)\sin^2(Qd/2)\right) \qquad \textbf{Equation 6.3.1.}$$

where ρ_d and d are the scattering length density and thickness of the monolayer respectively and $\Delta\rho$ is the difference in scattering length densities between the upper and lower phases (i.e. air and water in this study): $\Delta\rho = 6.35\times10^{-6}$ when the subphase is D_2O and $\Delta\rho = 0$ when the subphase is nrw. For the case where $Q = \pi/d$ the kinematic expression reduces to;

$$R(Q) = \frac{16\pi^2}{Q^4}(2\rho_d - \Delta\rho)^2 \qquad \textbf{Equation 6.3.2.}$$

It is clear from equation 6.3.2 that the reflectivity will be at a minimum when the squared term (in parenthesis) is at a minimum value. With this in mind the maximum reduction in reflectivity occurs when the scattering length density of the surface, or monolayer, is half that of the subphase when the subphase is D_2O, i.e. when $\rho_d = 3.18\times10^{-6}$ Å^{-2}. To help in interpreting the experimental data reflectivity profiles have been simulated for model systems.

189

Figure 6.3.6 (with no background signal) shows such a series of reflectivity profiles where a model monolayer is spread on D_2O and consists of a single uniform layer of thickness (20 Å) with a variable scattering length density. It is clear from this diagram that the reflectivity decreases as the scattering length density is initially reduced from that of a clean D_2O surface until a minimum is reached when $\rho_d = 3.18 \times 10^{-6}$ Å^{-2}. As ρ_d decreases further (i.e. the spread surface concentration of low reflecting polymer increases) the reflectivity profile tends towards the pure D_2O profile again due to the symmetry inherent in equation 6.3.2. In figure 6.3.6 the profiles for $\rho_d = 4.18 \times 10^{-6}$ Å^{-2} and $\rho_d = 2.18 \times 10^{-6}$ Å^{-2} are coincident, and likewise a model with $\rho_d = 5.18 \times 10^{-6}$ Å^{-2} gives and identical profile as a film with $\rho_d = 1.18 \times 10^{-6}$ Å^{-2}.

This pattern observed introduces ambiguities when fitting reflectivity data and emphasises the need to check the validity of the model adopted. The reflectivity curve for $\rho_d = 3.18 \times 10^{-6}$ Å^{-2} passes through a minimum value at $Q = 0.16$ Å^{-1}. On solving equation 6.3.2 it was expected that the reflectivity would become zero when minimised at $Q = \pi/d$. This difference is due to the kinematic expression being only a first approximation to the reflectivity. The validity of the minimum value observed in the simulated profiles is confirmed by substituting $d = 20$ Å into $Q = \pi/d$, and a Q value of 0.157 Å is returned. The trend highlighting the reflectivity dependence on the scattering length density of the spread layer is also present (see figure 6.3.7) where an incoherent background signal of 2.5×10^{-6} Å^{-2} has been included. This value is typical of the background signal observed experimentally in this study and is included here to exemplify the extent of reflectivity detail and thus structural information that is lost due to the intensity of the incoherent background signal.
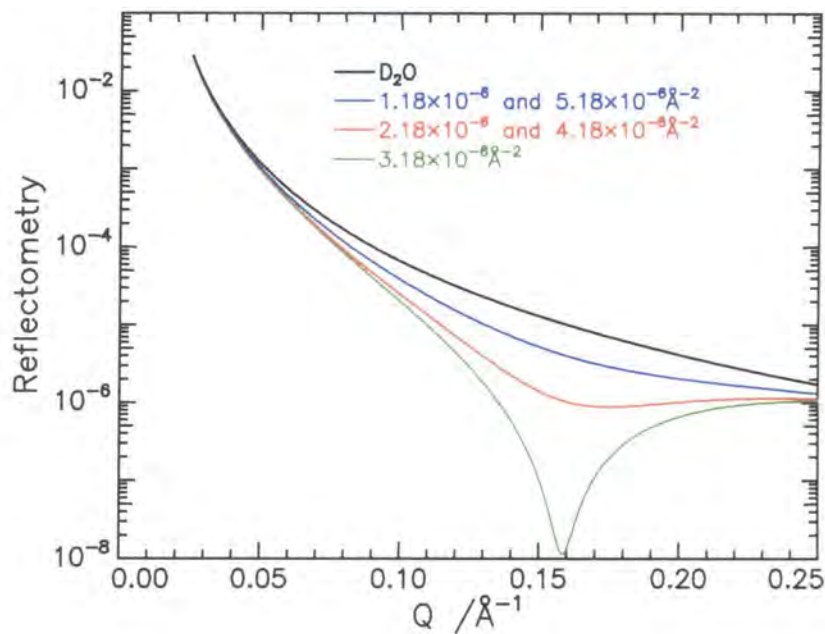
Figure 6.3.6. Simulated reflectivity profiles for a film spread on D_2O of thickness 20 Å with variable scattering length densities.
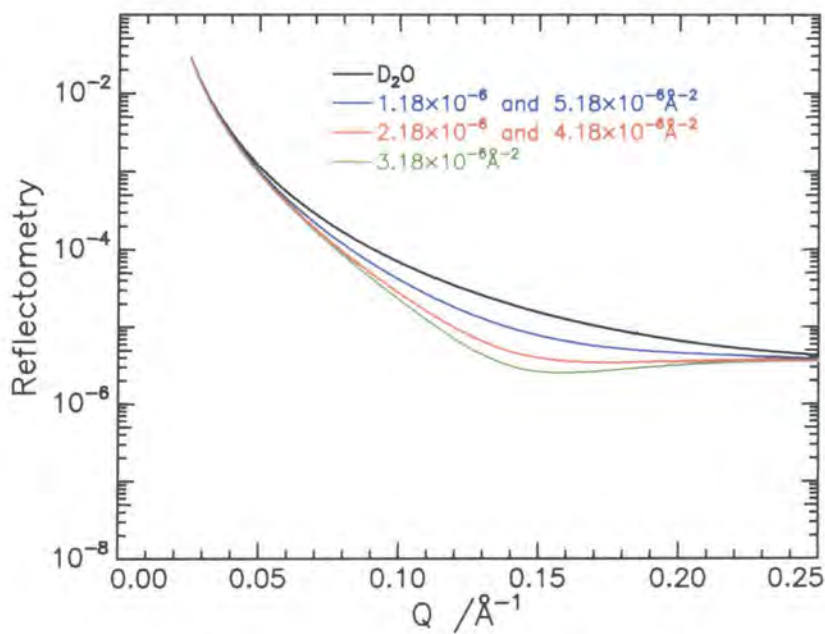

Figure 6.3.7. Simulated reflectivity profiles for a film spread on D_2O of thickness 20 Å with variable scattering length densities and a background reflectivity = 2.5×10^{-6} Å^{-2}.

It is also instructive to simulate reflectivity profiles for fixed scattering length density (4×10^{-6} Å^{-2} - average value found for experimental data) and examine the effect of varying the layer thickness between 10 and 50 Å. The results from such simulations are summarised in two plots, figure 6.3.8 where the reflectivity profiles are presented in their raw form, and in figure 6.3.9 where the incoherent background signal has been taken into account (background signal again is typically 2.5×10^{-6} Å^{-6}). Both plots reveal that the reflectivity profile is depressed from that of a clean D_2O surface even for a film of low thickness (in this example 10 Å). As the thickness increases further a minimum in the reflectivity is observed, and for a film of thickness 50 Å two minima are detected in the Q range presented here. Similar characteristics are observed in the data when the background signal is incorporated into the model, as in both sets of data the position of the minima observed shifts to lower Q values with increasing layer thickness.

The characteristics identified in the simulated profiles can be related to the experimental data collected and used as a first approximation to explain the phenomena observed in the copolymer systems. For the protonated species spread on D_2O the reduction in the reflectivity is non-uniform (figure 6.3.2) with increasing spread copolymer concentration. This trend suggests a thickening of the interfacial film with increasing surface concentration. However the increase is not proportional to the quantity of polymer on the surface, suggesting that the experimental behaviour is complex. Additionally a small minima is present in the experimental data at 3.0 mg m^{-2}, possibly representative of the polymer layer extending into the subphase at high surface concentration. Therefore evidence indicates that a combination of increasing scattering length density and thickening of the layer is responsible for the changes in reflectivity with increasing surface coverage.

Films spread on nrw have distinctly different reflectivities compared to those spread on D_2O. The coherent scattering length of both the upper and lower phases are zero therefore the $\Delta \rho$ term in equations 6.3.1 and 6.3.2 is zero. Thus the reflectivity profiles should scale directly with scattering length density and thickness. A second set of reflectivity profiles were simulated where the subphase is nrw and the scattering length density and layer thickness of a simple model layer were varied in turn.

Figure 6.3.8. Simulated reflectivity profile for a film spread on D_2O of scattering length density 2×10^{-6} Å^{-2} and variable layer thickness.
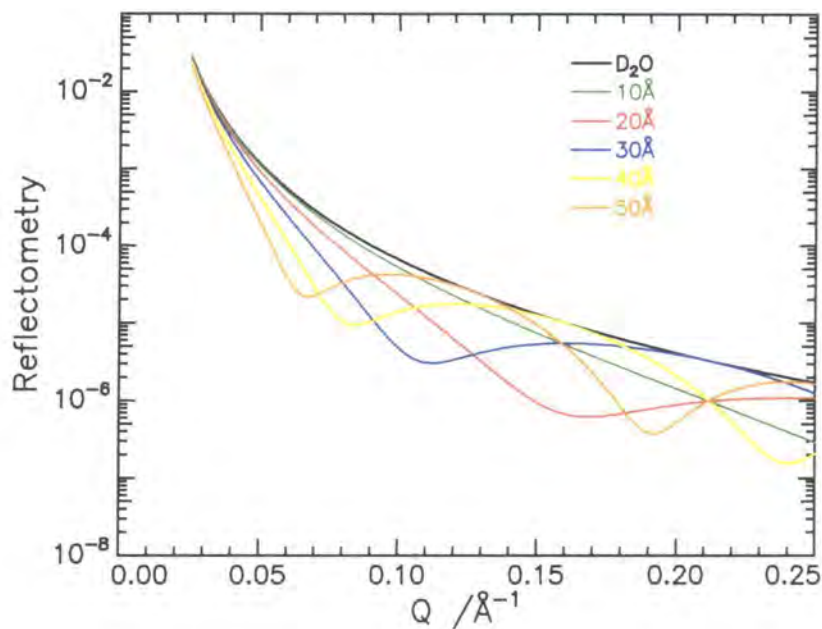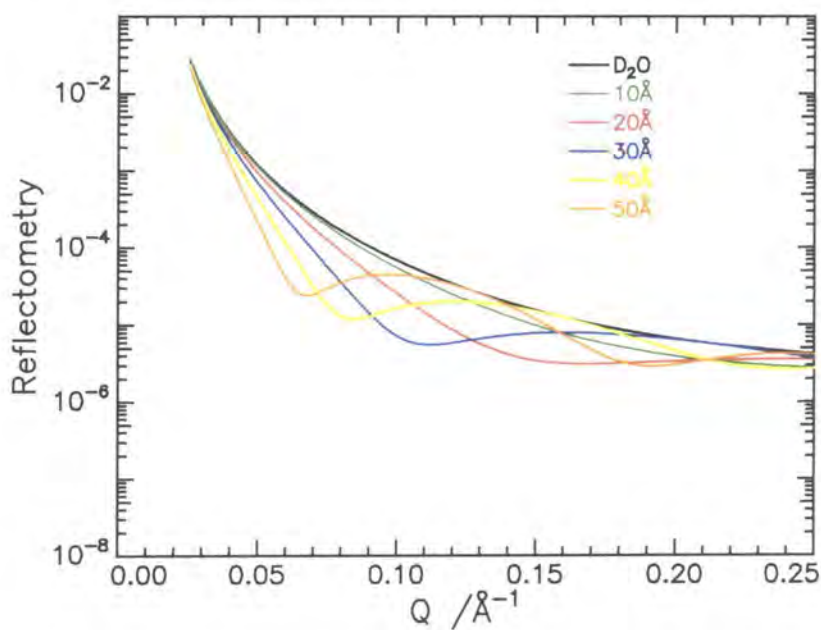

Figure 6.3.9. Simulated reflectivity profile for a film spread on D_2O of scattering length density 3×10^{-6} Å^{-2} and variable layer thickness with a background reflectivity $= 2 \times 10^{-6}$ Å^{-2}.

Firstly the scattering length was varied in 1×10^{-6} Å^{-2} increments from 1×10^{-6} Å^{-2} to 6×10^{-6} Å^{-2} while the thickness of the layer was set at 20 Å and the results from the simulations are given in figure 6.3.10 (raw reflectivity data) and 6.3.11 (incoherent background subtracted). Unlike the previous contrast the reflectivity profile continually increases in magnitude with increasing scattering length density of the model monolayer, as this is the only source of reflectivity in this copolymer/subphase contrast. All profiles have identical shape, decay smoothly as a function of Q and are offset from each other along the reflectivity axes. The data with the incoherent background included, figure 6.3.11, exhibit identical trends at low Q ($0.0255 \leq Q \leq 0.1$ Å^{-1}), but when the reflectivity signal reaches that of the incoherent background detailed structural information is lost and this limits the useful useable Q range.

The profiles in figure 6.3.12 exemplify the effect of changing the monolayer thickness on the reflectivity profile while the scattering length density is maintained at 3×10^{-6} Å^{-2}. As the thickness of the monolayer increases a series of minima are introduced to the profile in an identical manner as the data simulated using D_2O as the subphase. The position of the minima appears to shift to lower Q as the layer dimension increases. At the highest thickness simulated here multiple minima in the profile are evident. Again an incoherent background signal (5×10^{-6} Å^{-2}) has been incorporated into the simulation and these results are given in figure 6.3.13 where an identical response to layer thickening is observed.

Analysing the trends in the reflectivity profile for the part-deuterated copolymer/nrw contrast reveals that at low surface concentrations the reflectivity signal increases as the monolayer is compressed suggesting that an increase in scattering length density is responsible for such variations. At higher surface concentrations a small minima is observed, which indicates a thickening of the spread monolayer.

Overall the evidence provided by both sets of simulations (nrw and D_2O subphase) is confusing as it appears that one factor cannot be identified to be solely responsible for the trends observed in the reflectivity as a function of surface concentration. The characteristics of the experimental data do not vary proportionally to the trends exhibited by either the scattering length density or layer thickness alone indicating that the molecular

rearrangements within the monolayer are non-uniform and are due to changes in both parameters. The vital point to appreciate is that the surface film may be composed of multiple layers and that those dominating the reflectivity may differ. In the situation where the monolayer is spread on a nrw subphase the deuterated EO molecules are solely responsible for the reflectivity. In contrast when the subphase is D_2O subphase, the reflectivity is driven by the D_2O molecules and is depressed from that of a clean D_2O due to the presence of the polymer. The reflectivity profile for such a system will reflect the scale over which the scattering length density of D_2O is reduced below 6.35×10^{-6} $Å^{-2}$. Such differences can modify the profile shape to various degrees, thus increasing the difficulty in identifying an exact trend.

It was hoped that by comparing the trends in the simulated and experimental data that first approximations to the nature of the experimental system could be rationalised. Even the simplistic models used show that making such approximations can be prone to artefacts and a more robust analysis protocol must be applied.

Figure 6.3.10. Simulated reflectivity profile for a film spread on nrw of thickness 20 Å and a variable scattering length density.

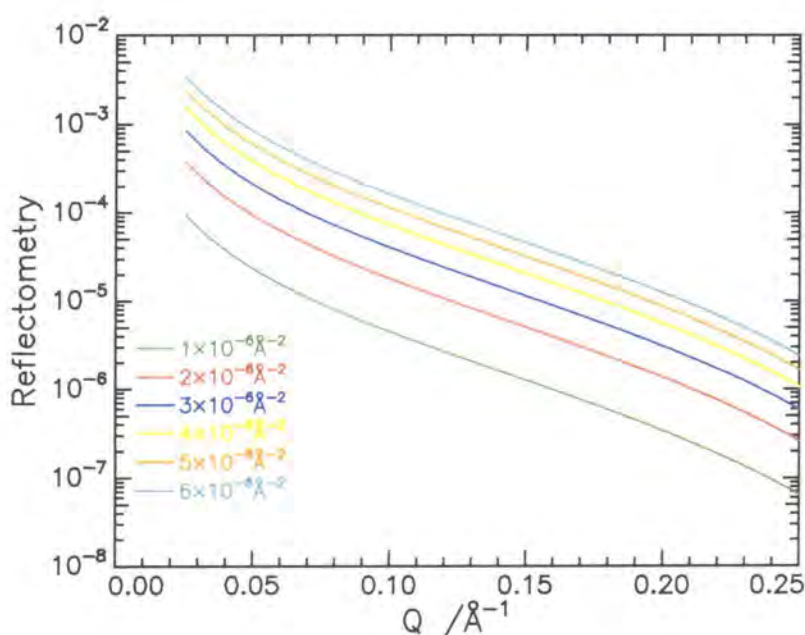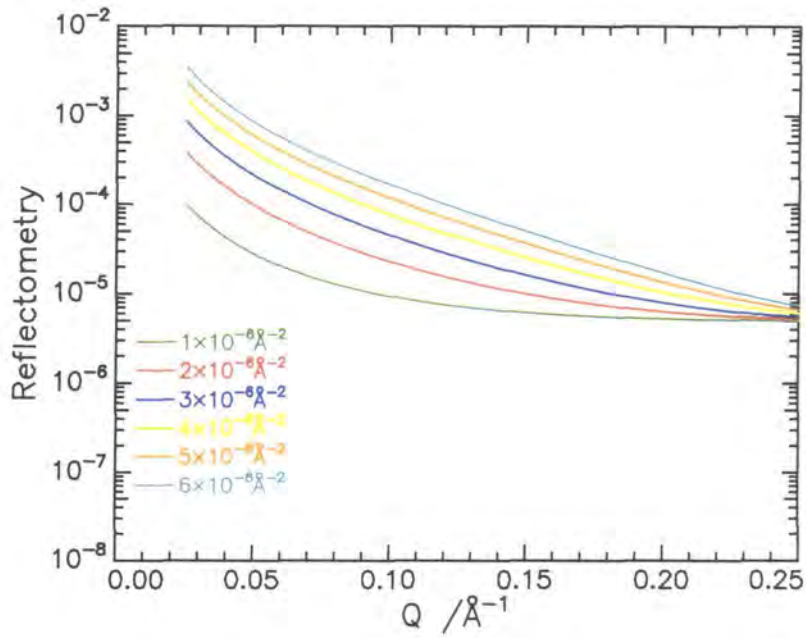**Figure 6.3.11.** Simulated reflectivity profile for a film spread on nrw of thickness 20 Å and a variable scattering length density with a background reflectivity $= 5.0 \times 10^{-6}$ Å^{-2}
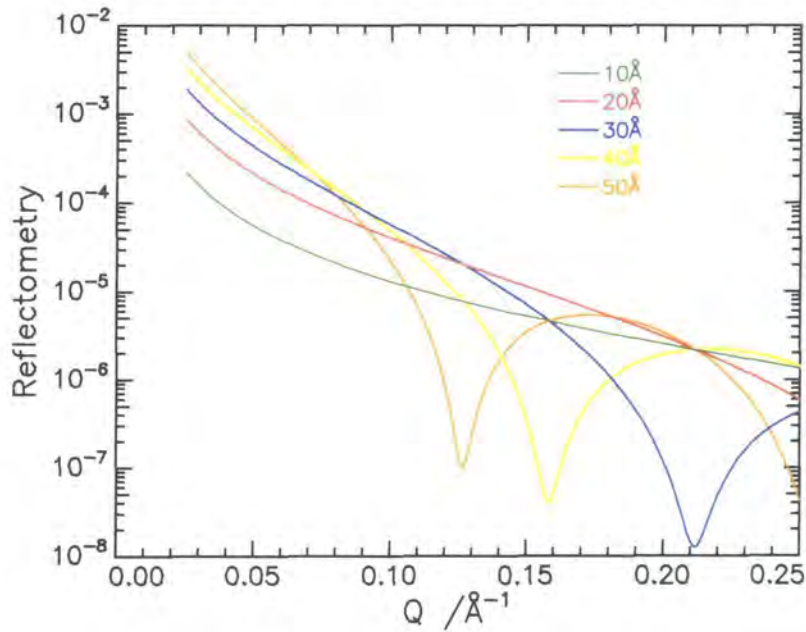
Figure 6.3.12. Simulated reflectivity profile for a film spread on nrw of scattering length density 3×10^{-6} Å^{-2} and variable layer thickness.
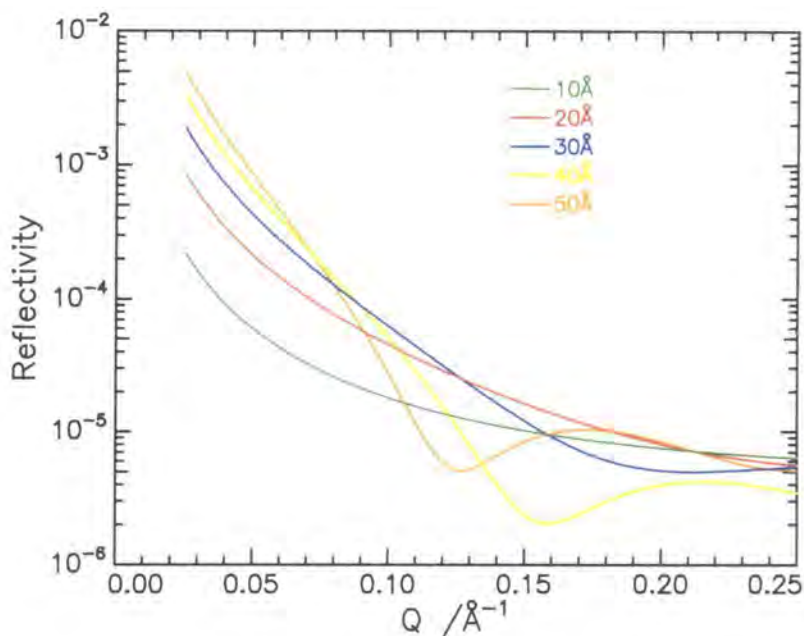
Figure 6.3.13. Simulated reflectivity profile for a film spread on nrw of scattering length density 3×10^{-6} Å^{-2} and variable layer thickness with a background reflectivity of 2.0×10^{-6} Å^{-2}.

6.3.2 Analysis

Quantitative descriptions of all the spread copolymer films have been obtained using the three methods outlined previously in Chapter Two: the optical matrix analysis[1], the kinematic approximation approach[2,3] and also the model independent Bayesian method[4,5]. Application of the complete kinematic approximation was not possible, because the copolymer backbone was not available in a fully (or even part) deuterated form, consequently a simplified approximation has been applied. The Bayesian approach has been applied to data for *n25* to confirm the results from the other two methods for which questions of uniqueness definitely arose.

In the following section the application and the results from each analysis method are discussed in turn for all contrasts using data obtained for *n25*. Identical fitting

procedures were adopted for the remaining materials and the results pertaining to these systems are presented in a concise form following the main discussion.

6.3.2.1 Optical Matrix Analysis

The reflectivity data for each surface concentration has been individually analysed with no priori assumptions. Initially, a single uniform layer model with layer thickness, d, and scattering length density, ρ, was applied and the calculated reflectivity was non-linearly least square fitted to the data by adjusting d and ρ. From the best-fit values, the volume fraction and number density of the species were calculated in addition to the layer thicknesses. The scattering length density for such a uniform layer is related to the volume fraction, ϕ_i, and the scattering length density of each component present, ρ_i, by;

$$\rho = \sum \rho_i \varphi_i$$
Equation 6.3.3.

The number density, n_i, of each component can be obtained from ρ and the scattering length, b_i, of species i via;

$$\rho = \sum n_i b_i$$
Equation 6.3.4.

Knowing n_i, the surface concentration can be calculated for each of the species present in the layer;

$$\Gamma_{s_i} = \frac{n_i m_i d}{N_A} \times 10^{20} \ mg \ m^{-2}$$
Equation 6.3.5.

where m_i is the molecular weight of species i and N_A is Avogadro's number.

The simplest model (uniform layer) was always used initially to produce an acceptable fit to the data, and additional layers subsequently incorporated until good agreement was achieved between the model and experimental reflectivity profiles. To overcome any uncertainty about the uniqueness of the model used to fit the data, reflectivity curves for all three polymer-subphase contrasts collected were fitted concurrently using the same model. Consistent layer dimensions was used as a criterion for the validity of a model for the spread polymer organisation. Furthermore a model was only accepted if the surface concentrations calculated from the fit parameters were in good agreement with the actual amount of copolymer spread. Raw reflectivity profiles were always used in the fitting procedure and the background signal was an adjustable fitting parameter.

In general, it was easier to fit data obtained at higher surface concentrations as the data collected at low monolayer coverage were subject to relatively large signal to noise ratios, especially when the subphase was nrw. It also proved difficult to obtain physically realistic fits to the data for the part deuterated copolymer/D_2O contrast at all film concentrations.

A typical one layer fit is shown in figure 6.4.1a-c for all contrasts of *n25* spread at a surface concentration of 2.0 mg m^{-2} (part deuterated on nrw (a), fully protonated and part deuterated on D_2O (b and c respectively)) where the symbols and solid line represent the experimental and fitted data respectively. The fitted model parameters for each fit are given in table 6.3.1.

Contrast	d_1 /Å	ρ_1 /10^{-6} Å^{-2}
Part deuterated / nrw	26 ± 2	2.83 ± 0.02
Protonated / D_2O	15 ± 1	2.07 ± 0.01
Part deuterated / D_2O	32 ± 2	6.33 ± 0.01

Table 6.3.1. Parameters for a single uniform layer fit for a surface concentration of 2.0 mg m^{-2} for a monolayer of *n25* copolymer.

It is clear from figure 6.3.14 that the model fails to reproduce the data well; moreover, the layer thicknesses returned for each model are not identical even when taking experimental error into consideration. The surface concentration of the copolymer can be calculated from the model parameters, using equation 6.3.5, if it is assumed that only the EO molecules contribute to the fitted scattering length densities obtained for this system. The best fit of the single uniform layer model (for nrw subphase) only accounts for 63 % of the spread amount. Despite repeating the fit with different starting values for ρ and d, improved fits could not be observed. A single uniform layer model is insufficient to reproduce the behaviour of the copolymer system.
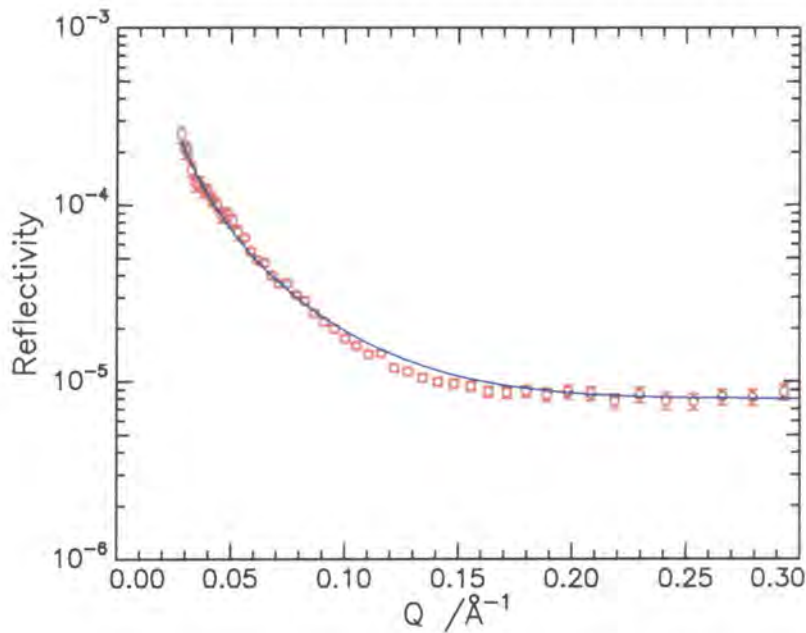
a) part deuterated on nrw

Figure 6.3.14. Single uniform layer fit (solid line) to the experimental reflectivity profile for a spread monolayer of surface concentration 2.0 mg m^{-2} for *n25* copolymer a) part deuterated on nrw, b) fully protonated on D$_2$O and c) part deuterated on D$_2$O.
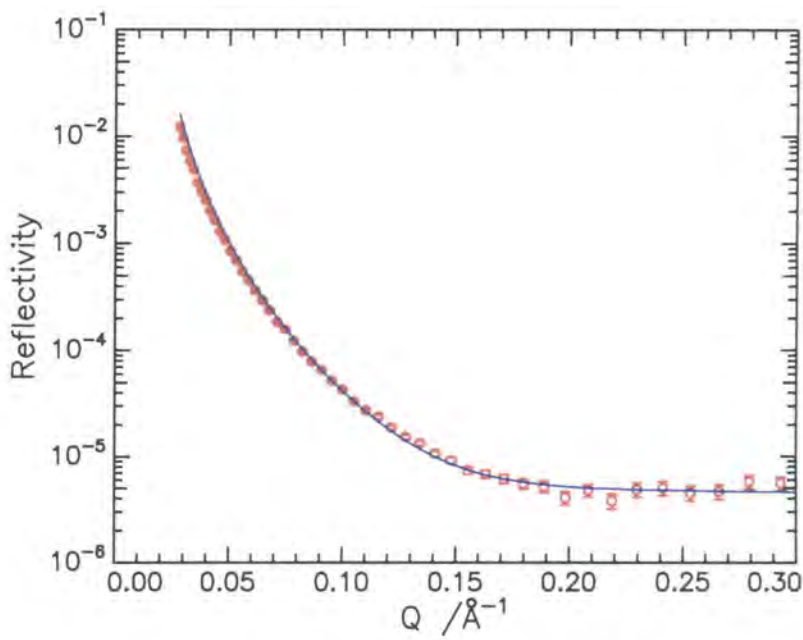
b) fully protonated on D_2O

c) part deuterated on D_2O

In attempt to improve the quality of fit a second uniform layer was introduced. The results from fitting the two layer model to the reflectivity data are presented in figure 6.3.15a-c, where it is clear that the quality of fits have improved, notably where the subphase was nrw. At first glance the models used appear to be successful but the layer dimensions and scattering length densities of the models (table 6.3.2) show that consistent layer dimensions were not returned.
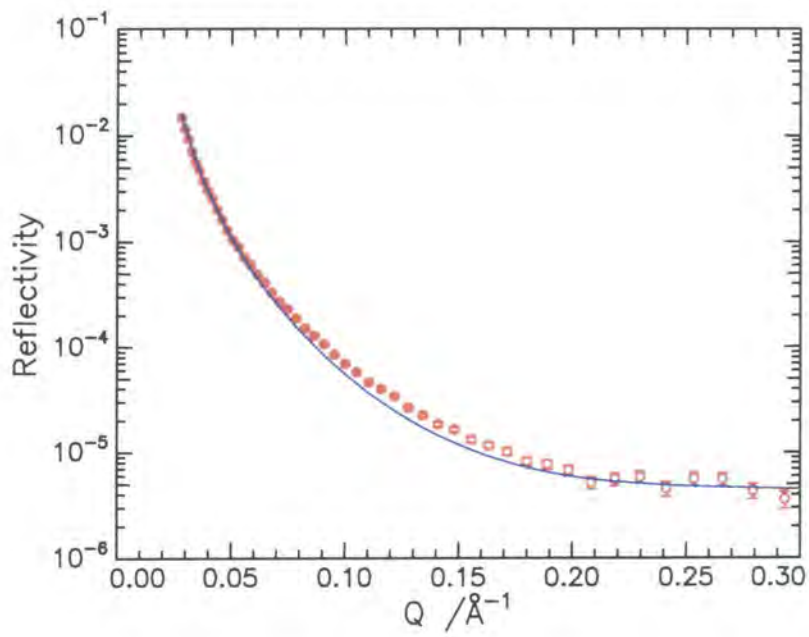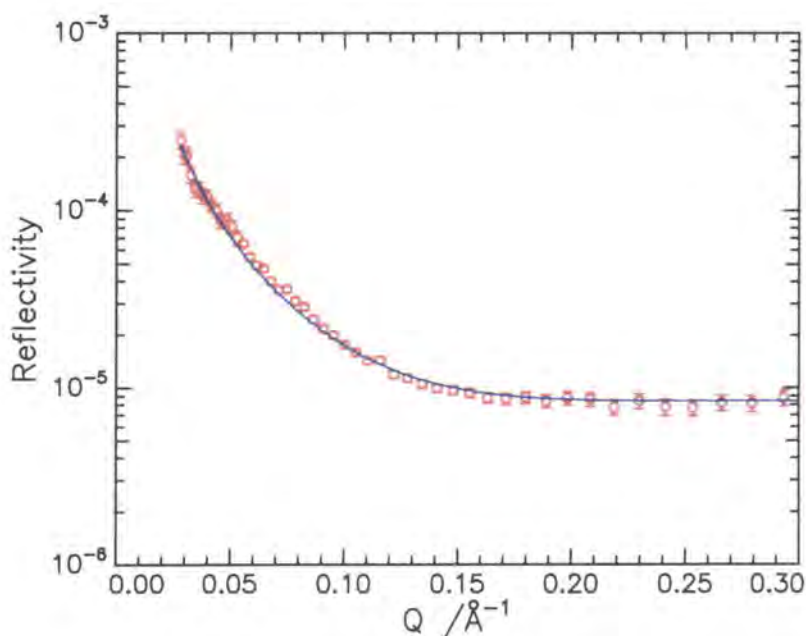

a) part deuterated on nrw

Figure 6.3.15. Double uniform layer fit (solid line) to the experimental reflectivity profile for a spread monolayer of *n25* copolymer at 2.0 mg m^{-2} a) part deuterated on nrw, b) fully protonated on D$_2$O and c) part deuterated on D$_2$O.
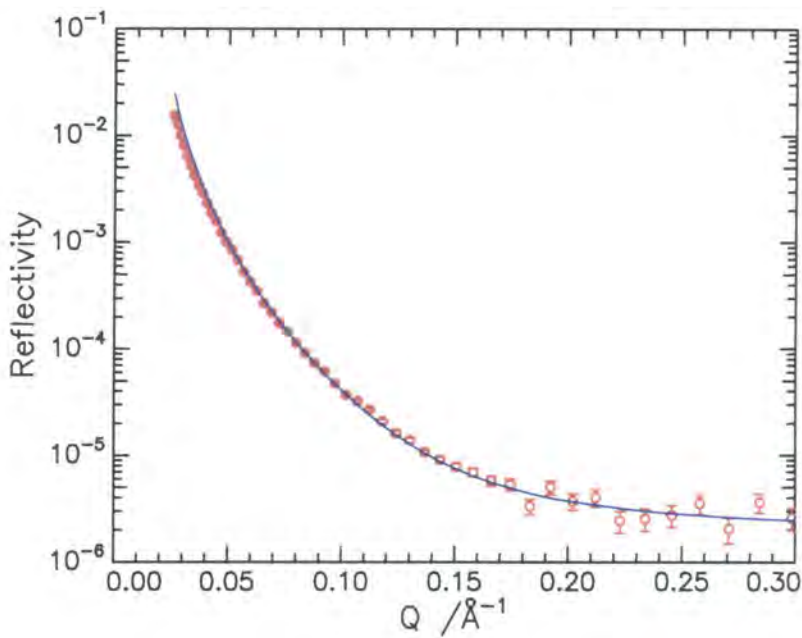
b) fully protonated on D_2O

c) part deuterated on D_2O

203
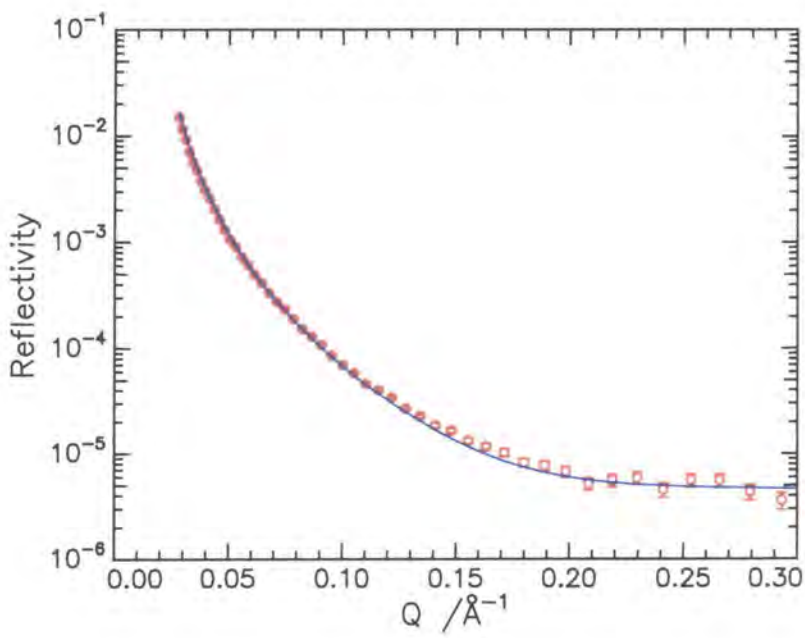
Contrast	Layer	$d/\text{Å}$	$\rho/10^{-6}\,\text{Å}^{-2}$
Part deuterated / nrw	1	7 ± 1	3.54 ± 0.02
	2	23 ± 2	1.95 ± 0.01
Protonated / D_2O	1	10 ± 1	1.12 ± 0.03
	2	19 ± 1	5.85 ± 0.02
Part deuterated / D_2O	1	$6 \pm 1 \pm$	6.21 ± 0.02
	2	28 ± 2	6.34 ± 0.01

Table 6.3.2. Parameters of the double uniform layer fit for a spread monolayer of surface concentration 2.0 mg m^{-2} for *n25* copolymer.

Again the surface concentration calculated from the fitted parameters for the deuterated PEO/nrw contrast only accounted for 66 % of the PEO. The volume fraction of PEO and water were determined from the D_2O subphase contrasts by solving the two simultaneous equations (6.3.6 and 6.3.7), where NB represents norbornene backbone, and the results are presented in table 6.3.3. The surface concentrations extracted depend on which layer thickness is substituted into equation 6.3.5 as the values range from 19-28 Å. In this case the average values were used, but only 56 % of PEO was accounted for. The double uniform layer model therefore does not provide an adequate description of near surface organisation despite the improvement in the fit to the data.

$$\rho_1 = \rho_{hEO}\varphi_{hEO} + \rho_w\varphi_w + \rho_{NB}\varphi_{NB}$$

Equation 6.3.6.

$$\rho_2 = \rho_{dEO}\varphi_{dEO} + \rho_w\varphi_w + \rho_{NB}\varphi_{NB}$$

Equation 6.3.7.

Layer	ϕ_{EO}	ϕ_w	Γ_{sEO}
1	0.88	0.12	0.78
2	0.09	0.91	0.24

Table 6.3.3. Volume fractions obtained from a double uniform layer model for *n25* at a surface concentration of 2.0 mg m^{-2}.

Introducing a further layer produced an excellent fit to all the experimental reflectivity data, as shown in figure 6.3.16a-c for each polymer/subphase contrast again at a surface concentration of 2.0 mg m^{-2}. The model parameters pertaining to the fits are given in table 6.3.4.

Contrast	Layer	$d/\mathring{A}$	$\rho/10^{-6}\,\mathring{A}^{-2}$
Part deuterated / nrw	1	3 ± 1	0.56 ± 0.2
	2	18 ± 2	3.34 ± 0.05
	3	10 ± 1	1.07 ± 0.02
Protonated / D$_2$O	1	4 ± 1	0.61 ± 0.01
	2	17 ± 1	1.04 ± 0.02
	3	12 ± 1	5.66 ± 0.03
Part deuterated / D$_2$O	1	$4 \pm$	0.60 ± 0.02
	2	17 ± 2	6.33 ± 0.01
	3	11 ± 1	6.34 ± 0.01

Table 6.3.4. Parameters of the three uniform layer fit for a spread monolayer of surface concentration 2.0 mg m^{-2} for *n25* copolymer.

It is evident from table 6.3.4 that the layer dimensions extracted from the best fits are identical for each contrast within experimental error. From the scattering length densities obtained, all three contrasts returned similar values for the upper layer. This suggests not only that the composition of this layer was constant, but also the scattering length density of the components in this layer remain unchanged as the polymer/subphase contrasts vary, indicating that this uppermost layer contains the hydrophobic backbone and air only, since the scattering length densities of the other components (PEO and water) vary with each contrast. The values for the second and third layers however differ significantly depending on the contrast studied. For the part deuterated/nrw contrast the scattering length density for both PEO containing layers is high indicating the presence of the deuterated EO species. The magnitude of the scattering length density in the upper layer is greater in

comparison to the lower, suggesting there is a dense layer of deuterated species at the near surface and the EO molecules become more diluted as they extend further into the subphase. The parameters obtained from fitting the protonated copolymer/D_2O contrast are consistent with the idea of graft penetration into the subphase. The scattering length density of the second layer is heavily depressed in relation to the highly reflecting D_2O molecules, thus indicating the majority of the near surface is occupied by hydrogenous EO molecules. The earlier prediction that the extent of graft solvation increases with penetration depth into the subphase is corroborated here also as the scattering length density of the layer is closer to the value for water (6.35×10^{-6} Å^{-2}) in relation to the upper subphase containing layer.
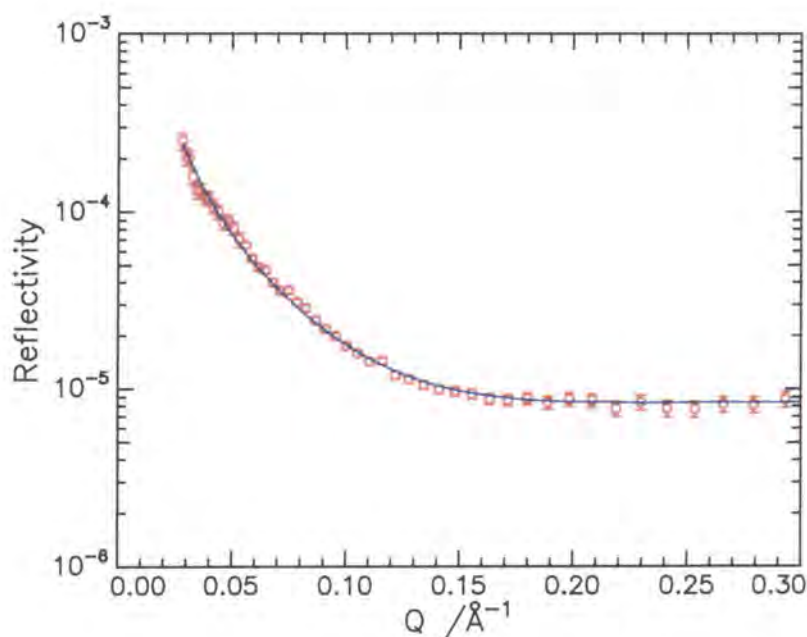
a) part deuterated on nrw

Figure 6.3.16. Triple uniform layer fit (solid line) to the experimental reflectivity profile for a spread monolayer for *n25* copolymer at 2.0 mg m^{-2} a) part deuterated on nrw, b) fully protonated on D_2O and c) part deuterated on D_2O.
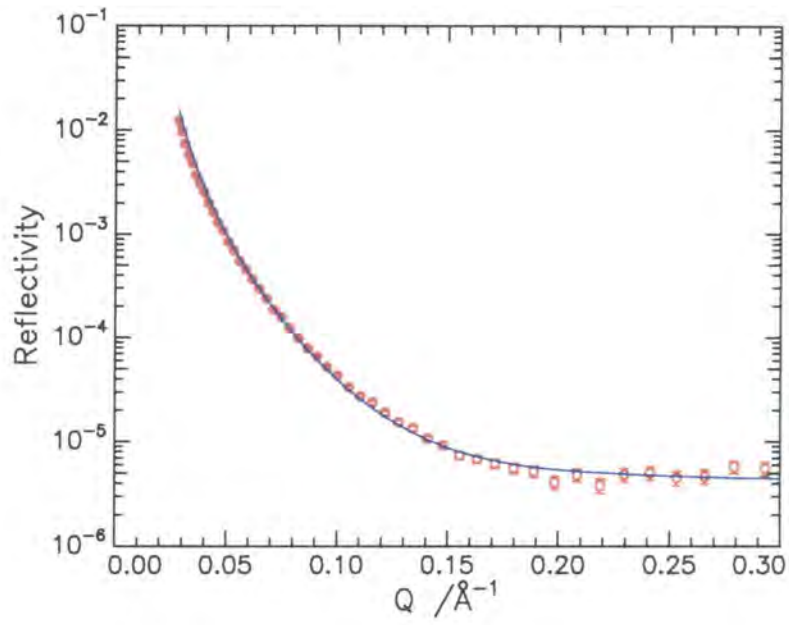
b) fully protonated on D₂O
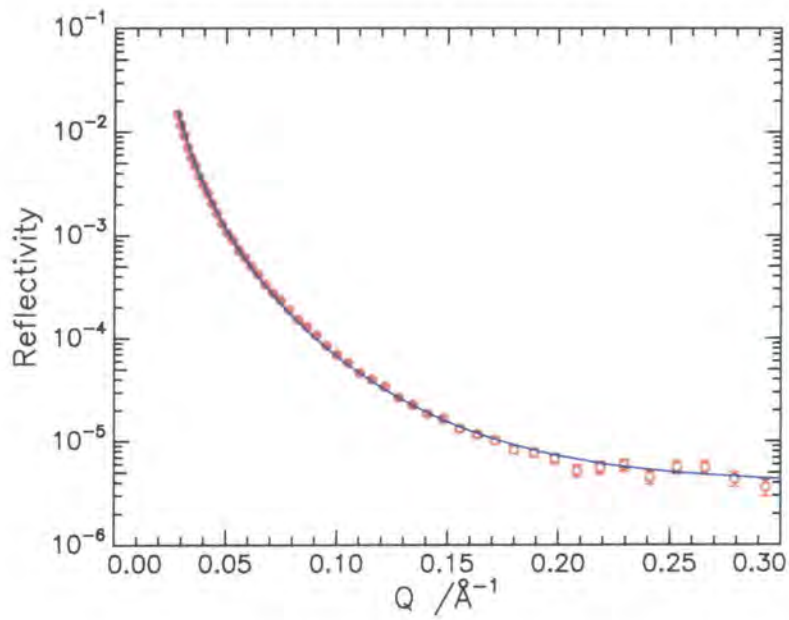
c) part deuterated on D₂O

From these results it was postulated that the hydrophobic backbone predominantly occupies the air phase and forms the uppermost layer allowing the grafts to penetrate the subphase, where the extent of graft dilution increases with extension into the aqueous phase. Assuming the upper layer consists of the backbone and air, while the lower layers contain PEO and water only, then the volume fraction of each component can be easily calculated by solving simultaneous equations and using the fitted parameters given in table 6.3.4. The volume fraction of NB in the uppermost layer was determined by substituting the average scattering length density value for this layer $\rho = 0.59 \times 10^{-6}$ Å^{-2} into equation 6.3.8 where $\rho_{NB} = 0.89 \times 10^{-6}$ Å^{-2}. The remaining layers contained EO and water only and their volume fractions were obtained by solving the simultaneous equations 6.3.9 and 6.3.10.

Layer one

$$\rho = \rho_{NB} \varphi_{NB}$$

Equation 6.3.8.

Layers two and three

h-PEO/D$_2$O contrast

$$\rho = \rho_{hEO} \varphi_{hEO} + \rho_w \varphi_w$$

Equation 6.3.9.

d-PEO/D$_2$O contrast

$$\rho = \rho_{dEO} \varphi_{dEO} + \rho_w \varphi_w$$

Equation 6.3.10.

Layer	d /Å	ϕ_{NB}	ϕ_w	ϕ_{EO}	ϕ_{AIR}	$n_{NB}/10^{-3}$ Å^{-3}	$n_{EO}/10^{-3}$ Å^{-3}	Γ_{NB}/mg m^{-2}	Γ_{EO}/mg m^{-2}
1	4±1	0.44	0	0	0.56	2.20	0	0.18	0
2	17±1	0	0.12	0.88	0	0	12.16	0	1.65
3	11±1	0	0.88	0.12	0	0	1.66	0	0.14

Table 6.3.5. Volume fractions, number densities and surface concentrations obtained from a triple uniform layer model for *n25* at a surface concentration of 2.0 mg m^{-2}.

The results obtained from such calculations and also the number densities of each polymer component (determined using equation 6.3.3) for the surface concentration of 2.0 mg m^{-2} are given in table 6.3.5. The surface concentrations of the individual components were calculated by substituting the model parameters from the table above into equation 6.3.5: $\Gamma_{NB} = 0.18$, $\Gamma_{EO} = 1.65$ in the second layer and $\Gamma_{EO} = 0.14$ in the third layer. The ratio of polymer composition i.e. PEO:PNB is 0.91:0.09, therefore theoretically PEO contributes 1.82 mg m^{-2} and norbornene contributes 0.18 mg m^{-2} to the actual quantity spread. Comparing these values to the individual contributions from the model fit values it was found that the PNB was completely accounted ($\Gamma_{sNB} = 100$ %), in comparison to 98 % of the PEO has been included in the model. Therefore exact agreement between the two surface concentrations for the PEO grafts was not obtained here. Numerous reasons for such behaviour can be suggested, for example error could have been introduced when determining the composition of the synthesised copolymer, which could influence the relative percentage compositions. The problems associated with NR and its difficulty to identify small changes in reflection especially from highly diluted molecules at large penetration depths offers a more feasible explanation. Another possible rationale involves the region of the reflectivity profile that contains the information pertinent to elucidating the interfacial structure (circa 0.2-0.25 Å^{-1} as Q correlates to $2\pi/d$) since in this region the error is high due to the reflectivity signal approaching the background value. The 2 % of PEO not accounted for was therefore attributed to experimental error not to a failure of the model description. An identical fitting procedure was adopted to analyse the reflectivity profiles for all other surface concentrations i.e. the simplest model was always selected initially and complexity only introduced when quality fits were not found. Over the surface concentration range studied all data were satisfactorily fitted with a triple uniform layer model. The results for each of the eleven surface concentrations studied for *n25* are summarised in the following tables: the layer thicknesses, volume fractions and number densities are given in table 6.3.6. In general the NB backbone was always fully accounted for, therefore attention was focussed on the percentage of PEO incorporated in the model and the calculated surface concentrations of PEO from the applied models are compared to the actual quantity spread in table 6.3.7.

Γ_s /mg m^{-2}	Layer	d /Å	ϕ_{NB}	ϕ_W	ϕ_{EO}	ϕ_{AIR}	n_{NB}/10^{-3} Å^{-3}	n_{EO}/10^{-3} Å^{-3}
4.0	1	5 ± 2	0.26	0	0	0.74	1.30	0
	2	27 ± 3	0	0.01	0.99	0	0	13.68
	3	14 ± 2	0	0.81	0.19	0	0	2.63
3.5	1	6 ± 1	0.22	0	0	0.78	1.10	0
	2	23 ± 3	0	0.01	0.99	0	0	13.68
	3	17 ± 2	0	0.82	0.18	0	0	2.45
3.0	1	5 ± 1	0.27	0	0.01	0.73	1.35	0.14
	2	20 ± 2	0	0.01	0.99	0	0	13.68
	3	17 ± 2	0	0.78	0.22	0	0	3.04
2.5	1	5 ± 1	0.34	0	0.03	0.63	1.70	0.41
	2	17 ± 1	0	0.01	0.99	0	0	13.68
	3	16 ± 3	0	0.87	0.13	0	0	1.80
2.0	1	4 ± 1	0.44	0	0	0.56	2.20	0
	2	17 ± 1	0	0.12	0.88	0	0	12.16
	3	11 ± 1	0	0.88	0.12	0	0	1.66
1.5	1	4 ± 1	0.63	0	0	0.40	3.00	0
	2	16 ± 1	0	0.19	0.81	0	0	11.18
	3	8 ± 1	0	0.84	0.16	0	0	2.21
1.0	1	4 ± 1	0.97	0	0	0.03	4.85	0
	2	13 ± 1	0	0.37	0.63	0	0	8.69
	3	7 ± 1	0	0.95	0.05	0	0	0.69
0.7	1	4 ± 1	0.73	0	0	0.27	3.65	0
	2	10 ± 1	0	0.43	0.57	0	0	7.87
	3	6 ± 1	0	0.96	0.04	0	0	0.55
0.5	1	4 ± 1	0.89	0	0	0.11	4.45	0
	2	7 ± 1	0	0.44	0.56	0	0	7.73
	3	7 ± 1	0	0.96	0.04	0	0	0.55
0.4	1	4 ± 1	0.89	0	0	0.11	4.45	0
	2	4 ± 1	0	0.36	0.64	0	0	8.83
	3	6 ± 1	0	0.86	0.14	0	0	1.93
0.3	1	3 ± 1	0.93	0	0	0.07	4.65	0
	2	3 ± 1	0	0.44	0.56	0	0	7.73
	3	5 ± 1	0	0.52	0.08	0	0	1.10

Table 6.3.6. Layer thicknesses, volume fraction compositions and number densities of the individual components from three uniform layers for $n25$.

Γ_{sTOTAL}/mg m^{-2}	Γ_{sEO}/mg m^{-2}	$\Gamma_{sEO\,cal}$/mg m^{-2}	Γ_{sEO}/$\Gamma_{sEO\,cal}$
4.0	3.64	3.27 ± 0.37	0.90
3.5	3.18	2.85 ± 0.37	0.90
3.0	2.73	2.61 ± 0.27	0.96
2.5	2.28	2.12 ± 0.20	0.93
2.0	1.82	1.78 ± 0.08	0.98
1.5	1.37	1.33 ± 0.17	0.97
1.0	0.91	0.86 ± 0.10	0.94
0.7	0.64	0.63 ± 0.10	0.98
0.5	0.46	0.46 ± 0.08	1.00
0.4	0.36	0.35 ± 0.09	0.97
0.3	0.27	0.27 ± 0.08	1.00

Table 6.3.7. Comparison of the calculated surface concentrations of PEO from triple uniform layers for *n25* to the actual quantity spread.

Each surface concentration required a triple uniform layer before the three contrasts returned consistent layer dimensions, which was the first criterion for a good model description. The second criterion was also met as the fraction of PEO accounted for (see table 6.3.7) was always relatively high and ranged between 0.9 and 1.00. Analysis of the calculated volume fractions obtained for each layer have led to the conclusion that the hydrophobic backbone remains predominantly in the air phase and forms the uppermost layer allowing the hydrophilic grafts to penetrate the aqueous subphase at all surface concentrations investigated. The uppermost layer chiefly contains the hydrocarbon backbone and air, and is confined to a thin 3-6 Å layer over the entire surface concentration range. The volume fraction of the air included in this layer increases slightly, albeit with no discernible regularity, as the monolayer is compressed. This increased air content may be due to some 'buckling' of the double bond regions of the hydrocarbon backbone out of the plane of the aqueous subphase surface as the film is compressed. Such a process is schematically given in figure 6.3.17. Evidently this cannot lead to a large increase in the spatial dimensions occupied by the backbone since none is observed. Molecular modelling

of the backbone alone shows that it adopts a helical structure when compressed at the ends of the chains. This may be occurring in the thin spread films as they are compressed and therefore no marked change in the dimensions of the layer would be anticipated. However, it is noted that the scattering length density of the backbone is low and neutron reflectivity will not be very sensitive to small changes in the dimensions of this layer. At this stage the architecture of the copolymer needs to be considered, namely the stereochemistry of the copolymer backbone (see Chapter Four). There is a mixture of stereochemistries of the unsaturated bonds in the hydrocarbon main chain, for the *n25* copolymer 66 % of these bonds are in the *trans* conformation and 33 % in the *cis*.
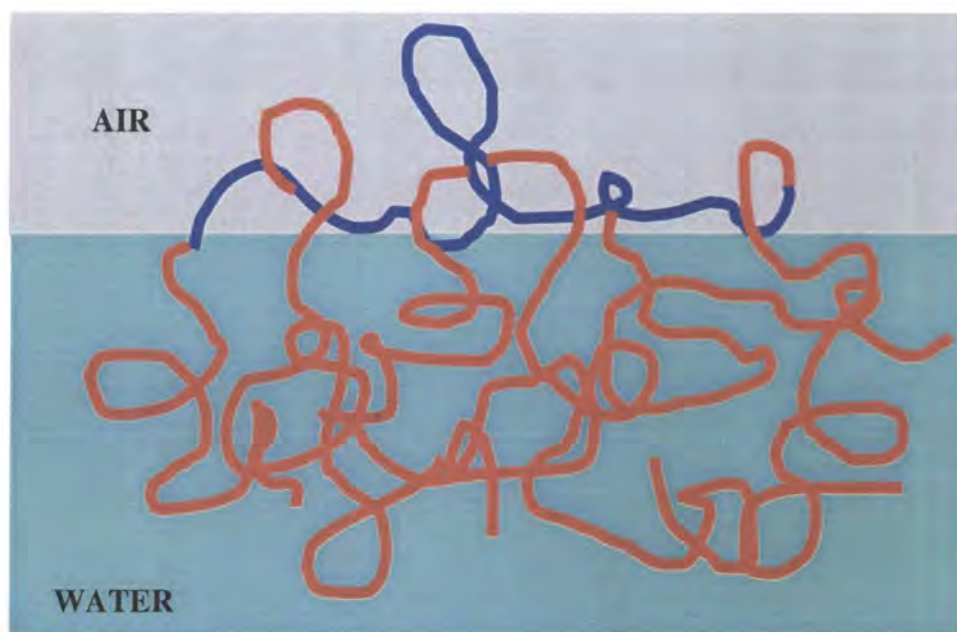
Figure 6.3.17. Sechmeatic representation of the backbone 'buckling' of the backbone at high surface concentrations and the PEO grafts 'curling' over the backbone.

Therefore for all the PEO grafts to penetrate the subphase a portion of the grafted chains must curl over the backbone. The driving force for this presumably arises from the energy minimisation obtained on immersion of the hydrophilic PEO grafts in water, but the concentrations of PEO in the backbone region must be very small since the scattering

length density of the upper layer is low and roughly constant for all contrasts. The remaining two uniform layers contain only PEO and water and their composition and thickness appear to be highly concentration dependent. The upper of these layers (see table 6.3.6) contains a high volume fraction of PEO in comparison to the lower subphase layer, indicative of dilution of the free ends of the grafts as they penetrate deeper into the subphase. As the monolayer is compressed, the thickness of the second layer increases steadily, while the thickness of the third layer increases overall, albeit not in a manner that is completely regular with the increasing surface concentration. The composition of these layers also changes upon compression. The volume fraction of the second layer increases from 0.56-0.91 as the surface concentration increases from 0.3-2.0 mg m^{-2}. Thereafter the volume fractions of this layer remains at a constant value of 0.99 as the monolayer is compressed to the maximum concentration investigated: 4.0 mg m^{-2}. The PEO content of the third layer increases overall from 0.08 to 0.22 at the highest concentration (4.0 mg m^{-2}).

A physical picture of the arrangement predicted from the fits is given by the selected volume fraction profiles given in figure 6.3.18. In these diagrams the distribution of the three components water (blue), hydrocarbon backbone (green) and the PEO grafts (red) are exemplified and the zero point on the x-axis represents the interface position. From these diagrams it is clear that the layer protruding into the air phase contains a high fraction of backbone diluted only by air, the layer thickness remains at circa 5 Å throughout monolayer compression. The volume fraction of the backbone decreases by a factor of approximately two as the surface concentration increases. The remaining layers contain PEO and water only and each layer exhibits a steady increase in thickness, while the volume fraction of EO infact rises with monolayer compression. The volume fraction of PEO in the upper layer is invariably higher than the lower layer, indicating that dilution of EO is greater as the graft explores the water phase.

a) 0.4 mg m^{-2}

b) 1.0 mg m^{-2}
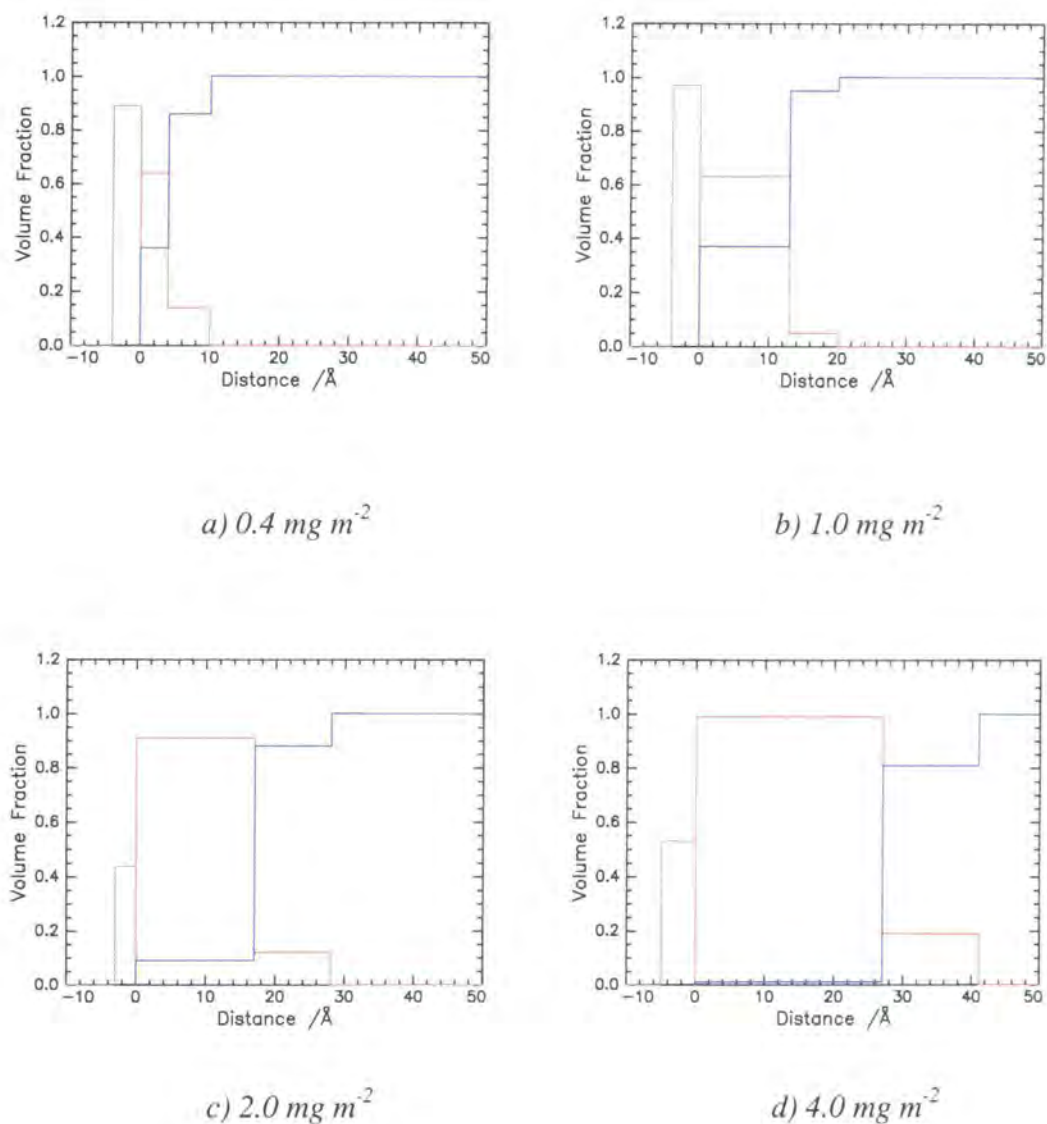
c) 2.0 mg m^{-2}

d) 4.0 mg m^{-2}

Figure 6.3.18. Volume fraction profile for a selection of surface concentrations a) 0.4 mg m^{-2}, b) 1.0 mg m^{-2}, c) 2.0 mg m^{-2} and d) 4.0 mg m^{-2} for *n25* copolymer. Each component is represented individually: backbone (green line), PEO (red line) and water (blue line).

Thus far the discussion of results has focussed on general changes in interfacial organisation as a function of surface concentration. The remainder of this discussion will focus on the dominant structural change, which is the change in PEO layer thickness with monolayer compression. The dependence of subphase penetration on the

surface concentration for *n25* is summarised in figure 6.3.19, where the total PEO layer thickness is plotted against surface concentration.
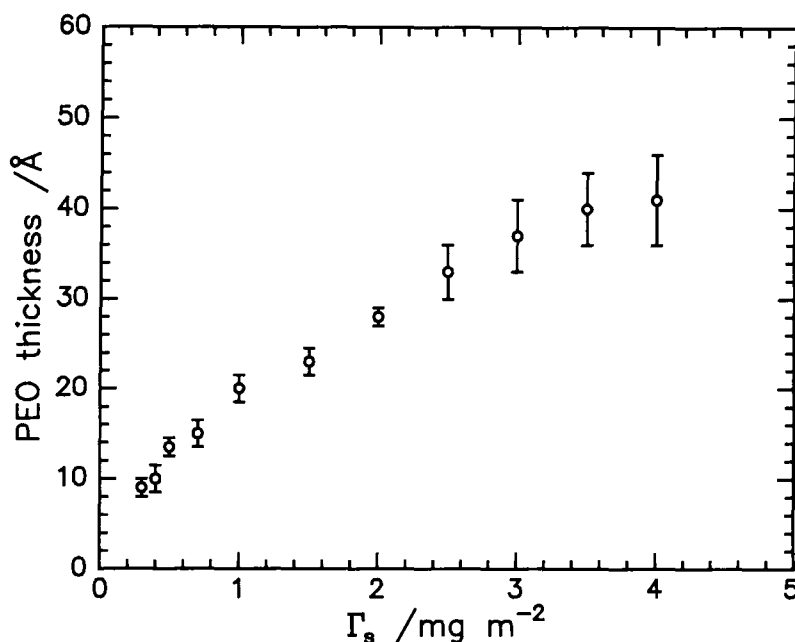
Figure 6.3.19. Plot of PEO layer thickness as a function of surface concentration for *n25*.

It is evident that the PEO layer thickness increases continually as the copolymers are compressed on the surface. Such an increase is observed even at low surface concentrations suggesting that the PEO grafts have already exceeded the overlap concentration on the two dimensional surface and are exploring the subphase to avoid thermodynamic unfavourable interactions on the surface. The calculated overlap concentration is 0.11 mg m^{-2}, considerably smaller than the lowest surface concentration investigated (0.3 mg m^{-2}). The thickness of the PEO layer increases rapidly and linearly when the monolayer is compressed over the low surface concentration range, (0.3 < Γ_s < 1.0 mg m^{-2}) but it is evident however that the rate of stretching begins to slow as the monolayer is compressed further (1.5 < Γ_s < 4.0 mg m^{-2}). NR results show that in the defined surface concentration range, the number density of molecules situated at the near

surface is approximately constant, but the free graft ends extend further into the subphase upon monolayer compression. Such results concur with the surface pressure isotherm obtained (see Chapter Five). At low surface coverage the surface pressure increases rapidly as the EO molecules begin to pack and occupy the near surface. As the monolayer is compressed further the surface pressure reaches an asymptotic value which corresponds to the region where the near surface number density is constant and the only rearrangement within the layer is possible and this occurs deep in the subphase, hence a constant surface pressure is recorded.

Qualitatively the organisation of the graft copolymer is similar different to homoPEO[6] where at low surface coverage (≤ 0.4 mg m^{-2}) the polymer is highly diluted by the subphase and the surface pressure increases rapidly. In contrast to the graft copolymer system a single uniform layer can describe the molecular arrangement. At higher surface concentrations within the range 0.4 - 1.0 mg m^{-2} the polymer penetrates the subphase distributed with a Gaussian profile. As the monolayer concentration rises the surface pressure reaches a constant value and the thickness of the film also increases but the number density of the uppermost layer remains constant. This behaviour was observed in films of the graft copolymer although the magnitude of the thickness in this case are much higher than those observed for PEO (30 Å at most) with a molecular weight of 36 000 g mol^{-1}, which is significantly higher than the grafts in this study (6600-2200 g mol^{-1}). This suggests that the PEO chains in the copolymer are stretched to a greater extent.

Discussion of Results

An identical fitting procedure was used to analyse the reflectivity data collected for the remaining two copolymers, *n15* and *n50*. The layer thickness, volume fractions and number densities of the individual layers in each model are given in Appendix A in table A.1 and A.2 for *n15* and *n50* respectively. A comparison of the surface concentration calculated from the model parameters to that spread experimentally is also reported in the Appendix A in tables A.3 and A.4 for *n15* and *n50* respectively. A summary of the results

obtained is presented here and the following discussion concentrates on examining the influence of the graft length of the copolymer on the near surface organisation.

For the *n15* and *n50* copolymers a triple uniform layer model was required to describe the near surface organisation adequately for the majority of surface concentrations. In both cases, as the surface concentration exceeded 3.0 mg m^{-2} an additional layer was needed before all criteria defining a good model were met.

In each case it was found that the hydrocarbon main chain remains at the uppermost surface, occupying a thin layer of circa 5 Å and acting as an anchor for the PEO grafts immersed in the aqueous phase. The only exception to this being the portion of PEO grafts that curl over the backbone and reside in the air phase due to the *trans* double bonds in the main chain. The volume fraction of PNB in this uppermost layer tends to irregularly fluctuate and slightly differing behaviour is predicted depending on graft length. The volume fraction of air included in this layer for the two short grafts (*n15* and *n25*) increases, albeit with no discernible regularity, as the monolayer is compressed. The driving force for such behaviour has been alluded to previously when the behaviour of *n25* was discussed, where changes in volume fraction were attributed to the hydrocarbon backbone 'buckling' out of the plane of the water surface and perhaps adopting a helical conformation as the film becomes increasingly concentrated (see figure 6.3.17). The volume fraction of air recorded in the layer for the longer graft, circa 0.35, is consistent for all monolayers with no change in layer dimensions being observed. This difference in behaviour is attributed to the additional EO segments attempting to reach their thermodynamic most favourable conformation i.e.. penetrating the subphase, thus pulling the backbone closer to the surface and enhancing the anchoring effect. This will restrict the flexibility of the backbone chain.

The remaining layers (upper and lower subphase layers) in each model contain only EO and water. The volume fraction of EO included in the upper subphase layer is consistently higher in comparison to the lower layers, i.e. the extent of dilution of the grafts increases with penetration depth. The influence of graft length on the organisation in the subphase, volume fraction profiles for PEO only can be compared for each surface concentration. To highlight the behaviour observed two volume fraction profiles are given in figure 6.3.20 for 0.7 mg m^{-2} and 3.0 mg m^{-2}. These reveal that the graft length has

minimal effect on the number density for each layer as the magnitude is similar for each copolymer. However the layer thickness increases with increasing graft length. The PEO layer thicknesses are plotted as a function of surface concentration in figure 6.3.21. It is evident that all materials exhibit similar trends with monolayer compression i.e. a rapid increase in PEO layer thickness at low surface coverage with the rate of stretching diminishing when coverage exceeds circa 1.5 mg m^{-2}, i.e. the extent of stretching of the PEO depends on both graft length and monolayer compression.

Examining the data in figure 6.3.21 reveals that the difference between the PEO layer thickness is smaller at low surface coverage because the majority of the grafts are likely to be lying flat on the surface. The difference becomes increasingly apparent as the monolayer is compressed and the grafts begin to stretch into the subphase. Interestingly the difference between *n25* and *n50* is large in comparison to that between *n15* and *n25*. The distinction between the latter two copolymer behaviour is negligible and is probably due to the modest difference in graft length (only 10 EO units) and the variation in the *cis/trans* ratio of the saturated bonds in the main chain. Approximately one half the double bonds in the *n15* material are in the *cis* configuration opposed to one third in the *n25* copolymer. The *cis* grafts can penetrate the subphase directly whereas the *trans* isomer needs to loop over the backbone, in effect 'loosing' numerous EO segments in the air phase, before entering the aqueous phase. Since *n25* copolymer contains a greater portion of *trans* bonds it is therefore even closer in length to *n15* than anticipated.
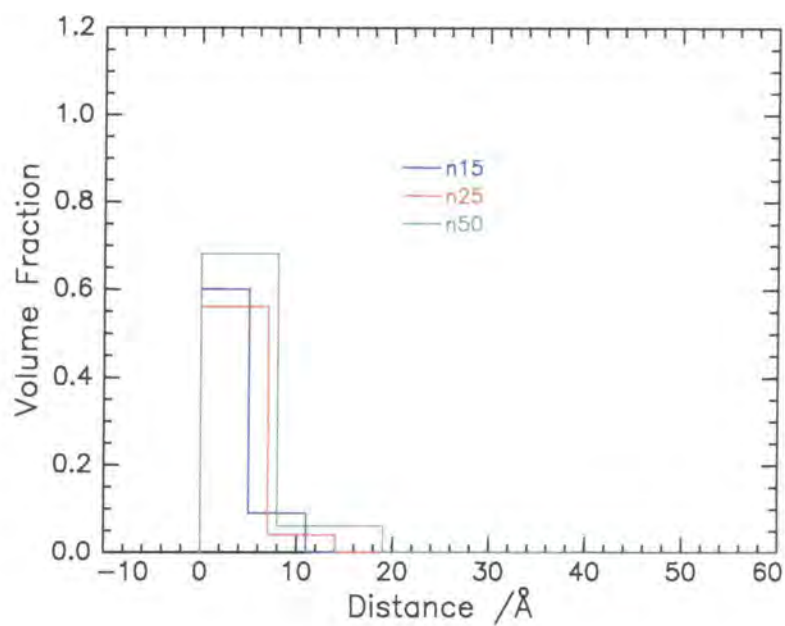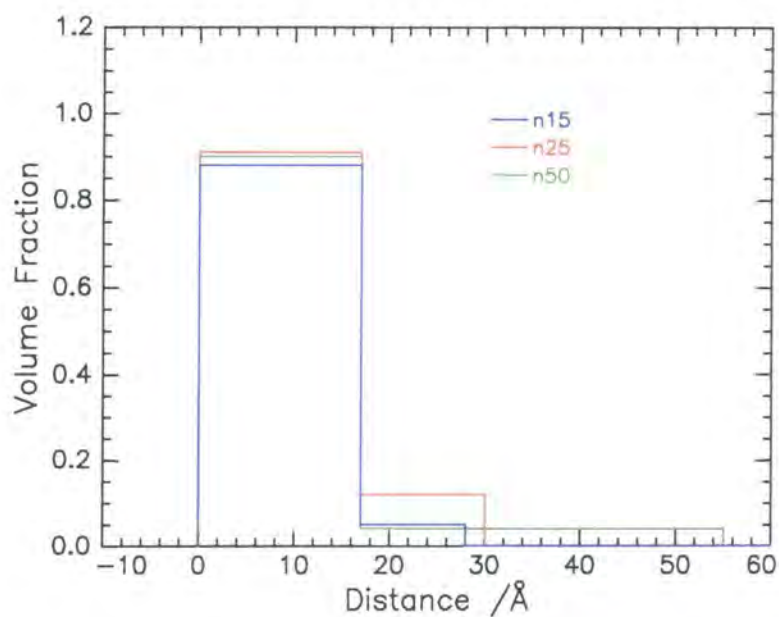
a) 0.7 mg m^{-2}

b) 3.0 mg m^{-2}

Figure 6.3.20 Comparison of volume fraction profiles for PEO for each copolymer for two differing surface concentrations: a) 0.7 mg m^{-2} and b) 3.0 mg m^{-2}.
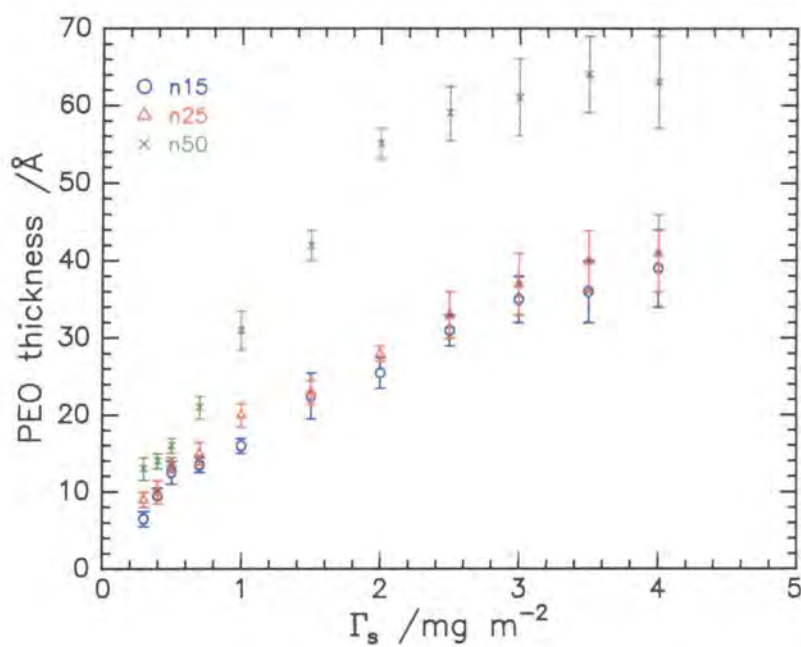
Figure 6.3.21. PEO layer thickness for all graft copolymers as a function of surface concentration.

6.3.2.2.1 Kinematic Approximation

The good agreement between calculated and actual surface concentrations and the physically acceptable description of optical matrix analysis notwithstanding, the kinematic approximation[8] was also applied to the neutron reflectometry data for two reasons. Firstly, the distributions of the copolymer graft and water components in the near surface region were obtained separately and secondly the separation between these two distributions becomes accessible in principle. Due to the unavailability of the backbone in a deuterated form however, only a subset of the relations available could be used, namely the PEO and water self partial structure factors extracted from the contrast conditions of part deuterated/nrw and fully protonated/D_2O respectively. To apply such relations successfully it was assumed that the protonated components of the copolymer do not contribute to the reflectivity. The latter is not too drastic an assumption because both backbone and hydrogenous PEO have low scattering length densities. Therefore for the part deuterated copolymer spread on nrw the reflectivity can be expressed as,

$$R(Q) = \frac{16\pi^2}{Q^2} b_{EO}{}^2 h_{EO}$$

Equation 6.3.11.

where EO represents ethylene oxide, b_{EO} the scattering length of the deuterated monomer and h_{EO} is the PEO self partial structure factor.

For the fully protonated copolymer spread on D_2O (assuming that the contribution to the specular reflection from the copolymer is negligible) the reflectivity can be written as;

$$R(Q) = \frac{16\pi^2}{Q^2} b_w{}^2 h_{ww}$$

Equation 6.3.12.

where W represents water, b_w the scattering length of heavy water and h_{ww} the water self partial structure factor term.

The background contributions were subtracted from all reflectivity profiles and for the reflectivity data obtained where D_2O was the subphase, the correction procedure of Crowley and co-workers[9] was applied (for further details see Chapter Three) before expressing the data in terms of partial structure factors. In the following discussion the results obtained for each partial structure factor will be presented separately.

PEO Self Partial Structure Factor

A selection of the background subtracted data for the *n25* part deuterated copolymer spread on nrw as derivatives of the PEO self-partial structure factor ($\equiv Q^4R(Q)/16\pi^2b^2$) are given in figure 6.3.22.
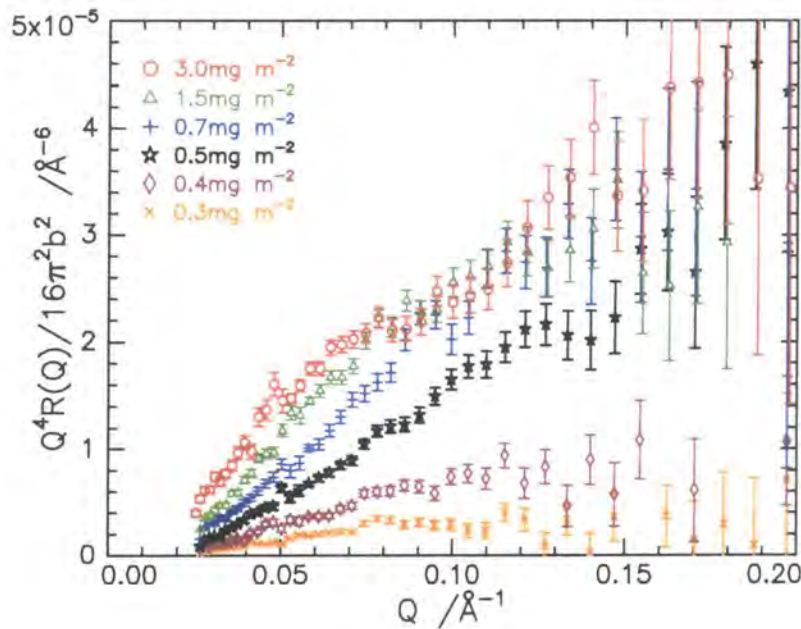

Figure 6.3.22. PEO self-partial structure factors (in the derivative form) for a selection of surface concentrations for *n25* part deuterated copolymer on nrw.

The data presented here are again representative of the series of copolymers investigated. In this case the partial structure factor is related to the number density of EO species, n_{EO}, by equation 6.3.13.

$$h_{EO} = \left| n_{EO}(Q) \right|^2 \qquad\qquad \textbf{Equation 6.3.13.}$$

The gradient of the initial part of the partial structure factor increases with monolayer compression, moreover the maximum in the data occurs mostly at highly values of Q as the surface concentration rises.

A variety of functional forms have been used to interpret these data and initially simple models such as the single uniform layer, half-Gaussian and half-parabolic distribution from the interface were used. Furthermore two composite models were later tested: a double uniform layer distribution and one with the EO segments distributed over a uniform layer with parabolic decay. The profiles of each model are sketched in Appendix B (figures B.1 and B.2) where the characteristic expressions for the number density and partial structure factors for all models are also given (equations B.1-B.10).

All functional forms described above were used to fit the data where the number density and layer thickness (for each layer in the distribution profile) were the adjustable fitting parameters for the non-linear least squares fitting procedure. Examples of typical fits for a Gaussian and uniform-parabola distribution are given in figure 6.3.23 and 6.3.24 respectively for *n25* spread at a surface concentration of 2.0 mg m^{-2}. By comparing these fits over the Q range studied it is evident that it is impossible to distinguish between the different models, as both fits are of equally good quality. Distinction between the functional forms only becomes evident at higher Q values but unfortunately the background contribution to the total reflectivity overwhelms any content from the layer organisation at these higher Q values.

Typical number density profiles for each model are given in figure 6.3.25a-d for a range of surface concentrations that are representative of the series investigated: 0.4, 1.0, 2.0 and 4.0 mg m^{-2}, and the values obtained from the fits for the layer thicknesses and number densities are given in table 6.3.8a-d.
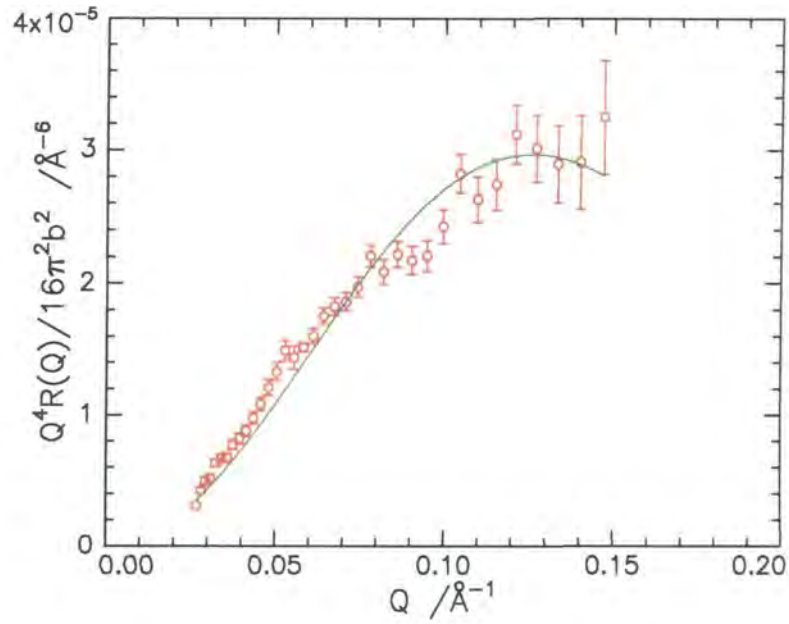
Figure 6.3.23. Typical fits to the PEO self-partial structure factor data for *n25* spread at a surface concentration of 2.0 mg m^{-2} assuming a Gaussian distribution.
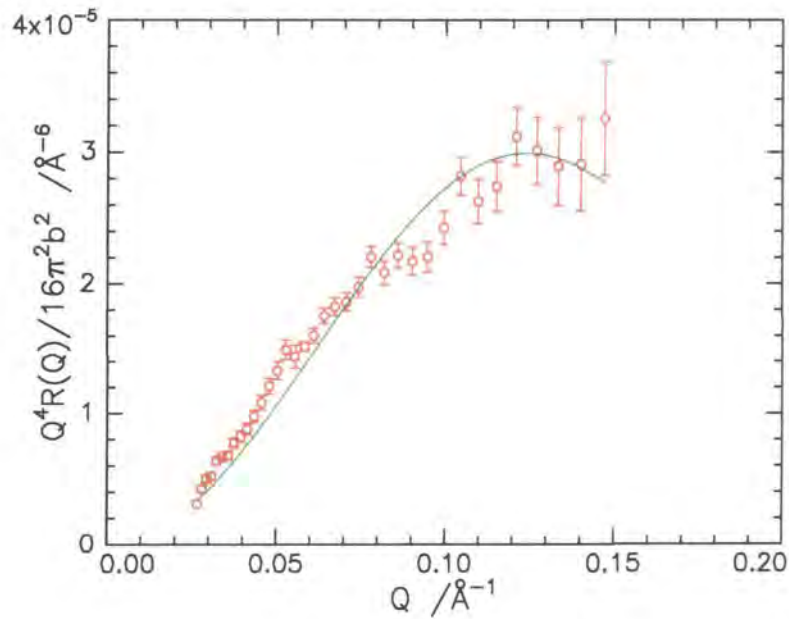
Figure 6.3.24. Typical fits to the PEO self-partial structure factor data for *n25* spread at a surface concentration of 2.0 mg m^{-2} assuming a uniform layer with parabolic decay distribution.

224
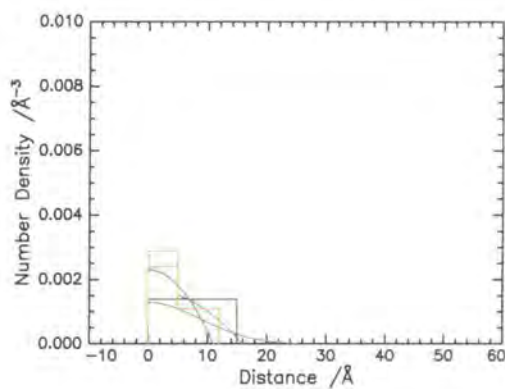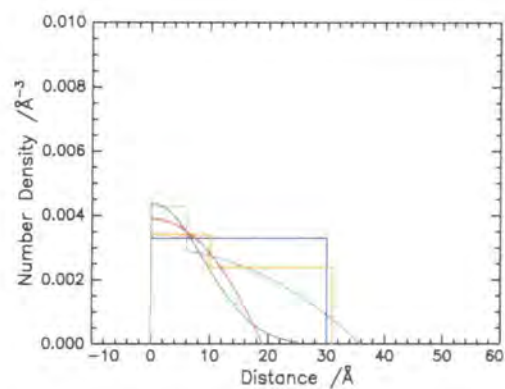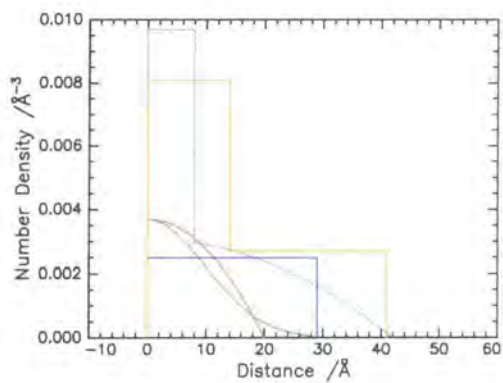
a) 0.4 mg m⁻²

b) 1.0 mg m⁻²

a) 2.0 mg m⁻²
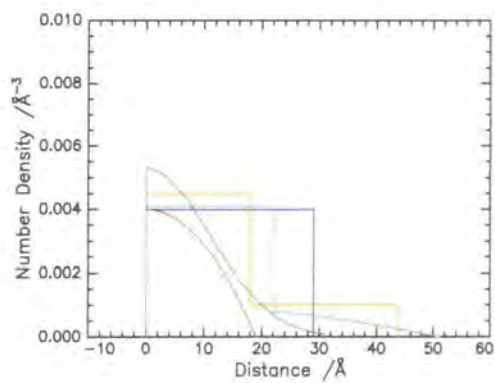
b) 4.0 mg m⁻²

Figure 6.3.25. Comparison between the number density profiles of PEO obtained for various layer model distributions for *n25* copolymer spread at a surface concentration of a) 0.4 mg m^{-2}, b) 1.0 mg m^{-2}, c) 1.0 mg m^{-2} and d) 4.0 mg m^{-2}.

Model	$d_1/\text{Å}$	$n_1/10^{-3}\,\text{Å}^{-3}$	$d_2/\text{Å}$	$n_2/10^{-3}\,\text{Å}^{-3}$
Uniform	23 ± 2	1.4 ± 0.5	-	-
Half-Gaussian	25 ± 2	1.3 ± 0.1	-	-
Half-parabola	11 ± 1	2.3 ± 0.7	-	-
Double uniform	5 ± 2	2.4 ± 0.6	7 ± 1	1.1 ± 0.2
Uniform layer with parabolic decay	5 ± 1	2.9 ± 0.2	11 ± 3	1.7 ± 0.1

a) $\Gamma_s = 0.4$ mg m^{-2}

Model	$d_1/\text{Å}$	$n_1/10^{-3}\,\text{Å}^{-3}$	$d_2/\text{Å}$	$n_2/10^{-3}\,\text{Å}^{-3}$
Uniform	30 ± 1	3.3 ± 0.4	-	-
Half-Gaussian	25 ± 1	4.4 ± 0.4	-	-
Half-parabola	19 ± 1	3.9 ± 0.3	-	-
Double uniform	10 ± 2	3.4 ± 0.5	21 ± 3	2.4 ± 0.3
Uniform layer with parabolic decay	6 ± 1	4.3 ± 0.1	30 ± 4	1.9 ± 0.2

b) $\Gamma_s = 1.0$ mg m^{-2}

| Model	$d_1/\text{Å}$	$n_1/10^{-3}\,\text{Å}^{-3}$	$d_2/\text{Å}$	$n_2/10^{-3}\,\text{Å}^{-3}$
Uniform	29 ± 1	2.5 ± 0.8	-	-
Half-Gaussian	33 ± 1	4.6 ± 0.1	-	-
Half-parabola	20 ± 1	3.7 ± 0.3	-	-
Double uniform	14 ± 2	8.1 ± 0.4	27 ± 2	2.7 ± 0.5
Uniform layer with parabolic decay	8 ± 1	9.8 ± 0.8	34 ± 2	2.5 ± 0.2

c) $\Gamma_s = 2.0$ mg m^{-2}

Model	$d_1/\text{Å}$	$n_1/10^{-3}\,\text{Å}^{-3}$	$d_2/\text{Å}$	$n_2/10^{-3}\,\text{Å}^{-3}$
Uniform	29 ± 1	4.0 ± 0.6	-	-
Half-Gaussian	31 ± 2	5.3 ± 0.3	-	-
Half-parabola	19 ± 1	4.0 ± 0.3	-	-
Double uniform	18 ± 1	4.5 ± 0.6	26 ± 1	1.0 ± 0.5
Uniform layer with parabolic decay	22 ± 1	4.1 ± 0.4	29 ± 1	1.4 ± 0.6

d) $\Gamma_s = 4.0$ mg m^{-2}

Table 6.3.8. Layer thickness and number density values of the fits to the PEO self partial structure factors for the selected surface concentration range for *n25* copolymer.

No models were applied to the lowest surface concentration spread film, 0.3 mg m^{-2}, because the partial structure factor data were too scattered to have confidence in fitted values.

After comparing the profiles obtained and the model parameters for each surface concentration it is evident that in general all models predict similar magnitudes of near surface number density but contrasting penetration depths. This emphasises the difficulty in identifying the precise distribution of the grafts in the subphase. The characteristic parameters obtained for all single layer models are of approximately identical magnitude, which suggests that little distinction can be made between molecular distributions. This lack of microscopic detail is possibly a reflection of the short chain length since any organisational change will be subtle and difficult to detect. The composite models predict slightly different behaviour, as the uppermost layer is relatively short and has a high number density while the extra layer (i.e. the second uniform layer or the parabolic tail) are of comparatively low number density and predict the graft chains extend deep into the subphase.

To determine which model describes the copolymer system most accurately two methods were applied. Firstly the 'goodness of fit' parameter, χ, from the least squares fitting routine for each model were compared. Table 6.3.9 gives these values for a cross-section of surface concentrations of *n25*.

Model	0.4 mg m^{-2}	1.0 mg m^{-2}	2.0 mg m^{-2}	4.0 mg m^{-2}
Uniform	8.56×10^{-13}	5.74×10^{-13}	6.46×10^{-13}	3.53×10^{-13}
Half-Gaussian	1.14×10^{-13}	4.28×10^{-13}	7.92×10^{-13}	5.67×10^{-13}
Half-parabolic	1.21×10^{-12}	6.24×10^{-13}	8.54×10^{-13}	4.64×10^{-13}
Double Uniform	1.37×10^{-13}	2.13×10^{-13}	1.64×10^{-13}	2.13×10^{-13}
Uniform layer with parabolic decay	1.43×10^{-13}	1.86×10^{-13}	1.13×10^{-13}	2.58×10^{-13}

Table 6.3.9. Comparison of goodness of fit values for various model fits to PEO partial structure factor data for *n25* at four different surface concentrations.

The results reveal that the χ values for the composite functional forms are significantly lower than any of the values obtained for any single layer model fit, indicating the fits of the composite models are closer to the experimental data. This is hardly surprising because four variable parameters were allowed to 'float' during the fitting procedure as opposed to two for the single layer fits. The decrease in χ therefore does not automatically indicate that either composite model provides a more realistic fit.

A comparison between the single layer models and double layer models can still be made, and in both cases it is evident that χ is concentration dependent. Consider first the single layer distributions where at low surface coverage a Gaussian layer returns the lowest values of χ, but as the surface concentration increases the uniform layer appears to provide a better fit to the experimental data. Such a trend represents the polymer molecules moving closer together, thus expelling water molecules throughout the whole layer as the monolayer is compressed. When comparing the double layer models difficulties arise as the χ values are extremely close making it impossible to predict which model best describes the experimental system. Clearly a second method is required to distinguish between the models. A comparison of the calculated surface concentration to that actually spread is most convenient. The expressions used to calculate the surface concentrations for each model distribution are given in Appendix B, equations B11-15.

Model	$\Gamma_{EO\ CALC}/\Gamma_{PEO}$			
	0.4 mg m^{-2}	1.0 mg m^{-2}	2.0 mg m^{-2}	4.0 mg m^{-2}
Uniform	0.72	0.89	0.31	0.26
Half-Gaussian	0.64	0.85	0.50	0.32
Half-parabolic	0.75	0.86	0.43	0.22
Double uniform	0.73	0.74	0.82	0.23
Uniform layer with parabolic decay	0.86	0.89	0.83	0.29

Table 6.3.10 Ratio of calculated PEO spread to quantity of PEO spread experimentally for each model distribution from fits of the PEO partial structure factor.

The values calculated are compared for each model by taking the ratio of the calculated PEO spread to the quantity of PEO spread experimentally and the results for the cross-section of surface concentrations for *n25* are given in table 6.3.10. It is evident from the results that in general the surface concentration of PEO from the uniform layer plus parabolic decay model provides the closest match to the actual quantity of PEO spread. However, the concentration of PEO calculated from this model is not in satisfactory agreement (i.e. $\pm 10\%$ maximum) with the experimental value. This may be due to the assumption that the protonated components of the copolymers make a negligible contribution to the reflectivity. To correct for this possibility, the optical matrix method was used to fit the uniform plus parabolic layer model to the reflectivities for all graft copolymer-subphase combinations.

The procedure adopted was identical to that used previously when the model consisted of uniform layers (outlined in section 6.3.2.1). Prior to fitting the composite model the data were modelled using a single parabola functional form (distribution theoretically predicted for end tethered polymers). The number density and layer thickness of the half-parabola were adjusted, but no acceptable fit to the data was obtained for any surface concentration. For the uniform parabola models the variable parameters were the number density and layer thickness of the uniform layer, n_1 and d_1, and the corresponding values for the half-parabola: n_2 and d_2. Model fits that met the required criteria were obtained and the layer thickness and volume fractions were extracted for all surface concentrations investigated and are given in table 6.3.11 along with the calculated number density values for *n25*.

The surface concentrations were also determined to analyse the quantity of PEO accounted for in the model, by summing the contributions from each layer using equation B.15. These values are given in table 6.3.12. Finally the results for the complete range of surface concentrations from the kinematic approximation are given in table 6.3.13 to allow a complete comparison of the characteristic parameters between the different fitting methods.

229

Γ_s /mg m^{-2}	d_1 /Å^{-1}	ϕ_1	d_2 /Å^{-1}	ϕ_2	n_1 /10^{-3} Å^{-3}	n_2 /10^{-3} Å^{-3}
4.0	25 ± 1	0.96	23 ± 2	0.41	13.27	5.67
3.5	22 ± 1	0.99	24 ± 3	0.31	13.68	4.28
3.0	12 ± 2	0.88	31 ± 2	0.32	12.16	4.42
2.5	13 ± 1	0.82	30 ± 2	0.41	11.33	5.67
2.0	11 ± 1	0.77	25 ± 1	0.26	10.64	3.59
1.5	6 ± 2	0.72	24 ± 1	0.24	9.95	3.32
1.0	11 ± 1	0.58	17 ± 4	0.08	8.02	1.11
0.7	5 ± 2	0.43	17 ± 1	0.15	5.94	2.07
0.5	5 ± 1	0.61	12 ± 1	0.06	8.43	0.83
0.4	5 ± 1	0.39	7 ± 1	0.12	5.39	1.66
0.3	5 ± 1	0.44	4 ± 3	0.06	6.08	0.83

Table 6.3.11. Layer thicknesses, volume fractions and calculated number densities for *n25* from optical matrix calculations with a uniform layer plus parabolic decay model. The subscripts 1 and 2 denote the uniform and parabolic layer respectively.

$\Gamma_{sTOTAL.}$ /mg m^{-2}	Γ_{sEO} /mg m^{-2}	$\Gamma_{sEO\,calc.}$ /mg m^{-2}	$\Gamma_{sEO}/\Gamma_{sEO\,calc.}$
4.0	3.64	3.34 ± 0.16	0.93
3.5	3.19	3.93 ± 0.17	0.92
3.0	2.73	2.47 ± 0.24	0.91
2.5	2.28	2.14 ± 0.15	0.94
2.0	1.82	1.85 ± 0.12	0.99
1.5	1.37	1.33 ± 0.20	0.98
1.0	0.91	0.91 ± 0.11	1.00
0.7	0.64	0.60 ± 0.11	0.95
0.5	0.46	0.44 ± 0.08	0.98
0.4	0.36	0.34 ± 0.06	0.94
0.3	0.27	0.27 ± 0.08	1.00

Figure 6.3.12. Calculated surface concentrations of PEO for *n25* from optical matrix calculations using a uniform layer with parabolic decay model.

Γ_{sTOTAL} /mg m^{-2}	Γ_{sEO} /mg m^{-2}	d_1 /Å^{-1}	n_1 /10^{-3} Å^{-3}	d_2 /Å^{-1}	n_2 /10^{-3} Å^{-3}	$\Gamma_{sEO\ calc.}$ /mg m^{-2}	$\Gamma_{sEO}/\Gamma_{sEO\ calc.}$
4.0	3.64	22 ± 1	4.3 ± 0.4	29 ± 1	1.4 ± 0.6	1.34 ± 0.01	0.29
3.5	3.19	15 ± 1	4.5 ± 06	27 ± 2	1.3 ± 0.3	0.91 ± 0.01	0.37
3.0	2.73	22 ± 1	4.5 ± 0.7	31 ± 3	1.3 ± 0.2	1.22 ± 0.01	0.47
2.5	2.28	26 ± 1	4.4 ± 0.3	31 ± 2	1.1 ± 0.5	1.27 ± 0.01	0.56
2.0	1.82	8 ± 1	9.8 ± 0.8	34 ± 2	2.5 ± 0.2	1.52 ± 0.01	0.83
1.5	1.34	6 ± 1	7.1 ± 0.1	35 ± 5	2.3 ± 0.1	1.19 ± 0.01	0.88
1.0	0.91	6 ± 1	4.1 ± 0.1	30 ± 4	1.9 ± 0.2	0.80 ± 0.01	0.89
0.7	0.64	6 ± 1	3.9 ± 0.1	16 ± 4	2.2 ± 0.4	0.56 ± 0.02	0.87
0.5	0.46	5 ± 1	4.0 ± 0.2	16 ± 3	1.8 ± 0.2	0.46 ± 0.01	1.00
0.4	0.36	5 ± 1	2.9 ± 0.2	11 ± 3	1.7 ± 0.1	0.31 ± 0.01	0.86

Table 6.3.13. Number densities, layer thicknesses and calculated surface concentrations from the PEO kinematic approximation for *n25* using the uniform layer with half-parabola decay model.

It is clear from the two sets of results that the total PEO layer thicknesses for both uniform-parabola models are in good agreement with each other. This similarity is highlighted in figure in figure 6.3.26 where the layer thicknesses of the uniform layer plus the half parabola are plotted as a function of surface concentration. The results from the model that provides the most detailed surface description, the triple uniform layer, is also included in this diagram. This latter model describes the distribution of both the hydrocarbon backbone and the PEO grafts where the backbone occupies the uppermost layer while the remaining layers (layers 2 and 3) describe the distribution of PEO in water.
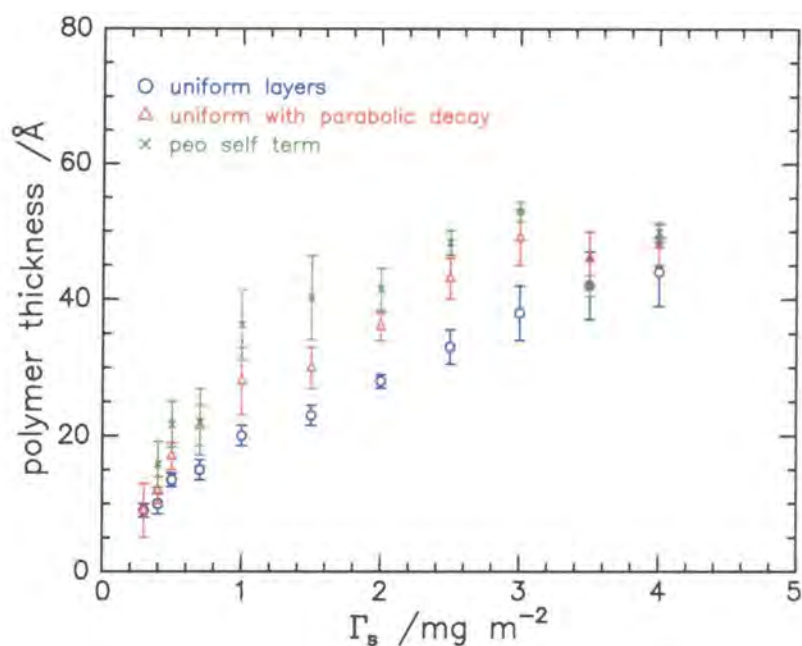
Figure 6.3.26. Comparison of the PEO layer height for *n25* at all surface concentrations studied for each fitting method: optical matrix analysis using a triple uniform model and a uniform layer with parabolic decay, and the kinematic approximation using a uniform layer with parabolic decay.

All models follow similar trends i.e. the total PEO layer thickness increases linearly and rapidly over the low surface concentration range but the rate of increase reduces slightly when the layer becomes highly compressed. The predicted thickness of the PEO layers from the triple uniform layer model are consistently lower than those detected by other models. This behaviour is probably due to the abrupt step in volume fraction of the uniform model in comparison to the more realistic smooth decay in polymer distribution of the parabolic form. To identify which model describes the interfacial organisation with greatest accuracy the calculated spread PEO is compared to the actual quantity spread in table 6.3.14.

Γ_{sEO} spread experimentally	$\Gamma_{sEO}/\Gamma_{sEOcalc}$		
	optical matrix triple uniform layers	optical matrix uniform plus parabolic	kinematic approx. uniform plus parabolic
4.0	0.90	0.93	0.29
3.5	0.90	0.92	0.37
3.0	0.90	0.91	0.47
2.5	0.93	0.94	0.56
2.0	0.96	0.99	0.83
1.5	0.97	0.98	0.88
1.0	0.94	1.00	0.89
0.7	0.98	0.95	0.87
0.5	1.00	0.98	1.00
0.4	0.97	0.94	0.86
0.3	1.00	1.00	-

Table 6.3.14. Comparison of experimental and calculated values for the quantity of PEO spread on the water surface.

The model containing the parabolic distribution accounts for fractionally more of the PEO in the monolayer and is also physically more realistic as the free ends of the PEO chains will not be located at the same depth as predicted by a uniform functional form. A uniform layer with parabolic decay therefore best describes the data and the distribution of the PEO grafted chains while the main chain remains on the uppermost surface at all surface concentrations. The differences between the partial structure factor and the optical matrix data need to be addressed, as the partial structure factor analysis correctly predicts the dimensionality of the system but not the number density, but the optical matrix method describe both well. This shortcoming of the partial structure factor analysis is due to the neglect of the protonated species. The most detailed surface description is obtained from the triple uniform layer model as this describes the distribution of the hydrocarbon backbone and the PEO grafts. The backbone occupies the uppermost layer while the

remaining layers and the uniform with parabolic decay models describe the distribution of the PEO grafts.

The variation in graft length shown in figure 6.3.26 and discussed above is typical of the *n15* and *n50* copolymer behaviour as the uniform-parabolic model fitted to the experimental data using the optical matrix method provided the best description of the near surface organisation. The layer thickness, volume fractions and quantity of spread PEO accounted for the optical matrix and kinematic approximation are given in Appendix A (tables A.1 and A.2 for *n15* and A.3 and A.4 for *n50* respectively) to allow a complete comparison.

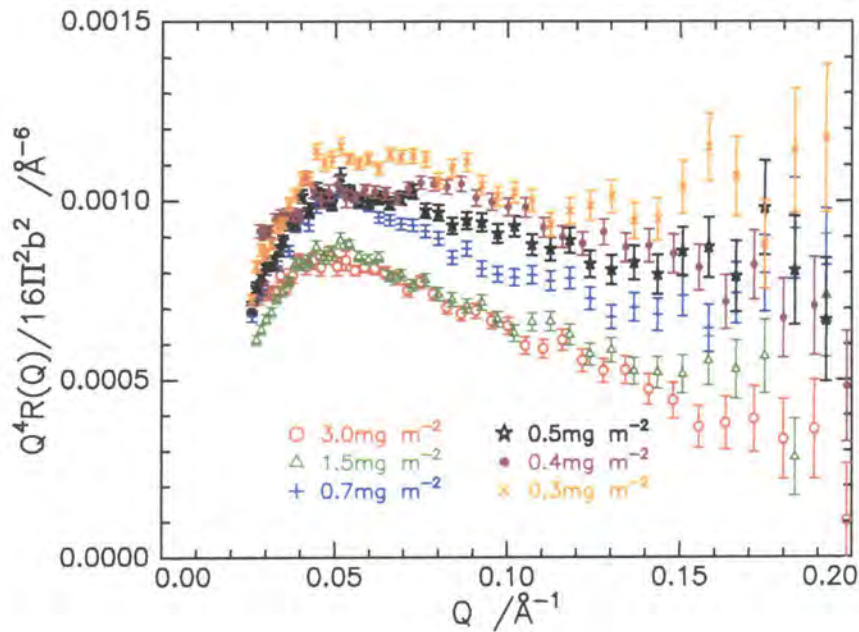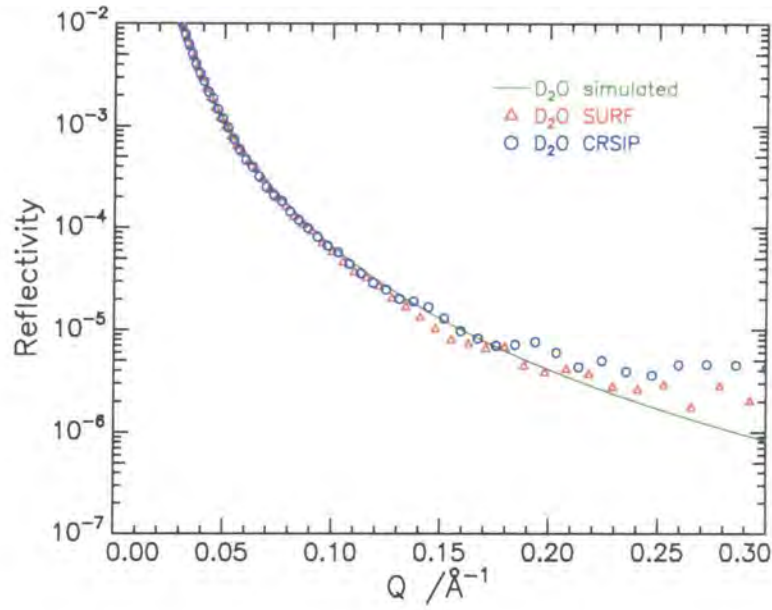### Water Self Partial Structure Factor

Figure 6.3.27. Water self-partial structure factor data for a selection of surface concentrations for *n25* fully protonated copolymer spread on D_2O.

It was anticipated that the water in the immediate near surface layer may, over a finite spatial range, have a different number density compared to that of the bulk aqueous

subphase. This is due to the effects of the spread film and any interactions between the segments of the PEO grafts and the water. The background subtracted and Crowley corrected data are presented in terms of the self partial structure factors obtained for water in figure 6.3.27 for a selection of surface concentrations of *n25*.

It is clear from this diagram that the behaviour exhibited is unusual as all data display a downturn at low Q, and this is typical for all three copolymers. Theoretically, as Q tends toward zero the water self-partial structure factor data should approach a value of 1.1×10^{-3} Å^{-6} ($Q^2 h$), which is the square root of the bulk density of water (0.0332 Å^{-3}). In general the magnitude of the self-partial structure factor decreases with increasing surface coverage due to the displacement of the water molecules with protonated polymer. Furthermore the value of the experimental structure factor also increases with decreasing Q as expected over the Q range $0.07 < Q < 0.2$ Å^{-1}, but unusually at circa $Q = 0.05$ Å^{-1} all data exhibit a downturn. It is difficult to rationalise the sudden dip in the data at low Q since Q is inversely proportional to penetration depth, therefore low or zero Q should correspond to infinite depth i.e. bulk water. Although this behaviour has been observed for many PEO[11,12,13] containing polymer films, it is not system dependent since this effect has been observed in films of poly (methyl methacrylate)[6,14] and a diblock polyelectrolyte copolymer[15] (poly (methyl methacrylate) and poly-4-vinyl pyridine quaternised with ethyl bromide). Explanations of such phenomenon are sparse, one suggestion however involves the slow dissolution of molecules from the film into the subphase, thus altering the bulk properties of water. This is not a possibility in the copolymer system studied here, as it forms an insoluble monolayer and no polymer is lost into the bulk phase when spread at the air-water interface over a 24 hour period (neutron reflectivity data is collected over a four hour period – for experimental evidence see Chapter Five). The only plausible explanation to date involves error being introduced during the set-up of the instrumentation. To test this idea the reflectivity data collected from a pure water surface from both instruments used (SURF and CRISP) was plotted in the partial structure form and compared to the data from a simulated profile. Such data are given in figure 6.3.28b while figure 6.3.28a shows the comparison of the raw reflectivity profiles as a function of Q and is included simply to prove that the profiles are coincident and exhibit no unusual features.

a) reflectivity data
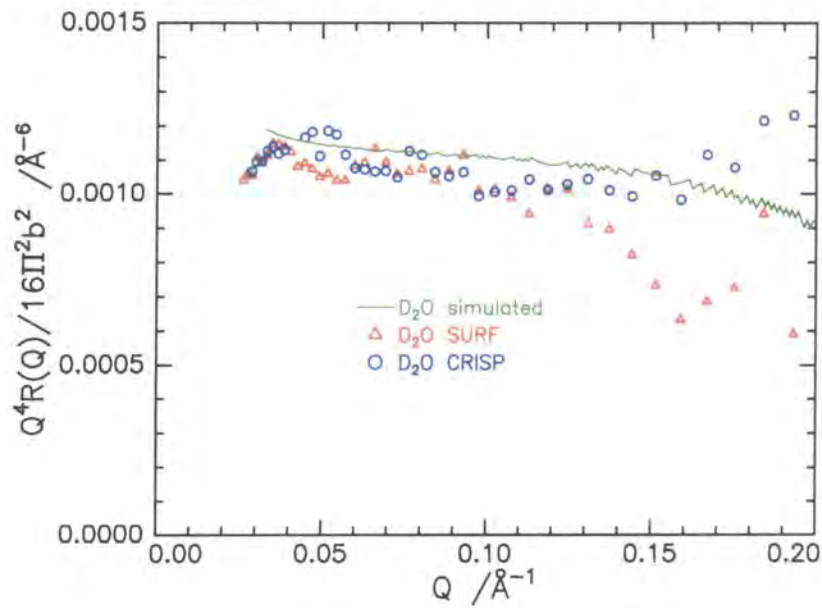
b) water self-partial structure factor data

Figure 6.3.28. Comparison of simulated and experimental neutron a) reflectivity data and also b) data in kinematic approximation form for water self-partial structure factor of a clean water surface.

By examining the partial structure profiles closely, marked differences between the plots are evident at low Q. The simulated profile remains at a constant value, close to that predicted theoretically for the number density of pure water (1.1×10^{-3} $Å^{-3}$), while the experimental profiles show a slight downturn between $0.0255 \leq Q \leq 0.05 \, Å^{-1}$. The region corresponds exactly to the data collected at the lower angle of incidence, which suggests that this feature is not connected to copolymer/subphase arrangement or a mere artefact of the data, but is inherent in the instrument. Further evidence for this idea stems from the differences observed in the data collected on the two reflectometers SURF (0.4 and 3.0 mg m^{-2}) and CRISP (0.3, 0.5, 0.7, and 1.5 mg m^{-2}) as is clear from figure 6.3.27 that the CRISP data exhibit a more dominant downturn. No reason has been identified to date to account for such behaviour, perhaps if for example the detector was slightly misaligned for the low incident angle data throughout all experiments then the Q value detected would either be slightly higher or lower than the actual value hence introducing ambiguity. It proved difficult to reproduce partial structure factor data due to the physically unrealistic dip in the data even when these data are disregarded. A basic outline however is provided below simply to highlight the problems encountered.

Initially two single layer models were adopted to describe the distribution of water molecules and were fitted to the experimental data. Both models are schematically represented in figure 6.3.29 where the first consisted of a uniform layer with a number density lower than that of pure water, followed by an infinitely thick layer of pure water, and the second consisted of a more physically realistic smooth transition from the number density to the bulk subphase. The number densities and water structure factors are given in Appendix B in equations B.16-19.

Since the number density of the polymer layer, n_{xi}, in both models must equate to n_{s0}, the number density of the bulk, when $Q = 0$. The only parameters that can be varied are n_{w1} and σ, the thickness of the polymer layer in the water subphase. Examples of typical linear least-square fits of both models to the data are given in figure 6.3.30.
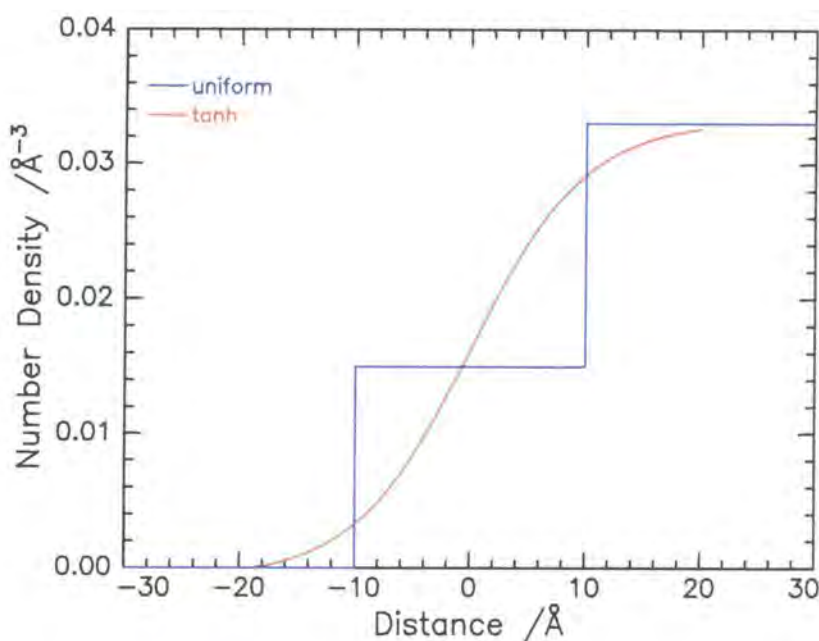
Figure 6.3.29. Schematic representation of number density profiles for a single uniform water layer (thickness 20 Å, number density 0.015 Å^{-3} and a tanh layer (thickness 10 Å).

The fits obtained for both models do not reproduce the data at all over the higher Q range, $0.15 \leq Q \leq 0.3$ Å^{-1}. Moreover even when the artefact (unusual downturn at low Q) as neither model provides a good fit to the data despite using a wide variety of starting parameters in the fitting routine. Over the low Q range the two model fits qualitatively follow the behaviour expected of such systems as they continue to rise and tend towards the value for the bulk density of water at zero Q. The layer thicknesses obtained are considerably lower in comparison to those predicted from the PEO self-term and optical matrix analysis methods but no significant emphasis is placed on these since the model fits are totally inaccurate. The water self-partial structure factor must therefore be more complicated than the single layer models.
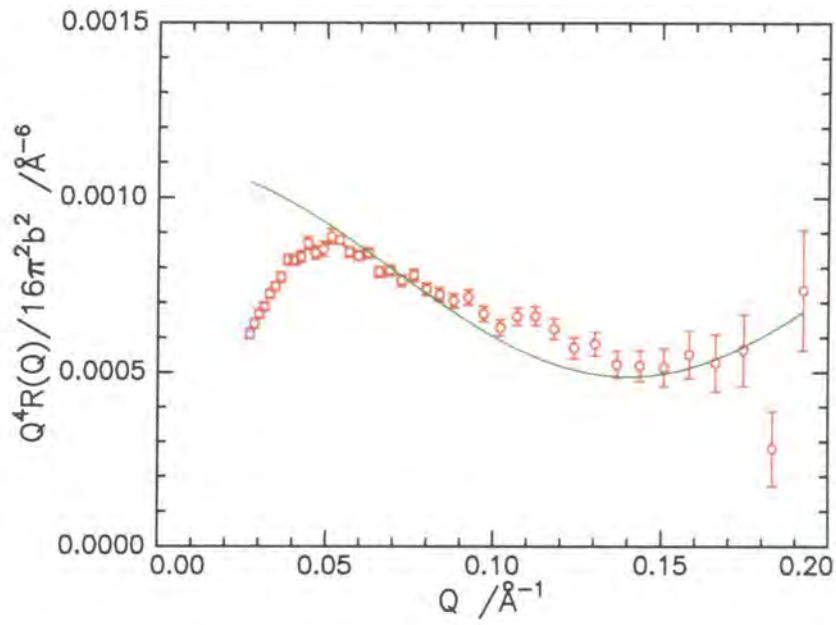
a) uniform model fit
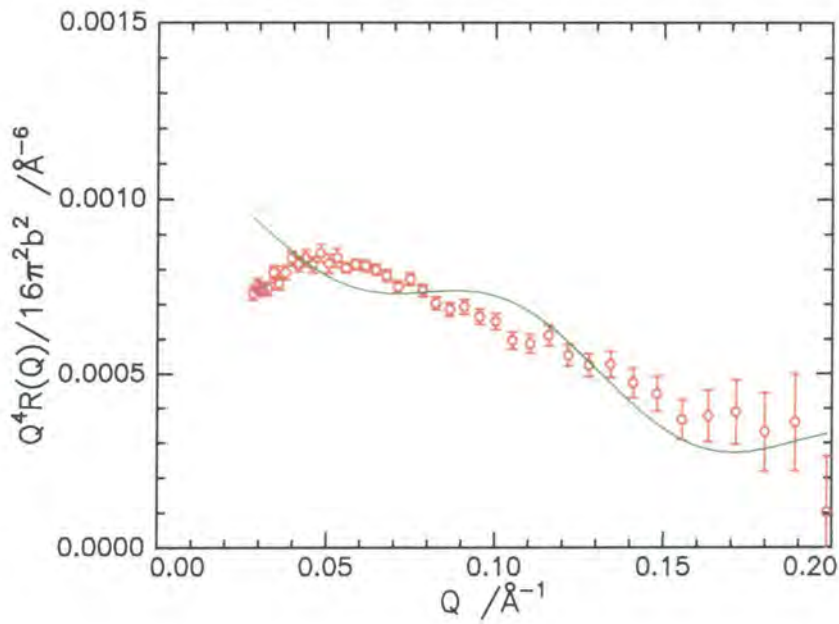
b) tanh model fit

Figure 6.3.30. Water self-partial structure factors for a surface concentration of 2.0 mg m^{-2} with a) uniform water and b) tanh model fits.

Complexity was introduced to the model by including an additional layer where the water number density is predicted to increase in uniform steps from the interface. Again the number density and partial structure factor are given in Appendix B.

Such a model was applied to experimental data of surface concentration was 3.0 mg m^{-2} where the downturn was disregarded. The composite model improved the quality of fit significantly (shown in figure 6.3.31), but the layer dimensions returned were somewhat lower than expected: 12 Å compared to 36 Å predicted from the uniform layer with parabolic decay model. This is because in this fitting procedure a significant portion of low Q data has been omitted and therefore the model fit to these data are not representative of the complete polymer monolayer. It was concluded therefore that this model does not reproduce the features of the experimental data sufficiently well to justify any further attempts to fit the remaining data and the detailed distribution of the water surrounding the PEO grafts remain unresolved. It is clear that this organisation is considerably more complex that the simple models that have been applied here. The key information is in principle obtainable from reflectivity at lower Q values than those used thus far, i.e. Q < 0.02 Å^{-1}, however no data can be obtained at such a low Q range for the D_2O subphase since the critical reflection intervenes at Q = 0.017 Å^{-1}.

Although the partial structure factor for the uniform model is oscillatory in nature, the value of n_{w1} controlling the amplitude oscillations and σ the frequency, the characteristic dip at very low Q in the data is not reproduced by the uniform model without introducing strongly oscillatory features over the whole range of Q. This provides further confirmation that the dip is inherent in the instruments CRISP and SURF.
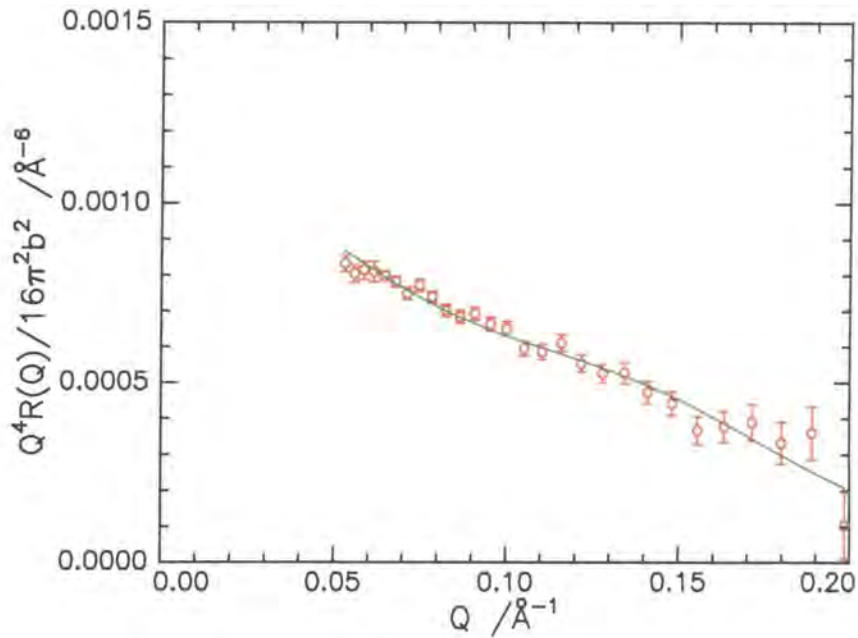
Figure 6.3.31. Water self-partial structure factors for a surface concentration of 3.0 mg m^{-2} with a double uniform layer model fit.

6.3.2.3 Bayesian Analysis

The final fitting method applied was the model independent method of Bayesian analysis[4] developed by Dr. D. Sivia currently at the Rutherford Appleton Laboratory. This method was applied to a selection of data for *n25*.

The fitting program used is based on a maximum entropy algorithm where the maximum entropy of a predicted volume fraction distribution is evaluated to determine how realistic the distribution is without any reference to the experimental data: models with high entropy are accepted as representing a more physically realistic solution over models with low entropy even if both models have identical normalised parameters. In each case the entropy of the model was measured relative to a double uniform profile. Thereafter models were 'free-form' where the composition profile was divided into 150 layers of equal thickness and the composition of each layer varied. The only constraint in the data was the

maximum model thickness, which was limited to 96 Å. This value was chosen as it is the length of the *n25* graft in a fully extended form (i.e. all bonds are in the *trans* configuration).

Figure 6.3.32 represents a typical fit obtained using maximum entropy methods and figure 6.3.33 the corresponding distribution profile for *n25* spread at a surface concentration of 2.0 mg m^{-2}. The magnitude of layer thickness obtained from model independent method agrees well (40 Å) with those obtained from optical matrix analysis (36 Å). It is also encouraging to find that the composition profile is in excellent agreement with those obtained from the optical matrix analysis and the partial kinematic approximation methods.
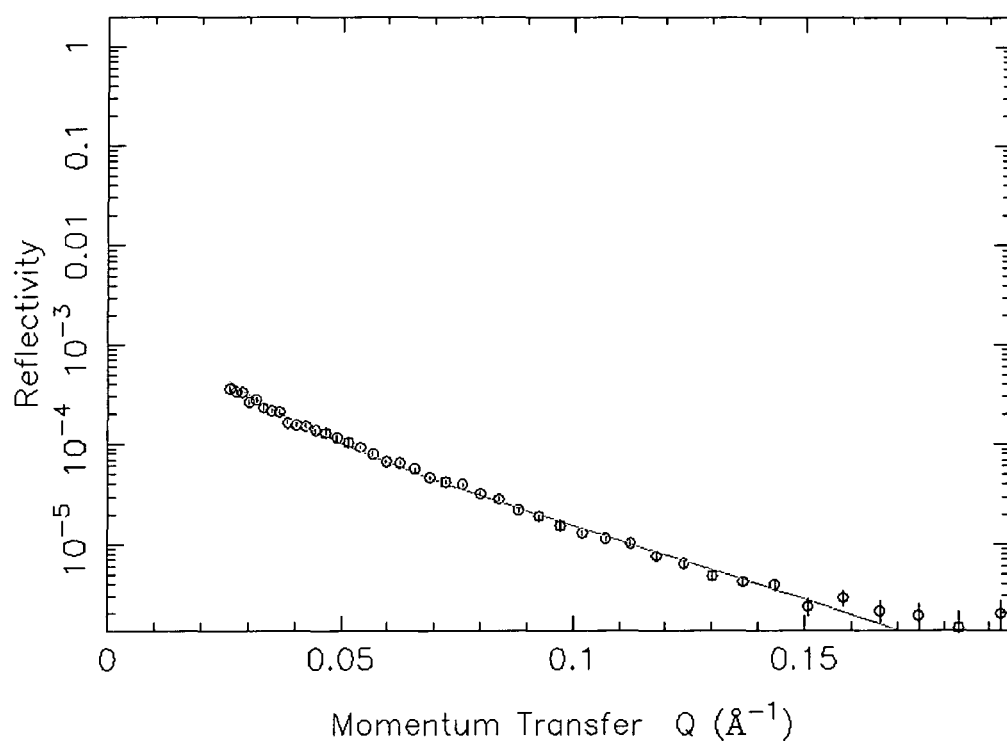
Figure 6.3.32. Typical maximum entropy fit to experimental data for *n25*, 2.0 mg m^{-2}.
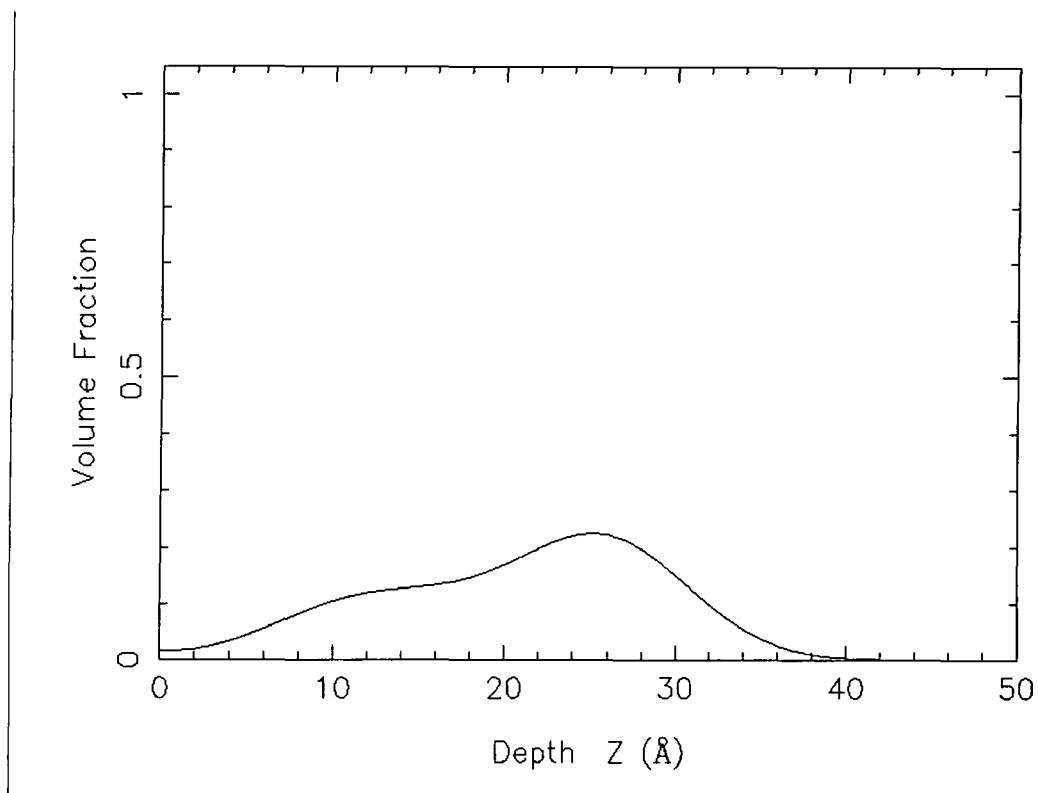
Figure 6.3.33. Composition profile obtained from maximum entropy methods for *n25*, 2.0 mg m^{-2}.

The remaining results obtained from this analysis approach are compared to the layer thicknesses obtained from the optical matrix calculations using the uniform with parabolic decay layer model in table 6.3.15.

Γ_s/mg m^{-2}	model dependent layer thickness		model independent layer thickness	
	layer thickness	$\Gamma_{sEO\,calc}$ / $\Gamma_{s\,EO}$	layer thickness	$\Gamma_{sEO\,calc}$ / $\Gamma_{s\,EO}$
4.0	50 ± 5	0.93	48 ± 3	0.96
3.0	45 ± 4	0.91	43 ± 4	0.94
2.0	40 ± 2	0.99	36 ± 2	0.89
1.0	30 ± 2	1.00	28 ± 5	0.92
0.7	20 ± 2	0.95	22 ± 3	0.94

Table 6.3.15. Comparison of results from the model dependent (optical matrix analysis) and model independent (Bayesian analysis) methods.

The layer thicknesses for both the model dependent and independent analysis methods are similar, supporting the model adopted in the earlier fitting procedures and the derived organisation at the surface. As a final check on the validity of the models the surface concentrations were calculated and they also agree within error to the spread films.

6.3.3 Comparison of Copolymer Behaviour to Brush Theory

Whatever model is adopted to analyse the reflectivity data quantitatively, all show that the PEO layer increases in thickness as the surface concentration of graft copolymer increases. Since the PEO grafts are definitely attached at one end to the interface between the subphase and air, the probability that the grafts form a brush like layer seems distinct.

Brush theory introduced in Chapter Two (section 2.3) is based on the premise that a polymer brush minimises the free energy of the system by stretching normal to the tethered interface or surface with increasing grafting density (number of grafts per unit area). The original Alexander[16]-de Gennes[17] scaling theory predicts that the brush height (h) scales as $h \propto N\sigma^{1/3}$, where N is the degree of polymerisation and σ is the grafting density (number of grafts per unit area). In the analytical self-consistent field theory of Milner, Witten and Cates[18,19] the relationship giving similar brush height dependencies is expressed in equation 6.3.34 where v is the excluded volume parameter.

$$h = \left(\frac{12}{\pi^2}\right)^{1/3} N(\sigma v)^{1/3}$$

Equation 6.3.14.

If the tethered chains are interacting and strongly stretched, then the behaviour of the system should theoretically follow equation 6.3.14. Therefore an increase in brush height is expected as a function of both increasing grafting density and degree of polymerisation of the graft. At a fixed grafting density therefore the layer height should scale as N and at a fixed graft length the brush height should exhibit a cube root dependence with surface density. The polymer height also depends on the solvent quality

(v) and equation 6.3.14 holds when the brushes are immersed in a good solvent. If the solvent quality is reduced at a fixed grafting density the brush height will decrease. As the solvent approaches theta conditions, v reaches zero, the equation above breaks down as additional energies are required to compensate for compression of the brush layer. However in this study the grafts are immersed in water, which is a good solvent for PEO, therefore the above relationship can be applied.

The self-consistent field theory has been extended by Shim and Cates[20] to include high surface densities ($\sigma > 0.70$) by considering finite extensibility of the chain and a modified elastic term. They found that the density profile is a little flatter at moderate ($0.025 \leq \sigma \leq 0.7$) to high ($\sigma \geq 0.7$) grafting densities than the pure parabolic distribution, and equation 6.3.14 remains valid for the majority of surface concentrations. The dependence only diverges when the surface density is close to saturation (i.e. $\varphi \approx 1$) where the brush height is predicted to scale uniformly with grafting density i.e. $h \propto M\sigma$, and the brush can crudely be pictured as slab of material.

The data obtained in this chapter cover over an order of magnitude in surface density and nearly a fourfold increase in molecular weight, thus allowing both dependencies on brush height to be examined individually.

In order to compare the results to the theoretical predictions the surface density values that correspond to the surface concentrations need to be determined. Surface density is directly proportional to the surface concentration (Γ_s) and values were calculated for the copolymer system by assuming that every PEO graft is immersed in the subphase and by applying equation 6.3.15.

$$\sigma = \frac{\Gamma_s N_A X}{m_n} \times 10^{-23} \quad \text{chains per Å}^{-2} \qquad \textbf{Equation 6.3.15.}$$

where m_n is the average mass of one repeat unit, X is the number of grafts on each molecule (always 50) and N_A is Avogadro's number.

Consider initially the dependence of layer thickness on surface grafting density of each graft copolymer system. A double logarithmic plot of PEO layer thickness against

grafting density allowed the exponent from a least squares fit to the data to be extracted. The data for each graft copolymer has been plotted in such a form in figure 6.3.34 using the uniform-parabolic decay model total layer thickness obtained from the optical matrix fitting method.
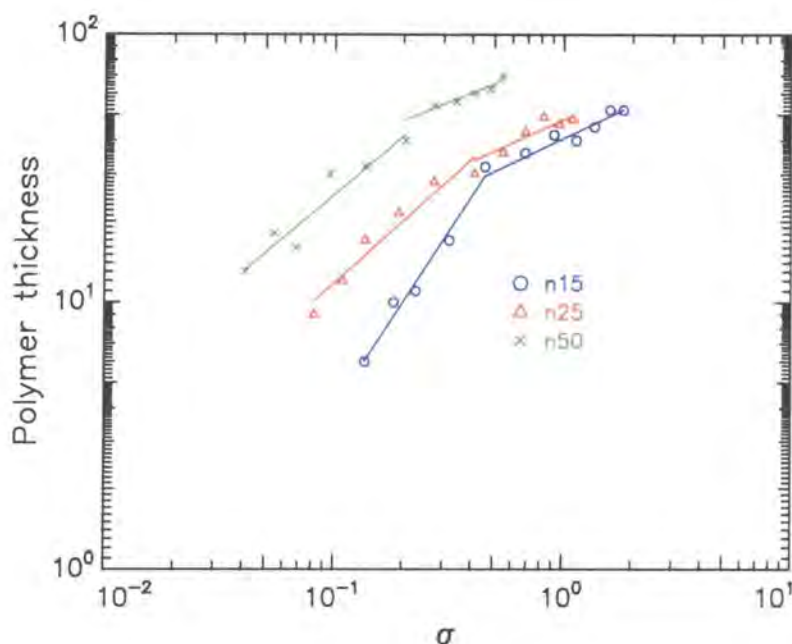
Figure 6.3.34. Double logarithmic plot of PEO layer thickness as a function of grafting density for all copolymers (symbols) and least squares fits to sections of the data are overlaid (lines).

It is evident from this diagram that each graft copolymer exhibits two individual linear dependencies of the PEO layer thickness on the grafting density. The difference in behaviour is possibly due to a phase change which occurs at a distinct grafting density value: approximately 0.46 for *n15*, 0.41 for *n25* and 0.14 chains $Å^{-2}$ for *n50* respectively where all values correspond to the surface concentration of circa 1.0/1.5 mg m^{-2}. The slope of the least squares fitted line in the 0.3-1.0 mg m^{-2} range is 1.32 for *n15*, 0.77 for *n25* and 0.72 for *n50*. All are much larger than the theoretical value of 0.33. For the *n15* copolymer the exponent is very large at 1.32. The difference in the exponents for the graft copolymers is attributed to the stereochemistry of the individual molecules. The *n25* and *n50*

copolymers are estimated (see Chapter Four) to contain an identical ratio of *cis/trans* double bonds in the backbone (66 % *trans*: 34 % *cis*), whereas the shorter graft contains a 50:50 mixture. It has been suggested earlier that the higher *cis* content of the *n15* material will enhance the penetration depth of the individual grafts as a decreased number of tethered chains are required to enter the air phase, and curl over the backbone before submerging in the aqueous phase. Furthermore, since they are shorter they might be more rod-like in character thus leading to a more extended layer thickness than anticipated. It should be noted that there are distinct differences between the theoretical models and the experimental situation that prevails here. Notably, the PEO grafts are of modest molecular weight and thus will have a considerably more stiff, rod like character than the flexible coil characteristics presumed in the theories. Therefore, as the chains begin to move from the two-dimensional surface into the subphase the rate of increase in penetration depth might be higher than expected. Secondly, the theories of the brush layers surrounded by solvent assume the grafts are fixed in their positions on the surface. This is almost certainly not true for the PEO grafts in the spread films over the surface concentration range discussed here, in addition to the capillary wave fluctuations there may be diffusion in the plane of the water surface, producing regions where the grafting density of the water surface (and hence layer thickness) is higher than in other regions. As the surface becomes saturated with tethered PEO the in-plane diffusion of the graft molecules will be reduced. A high near surface packing density is predicted from the model fits for the highest surface concentrations in this regime (i.e. $\Gamma_s \geq 2.5$ mg m^{-2}), where only the distal region of the model (lower layer in the subphase) alters with surface concentration. There was some difficulty in determining the exact crossover point from the first to the second regime, however after careful analysis it was concluded that the switch in behaviour occurs at 1.0 mg m^{-2} for *n15* and 1.5 mg m^{-2} for *n25* and *n50* copolymers. For these higher surface concentrations, the scaling exponent for the dependence of layer thickness in grafting density is 0.33, in agreement with theoretical predictions.

In each copolymer system the change to brush behaviour occurs at a defined grafting density and it was initially thought that this represented a dramatic conformation change, namely a mushroom to brush transition. The volume fraction profiles obtained

from optical matrix analysis however do not corroborate such a defined transition is there is no glaring change in distribution of the molecules. The range of surface concentrations studied by NR (0.3-4.0 mg m^{-2}) corresponds to a change in molecular area of over an order of magnitude, for example the area per PEO graft changes from 434 to 33 Å^{-2} for *n15*, 677 to 51 Å^{-2} for *n25* and 1286 to 96 Å^{-2} for *n50*. Such ranges of molecular areas emphasise the similarity between *n15* and *n25* in comparison to the relatively large area of *n50* which corroborates the results for monolayer thickness (see figure 6.3.21). The area associated with the overlap of individual tethered PEO chains marks the onset of graft interactions and was calculated using the radius of gyration for each PEO chain: 1256 Å^{-2} for *n15*, 1963 Å^{-2} for *n25* and 4072 Å^{-2} for *n50*. Such values are considerably higher than any of those studied here, thus implying that there was significant PEO overlap in each monolayer concentration studied. Interestingly the change in behaviour occurs when the PEO layer thickness obtained from the model fits surpasses the radius of gyration of each graft: $R_{gn15} = 20$ Å at $\Gamma_s = 1.5$ mg m^{-2}, $R_{gn25} = 25$ Å at $\Gamma_s = 1.4$ mg m^{-2} and $R_{gn50} = 36$ Å at $\Gamma_s = 1.2$ mg m^{-2}. The changes in behaviour exhibited in figure 6.3.35 therefore display a distinct dependence on the tethered chain conformation. Dramatic phase transitions have been predicted theoretically[21] and observed experimentally[22] for pancake to brush phases for solid-liquid interfaces. Such sharp transitions were found to be dependent on the strength of the polymer-surface and tethered polymer-grafting block interactions and also on the molecular weight of the of the tethered block. A combination of NR and calculation shows for the graft copolymer studied here that the PEO grafts are always interacting over the surface concentration range investigated therefore a classical mushroom-brush transition is not possible. It is predicted that at low surface concentrations the grafts are interacting predominantly in the plane of the surface with a few chains penetrating the subphase. This concurs with NR results, as the near surface volume fraction is high but the fraction of polymer present deeper in the subphase is considerably smaller. Results also show that the volume fraction increases as the monolayer is compressed the volume fraction increases indicating that the chains become more tightly packed on the surface hence the fraction extending into the water phase increases. It is thought that the chains reach a critical point where the surface becomes saturated with polymer and all PEO chains are in the subphase,

therefore the only change in conformation available to the chains is to stretch normal to the surface into the subphase. This process occurs in order to minimise Gibbs free energy as the energy gain obtained from maximising monomer/monomer interactions surpasses the loss of entropy as the chains begin to stretch and order normal to the surface. This critical conformation has been associated with the concentration where the PEO layer thickness concurs with the radius of gyration of the individual grafts. Therefore the sharp transition observed in figure 6.3.34 does not represent a classical change from isolated swollen mushrooms to stretched brush, but simply marks a change in response of the copolymer organisation to monolayer compression, i.e. predominantly 2-dimensional in-plane packing to 3-dimensional stretching normal to the surface.

The linear dependence predicted by Shim and Cates[20] has not been observed over the range of surface concentrations investigated here. This is reasonable as overall the volume fraction of the PEO containing region is still increasing (predominantly in the lower region of the polymer brush), hence the total layer cannot be modelled as a slab of material. Interestingly however the volume fraction profiles observed here agree well with the flat-parabola predicted by this theory. It is envisaged at higher surface concentrations that the volume fraction of the graft copolymer brush layer would be close to unity, hence at this point the grafts behaviour would be expected to agree with the modified theory.

Consider now the PEO layer height dependence on the degree of polymerisation, N, of the PEO chain. For constant grafting density (for example $\sigma = 0.35$), the PEO layer thickness as a function of N is plotted in figure 6.3.36 and the linear least squares fit gives $h \propto N^{1.06}$. This dependency is in excellent agreement with that of brush theory thus confirming that the PEO grafts are behaving as stretched wet brushes in the high concentration regime. This grafting density is typical of the behaviour throughout the high surface concentration range.
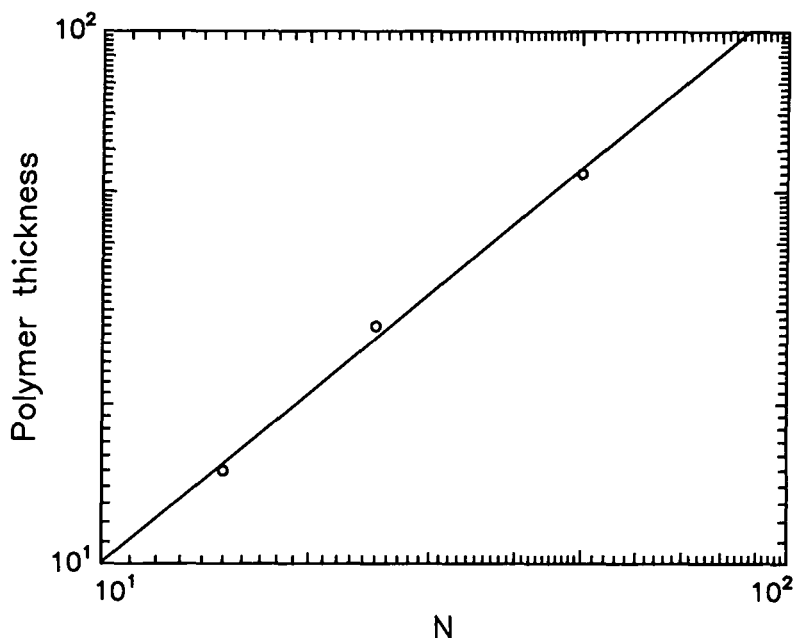
Figure 6.3.35. Double logarithmic plot of PEO layer thickness as a function of molecular weight at a grafting density of 0.28 and least squares fits to sections of the data are overlaid (line).

Neutron reflectometry has been applied to various amphiphilic polymer systems in attempt to test brush theory for example linear block copolymers of poly (methyl methacrylate)-poly (ethylene oxide) (PMMA-PEO) were spread at the air water interface[23]. It was found that the two blocks are mixed at low coverage but occupy separate layers at high concentrations, where the PMMA resides on the uppermost surface while the PEO enters the subphase. No brush behaviour was observed however. Another more pertinent example involves a graft copolymer where the backbone was PMMA and the pendent grafts were PEO[24], each containing 54 ± 2 EO monomers. The amphiphilic nature and graft length of this material is close to the *n50* copolymer used in this work, however the grafting density was random and considerably lower than that of *n50*. The PMMA-*g*-PEO copolymers organise in a manner akin to the well-defined PNB-*g*-PEO materials as the hydrophobic component occupies the uppermost layer while the grafts penetrate the subphase. The MMA containing layer remains fairly constant throughout monolayer

compression while the graft extend further into the subphase. Furthermore as the grafting frequency on individual molecules increased the PEO layer thickness increased. The depths explored however were all considerably lower than the values observed for *n50* material where grafting frequency is maximised (on individual molecules). The data were related to brush theory and although a dependence on surface density was observed the data were highly scattered about the least squares fit and the majority of points were in too narrow a range of surface coverage to identify the exponent. When the grafting densities are compared to those investigated in the work presented here, then polymer brush behaviour would not be expected as the grafting density for each study was lower than 0.41, the critical value observed in this study.

There have been numerous studies where the tethered polymers immersed in a good solvent have been used to test scaling predictions and they have had mixed success. Kent and co-workers[25-28] have studied similar dependencies using diblock copolymers at fluid interfaces and they did not observed the predicted scaling behaviour, but rather weaker dependencies on molecular weight and surface density ($h \sim M^{0.86}\sigma^{0.22}$). Agreement with scaling predictions was achieved by Taunton and co-workers[29] and Field[30] et. al. In their work neither the surface density or molecular weight was varied independently and it has been suggested by Kent[27] that such studies did not constitute a rigorous test. Therefore, to our knowledge this work is the first study where excellent agreement has been observed with limiting scaling behaviour and SCF theory for the dependence of tethered chain thickness where both the grafting density and graft length have been varied independently.

This work indicates that high grafting densities are required to induce polymer brush behaviour, and this is a quality exhibited in the graft copolymers with high grafting frequencies when spread at moderate to high surface concentrations.

6.4   Conclusions

Neutron reflectometry has been applied to elucidate the molecular organisation of thin films of the series of graft copolymers spread at the air - water interface. Three different methods have been employed to analyse the data including the model dependent optical matrix analysis method and the kinematic approximation. Furthermore the copolymer distribution was determined using the model independent Bayesian analysis method.

All methods applied predicted that when the graft copolymer formed a monolayer at the air - water interface the hydrophobic backbone sat on the uppermost surface of the water allowing the PEO grafts to penetrate the subphase. The PNB occupied a thin layer in the upper phase of constant thickness (circa 5 Å), while the PEO grafts penetrated the subphase at all surface concentrations. The optical matrix and PEO self-partial structure factor analysis methods best describe the PEO distribution from the interface with an uniform layer plus parabolic decay model. Such polymer distribution was verified by using the free form fitting method using Bayesian analysis. All analytical approaches provided detailed information regarding the distribution of PEO molecules, namely the volume fraction profile and extent to which they extend into the subphase. Such results prove that neutron reflectometry data can be successfully interpreted using simple models provided realistic models are adopted and their validity is tested rigorously.

As each monolayer was compressed an increase in the thickness of both PEO containing layers was observed. Moreover at high surface concentrations a dependence on graft length was also noted, i.e. the higher the degree of polymerisation of the graft chain the greater the exploration depth of the chain into the subphase. Number densities of PEO extracted from the model fit, comprising of a uniform layer with parabolic decay, to the reflectivity were able to account for 95-100 % of the PEO actually spread on the water surface. As the surface concentration was increased, the reduction in separation distance between the PEO grafts was accompanied by an expulsion of water from the PEO containing layer and a stretching of the grafts deeper into the subphase. Such behaviour is reminiscent of the stretching of polymer brushes, therefore the results obtained were

compared to recent theoretical predictions and for the extent of stretching was examined as a function of grafting density and also graft chain length.

At low surface coverage the linear dependency of graft stretching predicted by theory was not obtained, rather a stronger dependency was observed, possibly due to the modest graft length or the 2-dimensional mobility of the chains on the surface. A sharp transition was observed at circa 1.0 mg m^{-2} where the rate of stretching of PEO into the subphase changed. At higher surface concentrations the scaling exponent extracted concurs exactly with the cube root dependence predicted theoretically. The transition observed is expected to represent a change in conformational rearrangement as the molecules at low surface concentration pack predominantly in 2-dimensions, while at higher surface concentrations the only way the molecules can respond to monolayer compression is to stretch normal to the interface. The copolymer system also exhibits a dependency of brush thickness with graft molecular weight as the exponent extracted from experimental data is close to unity. The pendent chains on the graft copolymer therefore stretch in accordance with both scaling and self-consistent field polymer brush theory as they follow the relationship: $h \propto N^{1.06} \sigma^{0.35}$.

The water self-partial structure factor exhibited unusual behaviour due to an error in the set-up of the experimental apparatus and this unfortunately prevented information regarding the distribution of water molecules to be obtained.

Section 6.5   References

1) Russel, T. P. *Materials Science Reports* **1990** *5*, 171.

2) Lu, J. R.; Simister, E. A.; Thomas, R. K.; Penfold, J. *J. Phys Chem.*, **1992**, *97*, 6024.

3) Lu, J. R.; Simister, E. A.; Thomas, R. K.; Rennie, A. R.; Penfold, J. *Langmuir*, **1992**, *8*, 1837.

4) Sivia, D. S.; Webster, J. R. P. *Physica B*, **1998**, *248*, 327.

5) Sivia, D. S *Data Analysis: a Bayesian Tutorial,* Oxford Univ. Press, Oxford, **1996**.

6) Henderson, J. A.; Richards, R. W.; Penfold, J.; Thomas, R. K. *Macromolecules*, **1993**, *26*, 65.

7) Higgins, J. S.; Benoit, H. C. *Polymers and Neutron Scattering*, Oxford, Science, Oxford, UK, **1994**.

8) Lee, E. M.; Milnes, J. E. *J. Appl. Cryst.,* **1995**, *28*, 518.

9) Crowley, T. L.; Lee, E. M.; Simister, E. A.; Thomas, R. K.; Penfold, J.; Rennie, A. R. *Colloids and Surfaces,* **1990**, *52*, 85.

10) Henderson, J. A.; Richards, R. W.; Penforld, J.; Thomas, R. K.; Lu, J. R. *Macromolecules*, **1993**, *26*, 4591.

11) Henderson, J. A.; Richards, R. W.; Penfold, J.; Thomas, R. K. *Acta Polymer,* **1993**, *44*, 184.

12) Richards, R. W.; Rochford, B. R.; Webster, J. R. P. *Faraday Discussions*, **1994**, *98*, 263.

13) Peace, S. K. *Ph.D. Thesis,* University of Durham, **1992**.

14) Peace, S. K.; Richards, R. W.; Kiff, F. T.; Webster, J. R. P.; Williams, N. *Polymer,* **1999**, *40*, 207.

15) Brown, A. S. *Ph.D. Thesis,* University of Durham, **1999**.

16) Alexander, S. J. *J. Phys. (Paris)*, **1977**, *38*, 977.

17) de Gennes, P. G. *Macromolecules,* **1980**, *13*, 1069.

18) Milner, S. T.; Witten, T. A.; Cates, M. E. *Macromolecules.*, **1988**, *21*, 2610.

19) Milner, S. T.; Witten, T. A.; Cates, M. E. *Macromolecules.*, **1989**, *22*, 853.

20) Shim, D. F. K.; Cates, M. E. *J. Phys. France*, **1989**, *50*, 3535.

21) Szleifer, I. *Europhysics Lett.* **1998**, *44*, 721.

22) Ou-Yang, D.; Gao, Z. *J. Phys.* **1991**, *1*, 1375.

23) Gissing, S. K.; Richards, R. W.; Rochford, B. R. *Colloids and Surf. A: Physicochemical and Eng. Aspects,* **1994**, *86*, 171.

24) Peace, S. K.; Richards, R. W.; Taylor, M. R.; Webster, J.R.P.; Williams, N. *Macromolecules,* **1998**, *31*, 1261.

25) Kent, M. S.; Lee, L. T.; Farnoux, B.; Rondelez, F. *Macromolecules,* **1992**, *25*, 6240.

26) Kent, M. S.; Lee, L. T.; Factor, B.; Rondelez, F.; Smith, G. S. *J. Chem. Phys.* **1995**, *6*, 2320.

27) Kent, M. S.; Lee, L. T.; Factor, B. J.; Satija, S.; Gallagher, P.; Smith, G. S. *Macromolecules,* **1996**, *29*, 2843.

28) Kent, M. S. *Macromol. Rapid Commun.* **2000**, *6*, 21.

29) Taunton, H. J.; Toprakcioglu, C.; Fetters, L. J.; Klein, J. *Macromolecules,* **1991**, *23*, 571.

30) Field, J. B.; Toprakcioglu, C.; Ball, R. C.; Stanley, H.P.; Dai, L.; Barford, W.; Penfold, J.; Smith, G.; Hamilton, W. *Macromolecules,* **1992**, *25*, 434.

31) Auroy, P.; Auvray, L.; Leger, L. *Phys. Rev. Lett.* **1991**, *66*, 719.

Chapter Seven

Monte Carlo Simulations

Section 7.1   Introduction

Monte Carlo simulations of an amphiphilic graft copolymer at a model air-water interface have been performed to determine the interfacial behaviour and the results are presented in this chapter. All the simulation work outlined here was undertaken in collaboration with Dr. M. R. Wilson[1], currently at Durham University.

The aim of this collaborative study was to obtain an understanding, on a molecular level, of the interfacial organisation of polynorbornene-g-poly(ethylene oxide) (PNB-g-PEO) when spread at an air-water interface and the effect of lateral compression. To this end Monte Carlo simulations were used to model the behaviour of the amphiphilic copolymer when free at a hydrophobic-hydrophilic surface and subsequently a geometrical restraint was introduced on the molecules so they were confined within a predetermined volume. The volume available to the molecules was varied in an attempt to reproduce the experimental surface concentrations. A combined effort to analyse the data from simulations produced predictions of the layer thickness and polymer density distribution as functions of surface density of the grafted chains. These characteristic parameters were subsequently used to generate sample reflectivity profiles, which were compared directly with experimental data under identical surface concentrations.

This collaboration was established after Dr. Wilson accepted the challenge to design a simulation model that emulated a polymer monolayer spread at an air-water interface. This simulation model is described in the first section of this chapter where a brief outline of the Monte Carlo simulation procedure is also given. Since all calculations were completed by Dr Wilson[1] only a brief synopsis of the procedure will be presented here, and in addition the basic functions of the programs used at each step in the calculation are summarised in the second section of this chapter. On completion of each calculation I analysed the raw data therefore greater emphasis is placed on the third section where all results from the simulation studies are presented. In this section the criteria and selection of the optimal model is initially discussed. Furthermore the equilibrium conformation of the copolymer is discussed paying particular attention to the behaviour of the poly (ethylene oxide) (PEO) grafts as a function of lateral confinement. Finally the results obtained are compared to the physical system where

molecular organisation normal to the interface has been studied using neutron reflectometry (NR) (see Chapter Six).

Section 7.2   Model System

All Monte Carlo (MC) simulations were carried out using the model system that is represented schematically in figure 7.2.1. The copolymer used was PNB-*g*-PEO and is shown in figure 7.2.2. In all calculations the backbone consisted of 10 norbornene units each having a pendent graft containing 25 ethylene oxide (EO) monomer units. The backbone here is short in comparison to those used in experimental studies but inclusion of a material with a full-length backbone (50 norbornene units) would increase computer time considerably. Despite this restriction the model was still an appropriate approximation to the experimental system and also *n25* (middle copolymer) was expected to represent the series of copolymers analysed experimentally. In addition, available computer time limited the number of copolymer molecules included in the simulation to one, and rather than explicitly represent large numbers of water molecules in the calculation, a simplified model for the air-water interface was developed. In an attempt to imitate the hydrophobic/hydrophilic nature of such an interface, energy penalties were imposed (hard wall potentials) on each component of the amphiphilic material. The hydrocarbon backbone was restricted to occupy the upper phase (air) by imposing an energy penalty to any main chain molecules that entered the lower phase (water). Secondly each EO segment that moved from the water to air phase increased in energy by +8.8 kJ mol^{-1}. This value originated from the heat of solvation of an EO unit (5.3-8.8 kJ mol^{-1})^{2}. The thermodynamics of the water surface also needed to be included in the model i.e. the surface activity of the PEO required to be accounted for since thermodynamically PEO is driven to the air-water interface as it reduces the surface tension of water. This was done by introducing a potential well into the model system with a depth that was varied between 0 and 5 kJ mol^{-1}. To simulate the influence of the additional polymer molecules at the surface the copolymer was confined into the cylinder of radius b, by a second hard wall potential. The experimental effect of monolayer compression was easily imitated by varying the lateral confinement of the molecule in the simulation cell simply by varying the cylinder radius.

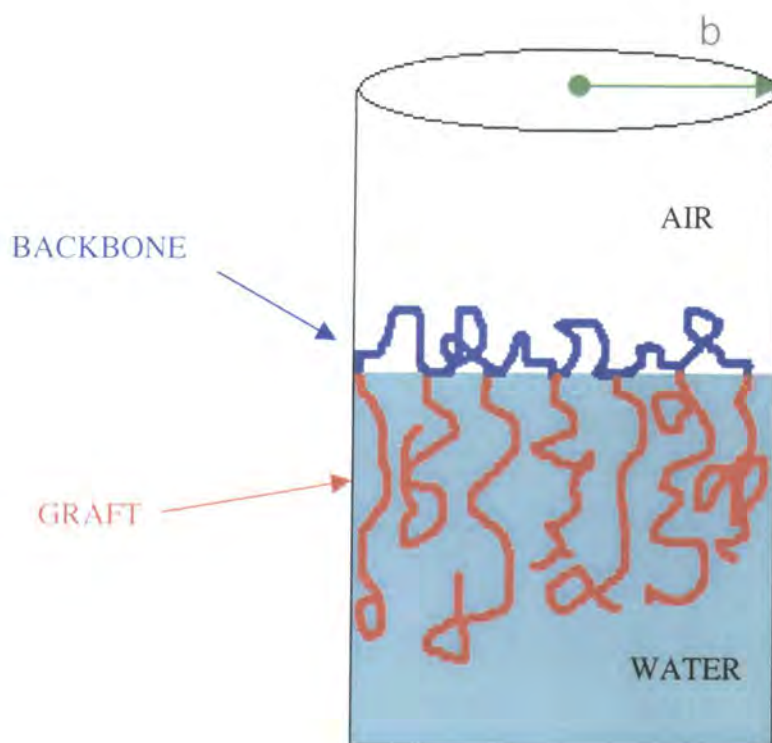**Figure 7.2.1.** Schematic representation of the model system used in the MC calculations where b, the radius of the cylinder, is variable.
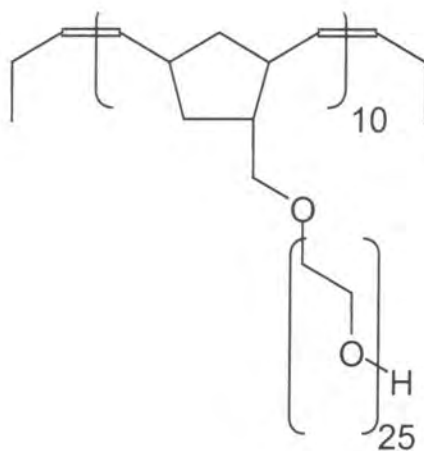

Figure 7.2.2. Schematic diagram showing the copolymer polynorbornene-*g*-poly (ethylene oxide) used in all Monte Carlo calculations. Two models were used, one with an all *trans* double bond in the backbone and one with a *trans-trans-cis* repeat pattern.

The geometry of the amphiphilic copolymer was represented by a series of atomistic potential energy functions,

$$E_{total} = \sum_{angle} K_\theta (\theta - \theta_{eq})^2 + \sum_{dihedral} \sum_{m=1}^{3} \frac{V_m}{2} [1 + \cos(m\varphi - \delta_m)] \sum_{i<j} \left(\frac{q_i \cdot q_j}{Dr_{ij}} + \frac{A_{ij}}{r_{ij}^{12}} - \frac{C_{ij}}{r_{ij}^6} \right) f_{ij}$$

Equation 7.2.1.

where θ and θ_{eq} are the actual and equilibrium bond angles, φ and δ_m are dihedral and phase angles, and K_θ, V_m are force constants representing bond bending and torsional motion respectively. A Coulomb plus Lennard-Jones potential was used to represent the energy between two non-bonded atoms i and j at a distance r_{ij} where the terms A_{ij} and C_{ij} can be expressed in terms of the well-depth (ε_{ij}) and collision parameters (σ_{ij}): C_{ij} ($C_{ij} = 4\varepsilon_{ij}\sigma_{ij}^6$) and A_{ij} ($A_{ij} = 4\varepsilon_{ij}\sigma_{ij}^{12}$) ($f_{ij} = 0.5$ for 1,4 12:6 nonbonded terms, $f_{ij} = 0.125$ for 1,4 electrostatic terms and $f_{ij} = 1$ for all other nonbonded interactions). The parameters in equation 7.2.1 were taken from the *all atom force field* model, OPLS-AA developed by Jorgensen and co-workers[3,4,5]. All bond lengths were constrained to their equilibrium values. Every atom was treated individually in the simulation. This avoids problems encountered in similar systems where hydrogen atoms have been combined with heavier atoms (*united atom* approximation)[6]. D in equation 7.2.1 is the distant dependent dielectric value and was designed to account for the effects of the aqueous solvent by screening the dielectric charges on the ethylene oxide units, thus reducing interchain electrostatic interactions. This approach does not include long range electrostatic interactions, but is still an acceptable approximation for the model system as such electrostatic energy is minimal for the PNB-*g*-PEO material.

Initially three variations of the model system described earlier were used in the MC calculation in attempt to identify the optimal model. The first model included an all *trans* configuration of graft copolymer, which was confined in the cylinder with no potential well, i.e. the surface activity of the PEO was not included. In the second model an all *trans* copolymer was again used but this time the model included the potential well. The third model is more akin to the experimental system as the molecule confined in the cylinder incorporates the stereochemistry of the synthesised material (two thirds

trans and one third *cis* double bonds in the main chain) and the surface activity of the PEO (potential well).

Calculations for each model were carried out for various values of b, which were selected to correspond to the surface concentrations (Γ_s) studied experimentally. The corresponding b and Γ_s values are given in table 7.2.1 and cover a surface concentration range of 0.3-2.5 mg m^{-2}. A limitation of the model prevented a full surface concentration range (encompassing 0.3-4.0 mg m^{-2}) being explored as the copolymer molecule could not be accommodated in the cylinder when b surpassed 15 Å.

b /Å	Surface concentration /mg m^{-2}
100 000	Free molecule
55	0.3
40	0.4
30	0.7
21	1.5
18	2.0
16	2.5

Table 7.2.1. Values of the cylinder radius used in the MC calculations and their corresponding experimental surface concentrations.

Section 7.3   Monte Carlo Simulations

The initial configuration of the copolymer was generated from gas phase energy minimisation calculation using the MM3 molecular mechanics force field in the Cache[7] molecular modelling program. This conformation was subsequently used as the input for the MC simulations. The MC simulation program used was the Durham University molecular modelling package (DUMMP) and all calculations were carried out using Metropolis MC sampling at 300 K which is in accordance with the experimental temperature: 298 K. A typical MC step involved random changes to a randomly selected bond angle θ' and a randomly selected dihedral angle φ' and dihedral angles and the molecule would also undergo a random translation, s', and rotation using quaternion, q'. Further details of this process are given elsewhere[1, 8], suffice to say here that the molecule moved in very small, random steps within the constraints of the model until an equilibrium conformation was reached.

When the initial dimensions of the polymer backbone exceeded the diameter of the cylinder a distance dependent repulsive potential was introduced for atoms at a distance $|r| > b$ from the centre of the simulation cell. The potential was gradually increased until all atoms were enticed into the confines of the cylinder walls, which was usually achieved over circa 1000 MC steps with minimal distortion of the gas phase conformation. Subsequently the copolymer system was allowed to equilibrate over a further 10^6 moves before the next step towards the final equilibrium state was taken. This involved the 'capturing' of the PEO grafts by the 'aqueous' media and typically this process occurred within 2×10^5 MC moves. An example of this process is given in figure 7.3.1 where four snapshots are given that represent the copolymer conformation at various stages of the equilibrium process. The resultant equilibrium conformation was found by continuing MC calculations for a further 25×10^5 trial moves.
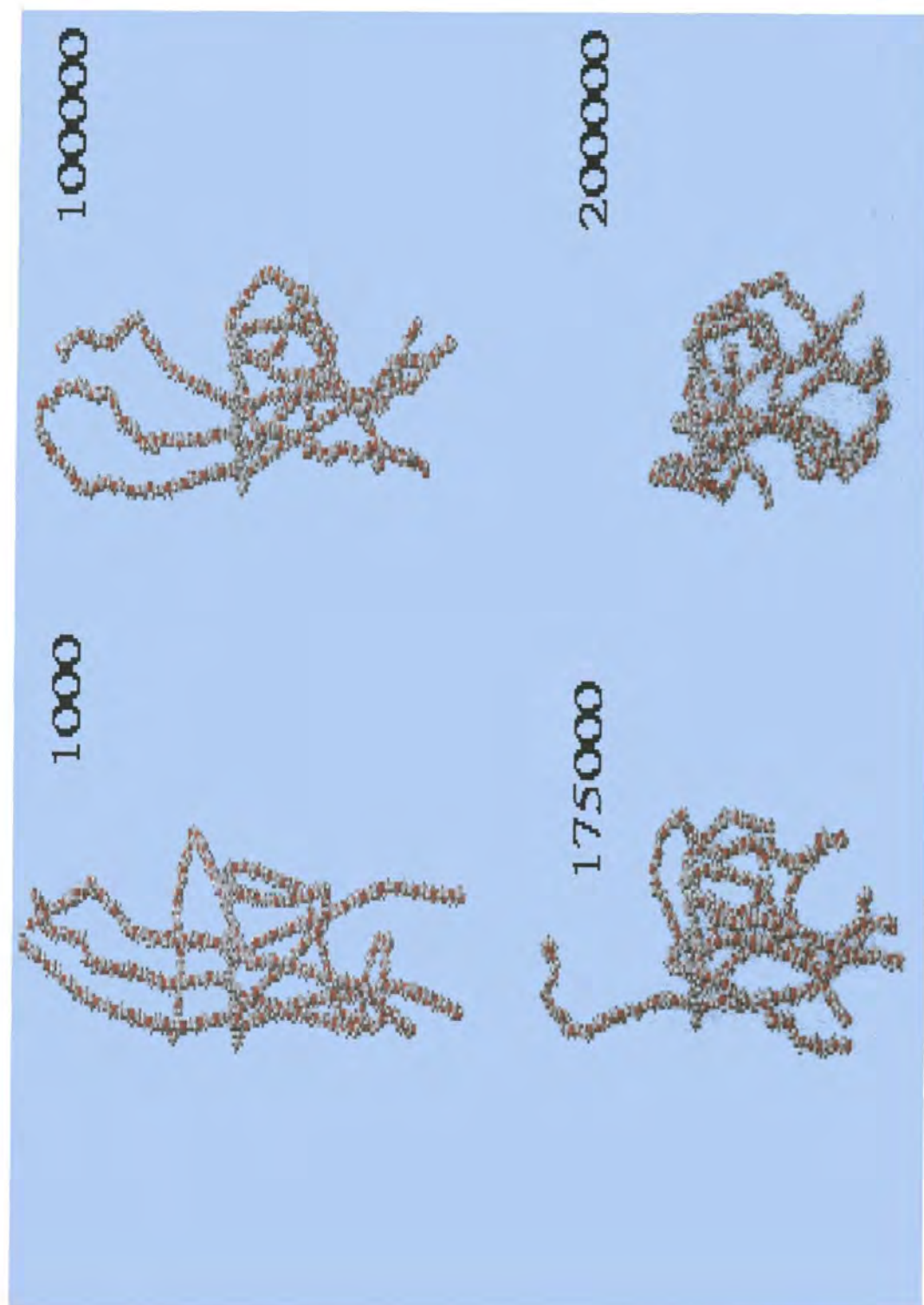
Figure 7.3.1 Typical equilibration process for the copolymer confined to a cylinder of radius b=20 Å. The numbers inset represent the number of MC moves.

Section 7.4   Results and Discussion

The results from Monte Carlo calculations were interpreted to provide a physical picture of molecular distribution, and compared to the parameters obtained from experimental data taken from Chapter Six.

The first step towards obtaining such results was to identify which simulation parameters replicated low surface concentration results to the best extent. This was done by calculating the number density of EO molecules per unit area perpendicular to the surface for each model system. The number density, n, was subsequently substituted into equation 7.4.1 to determine the volume fraction of PEO, ϕ_{EO}, in each unit layer.

$$n_{EO}b_{EO} = \rho_{EO}\varphi_{EO}$$ **Equation 7.4.1**

where ρ_{EO} is the scattering length density ($\rho_{EO} = 6.33 \times 10^{-6}$ Å^{-2}), and b_{EO} the scattering length ($b_{EO} = 4.58 \times 10^{-6}$ Å^{-4}) of the ethylene oxide monomer. Subsequently the scattering length density for each layer (ρ) was determined by applying equation 7.4.2 where the EO volume fraction is multiplied by the scattering length density of deuterated EO monomer

$$\rho = \rho_{EO}\varphi_{EO}$$ **Equation 7.4.2.**

The theoretical reflectivity profile was then calculated using these scattering length densities and an optical matrix method of calculation. The theoretical reflectivities they generate were compared to the experimental data obtained for the part deuterated copolymer spread on NRW to determine the success of the simulation.

Initially, the method was used with a cylinder radius of 57 Å for each model system. The reflectivity profiles generated for each simulation model are compared to the corresponding experimental profile (surface concentration of 0.3 mg m^{-2}) in figure 7.4.1.
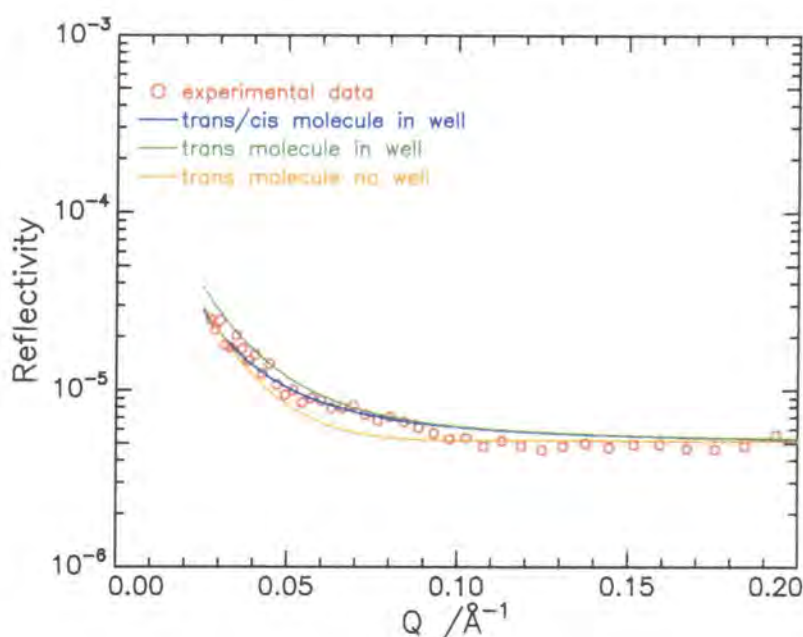
Figure 7.4.1 Comparison of the reflectivity profiles generated from MC calculations for each model system to the experimental profile (part deuterated *n25* on nrw) for a spread concentration of 0.3 mg m^{-2}.

If the simulated and experimental profiles are to represent identical interfacial organisations the profiles must follow similar trajectories of comparable magnitude and reproduce features such as the slope and shape of the profile. Figure 7.4.1 shows that the closest match to experimental data is observed when the attractive potential well is included. Physical characteristics of many polymer materials depend on their tacticity[9,10,11], therefore to determine whether stereochemistry influences organisation of the graft copolymer the reflectivity profiles were examined more closely. Differences between the profiles were evident, the incorporation of the true stereochemistry of the copolymer (6:4 *trans, cis* ratio of double bonds along the copolymer backbone) provided the best match to the experimental data, as expected.

The only variable in the model system that has not been tested thus far is the width allocated to the Lennard-Jones potential well that models for the surface activity of PEO. Values were therefore randomly selected ranging between 1 and 7 Å and MC calculations undertaken for the system with minimal surface coverage (0.3 mg m^{-2}). The validity of each model was tested again by comparing simulated and neutron reflectivity

profiles (see figure 7.4.2). Once the optimal potential well was found for this concentration then application of the simulation method to the remaining surface concentration could be made by varying the radius of the cylinder only, since the surface activity is defined by the potential well. The results given in figure 7.4.2 show that a potential with a depth of -3 kJ mol^{-1} of varying width all provide essentially identical reflectivity profiles as the experimental data. The interfacial organisation therefore appeared to have no dependence on the width of the well. It is also gratifying to note that the near surface molecular organisation of simulation and experiment were very similar (figure 7.4.3).

The simulated data is in good agreement with experimental results as both suggest that the majority of PEO grafts penetrate the 'aqueous' phase, and the chains are solvated to a greater extent as they explore further into the subphase. The volume fraction profiles reveal that the PEO grafts occupy a dense layer at the near surface that has a consistent number density for a depth of circa 5 Å. Thereafter the volume fraction of both simulated and experimental results decrease smoothly towards zero volume fraction, i.e. bulk subphase. The simulated data begins to disagree with neutron reflectometry results since the anticipated length of PEO graft penetration of 15 Å in the MC calculation is greater than the 10 Å predicted experimentally. This disagreement is out with experimental error (± 1 or 2 Å) but occurs in the low volume fraction region in the simulated data and experimentally this equates to a low scattering length density. This difference is discussed later.
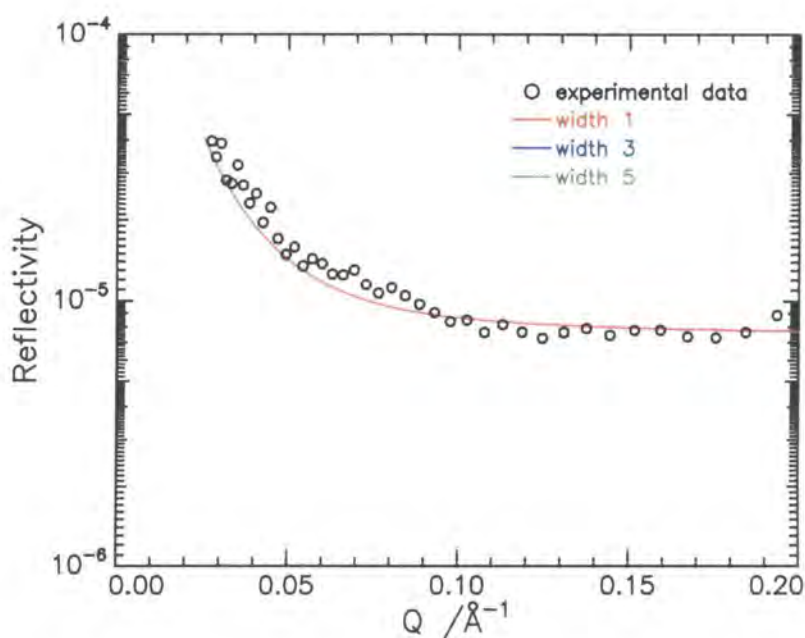
Figure 7.4.2. Reflectometry profiles for various widths of the potential well are compared to the experimental reflectivity profile for a surface concentration of 0.3 mg m^{-2}.
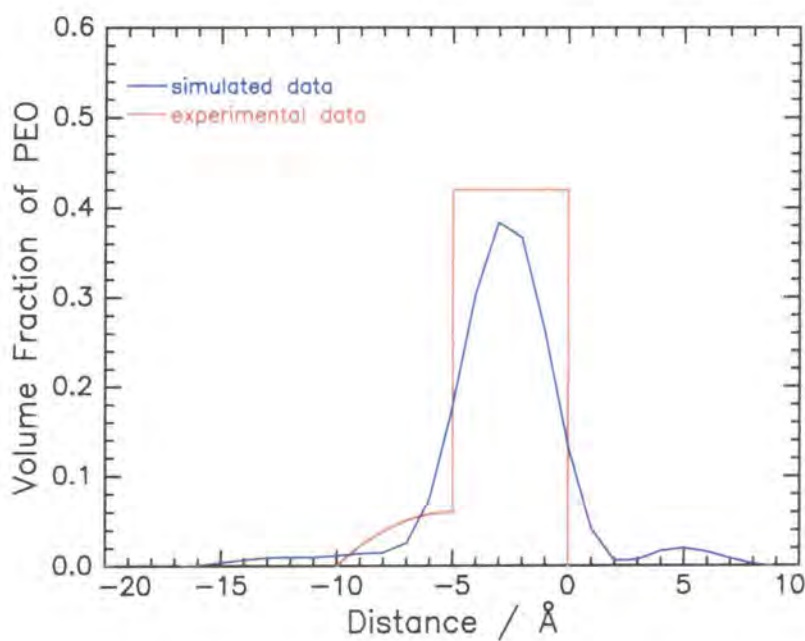

Figure 7.4.3. Comparison of volume fraction profiles for MC simulated and experimental copolymer distributions for a surface coverage of 0.3 mg m^{-2}.

One interesting feature present in the simulated data that has not been included in the model used to fit the neutron reflectometry data is the small hump in the 'air' phase at circa 5 Å. Experimentally this hump accounts for the portion of PEO grafts that curl over the backbone before penetrating the subphase. The driving force for this presumably arises from the energy minimisation as the PEO enters the aqueous phase and such a molecular organisation is clearly seen in the simulation snapshots in figure 7.4.4. Such detailed information is lacking from the experimental profile and is attributed to insensitivity of the neutron technique since the volume fraction of PEO present is small, $\varphi_{EO} < 0.02$ as small changes in either scattering length density of monolayer dimensions are not detected. A further check on the simulation is to calculate the surface concentration by summing the contributions from each layer and using equation 7.4.3.

$$\Gamma_{sTOT} = \sum \frac{n_{EO} dm_{EO}}{N_A} \times 10^{20} \ \mathrm{mg \ m^{-2}} \qquad \textbf{Equation 7.4.3.}$$

m_{EO} is the molecular weight of ethylene oxide monomer, d is the layer thickness, which is unity in each case, and N_A is Avogadro's number. The value calculated ($\Gamma_{sTOT} = 0.278$ mg m^{-2}) compares very favourably with the experimental value ($\Gamma_{sTOT} = 0.27$ mg m^{-2}), indicating that the graft copolymer is completely contained within the simulation cell and is totally accounted for in the volume fraction profile.

At this stage it appears that the MC simulation provides a more detailed description of interfacial organisation in comparison to the models adopted in neutron reflectometry studies as the former technique is able to divide the volume fraction profile into a number of 1 Å layers and is more sensitive to small fluctuations in polymer distribution. In summary, the optimal simulation is one that includes both the surface activity and the microstructure of the copolymer, moreover it provides good agreement between the simulated and experimental reflectivity data and copolymer distribution.

A selection of the results for different surface concentrations are given in pictorial form by a series of snapshots of molecular organisation in figure 7.4.4. When the surface concentration is low ($\Gamma_s = 0.3$ mg m^{-2} figure 4.7.4a) the copolymer essentially has two dimensional freedom and it chooses to lie flat on the 'water' surface

with the PEO grafts fanning out over the surface plane. Results have shown that as the radius of the cylinder decreases, the hard wall constraints impose strict lateral confinement on both the backbone and the grafts. This causes the PEO chains to move away from the surface and they begin to explore the lower phase. Such rearrangement is accompanied by small distortions in the backbone, which induce buckling of the main chain, and no longer lies flat on the surface. If the PEO chains in the *trans* configuration are to minimise their energy and reach their thermodynamic favourite state (i.e. in the subphase), then they are forced to curl over the backbone before penetrating the 'water' phase. This effect is prominent in the snapshot in figure 7.4.4c, where the surface concentration is high (2.0 mg m^{-2}). Comparing the series of snapshots of molecular orientation as a function of lateral compression, qualitative differences in interfacial arrangement are apparent. At low and intermediate surface concentrations the PEO remains close to the surface as the chains are 'curled up' to a considerable degree in a pancake type configuration. As lateral compression increases the chains are forced to stretch normal to the interface as indicated in figure 7.4.4b. In this conformation the grafts are interacting, rather than forming isolated mushrooms on the surface. This is confirmed as the extension of PEO is greater than the radius of gyration of an isolated chain (25 Å for *n25* and the copolymer used in the simulation). Further lateral confinement results in increased extension of the PEO grafts into the water, which is indicative of brush behaviour.

To obtain a quantitative insight into the distribution of the PEO grafts for each calculation, a volume fraction profile was compiled by determining the number density of PEO per unit area perpendicular to the interface and using equation 7.4.1 to calculate the volume fraction for each 1 Å layer. The profiles obtained from the simulation results are compared in figure 7.4.5 where each result is labelled in terms of surface concentration (see table 7.2.1 to equate b values to surface concentrations).
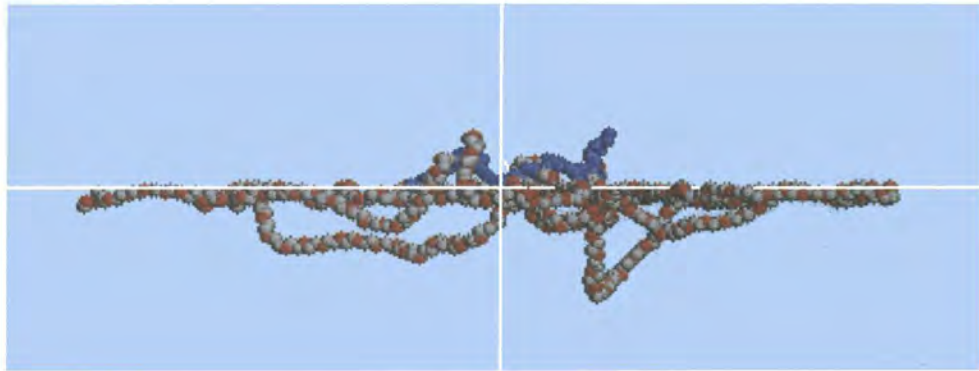
a) Γ_s=0.3 mg m^{-2}

b) Γ_s=0.7 mg m^{-2}

c) Γ_s=2.0 mg m^{-2}

Figure 7.4.4. Snapshots of molecular organisation from MC calculations where the surface concentration is increases from top to bottom.

It is evident from this diagram that the PEO grafts occupy both the upper (positive distance) and lower (negative distance) phases and there is an excess of EO at the surface which appears as a sharp peak at the interface. This surface excess is expected since EO lowers the surface tension of water. Portions of the grafts remain out of the 'water' phase, as they need to curl over the backbone in order to penetrate the subphase. The majority of the PEO however is present in the lower phase and the extent of subphase exploration depth is dependent on the radius of the simulation cell. It is clear from the snapshots in figure 7.4.4 and also from the volume fraction profiles that the penetration depth of the grafts into the subphase increases as the surface concentration increases (decreasing b). Interestingly the shape of the volume fraction profile is similar to that observed experimentally as there is a uniform layer of high volume fraction at the near surface followed by a smooth decay to the bulk subphase. Furthermore the distribution profiles follow similar trends with increasing surface concentration as the thickness of both the uniform near surface layer and decay region increases. In addition to deeper penetration, increased lateral confinement causes an increase in the number density of EO within the subphase, hence this must be accompanied by an expulsion of water from the PEO containing layer. A similar pattern is observed for the PEO resident in the 'air' phase and is attributed to the twisting of the backbone forcing the loops of PEO to protrude further to pack more efficiently before the free end plunges into the 'water'. Although a portion of the PEO graft must be resident in the air phase (as NR reveals that all grafts penetrate the subphase) the increase in volume fraction predicted from the simulation model is not realistic as such high volume fractions of PEO would have been detected experimentally by NR.

An increase in surface concentration results in an increase in the surface grafting density (number of grafts per unit area) by the PEO grafts. The depth of PEO penetration into the 'aqueous' phase as predicted from the MC simulations does not increase linearly with grafting density (assuming all grafts are immersed) over the concentration range studied. Instead the thickness of the PEO containing layer region rises rapidly at low surface coverage ($\Gamma_s < 1.0$ mg m^{-2}) and at high coverage ($\Gamma_s > 1.0$ mg m^{-2}) the rate of stretching changes sharply and the penetration depth increases slowly.
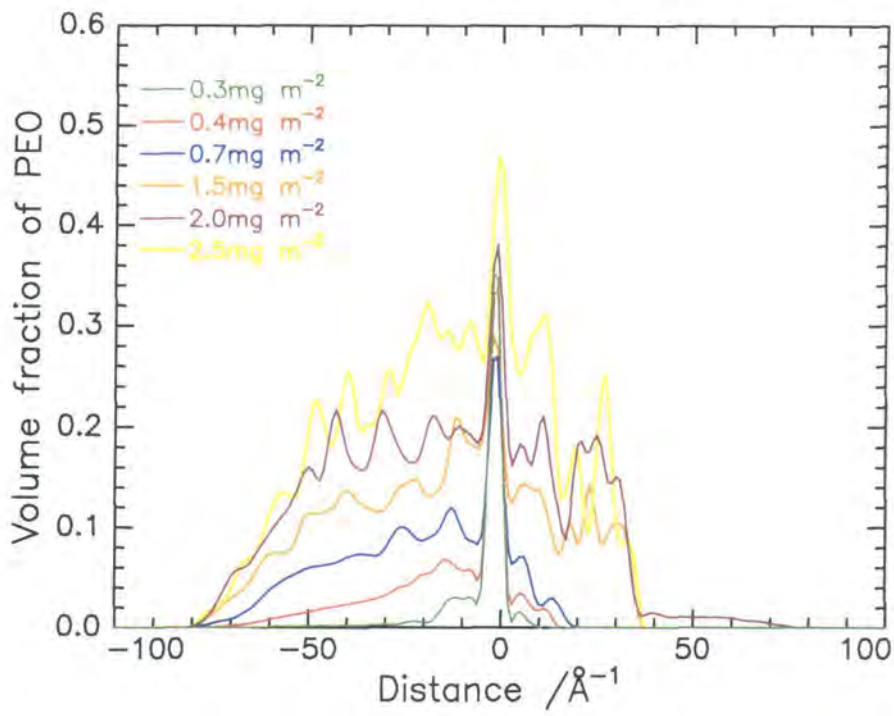
Figure 7.4.5. Comparison of the volume fraction of PEO from MC simulations as a function of surface concentration.
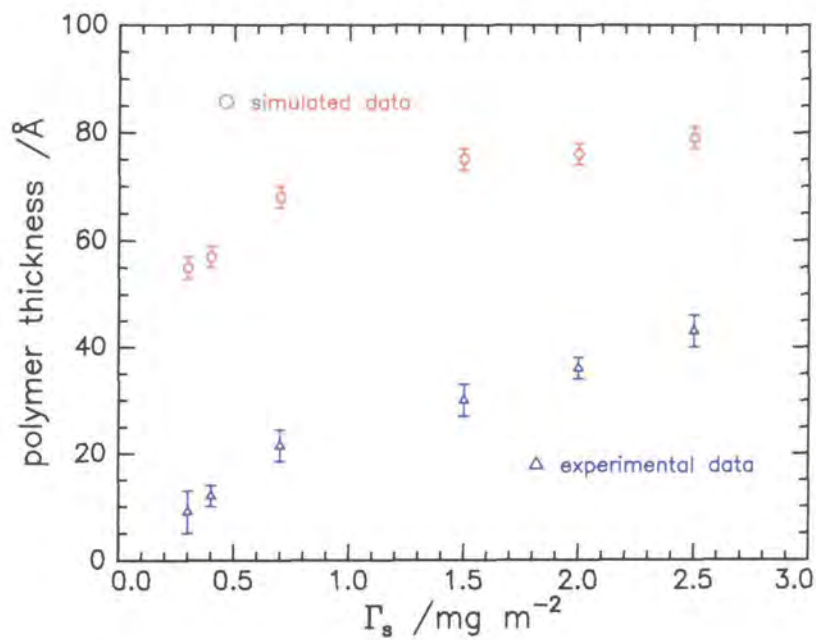

Figure 7.4.6. Comparison of the PEO layer thicknesses obtained from simulation and experimental studies as a function of surface concentration.

The PEO layer thicknesses obtained from MC studies consistently exceed those obtained from neutron reflectometry (NR). However it is extremely pleasing to note that both simulations and experimental work follow identical qualitative trends. Both techniques reveal that the extent of stretching increases rapidly over low surface concentrations, and a dramatic change in behaviour is observed at circa 0.7 mg m^{-2} where the PEO thickness continue to increase but at a reduced rate. Although the magnitude of the maximum PEO penetration depth (circa 80 Å) is high, it is still physically realistic as the value is less than the end to end distance of the fully stretched PEO graft, 96 Å. The radius of gyration of an isolated PEO graft immersed in a good solvent is 25 Å which is considerably lower than the layer thickness of PEO observed in MC simulations for the lowest surface concentrations investigated. This phenomenon suggests that the grafts on the simulated molecule are interacting with each other at all surface concentrations and to compensate for this they stretch away normal the interface. This concurs with the theoretical value where intermolecular interactions are predicted to begin at Γ_s=0.11 mg m^{-2}.
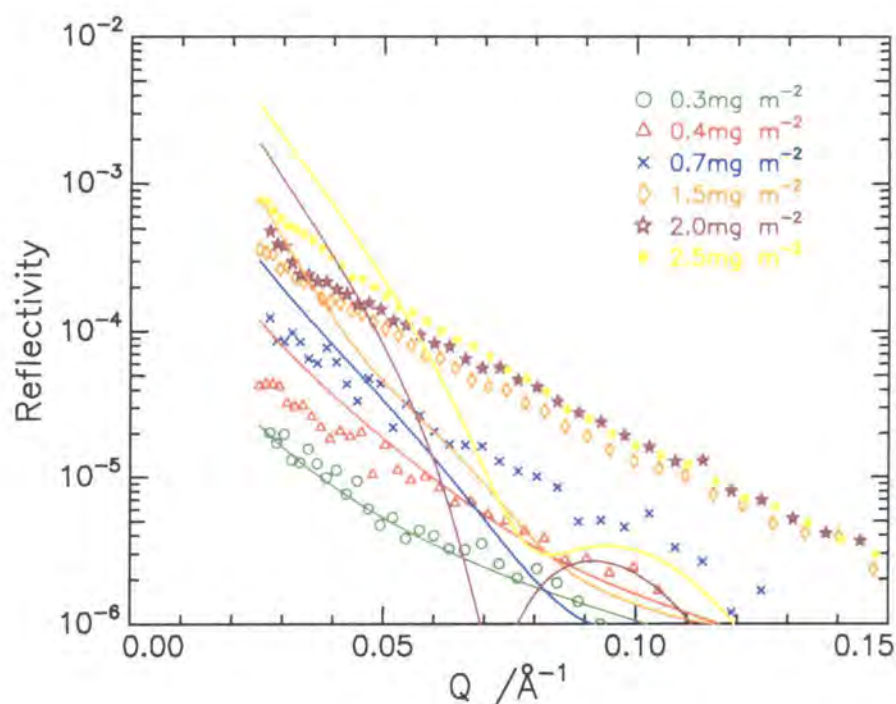

Figure 7.4.7. Simulated neutron reflectivity profiles (solid lines) in comparison to the experimental results (symbols) for a range of surface concentrations.

To emphasise the difference between the two sets of results the neutron reflectometry profiles were simulated for the MC calculations (as outlined earlier) for each surface concentration and are compared to the experimental data in figure 7.4.7. In this diagram the background signal is subtracted from all data and the simulated profiles are represented by the solid lines while the symbols represent the experimental data collected. From this diagram it is clear that the two sets of data only agree at low surface coverage (i.e. only at 0.3 mg m^{-2}). At the highest surface concentrations investigated minima are observed in the profiles and upon further compression the minima move to lower Q, clear symptoms of an overestimation in layer thickness.

The cylindrical simulation cell and model polymer were not sufficiently sophisticated to reproduce the behaviour exhibited by the experimental system. There are distinct differences between the model system and the experimental situation that could account however for the failure of the model adopted. Notably, the model is simplified in comparison to the 'real' system. The copolymer molecule used in the model is one fifth of the molecular weight in the experimental system, therefore any intramolecular interactions that occur between the grafts for example will be reduced in the simulation. This would lead to an inflated PEO thickness. Intermolecular interactions can also occur experimentally therefore physically the polymers are more likely to be entangled and hence a higher surface concentration would be required before stretching comparable to that predicted by the simulation is observed. Secondly, the simulation cell confines the molecule in a pre-determined volume equating to one-fifth of the area per molecule experimentally. This is almost certainly not the case for the copolymer in the spread films as the molecule is not restricted to any single region in the film but has two-dimensional freedom (at low Γ_s < 1.0 mg m^{-2} but as the monolayer is compressed further the near surface becomes densely packed). In addition to the capillary wave fluctuation there may be in plane diffusion which would lead to patches of the spread film that have a high grafting density, hence higher layer thickness, than in other areas. The highly dense layers might be limited to small regions of the film hence the results from neutron reflectometry studies might be dominated by the lower grafted regions and the dimensions obtained will be more characteristic of these regions than those of the whole film. Theoretically, a constant potential was associated with the near surface layer to account for the lowering of the surface tension by PEO. In reality the thermodynamics of the surface are more complex as indicated by

the surface pressure isotherm, where the surface pressure rises rapidly until circa 1.5 mg m^{-2} whereupon it reaches an asymptotic plateau (see Chapter Four). There are various other factors that contribute to the thermodynamics of the near surface including the competition between the excluded volume interactions between neighbouring grafts that induce chain stretching and the entropy penalty associated with the chains moving from their random walk dimensions. Such factors are difficult to isolate and hence have not been included in the simulations.

Section 7.5   References

1)   Miller, A. F.; Cook, M. J.; Richards, R. W.; Wilson, M. R. *unpublished results.*

2)   Orwoll, R.A. *Chapter VII, Polymer Handbook, 4th Ed.* **1999**, 649.

3)   Jogensen, W. L.; Maxwell, D. S.; Tirado-Rives, J. *J. Am. Chem. Soc.*, **1996**, *118*, 11225.

4)   Jogensen, W. L.; Maxwell, D. S.; Tirado-Rives, J. *Support material from J. Am. Chem. Soc.*, **1996**, *118*, 11225.

5)   Jorgensen, W. L.; Nguyen, T. B. *J. Comput. Chem.*, **1993**, *14*, 195.

6)   Tobias, D. J.; Tu, K.; Klein, M. L. *Curr. Opin. in Colloid and Inter. Sci.,* **1997**, *2*, 15.

7)   *CAHChe Satellite: A chemists Guide to CAche for Window ,***1995**, Oxford Molecular Group Inc.

8)   Wilson, M. R. *Liq. Cryst.* **1996**, *21*, 437.

9)   Brinkhuis, R. H. G.; Schouten, A. J. *Macromolecules*, **1991**, *24*, 1487.

10)   Brinkhuis, R. H. G.; Schouten, A. J. *Macromolecules*, **1992**, *25*, 2725.

11)   Grohens, Y.; Brogly, M.; Labbe, C.; Schultz, J.; Prudhomme, R. E. *Macromolecular Symposia*, **1997**, *119*, 165.

Chapter Eight

Surface Quasi-Elastic Light Scattering

Section 8.1   Introduction

The propagation characteristics of the capillary waves and the viscoelastic properties of spread films of each graft copolymer have been probed using surface quasi-elastic light scattering (SQELS). This chapter reports the results from three separate SQELS experiments and each is discussed in turn.

Firstly, a time dependence experiment was undertaken for monolayers of each copolymer at a fixed wavenumber, q, to assess the homogeneity and stability of the films at fixed surface concentrations. The propagation characteristics of each film were extracted using the damped cosine fit[1] and these results are reported as a function of time.

Secondly, the surface concentration dependence of the dynamic properties of each copolymer were probed using a wave mode of fixed q, where $q = 350 \pm 2$ cm^{-1}. The variation in the frequency and damping of the capillary waves as a function of surface concentration is initially reported and subsequently values for the viscoelastic parameters, namely the surface tension, dilational modulus and the dilational viscosity (extracted using the spectral fit[2]) are given. These results are presented initially for *n25* and are followed by a discussion where the findings are compared to the remaining copolymers in the series. In this section the dynamic behaviour of the surface waves are correlated to copolymer architecture and monolayer organisation.

The third study involved analysing both the capillary wave propagation and viscoelastic parameters as a function of q and the results from the damped cosine and spectral fits are presented for all copolymers before being interpreted.

Finally the characteristic behaviour of the studies is summarised and the influence of surface concentration, surface frequency and graft length is discussed.

Section 8.2   Time Dependence

To ascertain whether the copolymer forms laterally homogeneous monolayers, or 'islands' when spread at the air-water interface, correlation functions were repeatedly recorded at regular time intervals (circa 5 minutes) over a period of 24 hours. A typical normalised correlation function is given in figure 8.2.1 where the circles are the experimental data for a monolayer of *n25* with a surface concentration of 0.3 mg m^{-2} obtained at 348 cm^{-1}, and the solid line is the fit of the damped cosine function (see Chapter Three for further details). The residuals of the fit are given in figure 8.2.2 and it is clear that the fit is not only reasonable, but there is minimal (0.001 %) deviation from the experimental data. Such behaviour is typical of all delay times analysed in this study. If inhomogeneity was present in the film then it would be detected by observing fluctuations in the frequency and damping values as the incident beam either samples clean water or the polymer film. Furthermore dispersion of material into the subphase would induce a consistent variation in the propagation characteristics over time.

Each correlation function obtained was analysed and values for the frequency and damping obtained. A range of surface concentrations (between 0.08 and 5.0 mg m^{-2}) were probed at circa 350 cm^{-1}, and the damping results for 0.3 and 2.0 mg m^{-2} films are given in figure 8.2.3. These findings are representative of the series of copolymers and also of the surface concentration range studies: 0.1-5.0 mg m^{-2}. The results from both monolayers reveal there is no damping (or frequency) dependence on time within a ten hour period as there is little variation in the magnitude of either propagation parameter, within the boundaries of experimental error. This behaviour suggests that both films are coherent and there is no relaxation or dissolution of materials into the subphase over time. The results for the higher surface concentrations, for example, Γ_s = 2.0 mg m^{-2} also eliminate the possibility that the copolymer molecules form aggregates, or bilayers on the surface at higher coverage since there appears to be no variation in the damping of the capillary wave.

The stable nature of the films determined using light scattering agrees well with similar surface pressure studies (Chapter Five). In the latter experiments however measurements were taken immediately after spreading the film and a small relaxation over the initial 10/15 minutes was observed, which was attributed to molecular relaxation. Such behaviour was not apparent in the SQELS results since measurements
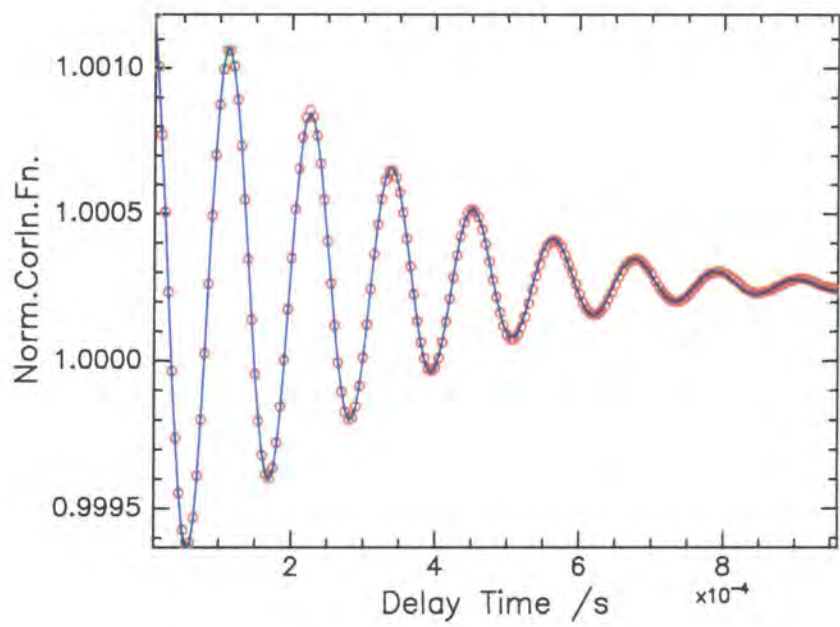
Figure 8.2.1. Experimental correlation function (circles) and a fit to the data (solid line) for q = 348 cm^{-1} and Γ_s = 0.3 mg m^{-2}.
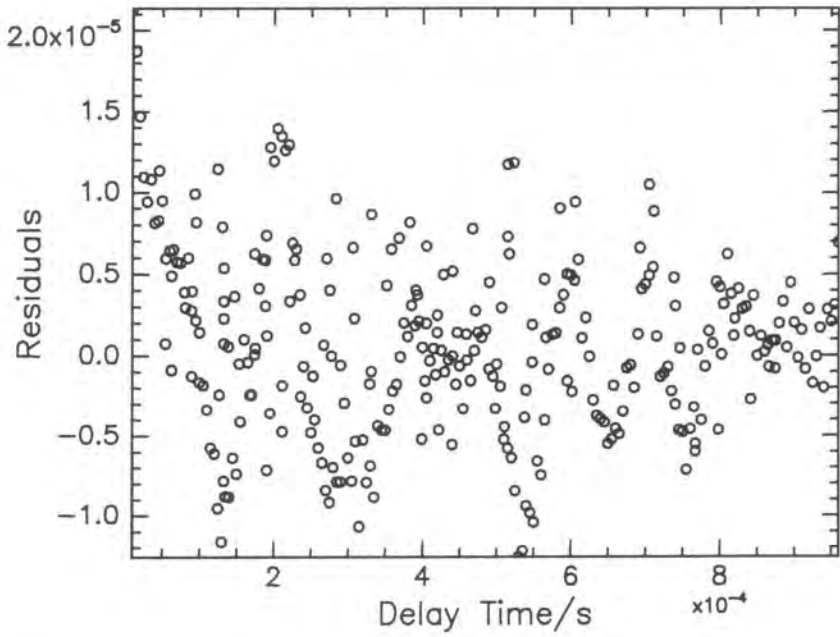
Figure 8.2.2. The residuals from the fitting process of the experimental correlation function in figure 8.2.1.

only started after a period of 30 minutes had elapsed following film formation. This was to allow sufficient time for the vibrations of the equipment, caused by aligning and focussing, to disappear.
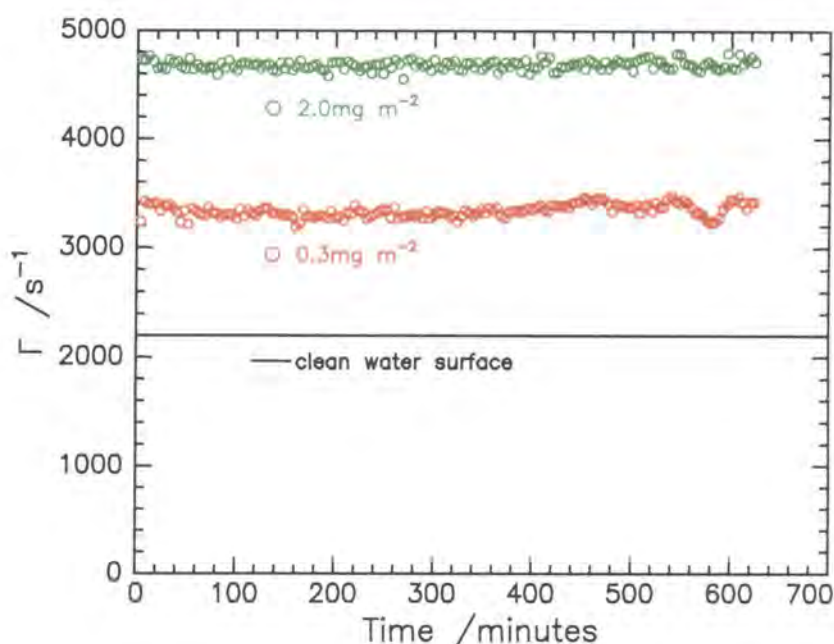
Figure 8.2.3. Capillary wave damping as a function of time for two monolayers of *n25*: 0.3 mg m^{-2} (red symbols) and 2.0 mg m^{-2} (green symbols), where q = 350 cm^{-1}. Data for a pure water subphase is overlaid for comparison (solid line).

The lowest surface concentration subjected to stability measurements was 0.08 mg m^{-2} and the results given in figure 8.2.4 for such a film of *n25* reveal very different characteristics.

The damping fluctuates continuously over the initial 5/6 hour period from values where the damping is essentially that of water and a finite value with a higher damping. This behaviour is indicative of islands existing on the water surface that are moving into and out of the light beam. The islands appear to aggregate over time thus forming larger islands that take longer periods of time to move in and out of the beam. The non-uniform film obtained here is in agreement with the surface concentration predicted for *n25* (0.11 mg m^{-2}) that marks complete coverage of the 2-dimensional surface. The damping eventually stabilises at the higher value as experimental time increases.

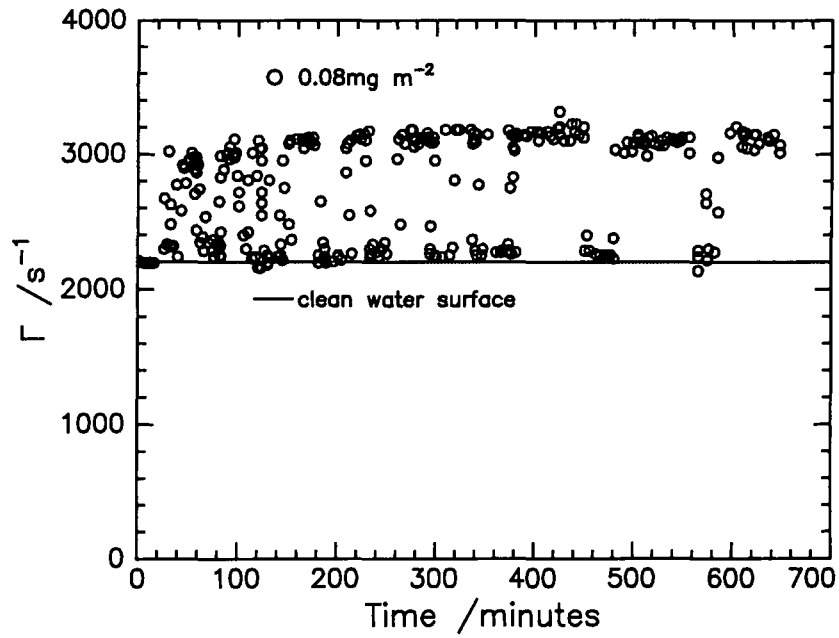**Figure 8.2.4.** Capillary wave damping as a function of time for a surface concentration of 0.08 mg m^{-2} for *n25* (symbols), where q = 348 cm^{-1}. Data for a pure water subphase is overlaid for comparison (solid line).

Section 8.3   Surface Concentration Dependence

Initial light scattering studies were carried out by collecting ten correlation functions at 0.5 mg m^{-2} intervals exploring a full concentration range from 0.1 to 5.0 mg m^{-2}. Finer divisions of surface concentration were subsequently examined over regions of interest. All data were collected using a constant wavenumber of circa 350 ± 2 cm^{-1}, which corresponds to a frequency of $55\,000 \pm 400$ s^{-1} for a clean water surface. The experimental process was repeated several times and results were highly reproducible provided the height of the liquid surface was constant. It was discovered that small variations in height had a profound effect on the q value, which exemplifies the sensitivity of SQELS to the sample and its environment. Consistency of the subphase height was achieved by using a teflon dipstick.

8.3.1   Results: Capillary Wave Frequency and Damping

Values for frequency and damping of the capillary wave were determined for each surface concentration using the damped cosine fit[1]. Figures 8.3.1 and 8.3.2 reveal the variation in frequency and damping with surface concentration respectively for *n25*, where each point is the average of ten correlation functions and the error bar is inside the data points.

The frequency of the capillary waves increases smoothly from the value of a pure water surface (55 000 s^{-1}) to a maximum of 56 000 s^{-1} at 0.3 mg m^{-2} before decreasing rapidly within 0.1 mg m^{-2} to circa 52 4000 s^{-1}. Thereafter the value slowly decreases to reach an asymptotic plateau value of circa 51 500 s^{-1}, and as the monolayer is compressed further no significant variation is observed. The changes in magnitude of the frequency values are extremely small but nonetheless significant, as they are pronounced and highly reproducible.

The capillary wave damping also reveals a dependence on the surface concentration. At low surface coverage the values of damping are close to that of a clean water surface (2200 s^{-1}) but the damping rises immediately to a maximum value nearly two and a half times that of pure water at 0.4 mg m^{-2}. As the monolayer is compressed further the damping values fall slightly and reach a plateau value of

approximately 4800 s^{-1}. This value is maintained as the surface density is increased up to 5 mg m^{-2}.
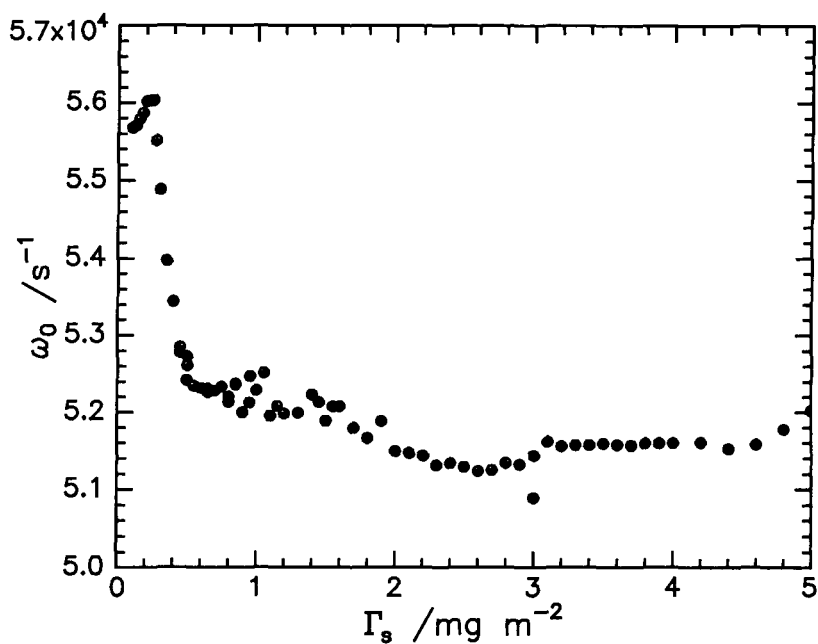
Figure 8.3.1. Frequency of capillary waves as a function of surface concentration for *n25*, q = 350 cm^{-1}.
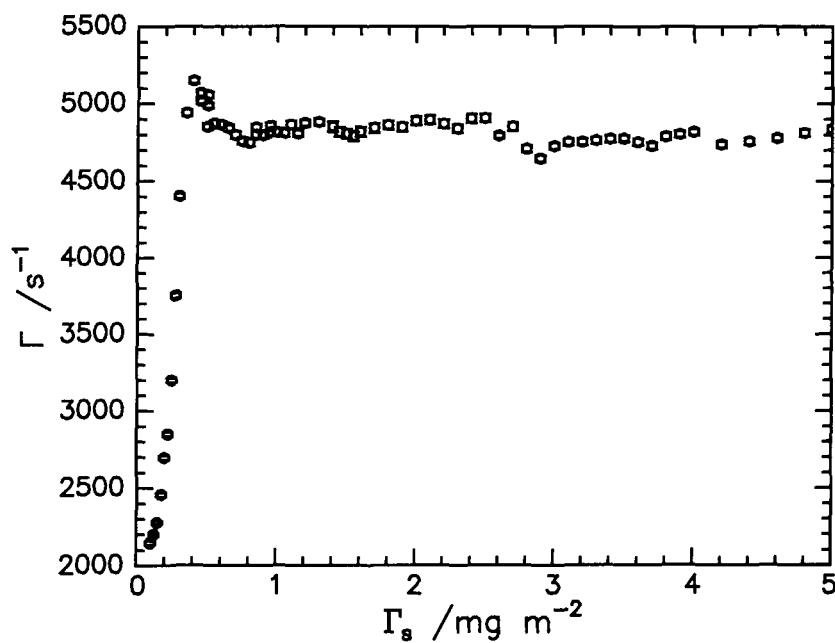
Figure 8.3.2. Damping of capillary waves as a function of surface concentration for *n25*, q = 350 cm^{-1}.

8.3.2 Results: Viscoelastic Parameters

The data were analysed in accordance with the recent molecular theory for SQELS (see Chapter Two for details) developed by Buzza and co-workers[3]. The three viscoelastic parameters allowed to float using a spectral fitting procedure were the surface tension, γ_o, dilational modulus, ε_o, (both restricted to values between 0 and 100 mN m^{-1}) and the dilational viscosity, ε', which was allowed to explore both positive and negative values ranging from -1×10^{-3} to 1×10^{-3} mN m^{-1}. The fitting procedure was repeated numerous times from various starting parameters to ensure that the final set of values were in fact from the global minimum fit.

The results obtained for the surface tension from light scattering (dynamic data) for *n25* are given in figure 8.3.3 (circles) and the static surface tension values (solid line) obtained from surface pressure studies are overlaid for comparison.
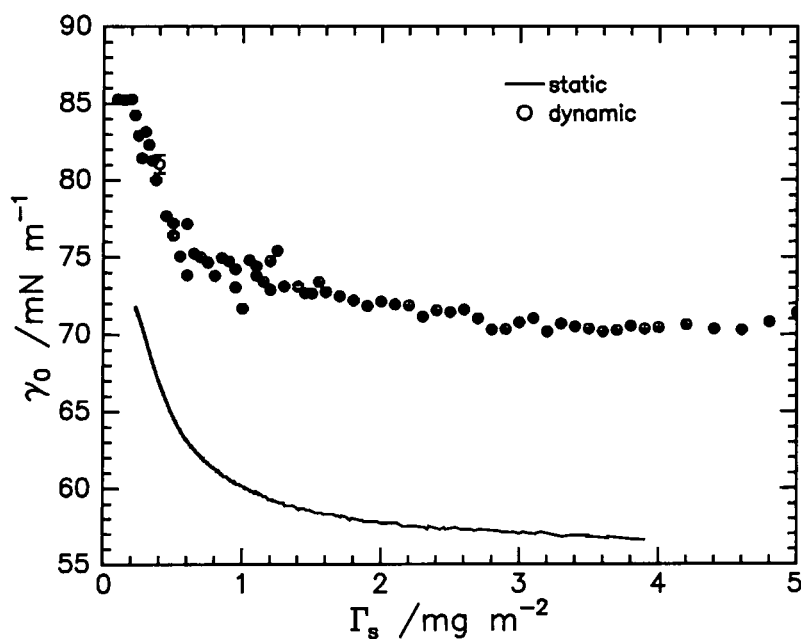
Figure 8.3.3. Surface concentration dependence of the dynamic (symbols) and static (solid line) surface tension values obtained for *n25* from SQELS and surface pressure isotherm respectively.
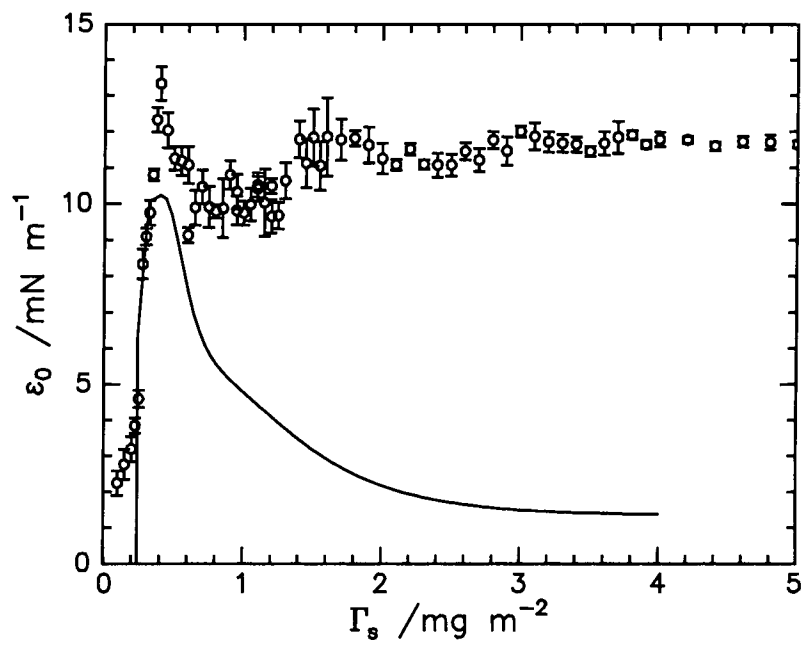
Figure 8.3.4. Surface concentration dependence of the dynamic (symbols) and static (solid line) dilational modulus values obtained from SQELS and surface pressure isotherm respectively.

Figure 8.3.5. Variation in dilational viscosity for *n25* as a function of surface concentration.

It is clear from this plot that the dynamic and static values exhibit similar qualitative characteristics with increasing surface concentration, but absolute agreement is not obtained as the dynamic values are consistently circa 15 mN m^{-1} higher than the corresponding static values. This behaviour indicates that the spread film undergoes considerable relaxation processes when perturbed by capillary oscillation.

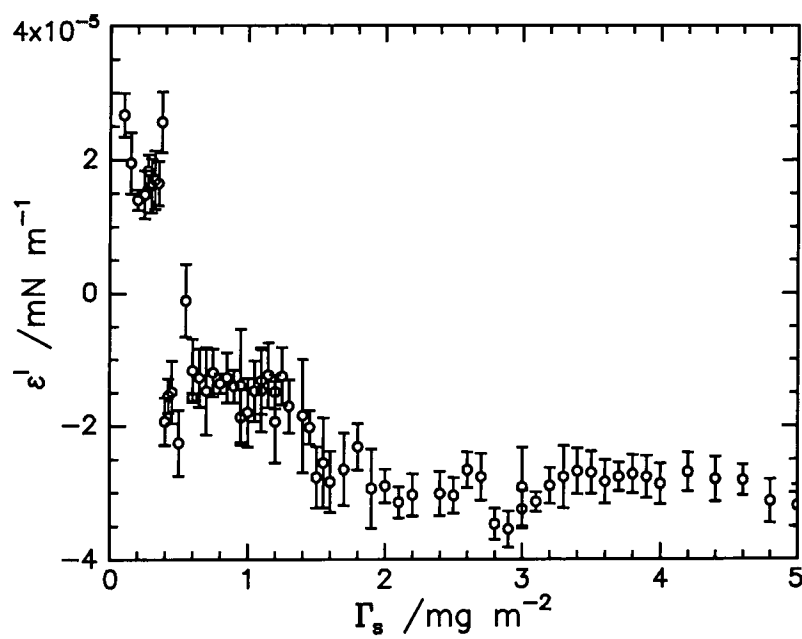The results for the dilational modulus are presented in figure 8.3.4, where the symbols represent the light scattering data and the solid line corresponds to the static values. The static data, ε_{oST}, are the Gibbs elasticity, and were calculated from surface pressure isotherm results using the following relationship;

$$\varepsilon_{oST} = \Gamma_s \frac{d\pi}{d\Gamma_s}$$

Equation 8.3.1.

In order to evaluate ε_{oST} a least squares fitting routine was used to fit a polynomial function to the experimental surface pressure isotherm data. The numerical derivative of this function was determined over the entire surface range studied and substituted into equation 8.3.1.

The experimental dilational moduli reveal a strong surface concentration dependence as a rapid increase is observed from near zero at low surface concentrations to a maximum of 13 mN m^{-1} at 0.4 mg m^{-2}. Thereafter the magnitude of the modulus data decays to 10 mN m^{-2} and remains roughly constant upon further compression, until circa 1.5 mg m^{-2} where a slight increase in value is detected. The error bars over the higher surface concentration region are marginally larger in relation to the lower concentration data, however the step increase observed is not an artefact of the data as the results were reproducible.

Comparing the two sets of results in figure 8.3.4 reveals that the data are coincident at low monolayer concentrations, where $\Gamma_s < 0.4$ mg m^{-2}. Both moduli exhibit a maximum at 0.4 mg m^{-2} the static values then drop below the equivalent dynamic data but follow similar trajectories until $\Gamma_s = 1.0$ mg m^{-2}. This observation reinforces the view that relaxation processes occur within the monolayer on perturbation by a capillary wave. The behaviour of the two moduli begins to diverge as the surface becomes more concentrated (≥ 1.0 mg m^{-2}), the static data decaying continually with increasing surface density. This difference is due to the small value calculated for the

differential, $\partial\pi/\partial\Gamma_s$, as the change in the surface pressure data is small as a function of surface concentration over the plateau region of the isotherm. This error is illuminated when the differential is used to calculate the Gibbs elasticity, (equation 8.3.1), hence the calculated data in this region were disregarded.

The dilational viscosity behaviour is presented in figure 8.3.5 and is unique to the PNB-*g*-PEO copolymer system studied here. At low surface concentrations (< 0.4 mg m^{-2}) the spectral fits consistently returned positive viscosities within the range $1\times10^{-5} \leq \varepsilon' \leq 3\times10^{-5}$ mN m^{-1}. Within these limits the values follow the trajectory of an inverted parabola where the viscosity decreases as the spread layer is initially compressed until a local minimum value is reached at 0.2 mg m^{-2}, and subsequently the viscosity rises until $\Gamma_s = 0.4$ mg m^{-2}. Thereafter there is a distinct change in behaviour as the viscosity jump from positive to negative values. The negative values extracted are of similar magnitude to the positive data, and increase slightly in a parabolic manner as the monolayer is compressed further. At circa 0.6 mg m^{-2} the dilational viscosity remains constant at approximately 1.5×10^{-5} mN m^{-1} until the surface coverage exceeds circa 1.5 mg m^{-2}. At this point a further decrease in the viscosity is observed to a new constant value of -3×10^{-5} mN m^{-1} at circa 2.0 mg m^{-2} and remains constant upon further compression.

8.3.3 Discussion: Frequency and Damping for all Graft Copolymers

To ascertain the dependence of the capillary wave propagating characteristics on the architecture of the graft copolymer the frequency and damping parameters were determined for the remaining two copolymers in the series: *n15* and *n50*. The parameters obtained for the capillary waves for all materials are compared in figures 8.3.6 (frequency) and 8.3.7 (damping) where the surface concentration range presented has been reduced to 0 to 2 mg m^{-2} in order to concentrate on the region that exhibits the most interesting behaviour.

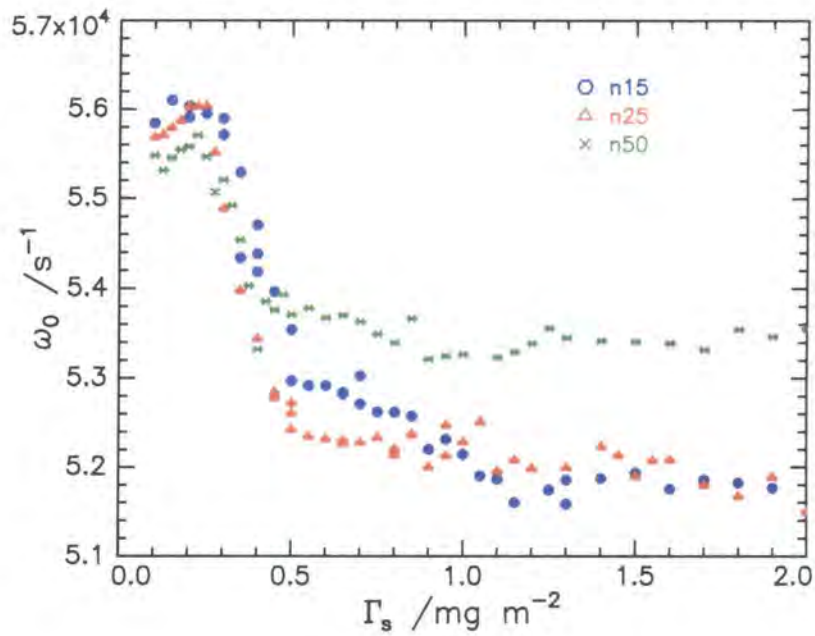**Figure 8.3.6.** Comparison of the capillary wave frequency for each graft copolymer as a function of surface concentration.
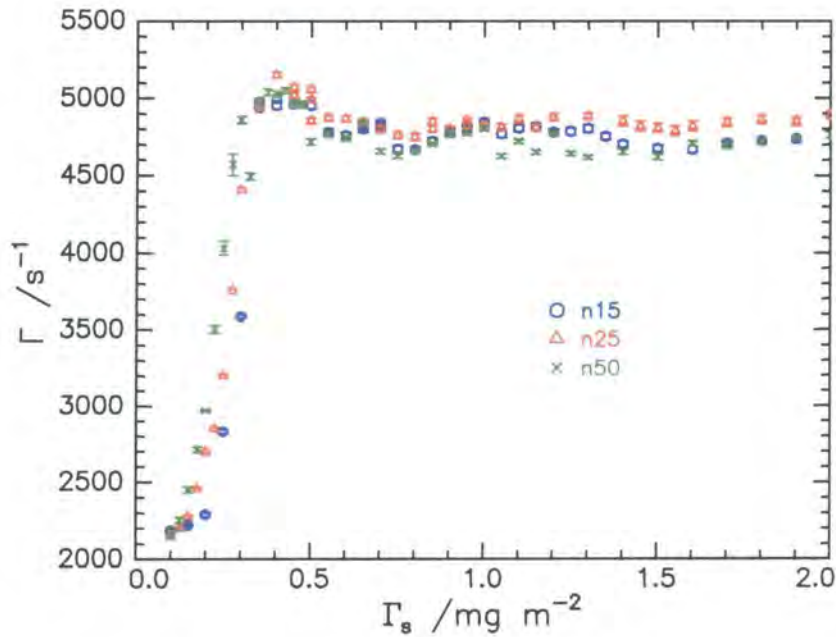

Figure 8.3.7. Comparison of the capillary wave damping for each graft copolymer as a function of surface concentration.

In general the frequency and damping of the capillary waves exhibit similar dependencies on the surface concentration for each graft copolymer in the series. Small differences however are observed at high surface coverage in the frequency data as the values decrease from their maximum and slowly approach individual asymptotic frequencies between 0.5 and 1.0 mg m^{-2}. The asymptotic values observed were dependent on the graft length: *n15* copolymer equilibrates at circa 51 800 s^{-1}, *n25* at 52 000 s^{-1} and *n50* at circa 53 500s^{-1}. This trend of asymptote frequency increase with increasing surface concentration follows that observed in the surface tension data obtained from surface pressure isotherm studies (static data) as expected, since the frequency and surface tension are related: $\omega_o^2 \propto \gamma_o$.

The damping data is given in figure 8.3.7 and the values for all three copolymers are coincident over all surface concentrations, within experimental error. The maximum value observed in figure 8.3.7 for each monolayer occurs at identical surface concentration: 0.4 mg m^{-2}. The maximum observed is indicative of resonance between the capillary and dilational modes[4] and concurs with the maximum observed in the frequency data. Resonance occurs when the real frequencies of the two modes are identical i.e. the capillary and dilational waves are oscillating at identical rates.

The value associated with the critical (resonance) concentration has previously been identified by surface pressure isotherm work (Chapter Five) as marking the onset of changes in monolayer conformation and was interpreted as the onset of significant penetration of PEO into the subphase. Neutron reflectometry (NR) studies contradicts this suggested change in organisation as NR revealed that the PEO grafts were always immersed in the subphase over the full range of surface concentrations investigated, 0.3-4.0 mg m^{-2}. Furthermore the theoretical surface concentration where the in-plane surface becomes sterically crowded was determined to be 0.11 mg m^{-2} for *n25*, which is much lower than the resonance concentration of 0.4 mg m^{-2}. One striking feature that was present in the organisation results from NR was the abrupt change in behaviour that marked the onset of significant stretching of the graft into the subphase, which was akin to theoretical polymer brush behaviour. The results from this NR study are presented in the form of graft layer thickness as a function of surface concentration and are compared directly to the damping data in figure 8.3.8 for *n25*.

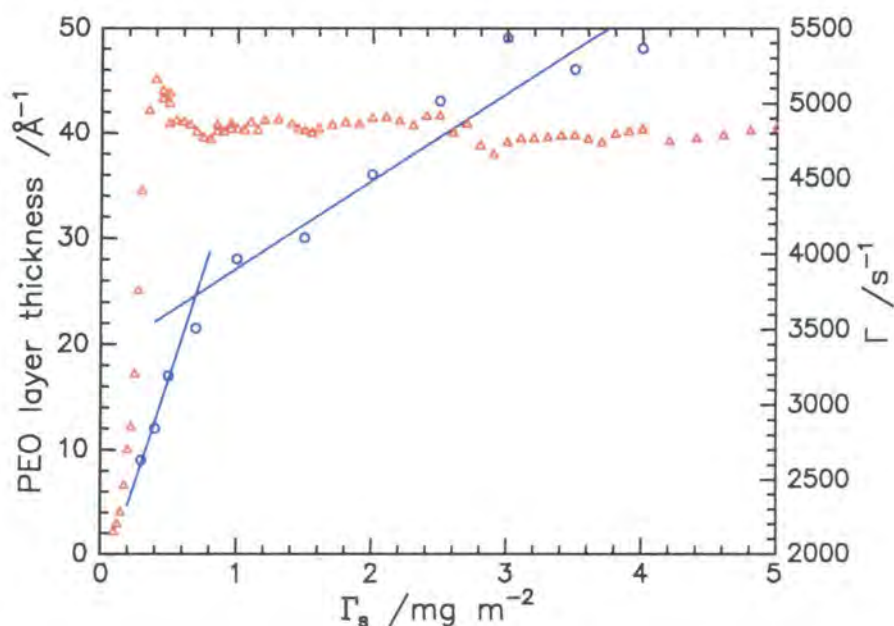**Figure 8.3.8.** Comparison of capillary damping data (red triangles: right axes) to the PEO layer thickness (blue circles: left axes) both as a function of surface concentration (bottom axes) for *n25*.

Figure 8.3.9. Comparison of surface tension (red triangles: right axes) to the PEO layer thickness (blue circles: left axes) both as a function of surface concentration (bottom axes) for *n25*.
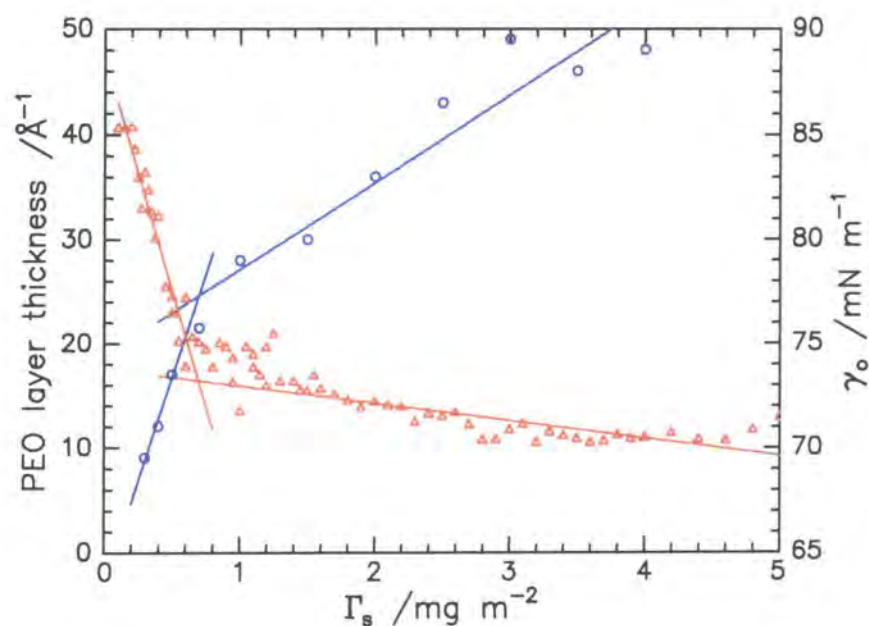
From figure 8.3.8 it is immediately apparent that PEO penetration into the subphase can be divided into two separate regimes. Uncertainties arise when deciding the boundaries of each regime as the data point at 1.0 mg m^{-2} could belong to either. If this value is temporarily ignored and the remaining two sets of data points are fitted by a linear least squares fit, then it becomes obvious that a crossover in behaviour occurs at circa 0.7 mg m^{-2} (where the two linear least square fits intersect). This is extremely close to the surface concentration where the maximum in damping is observed, suggesting that the resonance condition is induced by the distinct change in monolayer organisation. Conclusive evidence for this is obtained from figure 8.3.9 where the surface tension values obtained from SQELS are compared to the PEO layer thicknesses, again for *n25*. Dramatic changes in the surface pressure isotherms, hence surface tension, are indicative of different organisations. In this diagram the crossover observed in the data describing the organisation coincides almost exactly with the change in behaviour of surface tension as the monolayer moves from a liquid expanded to a liquid condensed state. From this comparison it can therefore be concluded that the changes detected in the capillary wave propagation are correlated to the marked change in molecular surface arrangement.

The maximum damping value observed here is considerably sharper than that observed for homoPEO films[5] where the data exhibited a broad maximum centred at 0.4-0.6 mg m^{-2}. This difference is possibly due to the homoPEO slowly moving from a 2 to a 3-dimensional molecular organisation as the PEO extends into the subphase as loops and tails. Such an organisation change contrasts the sharp structural change observed in the graft copolymer films where the PEO chains are more likely to have a tail conformation due to their high grafting density. The surface dynamics of various amphiphilic polymers containing PEO[6,7] have been reported in the literature but the work of most relevance here is that of a spread film of poly(methyl methacrylate)-*g*-poly(ethylene oxide), PMMA-*g*-PEO[8]. In this case three copolymers were studied where the number of grafts varied from 20 to 60, were arranged randomly along the MMA backbone and each graft consisted of 54 ± 2 EO units. In each system it was found that the damping data exhibited a maximum and its position was dependent on the grafting frequency. In this study all copolymers have similarly high grafting frequencies (each backbone units contains a graft) and differ only in the degree of polymerisation of the PEO graft. The maximum in damping for each copolymer

observed occurs at identical concentrations suggesting the graft length has no influence over the resonance condition. This result is not surprising as NR reveals there is no dramatic difference in monolayer organisation at low surface coverage ($\Gamma_s \leq 0.5$ mg m^{-2}), and moreover the surface pressure isotherms are essentially identical ($\Gamma_s \leq 0.7$ mg m^{-2}), which indicates that the near surface properties are being dominated by the PEO present. At higher surface concentrations the capillary waves oscillate with different frequencies and this concurs with the differences observed in the surface pressure isotherm data. Evidence from neutron work emphasises such differences as the extension of PEO grafts into the subphase increases as a function of graft length, and it is thought that the different monolayer organisations are influencing the capillary wave behaviour at high surface concentration. To determine whether the maximum in damping is due to classical resonance $\dfrac{\varepsilon_0}{\gamma_0} = 0.16$ the surface viscoelastic parameters were extracted for all materials using an identical procedure as that outlined earlier for *n25*.

Figure 8.3.10 reveals the trend in both static (solid lines) and dynamic (symbols) surface tension values with surface concentration for each copolymer. In all cases relaxation processes occur in the monolayer as the dynamic and static values obtained from light scattering and surface pressure isotherm studies respectively, follow similar dependencies but the dynamic data are always circa 15 mN m^{-1} higher. The magnitude of the light scattering data is unusually high, but such values were consistently returned when a wide range of values were used as starting parameters. Furthermore the data was highly reproducible even when experiments were repeated after a period of six months. The large difference in surface tension therefore emphasises that the monolayer is undergoing considerable relaxation when perturbed by the capillary wave. At low surface coverage it is difficult to identify any trend between the copolymers from the light scattering data simply due to the small fluctuations between points, which are attributed to experimental error. Errors originate due to the sensitivity of SQELS to the surrounding media, therefore small changes in thermal gradients of either the superphase or the subphase, or external vibrations can influence the correlation function and hence the extracted parameters. As the monolayer is compressed to circa 0.8 mg m^{-2} however the surface tension values begin to diverge and become dependent on copolymer composition. The trend observed (increase in surface tension with increasing

PEO content) agrees with that observed in the static measurements and has been discussed in Chapter Five.
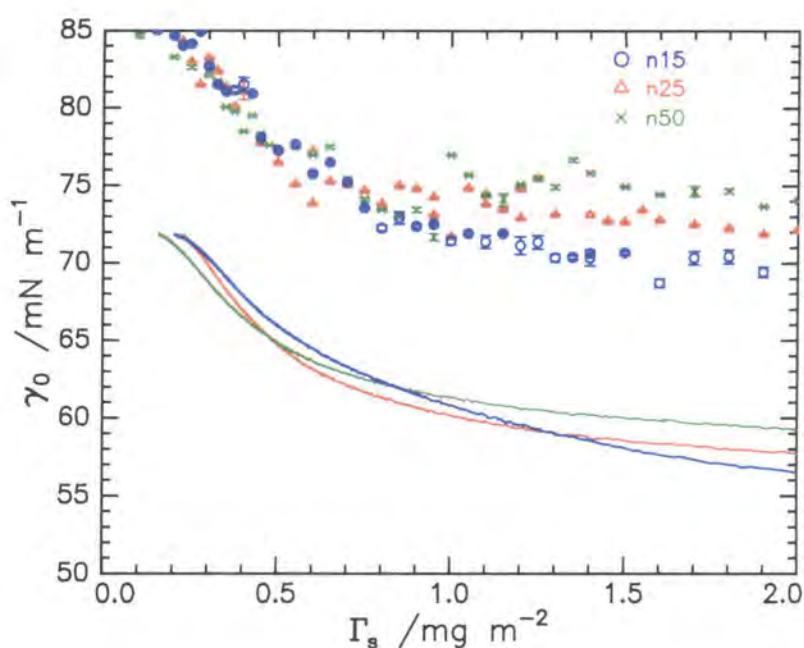
Figure 8.3.10. Comparison of the variation in dynamic (symbols) and static (solid line) surface tension as a function of surface concentration for all graft copolymers.
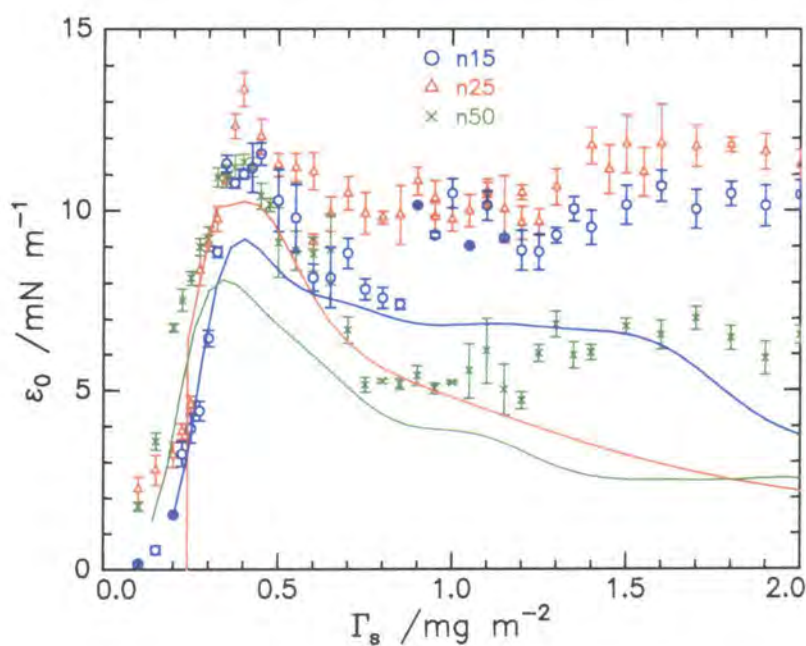

Figure 8.3.11. Comparison of the variation in dynamic (symbols) and static (solid line) dilational modulus as a function of surface concentration for all graft copolymers.

The dilational modulus parameter for all copolymers (see figure 8.3.11) displays similar dependencies on surface concentration as *n25*, especially at low surface coverage. All the copolymers exhibit a maximum in dilational modulus at $\Gamma_s = 0.4$ mg m^{-2}. Only subtle differences in the magnitude of the dilational modulus are apparent at low concentration values (≤ 0.4 mg m^{-2}) the modulus increasing, albeit marginally, with increasing graft length. The dilational modulus for all graft copolymers converge at the maximum point, and as Γ_s increases the moduli values decrease slightly and begin to diverge, where the original trend observed at low surface concentrations is reversed. In general the moduli reach a small plateau between circa 0.8 and 1.0 mg m^{-2}, followed by a broad maximum starting at circa 1.2 mg m^{-2}.

The surface concentration value where the distinct maximum in dilational modulus is observed concurs with the maximum observed in the damping, and as alluded to earlier NR studies have associated this surface concentration region to a distinct change in molecular organisation. This behaviour emphasises that the surface viscoelastic moduli (both surface tension and dilational modulus) are sensitive to the molecular organisation within the monolayer and the maximum value is indicative of mode mixing as the dilational modulus increases hence bringing the dilational frequency closer to that of the capillary mode. The plateau values observed for *n15* and *n25* (approximately 10.5 and 12 mN m^{-1} respectively) are extremely close, and are markedly different for *n50* which has a significantly lower value of 7 mN m^{-1}. The similarity between the two shorter grafts is accredited to the modest difference in length, accompanied by the differences in their stereochemistries (see Chapter Four), which leads to both PEO grafts extending into the subphase to similar depths. This contrasts the relatively long graft length and penetration depth of *n50*. If this argument is accepted, then it can be stated tentatively that as the graft length increases the dilational modulus decreases, this relationship will be discussed later.

It was alluded to earlier that the main feature of the frequency and damping data as a function of surface concentration was the presence of the maximum at 0.4 mg m^{-2}, which is a symptom of resonance[4]. Classically resonance occurs when the ratio of dilational modulus (ε_o) to surface tension surface tension (γ_o) is 0.16. The ratio of values for the moduli of each mode (ε_o / γ_o - obtained from light scattering) were plotted as a function of surface concentration, in figure 8.3.12. All copolymers have similar

behaviour, a small modulus ratio at low surface concentration rapidly increasing to a maximum at 0.4 mg m^{-2}. As compression increases the values decrease slightly and reach a steady value with *n15* and *n25* behaving in a similar manner but *n50* has a larger decrease. The classical resonance conditions are met (i.e. $\varepsilon_0/\gamma_0 = 0.16$) at 0.4 mg m^{-2} and this concentration concurs with the maxima observed in the damping data.
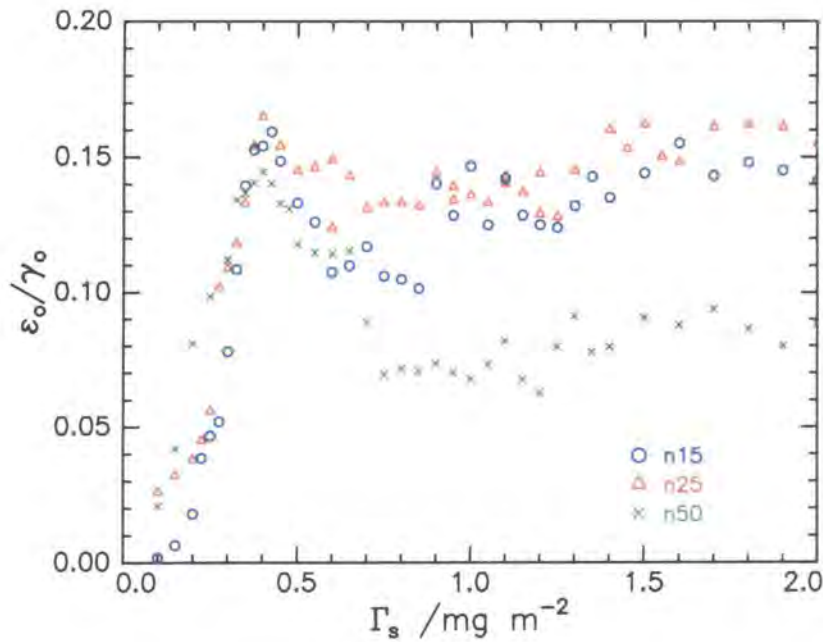
Figure 8.3.12. The ratio of ε_0/γ_0 versus surface concentration. Classical resonance between the capillary and dilational waves occurs when $\varepsilon_0/\gamma_0 = 0.16$.

First order approximations describing the propagating characteristics of the capillary and dilational modes are given in equation 8.3.2 and 8.3.3 respectively and are valid at low q values. These equations are of the form $\omega = \omega_o + i\Gamma$.

Capillary frequency $\qquad\qquad \omega_C = \sqrt{\dfrac{\gamma q^3}{\rho}} + i\dfrac{2\eta q^2}{\rho} \qquad\qquad$ **Equation 8.3.2.**

Dilational Frequency $\qquad\qquad \omega_D = \dfrac{1}{2}\left(\sqrt{3} + i\right)\left(\dfrac{\varepsilon^2 q^4}{\eta\rho}\right)^{1/3} \qquad\qquad$ **Equation 8.3.3.**

where ω_C and ω_D are the overall frequencies of the capillary and dilational modes respectively, ρ is the density and η the viscosity of the system. When the two modes are resonating the real frequencies are coincident (i.e. $\omega_C = \omega_D$) hence;

$$q = \dfrac{\left(3/4\right)^3 \varepsilon^4 \rho}{\gamma^3 \eta^2} \qquad\qquad \textbf{Equation 8.3.4.}$$

By substituting the dilational modulus and surface tension values extracted at resonance into equation 8.3.4, the q value calculated was 337 cm^{-1}, which is in good agreement with the experimental value of 348 cm^{-1}. This is a further indication that the two modes are resonating.

The data pertaining to the dilational viscosity for all three copolymers is given in figure 8.3.13 and each exhibits a discontinuity at the resonance concentration. At surface concentrations below the discontinuity ($\Gamma_s \leq 0.4$ mg m^{-2}) the viscosity follows an inverse parabolic trajectory with a minimum at 0.2 mg m^{-2} before a sharp divergence to negative values. There is no evidence of any copolymer composition dependence here as all data are coincident. An additional decrease in viscosity is observed for all copolymers at circa 1.3 mg m^{-2} and occurs in response to the increase in the dilational modulus. The high error in both dilational modulus and viscosity in relation to the surface tension data is due to the presence of noise in the correlation function. This arises from the weak coupling between the capillary and dilational modes and the

scattered light responding to slight alterations in the polarisation of light normal to the surface.
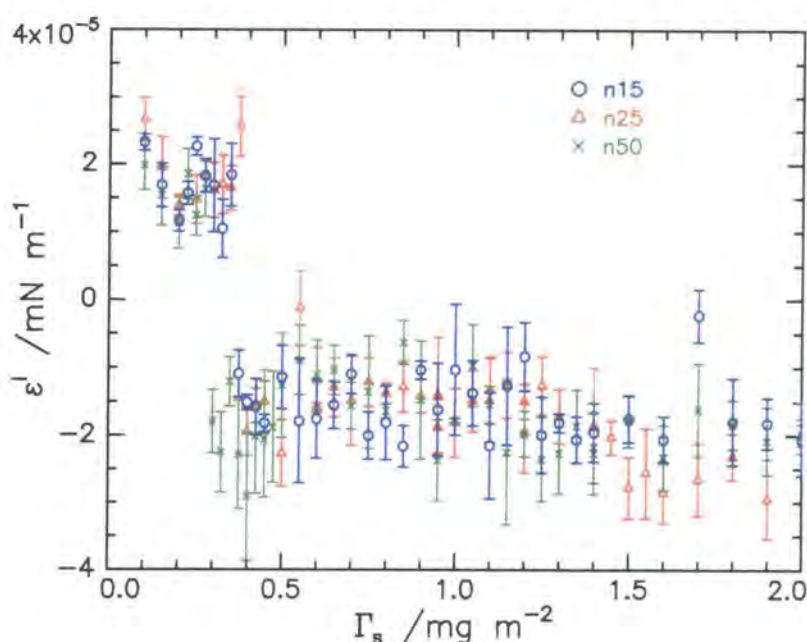
Figure 8.3.13. Comparison of the variation in dilational viscosity as a function of surface concentration for all graft copolymers.

If the behaviour of the two dilational parameters are analysed in tandem close to the resonance concentration (0.4 mg m^{-2}), it is clear that their behaviour is linked, as the dilational modulus displays a maximum, while its viscosity exhibits a minimum. Such behaviour is typical of that exhibited by all graft copolymer materials. The relationship between the real and imaginary components of the dilational mode can be related to the Kramers-Kronig type relationships[9] that describe the response of a system subjected to harmonic impulses. This is a particular example of storage and loss compliances and these have previously been used to describe the dielectric behaviour of some polymers[10] and the dilational behaviour of the graft copolymer PMMA-*g*-PEO[8]. Kramers-Kronig relations involve two equations that describe both the real and imaginary parts of the model system, and knowledge of the real part directly allows the imaginary part to be defined and vice versa. Relating the Kramers-Kronig relations to the systems here we can equate the real part to the dilational modulus and the imaginary part to the dilational viscosity. Typically however the Kramers-Kronig equations are given in terms of frequency rather than surface concentration, but they can still be applied here if the

dilational behaviour is modelled by a spring that lies in the surface plane. At fixed q the applied frequency, ω, is constant and it is the natural resonant frequency, ω_o, that varies hence for a spring in the surface plane, $\omega_o = \left(k/m\right)^2$, where k is the spring constant and m the mass of the spring. The compression and expansion cycles of the model spring occur in response to an oscillatory force, $F\exp(-i\omega_o t)$, which represents the in-plane (dilational) elastic behaviour of the monolayer. Changes in the surface concentration are therefore accounted for in the model by altering the force applied to the spring. Increasing the surface concentration of the film is expected to increase the natural resonant frequency as the stiffness of the film hence k should also increase. At some critical force (and hence Γ_s) the frequency of the dilational mode is altered so it is identical to the oscillatory driving force i.e. they are in resonance. As the force increases further (increasing surface concentration) the dilational mode moves away from the resonance condition. This behaviour can be expressed mathematically where a sinusoidal force is applied to the surface spring and causes a displacement of the spring. The position of the spring at time, t, is given by;

$$\xi(t) = \chi(\omega)F\exp(-i\omega t)$$ **Equation 8.3.5.**

where $\chi(\omega)$ is the transfer function, which is the response of the system to the force. The transfer function for the displacement response, $\chi_D(\omega_o)$, is expressed as;

$$\chi_D(\omega_o) = -\frac{1}{m\left(\omega^2 - \omega_o^2 + 2i\omega''\omega\right)}$$ **Equation 8.3.6.**

where ω_o is the natural frequency induced by the applied force and ω'' is its associated damping. The transfer function accounts for the modification of behaviour within the system in response to the applied force and can be identified with a mechanical component, for example the displacement or velocity function. To transfer the displacement response of the surface film into its real and imaginary components the denominator of equation 8.3.6 is multiplied by its complex conjugate. The form of the real and imaginary parts of this function are given in figure 8.3.14 and correspond to the real and imaginary components of the dilational mode, i.e. the modulus and viscosity. It

is obvious from this diagram that the experimental dilational characteristics of the copolymer films are mirror images of the real and imaginary displacement transfer functions i.e. the theoretical real component corresponds to the experimental imaginary, but the theoretical imaginary corresponds to the reverse of the real experimental data. Therefore this analogy does not describe the response of the experimental system to oscillatory stress.

Alternatively if the velocity response of the surface film is considered then the transfer function becomes;

$$\chi_V(\omega_o) = -i\omega\,\chi_D(\omega_o) = \frac{i\omega}{m\left(\omega^2 - \omega_o{}^2 + 2i\omega''\omega\right)}$$

Equation 8.3.7.

The real and imaginary components are again identified by multiplying the denominator by its complex conjugate and this gives;

$$\chi'(\omega) = \frac{2\omega''\omega^2}{m\left[\left(\omega^2 - \omega_o{}^2\right)^2 + 4\omega''^2\omega^2\right]}$$

Equation 8.3.8.

$$\chi''(\omega) = \frac{\omega\left(\omega^2 - \omega_o{}^2\right)}{m\left[\left(\omega^2 - \omega_o{}^2\right)^2 + 4\omega''^2\omega^2\right]}$$

Equation 8.3.9.

The form of these functions are given in figure 8.3.15 and it is clear that the features exhibited by the classical Kramers-Kronig behaviour are reproduced exactly in the experimental system for the dilational modulus as these data exhibit a maximum value at resonance. The viscosity is also reproduced as the imaginary component exhibits an arched increase just above and below the sharp drop in viscosity that occurs at the resonance surface concentration.
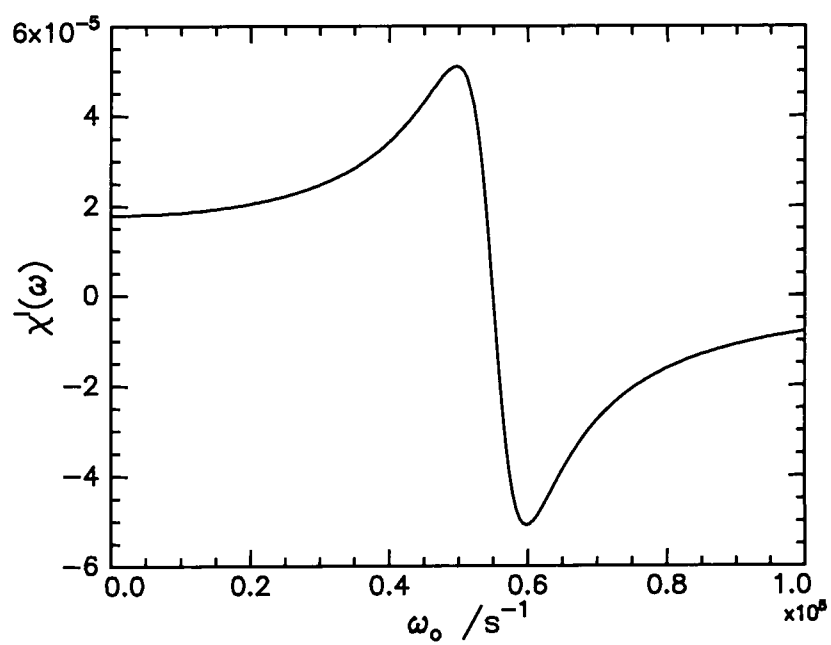
a) Real Component
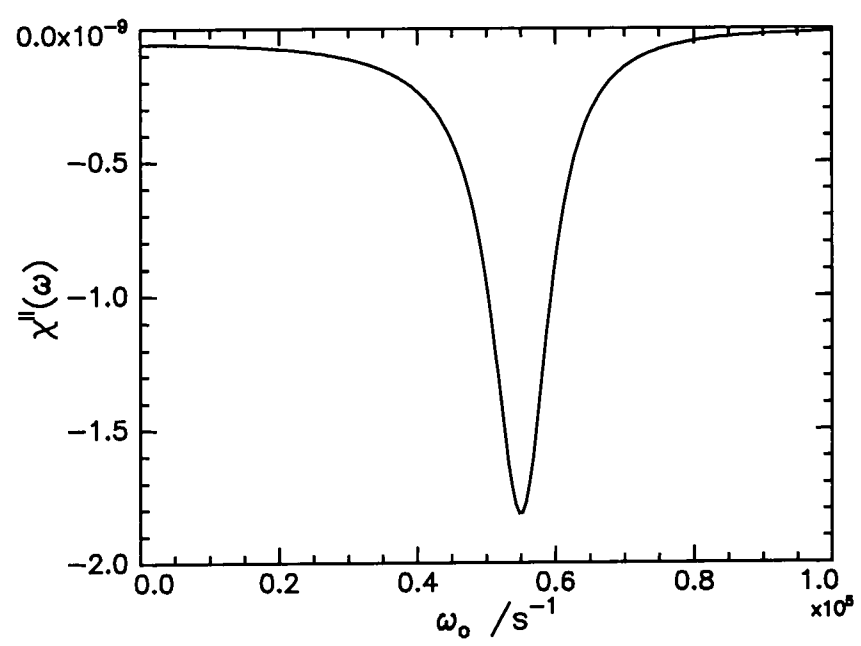
b) Imaginary Component

Figure 8.3.14. Transfer functions for the displacement response of an oscillator subjected to an oscillatory force where a) represents the real component and b) the imaginary.
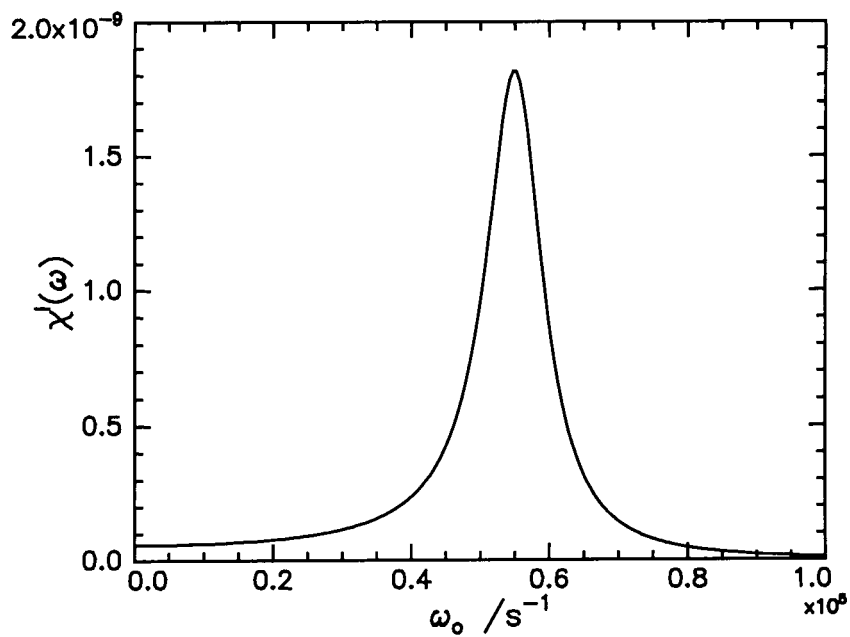
a) Real Component
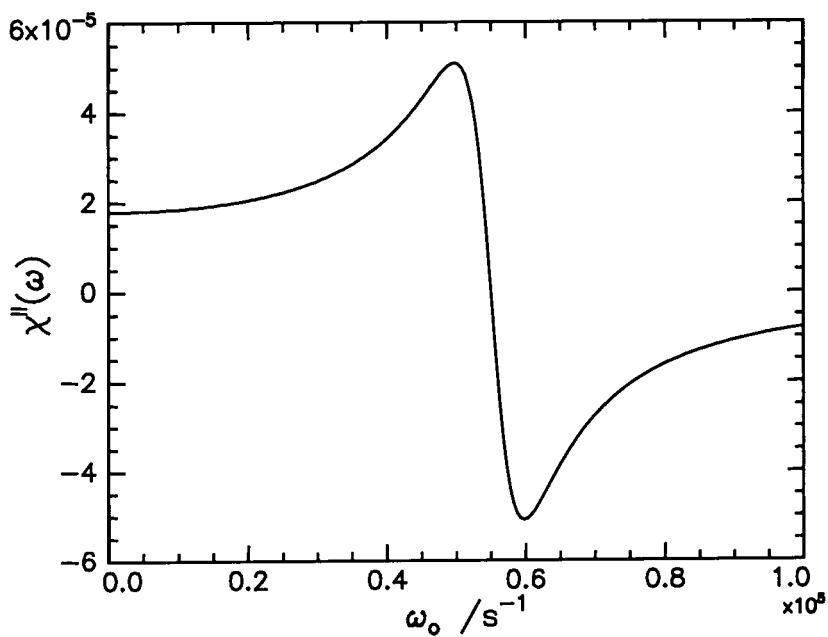
b) Imaginary Component

Figure 8.3.15. Transfer functions for the velocity response of an oscillator subjected to an oscillatory force where a) represents the real component and b) the imaginary.

The agreement obtained between the theoretical Kramers-Kronig behaviour and the experimental data revealed that the dilational properties of the graft copolymer film are acting as a transfer function and are thus modifying the dynamical properties of the spread film in response to some oscillatory force, in the plane of the copolymer monolayer. This behaviour is observed when the dilational and capillary modes are resonating, and since these modes are strongly coupled the oscillatory force is likely to have arisen from the capillary wave.

The viscoelastic behaviour of PMMA-g-PEO has previously been discussed in relation to Kramers-Kronig relationships[8] and furthermore, if the experimental data for homoPEO is carefully analysed, trends reminiscent of those observed here can be detected[5]. Initially it was questioned whether direct comparisons could be made between the viscoelastic property of this system (PNB-g-PEO) and literature studies as the transverse shear viscosity was set to zero here in accordance with current theory hence only three viscoelastic parameters were fitted. Such an approach contrasts previous SQELS work where the fourth parameter was included in the analysis. This additional parameter however does not influence the dilational properties significantly and the behaviour observed here is reminiscent of films of both homoPEO and PMMA-g-PEO, and therefore warrants discussion. For such films spread at an air-water interface the differences in dynamic and static surface tension values indicate that the films relax in response to perturbation. The extent of relaxation observed is however small in comparison to the behaviour exhibited by PNB-g-PEO studied here. Perhaps this is inherent of the high grafting density, which increases the elasticity of the film, therefore the film takes an extended period of time to relax. The dilational modulus for homoPEO exhibits identical qualitative behaviour at the resonance concentration as observed in this study, as both moduli increase from near zero to a maximum of circa 10/15 mN m^{-1} where the coupling of the two modes is maximised. Thereafter the moduli decay to different extents. This behaviour is the exact opposite to that observed for PMMA-g-PEO as the dilational modulus decreases after initial compression and reaches a minimum at resonance. The dilational viscosity for homoPEO gradually increased with film compression until the resonance concentration (0.6 mg m^{-2}). At this point the values fell suddenly and changed sign, but subsequently increased towards zero upon further monolayer compression. This is precisely the behaviour detected in this study. Interestingly the PMMA-g-PEO system again exhibited opposing behaviour

as the values were consistently negative and moreover the values start an order of magnitude lower and become more negative as the surface concentration increases. Thereafter a discontinuity is observed when the modes are resonating where the viscosity becomes abruptly less negative, and after further compression the viscosity continues to fall in a concave manner.

Collating the viscoelastic behaviour of PEO containing films it appears that over the lower surface concentrations the viscoelasticity of the graft copolymer studied here is similar to the properties of homoPEO. This indicates that the behaviour of the graft copolymer is being dominated by its PEO component, which is not surprising due to the high content of the PEO present. The trend common to all PNB-*g*-PEO copolymers and homoPEO is the maximum observed in the dilational modulus and the dramatic divergence in the dilational viscosity from positive to negative values, which occur at the resonance concentration. In both systems the striking changes observed are correlated to changes in monolayer organisation. The transitions outlined are more pronounced in the graft copolymer perhaps because the geometry of the PEO is being constrained due to the tethering effect of the hydrophobic backbone. In fact the molecular transition observed for the graft copolymer studied here undergoes a sharp phase transition whereas the homoPEO stretches only weakly into the subphase as loops and tails. It is difficult to rationalise the behaviour of the PMMA-*g*-PEO copolymer films as the behaviour is basically inverted in comparison to other PEO containing films. One difference between the different graft copolymers is the grafting frequency as the degree of grafting was low and random for PMMA-*g*-PEO but was well-defined for PNB-*g*-PEO, as every PNB backbone unit contained one pendent chain. The viscoelastic behaviour must therefore be influenced significantly by the PMMA constituent. Two studies of homoPMMA have been separately undertaken, in the first however the dilational characteristics could not be isolated as the error associated with the experimental data were too high and the results from the second study are under debate as the viscoelastic parameters were extracted using a somewhat inaccurate description of the power spectrum of scattered light. The study of a linear diblock of PMMA-PEO (mole ratio 1:1) revealed a maximum value in both dilational modulus and viscosity at a surface concentration of circa 1.5 mg m^{-2}, which was attributed to the de-mixing of the individual components. The dilational viscosity behaviour was reminiscent of the PMMA-*g*-PEO film except the values were consistently positive. It is

therefore concluded that the viscoelastic behaviour is not simply the sum of the two individual components but is unique to each copolymer. It proved difficult to explain the observed behaviour on a molecular level for PMMA-*g*-PEO as the copolymers were ill defined and had few PEO grafts spaced randomly along the main chain.

It is concluded that the high grafting densities associated with the architecture of the graft copolymer were responsible for the unusual features observed in the dilational mode. The changes observed in dynamic behaviour are expected to be due to the sharp transition in molecular organisation, which are also unique to the graft copolymer system studied here.

The resonance surface concentration (0.4 mg m^{-2}) has previously been associated with the dramatic change in molecular organisation as the PEO grafts begin to stretch significantly from the interface and form classical polymer brushes. The variations observed in the viscoelastic behaviour of the film are therefore associated with the structural changes within the monolayer.

Immediately after the resonance concentration negative dilational viscosities were consistently returned and maintained over the remaining surface concentration values. It is difficult to interpret these negative values physically because the viscosity is associated with the dissipation of energy but the negative values indicate that mechanical energy is somehow being transferred into the dilational mode from an external source[11]. Negative values were first observed by Earnshaw for a solution of primary alcohols[12] and have been observed for numerous systems including surfactant[13] and polymer solutions[14], and also surfactant[15] and polymer monolayers[5-7,16]. For systems where a surface excess layer is present, negative values are associated with adsorption barriers[17] and the diffusive exchange[18] of material between the surface and the bulk material until equilibrium is reached. Alternative explanations involve spread monolayers as the systems studied (including this graft copolymer) are insoluble and are in an equilibrium state. One possible source of negative dilational viscosities is the Marangoni effect[19] where local variations in surface tension are converted into mechanical energy. Fluctuations in the surface tension occur due to slight differences between the surface chemical potentials or thermal variations, however the effect of these fluctuations is too small to account for the negative viscosities. Currently, the viscosity is described as an effective parameter due to the dispersion equation not describing the surface behaviour adequately. Negative viscosities were observed for

monolayer of PMMA-*g*-PEO which prompted a re-analysis of the dispersion behaviour, but despite the recent developments [3], this study proves that the dispersion equation still does not give a thorough description of viscoelastic properties of a spread film at an air-water interface. Phenomenologically therefore negative dilational viscosities are interpreted to represent a decrease in the damping of the dilational mode compared to when the viscosity is zero[7,8].

The molecular description of the surface dynamics by Buzza and co-workers[3] predicted that the viscoelastic parameters scale with polymer grafting density, σ, for a brush like layer as brush like monolayers as;

$$\pi \approx \sigma^{11/6} b^{5/3} N k_B T \qquad \qquad \textbf{Equation 8.3.10.}$$

$$\varepsilon \approx \sigma^{11/6} b^{5/3} N k_B T \qquad \qquad \textbf{Equation 8.3.11.}$$

$$\varepsilon' \approx \sigma^2 \eta b^5 N^3 \qquad \qquad \textbf{Equation 8.3.12.}$$

where the polymer has a degree of polymerisation N with monomer step length b, T the temperature, η the viscosity of the water subphase and Boltzmanns constant, k_B. The surface density is directly proportional to surface concentration, therefore the above scaling relationship is still valid if Γ_s is substituted for σ. It was found that the experimental data for the surface pressure scales as $\pi \sim \Gamma_s^{1.88-2.21}$ where the exponent equates to 2.05 ± 0.2 for all graft copolymers when $\Gamma_s > 1.0$ mg m^{-2}, i.e. where the PEO grafts behave as polymer brushes. This experimental exponent is in good agreement with the theoretical value (11/6) in equation 8.3.8. The dilational modulus was found to scale as $\varepsilon_o \sim \Gamma_s^{0.23}$ for *n25* (and the extracted exponent is 0.22 and 0.30 for *n15* and *n50* respectively), which does not agree well with the scaling equation 8.3.11. The behaviour of the dilational viscosity has previously been discussed in terms of Kramers-Kronig relations and is constant over the surface concentration range where the grafts comply with polymer brush theory. The data does exhibit a slight increase in value at low surface concentrations, but the range is too small to justify fitting. This study reveals that agreement between experimental behaviour and the scaling relationships is observed only for the surface tension of the polymer films, and furthermore no

parameter present in equation 8.3.12 could be responsible for negative dilational viscosities. This analogy consolidates earlier predictions that the current dispersion equation is inadequate for spread films at an air-water interface. The two additional parameters that were introduced into the current theory, namely the bending modulus and the coupling coefficient, have been discounted here. The bending modulus of the film only becomes important when the surface tension reduces to near zero values, which is certainly not the case in this system. The coupling coefficient was also ignored in the calculations, is only significant when the brush layer thickness is circa 1 µm, and the thickest layer observed here was circa 90 Å.

To confirm that the real frequencies coincide at resonance and also to understand the behaviour of each mode as a function of surface concentration, the individual capillary and dilational frequencies were calculated by substituting the viscoelastic parameters obtained from the spectral fit into the dispersion equation. The equation was solved providing two sets of frequency and damping roots, one relating to the capillary and the other to the dilational waves. The frequencies of each mode for *n25* are given in figure 8.3.16a and are typical of all the copolymers. From the results presented here it is evident that the capillary and dilational modes converge and intersect at circa 0.4 mg m^{-2}. Thereafter the two frequencies diverge as the capillary motion dominates the lower frequency mode over a range of surface concentrations until surprisingly the dilational frequency increases and becomes coincident with capillary frequency again at circa 1.5 mg m^{-2}. As the monolayer is compressed further both mode frequencies remain equal. This unexpected behaviour appears to suggest that there is a second resonance concentration, and further evidence for this is obtained from figure 8.3.12 as ε_0/γ_0, is approximately 0.16 in this surface concentration range. To determine whether such behaviour is in fact due to a second resonance the corresponding damping values for the capillary and dilational modes are examined and are given in figure 8.3.16b.
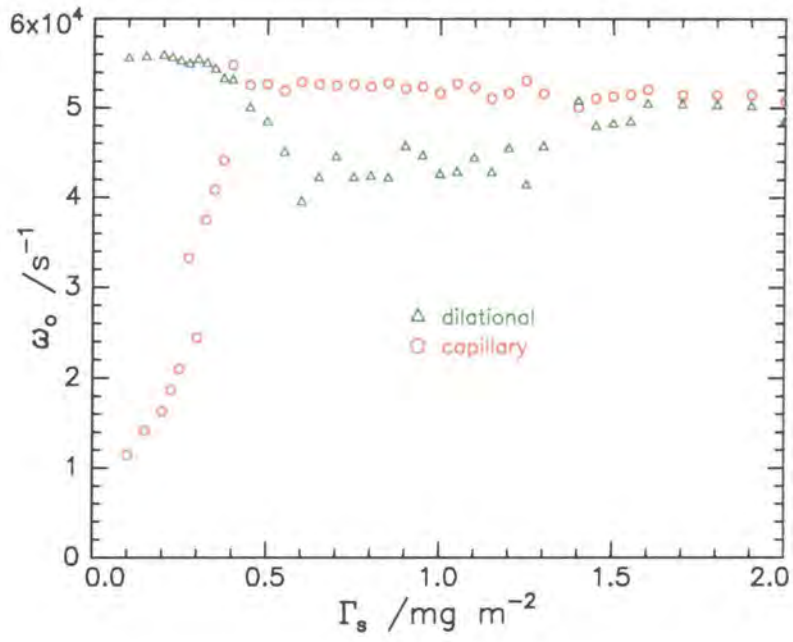
a) frequency
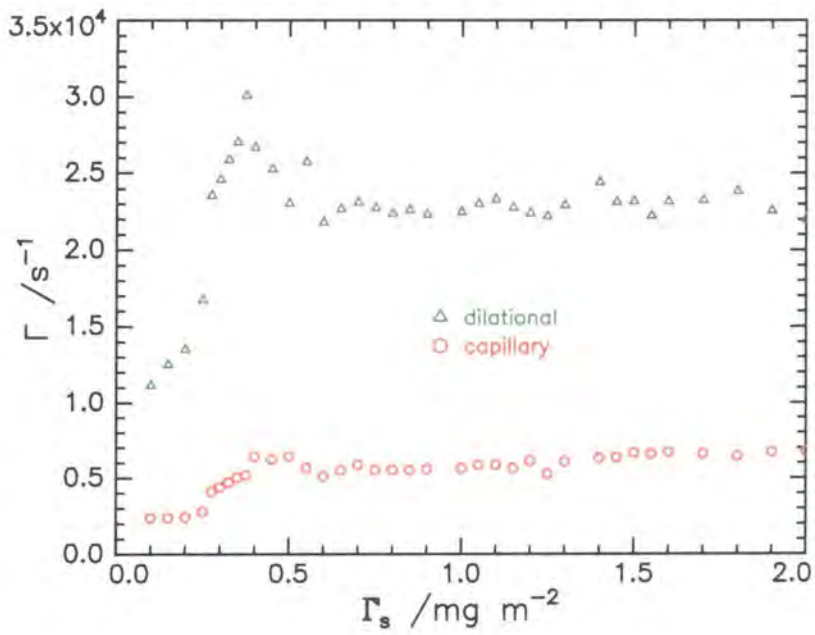
b) damping

Figure 8.3.16. Comparison of capillary and dilational a) frequency and b) damping for *n25* as a function of surface concentration.

The damping behaviour of the capillary mode is reminiscent of that observed experimentally in figure 8.3.2. The dilational damping is significantly higher in magnitude and exhibits a strong maximum at 0.4 mN m^{-2}, indicative of resonance. Such a strong maximum is not observed experimentally due to the weak coupling between the dilational and capillary modes and the domination of the scattered light by the capillary mode.

In general it was found that the error in the viscoelastic parameters increased with increasing surface concentration due to greater deviations between the individual correlation functions. When this error was taken into account for the moduli ratio it was discovered that on average the ratio at high surface concentration was subject to an 8% error. This indicates that a calculated ratio of 0.16 could range from 0.15 to 0.18 hence it was concluded that no emphasis should be placed on the results over this surface concentration range. It is important to note that the error is minimal at low surface concentrations (1%), therefore there is no ambiguity with the resonance concentration at 0.4 mg m^{-2}.

Alternative explanations for the change in dilational frequency are required and one possibility includes the existence of other modes on the surface. These have been acknowledged in the literature[21] but are experimentally inaccessible to date. It is therefore impossible to assess whether the presence of additional surface modes influences those accessible by light scattering (transverse and longitudinal) either periodically or continuously. Quantifying such behaviour would involve the development of a complementary analysis technique, a re-analysis of monolayer behaviour and also a complete modification of current theory as a new dispersion equation would be required.

In attempt to improve our understanding of the behaviour of the individual capillary and dilational waves the characteristics of two modes are conceptualised by comparing their behaviour to two loss free coupled oscillators. This is an idealised model as in reality the characteristics of the water surface include dissipative effects hence are complex. Nonetheless such a model has been applied to the copolymer system as a first approximation.

Consider a model system where two oscillators are connected but have different free frequencies Ω_1 and Ω_2. If these two oscillators are linked together in a single system as two pendula connected by a string for example, neither will be able to move

independently since the frequency of one oscillator will influence the other. The new frequencies experienced by each oscillator are linked to the free frequencies (Ω_1 and Ω_2) via the coupling strength κ,

$$(\omega - \Omega_1)(\omega - \Omega_2) = \kappa^2$$ **Equation 8.3.13.**

where the solutions to this quadratic equation, ω_1 and ω_2, are the normal frequencies associated with each mode. It is therefore easy to see that when κ is zero there is no coupling between the mode i.e. $\Omega_1 = \omega_1$ and $\Omega_1 = \omega_2$. As coupling is introduced κ becomes positive and the individual frequencies begin to diverge i.e. $\omega_1 > \Omega_1$, $\omega_2 < \Omega_2$. When coupling is maximised (i.e. at resonance) the high frequency mode would reach a maximum value while the low frequency mode would be minimised. This simple model can be directly related to the copolymer system where the transverse and longitudinal modes would be propagating with free frequencies Ω_1 and Ω_2. However these modes are always coupled therefore the 'real' frequencies, ω_1 and ω_2 relate to the capillary (high frequency) and dilational (low frequency) modes respectively. When the copolymer system at resonance, we should observe the capillary and dilational frequency modes reaching their maximum and minimum values respectively. Such characteristic behaviour is observed for the individual frequencies of the graft copolymer system in figure 8.3.16a, where the maxima and minima are observed between 0.4-0.6 mg m^{-2}. This surface concentration range matches the concentration associated with classical resonance which confirms that the two modes are in resonance at 0.4 mg m^{-2}.

One other interesting feature present in figure 8.3.16a was discussed earlier and involves the sudden increase in the dilational frequency at 1.4 mg m^{-2}. This is accompanied by a slight decrease in capillary frequency but since the possibility of resonance has already been eliminated then it is suggested that the coupling between the two modes changes. To try to understand such behaviour the coupling is examined more closely. The coupling coefficient for an air-water interface is;

$$[\eta(q - m)]$$ **Equation 8.3.14.**

where the quantity, m, is associated with coupling of the surface modes and is expressed as:

$$m = \mathrm{Re}\left|\left(q^2 + \frac{i\omega\rho}{\eta}\right)^{\frac{1}{2}}\right|$$

Equation 8.3.15.

These expressions show the only parameter that influences the coupling of the two modes during the surface concentration experiment is the surface wave frequency because q, ρ and η are constant. This implies that the coupling varies in accordance with the propagating characteristics of the capillary waves i.e. the real frequency and damping since $\omega = \omega_o + i\Gamma$, and these parameters for *n25* (figure 8.3.1 and 8.3.2) have been re-examined. No outstanding feature was observed over the relevant surface concentration range, which suggests that the coupling between the capillary and dilational modes do not change. The energy transfer into the dilational mode must therefore have originated from one of the other five surface modes present for example splay or twist modes.

The coupling behaviour outlined for *n25* is common to the copolymer series.

Section 8.4 Frequency Dependence

In this section the results from the dependence of surface viscoelastic properties on wavenumber, q, ($\equiv$ capillary wave frequency) of each graft copolymer will be outlined. In these experiments one surface concentration was selected, namely 0.4 mg m^{-2}, and the dynamical behaviour of each copolymer film was monitored over a wide range of wavenumbers, from 220 to 1800 cm^{-1} for a clean water surface. To obtain such a range of q values a 400 mW laser was used as the light source. The surface concentration of 0.4 mg m^{-2} was selected because it was identified in the previous section to be the resonance concentration. When the modes are in resonance the conditions for examining both modes are optimised because the coupling between them is maximised.

8.4.1 Results: Frequency and Damping

A double logarithmic plot of capillary wave frequency and damping is given in figure 8.4.1 for a spread film of *n25* at 0.4 mg m^{-2}. In this diagram the symbols represent the experimental data and the lines are the theoretical values for a fluid surface calculated by substituting a surface tension of 65 mN m^{-1}, (the average value inferred from dynamic data across the frequency range), and literature values for the density and viscosity of pure water at 296 K into the dispersion equation. All other parameters (transverse shear viscosity, dilational modulus and viscosity) were set to zero, therefore any deviation between experimental and theoretical results reflects the influence of the dilational modulus and viscosity of the surface waves. As expected the introduction of a monolayer to the water surface depressed the frequency slightly and considerably increased the damping of the capillary waves on the surface. Theoretically the propagating characteristics of the capillary waves are expected to scale as $\omega_0 \sim q^{3/2}$ and $\Gamma \sim q^2$ and the dilational damping as $\Gamma \sim q^{4/3}$.
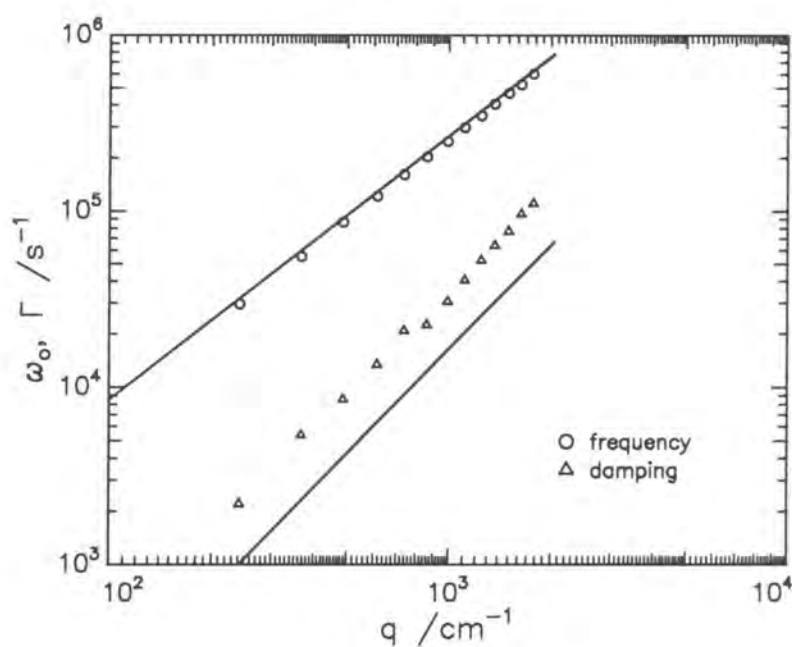
Figure 8.4.1. Double logarithmic plot of capillary wave frequency and damping as a function of wavenumber for *n25* at 0.4 mg m^{-2} (symbols) and values calculated for a clean water surface.
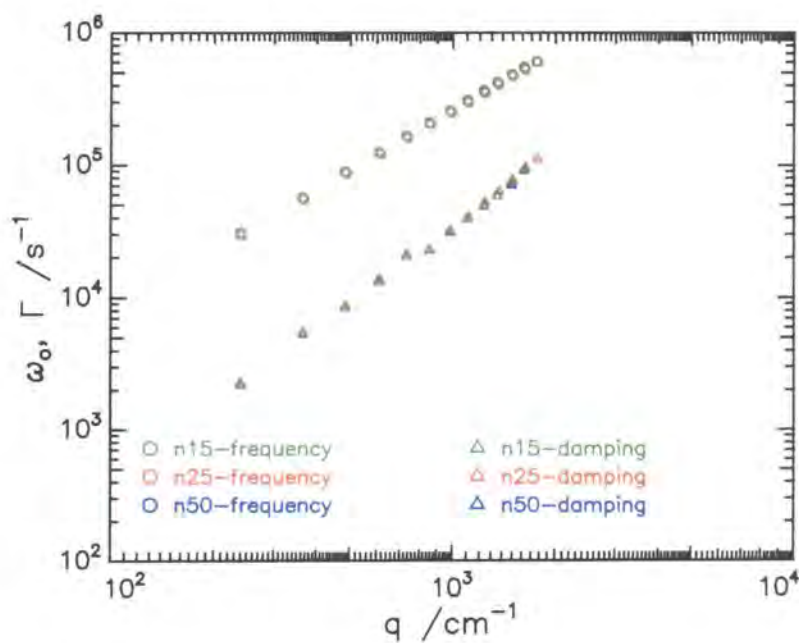
Figure 8.4.2. Comparison of frequency and damping behaviour as a function of q for the series of copolymers.

In order to compare the experimental results with these predictions the data were fitted with a linear least squares fit, and the frequency data was found to scale according to $\omega_o \sim q^{1.51}$ which is in excellent agreement with the theoretical exponent. The experimental damping values are greater than those for a water surface because no viscosity was included in the simulation and it is this term that influences the damping. The behaviour is however unusual as the data exhibits two separate regimes which are divided by a discontinuity in the data at circa 1000 cm^{-1} ($\omega \approx 18\ 600$ s^{-1}). This behaviour was highly reproducible and is therefore not an artefact of the experiment. It also should be emphasised that the unusual damping behaviour does not have an instrumental source as occasionally observed[22], but is a real feature of the data, indicating a unique phenomenon is occurring in the copolymer film. The scaling behaviour of each set of data was determined individually: for low q values $\Gamma \sim q^{1.97}$ and for high q values $\Gamma \sim q^{2.23}$. The exponent for the low frequency data is essentially the expected value of two, suggesting that the damping in this region is influenced predominantly by the capillary mode. The higher range of frequency data exhibit a greater dependence on damping and diverge from those of an un-damped surface.

Similar behaviour has been previously observed in both surfactant[13] and polymer[22,23] systems, where the damping has both diverged and converged towards the values predicted for water and is indicative of changes in coupling between the capillary and dilational modes.

The experimental frequency and damping behaviour are compared as a function of graft length in figure 8.4.2. The data for each copolymer are coincident and the discontinuity observed in the damping data occurs at identical wavenumbers, and to a similar extent. This indicates that the unusual characteristics observed in the damping are not dependent on graft length. This phenomenon will be discussed in detail later.

The scaling exponents for the frequency and damping dependence on q were obtained from each copolymer and are given in table 8.4.1. All frequency values follow the theoretical dependency for capillary waves and in each case dual damping behaviour is observed. In all copolymers the damping behaviour at low q (i.e. $q \leq 1000 \text{cm}^{-1}$) appears to be dominated by capillary damping as all scaling exponents agree well with the theoretical capillary dependence. At high q all deviations from the damping data occur to identical extents and the average scaling exponent predicts a stronger

dependence on q than either the capillary or dilational mode. These results confirm that there is no discernible trend as a function of graft length.

Copolymer	Frequency exponent	Damping exponent / low q	Damping exponent / high q
n15	1.50	1.98	2.14
n25	1.51	1.97	2.23
n50	1.52	1.95	2.10

Table 8.4.1. Comparison of scaling exponents for the frequency and damping behaviour of all graft copolymers as a function of q.

8.4.2 Results: Viscoelastic Parameters

The viscoelastic parameters were obtained using the spectral fitting method. The transverse shear viscosity was again set to zero while the remaining viscoelastic parameters were allowed to float as before. The wavenumber dependence on each viscoelastic parameter is presented individually in the following section for all copolymer materials.

Surface Tension

The surface tension data obtained for each copolymer is presented in figure 8.4.3. The data are highly scattered but have a weak dependence on q, as the data slowly decrease with increasing q. The extent of decrease observed here is significant as the difference between q values is circa 5 mN m^{-1} for each copolymer. The magnitude of the surface tension observed here (circa 68 mN m^{-1}) is considerably lower than the dynamic value observed in the concentration dependence studies for a surface concentration of 0.4 mg m^{-2} (82 mN m^{-1}). In fact the surface tension observed in the frequency studies concurs with the static value taken from the surface pressure isotherm suggesting that the film is already in a relaxed conformation.
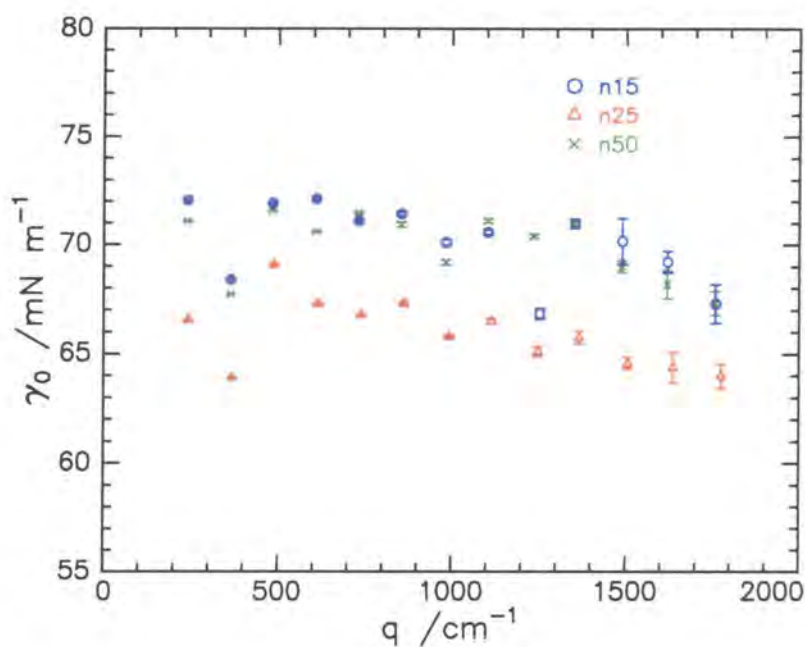
Figure 8.4.3. Wavenumber dependence of surface tension for a spread film of 0.4 mg m^{-2} for all copolymers.
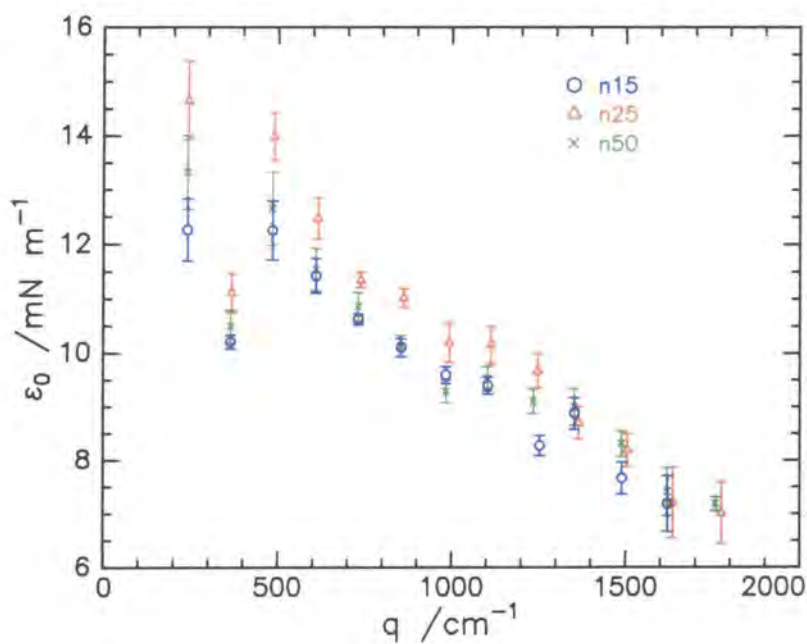
Figure 8.4.4. Wavenumber dependence of dilational modulus for a spread film of 0.4 mg m^{-2} for all copolymers.

Dilational Modulus

The variation of dilational modulus with surface wavenumber is given in figure 8.4.4 and all data exhibit a discernible trend, which is significantly more pronounced than that of the surface tension. The magnitude of the modulus for all copolymers decays rapidly as in general, the dilational modulus decreases linearly from circa 14 mN m^{-1} to half its original value. The data obtained for the second wavenumber investigated i.e. 375 cm^{-1}, corresponding to a frequency of 51 800 s^{-1}, is consistently lower than the remaining data and does not conform to the trend exhibited. It is difficult to assess at this stage whether this variation is due to error or simply an artefact of the fitting procedure. It is assumed however to be physically real as identical values were returned after repeatedly fitting the correlation functions with numerous starting parameters, and it was also experimentally reproducible.

The behaviour of the copolymers are again indistinguishable consolidating earlier predictions that surface behaviour does not depend on the range of graft lengths tested here.

Dilational Viscosity

A plot of dilational viscosity as a function of wavenumber (figure 8.4.5) also exhibits an intriguing trend. At low q values the viscosity is positive and high. The behaviour predicted by the second wavenumber again does not conform to the observed trend, but is included in the remaining analysis as it was highly reproducible. As the wavenumber increases, the viscosity turns negative at circa 1000 cm^{-1} (23 000 s^{-1}). Interestingly, the change in sign of the dilational viscosity coincides with the wavenumber where the discontinuity in damping was observed (see figure 8.4.2). The magnitudes of the dilational viscosities detected are identical within experimental error for all copolymers studied, consolidating the absence of dependence of viscoelasticity on graft length.
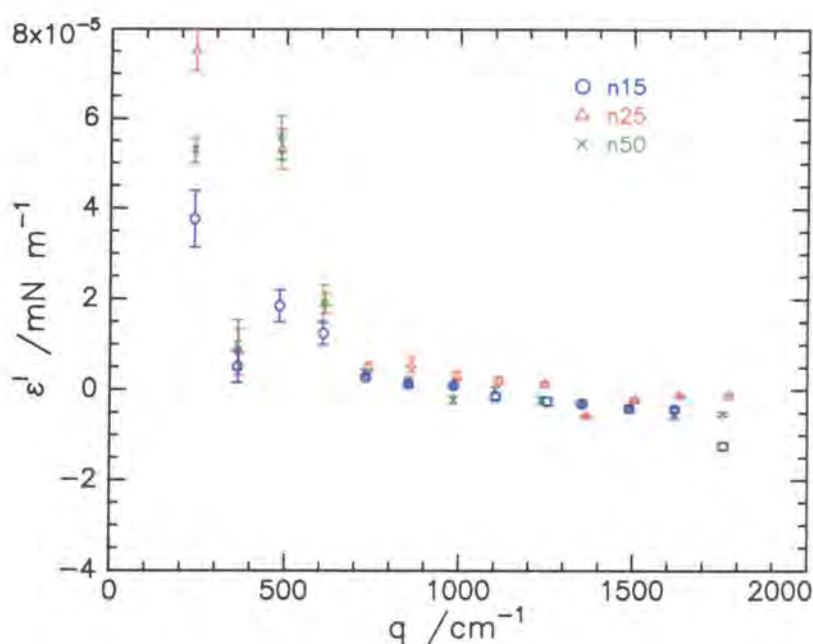
Figure 8.4.5. Wavenumber dependence of dilational viscosity for a spread film of 0.4 mg m^{-2} for all copolymers.

8.4.3 Viscoelastic Relaxation

In attempt to understand the complex viscoelastic behaviour of the system simple models have been applied to experimental data to describe the relaxation processes occurring within the monolayer. This method has previously been used to interpret the frequency dependent behaviour of numerous systems with varying degrees of success. For example the homopolymers[14] PMMA and PEO were successfully interpreted using such models and since the behaviour of the graft copolymers is strongly influenced by PEO here seemed appropriate to apply these models to the graft copolymer system.

The two most commonly used models[24] are the Maxwell fluid and the Voigt solid. Each model can simply be represented using two mechanical components, a spring and a dashpot, and are connected in either series (Maxwell) or parallel (Voigt).
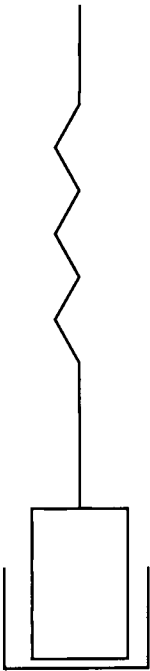
a) Maxwell fluid
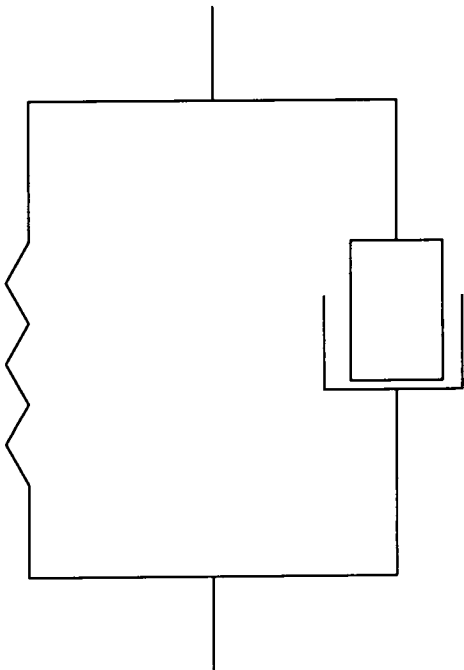
b)   Voigt solid

Figure 8.3.6. Schematic representation of a) Maxwell element consisting of a spring and dashpot in series and b) Voigt model consisting of a spring and dashpot in parallel.

The spring represents the elastic contribution of the monolayer and has an associated stiffness that corresponds to the shear modulus. The dashpot (a piston moving in oil) accounts for the viscous nature of the film quantified by the frictional resistance. It is imperative to remember that the models are only simple, phenomenological systems and the spring and dashpots do not easily correlate to the physical parameters. The elements describing each model system are schematically represented in figure 8.3.6a and b.

When a monolayer is spread on a liquid surface the capillary waves import an oscillatory stress and strain. These two properties are related via the complex dynamic modulus, $G^*(\omega)$;

$$G'^*(\omega) = G'(\omega) + iG''(\omega)$$

Equation 8.4.1.

where $G'(\omega)$ and $G''(\omega)$ are the storage and loss moduli respectively.

The storage modulus is associated with the storage and release of energy within the periodic surface motion and corresponds to the dynamic surface tension. The loss modulus describes the dissipative properties of the motion and conventionally was related to $\omega^2 \gamma'$. In this work γ' was set to zero, however theoretically the relaxation processes can be observed through either the capillary or dilational waves. All data were collected at the resonance concentration where frequencies of the dilational waves are experimentally accessible, and at resonance the equivalent expressions for the storage and loss modulus can be used i.e. $G'(\omega) = \varepsilon_0$ and $G''(\omega) = \omega_0^2 \varepsilon'$.

The expressions for the storage and loss modulus for the Maxwell model are given by;

$$G'(\omega) = G_e + \frac{G_i \omega_0^2 \tau^2}{1 + \omega_0^2 \tau^2}$$

Equation 8.4.2.

$$G''(\omega) = \frac{G_i \omega_0 \tau}{1 + \omega_0^2 \tau^2}$$

Equation 8.4.3.

where G_e is the equilibrium (i.e. static) elastic modulus for a spread film and is included here to incorporate any 'solid-like' behaviour in the film. G_i is the strength of the relaxation process, which has a relaxation time τ.

The equivalent expressions for the Voigt model are;

$$G'(\omega) = G_i \qquad\qquad \textbf{Equation 8.4.4.}$$

$$G''(\omega) = G_i \omega_o \tau \qquad\qquad \textbf{Equation 8.4.5.}$$

For the Voigt model it is noted that no frequency dependence is predicted for the dilational modulus or viscosity. It is obvious therefore that this model will not describe the viscoelasticity of the graft copolymers as both dilational parameters decrease linearly as a function of frequency. The Voigt model was disregarded at this stage and attention was focussed on the Maxwell model, which includes a frequency dependence.

The surface tension and dilational modes are dependent on the frequency for all graft copolymer films as both moduli exhibit a systematic decrease. However, the Maxwell model predicts that the modulus increases while the viscosity simultaneously decreases, and such behaviour is clearly not reproduced experimentally as both parameters exhibit a decrease (see figure 8.4.4 and 8.4.5). It was concluded therefore that the Maxwell model does not describe the viscoelastic properties of the monolayer either.

In summary, this brief analogy reveals that the viscoelastic behaviour of the graft copolymer films is not reproduced by the simple arrangement of a single dashpot and spring. This clearly indicates that the behaviour exhibited here is much more complex than that described by the simple Maxwell and Voigt phenomenological models, and it is not apparent how any number of springs and dashpots could be arranged to model the viscous properties of the copolymer films. This result is in agreement with other copolymer films studied as these models did not adequately describe the viscoelasticity of linear and graft copolymers containing PMMA and PEO either. It was therefore concluded that the simple two-component phenomenological models fail to describe the surface viscoelasticity therefore alternative analysis methods were sought.

8.4.4 Discussion

There are two features present in the viscoelastic parameters that are unusual and merit further discussion. Firstly the surface tension values. The magnitude of the surface tension obtained in the frequency dependence studies, at q~350 cm^{-1} is approximately 15 mN m^{-1} lower than the equivalent values obtained in the surface concentration studies. Interestingly the value observed here concurs with the static value obtained. Both sets of results were obtained using identical experimental procedures and fitting methods where numerous starting values were used and the global minimum solution found. Each experiment was repeated many times, several months apart and the results obtained from each study were in good agreement. This immediately suggests that in the frequency dependent study the film does not undergo relaxation processes when perturbed by a capillary wave, but it is not clear why this would occur. The only difference between these two sets of experiments was the temperature and changes in this variable will alter the density and viscosity of the subphase. For a pure water surface a temperature change of circa 4 °C (the difference observed experimentally) induces a variation of ±0.1 mN m^{-1}. Although this value is considerably smaller than that observed here, it indicates that the temperature can influence the surface tension and is one reasonable explanation of the observed phenomenon. In both experiments the surface tension is driven by the capillary wave and is dependent on the density, ρ, of the subphase and q value;

$$\gamma_o \approx \mathrm{Re}\left|\frac{\omega_c{}^2\rho}{q^3}\right| \qquad\qquad \textbf{Equation 8.4.6.}$$

In addition to temperature variations the wavenumber has an associated error of ±2 mN m^{-1} due to small fluctuations in the height of the subphase. If this error value and the variation in the density are substituted into equation 8.4.6 for a constant frequency value the variation in the surface temperature parameter can be determined for the worst possible combination. This value was found to be relatively high at 2.5 mN m^{-1}, hence it is proposed that the difference between concentration and frequency studies was due to a combination of variations in the experimental temperature and wavenumber.

Secondly, the two viscoelastic moduli, surface tension and dilational modulus, decrease with increasing surface concentration. This behaviour is unusual as intuitively it is expected that the overall elasticity of a surface would increase with rising frequency. One reasonable explanation could be that the decrease observed for the transverse and dilational modes, is being compensated for by an increase in one, or more of the other modes that are inaccessible by SQELS, for example in splay or twist modes.

PEO is the major component of the graft copolymer, constituting 87-94 % by mass (depending on graft length) therefore it seems appropriate to discuss the characteristic viscoelastic parameters in relation to those exhibited by a spread layer of the homoPEO[5]. As alluded to earlier a fourth parameter (transverse shear viscosity) was fitted for homoPEO films but this parameter has been disregarded here as its effect on the viscoelasticity is minimal. The only other difference between experiments is the frequency range probed as q is extended here to 1800 cm^{-1} compared to the limiting value of 1100 cm^{-1} for previous studies, but a comparison over the lower q range is still viable.

This comparison reveals significant similarities between the viscoelastic properties of homoPEO, in particular the dilational behaviour and the graft copolymer studied here but first let us consider the surface tension. The values for PEO and the graft copolymer both exhibit weak dependencies on frequency. For homoPEO the surface tension is increasing with frequency and contradicting this the graft copolymer decreases. The difference in the trend is either inherent of the copolymer architecture or the values are not strictly true for homoPEO due to the incorporation of the transverse shear viscosity. The latter parameter has minimal effect on the viscoelastic properties, hence the former explanation is more reasonable and is confirmed when the behaviour is compared to the viscoelasticity of the graft copolymer PMMA-*g*-PEO. This graft copolymer interestingly revealed the surface tension decreased linearly with q only at high surface concentrations. This indicates that such an observed trend is inherent of the graft copolymer and occurs at high surface density of PEO.

The characteristics of the viscoelastic parameters pertaining to the dilational modulus for films of homoPEO and the graft copolymer (PNB-*g*-PEO) are similar as both decrease from circa 10 mN m^{-1} with increasing frequency. Differences arise in the rate of decrease however as the decay for homoPEO takes an exponential form whilst ε_o

for the graft copolymer decays monotonically. The data from PMMA-*g*-PEO have a large error associated with each point at high q and no discernible trend was elucidated at high surface coverage.

The frequency dependence of the viscosity parameters observed here are similar to homoPEO, both decay rapidly from positive to negative values. The hydrocarbon backbone and the resulting tethering organisation of the PEO must influence the dilational behaviour because the trends between homoPEO and the copolymer are only qualitatively reproduced, the magnitudes of the viscosities differ. Moreover the frequency where the viscosity switches from positive to negative is lower in the homopolymer. The decay observed for the graft copolymer here could be interpreted as a relaxation dependence in the destabilisation process, which actually causes the viscosity to be negative. The dilational viscosities determined for PMMA-*g*-PEO were systematically negative but interestingly when the trend in results are compared with those obtained for PNB-*g*-PEO as a function of surface concentration they are mirror images, reflected in the x-axes.

It appears that the viscoelastic characteristics for the dilational mode for PNB-*g*-PEO are strongly influenced by the PEO present suggesting that it is the PEO that is responsible for the changes in viscoelastic behaviour. However the copolymer architecture also has influence because only qualitative similarities are observed between PEO and the copolymer system. The similarity of the results for the series of copolymers reveals a lack of dependence of behaviour for the frequency, damping, or viscoelastic properties on the graft length.

The results presented for each copolymer were obtained at the resonance concentration, hence the coupling between the dilational and capillary modes is maximised. The coupling between these modes can be theoretically represented by a pair of coupled oscillators[9,25].

The theory behind classical coupled oscillators has previously been outlined in section 8.3.3 and was applied to determine the resonance concentration. The fundamental expression is repeated below in equation 8.4.7.

$$(\omega - \Omega_1)(\omega - \Omega_2) = \kappa^2 \qquad \textbf{Equation 8.4.7.}$$

where Ω_1 and Ω_2 are the natural frequencies of the uncoupled oscillators, κ the coupling constant, and the solutions ω_1 and ω_2 are the complex frequencies of the normal modes

(capillary and dilational) i.e. $\omega = \omega_o + i\Gamma$. In reality however the surface waves dissipate energy, therefore the best physical description involves coupled lossy oscillators. To obtain a mathematical description of the physical system including the dissipative effects equation 8.3.7 was modified to include the complex frequencies. As a consequence κ^2 can take on positive or negative values and when $\kappa^2 > 0$ the coupling is classified as reactive, or resistive if $\kappa^2 < 0$. κ will never equate to zero in this study as the upper and lower phases do not have equal densities and viscosities.

When the coupling constant is real (i.e. reactive coupling) the solutions ω_1 and ω_2 are also real. Equation 8.4.7 can be re-written in the form of equation 8.3.8 where $\overline{\omega} = \frac{1}{2}(\omega_1 + \omega_2)$ and $\Delta\omega = \frac{1}{2}(\omega_1 - \omega_2)$.

$$(\Omega - \overline{\omega})^2 = \kappa^2 + (\Delta\omega)^2 \qquad\qquad \textbf{Equation 8.4.8.}$$

This equation reveals that the characteristic differences between the frequencies of the coupled modes ($\Delta\omega$) and the natural frequencies of the uncoupled modes follow a hyperbolic dependence and both influence the behaviour of the normal modes. The hyperbola is centred at $\overline{\Omega} = \frac{1}{2}(\Omega_1 + \Omega_2)$ and is in the complex plane. Increasing $\Delta\omega$ therefore leads to the normal modes having almost identical frequencies as the uncoupled oscillator, i.e. the two modes are far removed from resonance. However when the normal oscillations are equal (i.e.$(\Delta\omega)^2 = 0$) the modes are in resonance. Under such conditions and as the coupling changes it transpires that the damping of each mode begins to converge along the imaginary axes and eventually combine whereupon the real terms of the natural modes (i.e. the frequencies) separate on the real axes. At this point and thereafter the normal modes become mixed and the behaviour of each mode is not able to be isolated. Such behaviour is referred to as mode mixing as neither mode solely displays capillary or dilational characteristics. It is of interest to note here that in all systems the dilational mode is heavily damped in comparison to the capillary wave therefore to meet the conditions for reactive mode mixing the damping of the dilational mode must decrease as that of the capillary mode increases.

Theoretically reactive mode mixing (when $\kappa^2 > 0$) can occur via two routes, one involves the transverse shear viscosity[26] and the second the dilational viscosity[27]. The first route is now obsolete since the transverse shear viscosity is no longer included in the dispersion equation (i.e. $\gamma' \equiv 0$). Earnshaw predicted however that an increase in the transverse shear viscosity, in the absence of dilational viscosity, caused the damping of the capillary wave to increase and that of the dilational mode to simultaneously decrease. The dampings converge at a critical value of transverse shear viscosity and therefore induce mode mixing.

More recently it has been predicted theoretically[27] and observed experimentally[13] that changes in the dilational viscosity bring about the conditions for mode mixing. If the dilational mode becomes unstable, then negative dilational viscosities are observed, which effectively cause the damping to converge, and as the viscosity decreases further the real frequencies begin to diverge hence mode mixing is induced. This phenomenon of mode mixing is explained more clearly by generating data where the frequency and damping of both the capillary and dilational waves have been calculated as a function of dilational viscosity using the dispersion equation. In each calculation the wavenumber was set to 350 cm^{-1}, the surface tension and dilational modulus were kept constant at 68 and 12 mN m^{-1} respectively while the dilational viscosity was varied from 2×10^{-5} through 0 to -2×10^{-5} mN m^{-1}. These data are plotted in the complex plane where normalised damping is plotted against normalised frequency. These normalised parameters are;

$$\omega_{o\,norm} = \frac{\omega_o}{\sqrt{\left(\gamma_o\, q^3/\rho\right)}}$$

Equation 8.4.9.

$$\Gamma_{norm} = \frac{\Gamma}{\left(2\eta\, q^3/\rho\right)}$$

Equation 8.4.10.

Figure 8.4.7 shows such a dispersion plot for three sets of generated data where the viscoelastic parameters assume values outlined earlier and were generated by varying q. At positive values of dilational viscosity the dilational and capillary modes retain their individual characteristics as the dilational mode sweeps down from right to

left as q decreases, while the capillary mode follows a semi-circular arc, dropping down from co-ordinates (2, 1) and sweeping through from right to left. As the dilational viscosity decreases the dilational damping moves to higher normalised frequencies until an abrupt change in behaviour is observed at $\varepsilon' = -2 \times 10^5$ mN m^{-1}.
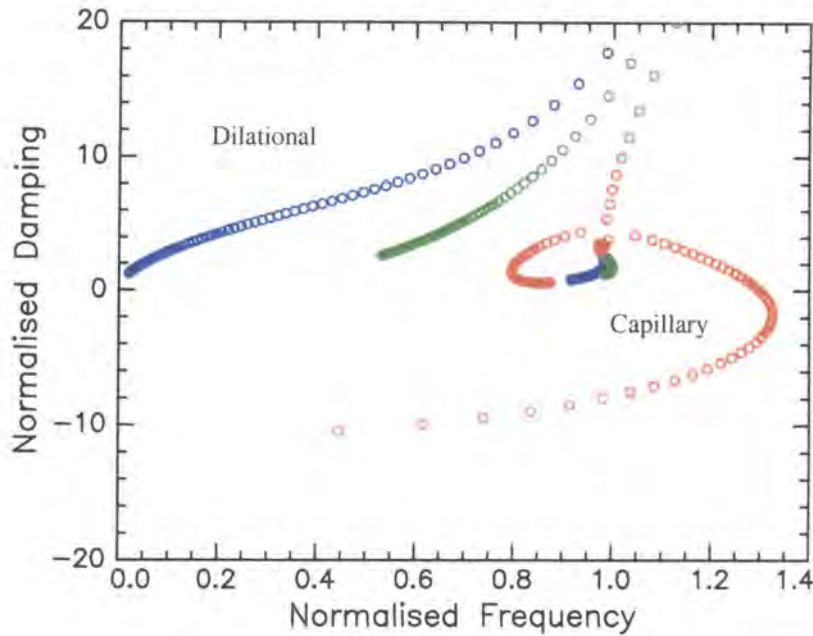
Figure 8.4.7. Generated data from the dispersion equation plotted in the complex plane where the surface tension and dilational modulus are constant at 68 mN m^{-1} and 12 mN m^{-1} respectively and the different behaviour observed is due to variations in the dilational viscosity ε' : $\varepsilon' = 2 \times 10^{-5}$ mN m^{-1} (blue); $\varepsilon' = 0$ (green) and $\varepsilon' = -2 \times 10^{-5}$ mN m^{-1} (red).

These data reveal that for $\varepsilon' \geq 0$ the dilational mode sweeps down from left to right while the capillary mode comes down vertically initially and then sweeps in a semi-circular arc from left to right. A negative value for ε' causes dramatic changes as the capillary mode sweeps from left to right over an expanded range of both normalised frequency and damping and the decays. The dilational mode in this situation initially decreases and at a critical q value it begins to curl and take on characteristics akin to the capillary mode. This change occurs at an identical wavenumber where the capillary mode jumped to assume behaviour representative of the dilational mode. Such characteristics are indicative of mode mixing hence we would expect the normalised damping to decreases from left to right if mode mixing were to occur induced by negative dilational viscosities.
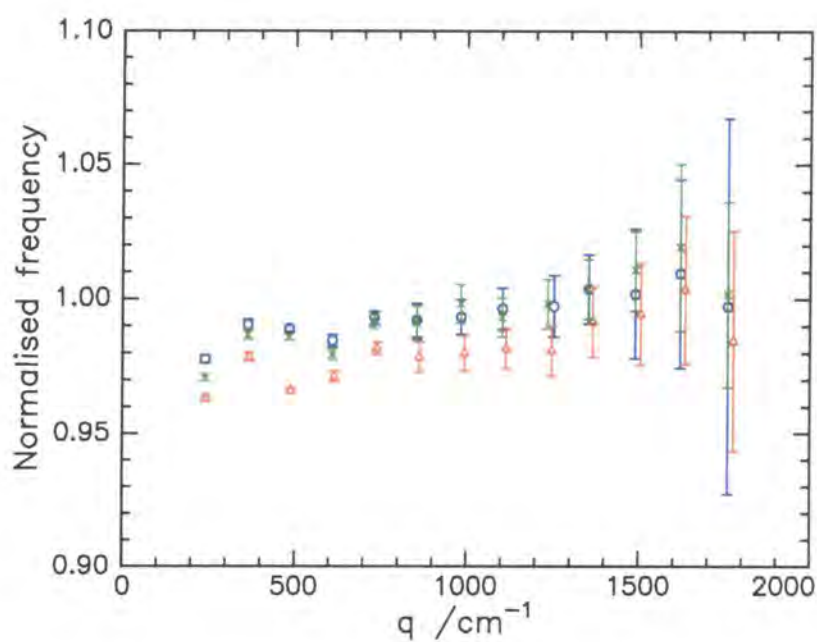
a) Frequency
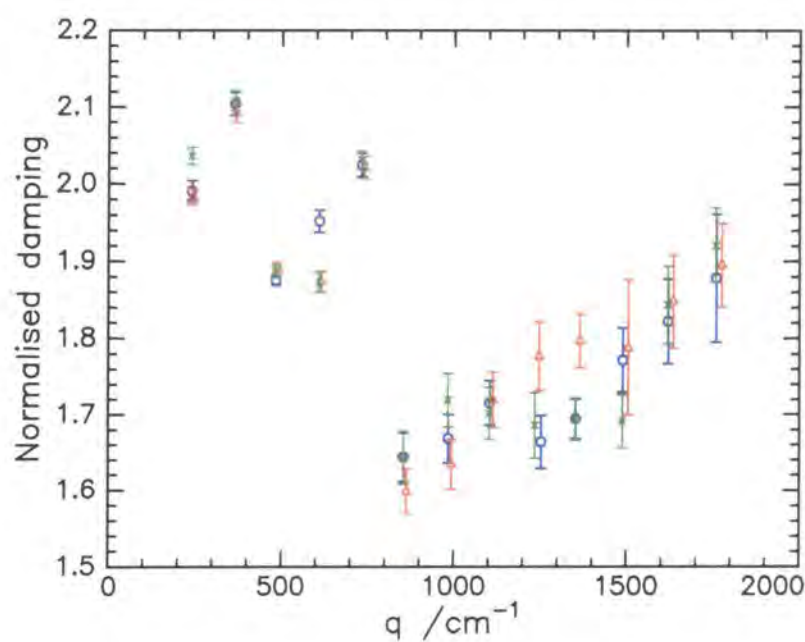
b) Damping

Figure 8.4.8. Normalised a) frequency and b) damping experimental data for all copolymers as a function of q.

At some normalised frequency (q value) the normalised damping should jump and increase from left to right as the capillary mode decays and the surface modes become dominated by the dilational mode. Mode mixing of this nature (via reactive coupling) has been observed experimentally in a surfactant system[13] and in a polymer monolayer[7] at the air-water interface, but to date there is no experimental evidence for mode mixing due to resistive coupling. Resistive coupling theoretically occurs when $\kappa^2 < 0$ and the solutions to equation 8.4.7 are imaginary. For this case the conditions leading to mode mixing are the exact opposite those for reactive coupling, i.e. the frequencies converge and become equal and the damping of each mode converges.

Experimental data is rarely as well-behaved as the generated data because in reality the two modes will be influenced by a mixture of the viscoelastic parameters over the entire q range investigated. The experimental frequency and damping data as a function of q (figure 8.4.2) for the graft copolymer system suggests that mode mixing occurs at high q. Analysing the normalised frequency and damping behaviour as a function of wavenumber corroborates such an idea as it is clear in figure 8.4.8a that the frequencies do not alter significantly as q varies, but the damping exhibits a discontinuity. At low q the damping decreases with wavenumber until a discontinuity is observed in figure 8.4.8b when q equals circa 1000 cm^{-1}. Thereafter the normalised damping increases with increasing q. This dramatic change in behaviour is indicative of mode mixing.

In attempt to consolidate such predictions and to help determine what is happening to each mode within the system, data were generated by solving the dispersion equation using average values for the viscoelastic moduli at the discontinuity point ($\gamma_o = 68$ mN m^{-1}, $\varepsilon_o = 8$ mN m^{-1}). The one parameter that undergoes significant change at this point is the dilational viscosity as it jumps from positive to negative, therefore three sets of data were calculated using values for ε' of that concur with those observed experimentally: $\varepsilon' = 1 \times 10^{-5}$, $\varepsilon' = 0$ and $\varepsilon' = -1 \times 10^{-5}$ mN m^{-1}. The frequency and damping dependence on q for each set of data are given in a double logarithmic plot in figure 8.4.9. It is apparent from these diagrams that the dilational viscosity has little effect on the capillary frequency but has a profound influence on the dilational frequency and damping.

331
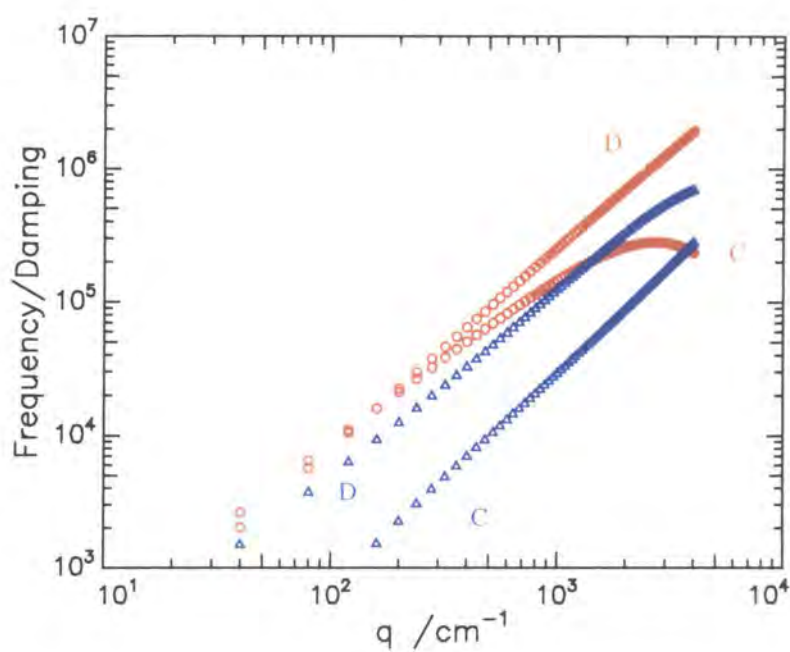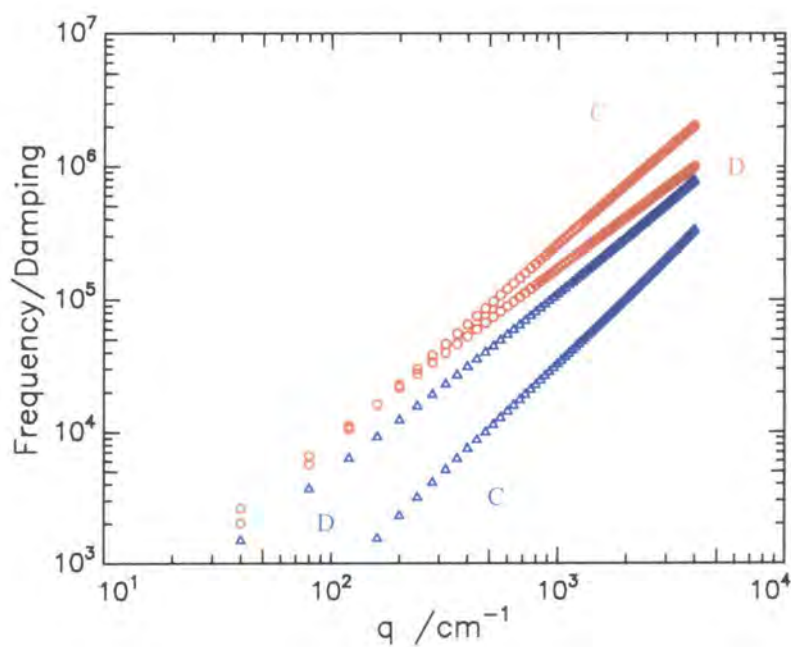
a) $\varepsilon' = 1 \times 10^{-5}$ mN m^{-1}

b) $\varepsilon' = 0$
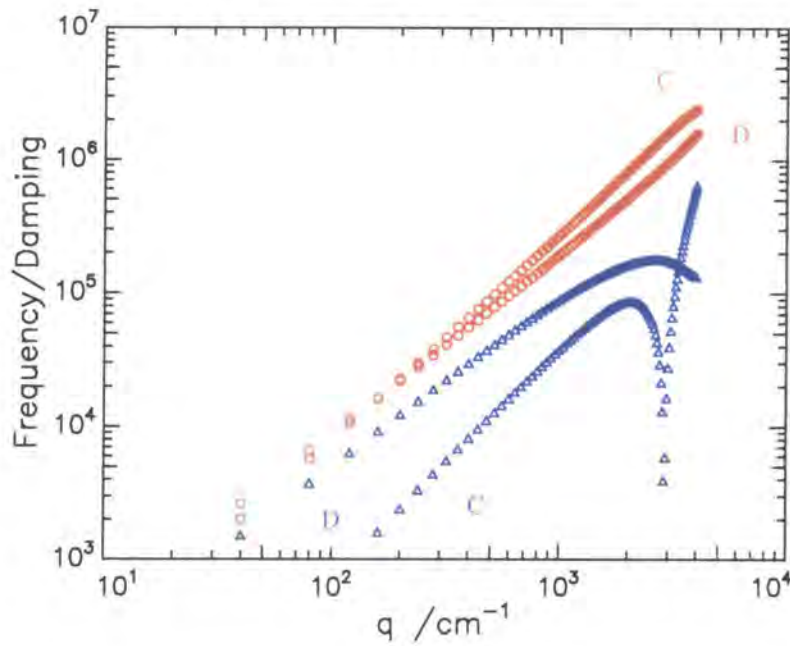
c) $\varepsilon' = -1 \times 10^{-5}$ mN m^{-1}

Figure 8.4.9. Double logarithmic plots of frequency (o) and damping (Δ) of the capillary (C) and dilational (D) waves taken from data generated from the dispersion equation where the surface tension and dilational modulus are kept constant at 66 mN m^{-1} and 8 mN m^{-1} respectively while the dilational viscosity varies: a) $\varepsilon' = 1 \times 10^{-5}$ mN m^{-1}; b) $\varepsilon' = 0$ and c) $\varepsilon' = -1 \times 10^{-5}$ mN m^{-1}.

When ε' is positive the capillary wave parameters follow the theoretical dependencies on q, while both the dilational parameters begin to decrease at high q but to differing extents (the frequency decreases further than the damping). At $\varepsilon' = 0$ both modes exhibit linear dependencies on q and these agree well with the theoretical prediction. As ε' turns negative very different behaviour is observed. At high q the capillary and dilational frequencies begin to converge and conversely the dampings diverge. At such high q the dilational damping decreases slowly while the capillary damping decreases swiftly and change gradient at a specific q value and thereafter increases exponentially at the expense of the other mode.

The q dependence observed is higher that that predicted for either capillary or dilational damping. Such characteristic behaviour is indicative of resistive mode mixing.

Comparing these results to the experimental data indicates that this type of mode mixing is occurring in the graft copolymer films since a sharp drop in the damping data was observed at intermediate q (1000 cm^{-1} - figure 8.4.2) and as q increased further the damping exhibited a stronger dependency. Further evidence to consolidate that the mode mixing is observed due to resistive coupling is obtained by comparing the normalised frequency and damping characteristics as a function of q of the above data where $\varepsilon' = -1 \times 10^{-5}$ mN m^{-1} with the data where reactive coupling occurs (see figure 8.4.7 where $\gamma_o = 68$ mN m^{-1}, $\varepsilon_o = 12$ mN m^{-1} and $\varepsilon' = -2 \times 10^{-5}$ mN m^{-1}).

It is clear from both frequency and damping dependencies that the different routes towards mode mixing display opposite behaviour. The frequencies in figure 8.4.10a at high q converge when the modes are mixed via resistive coupling, while the frequencies move away from each other when reactive mode mixing occurs. In the latter case the capillary frequency decays and the dilational mode assumes capillary behaviour. Meanwhile the damping behaviour also differs depending on the nature of the coupling as observed in figure 8.4.10b. When the coupling is reactive it is clear that the dampings coincide at high q, while the damping behaviour of each mode converges slightly before diverging rapidly for resistive coupling. Therefore the mode mixing that occurs for graft copolymer films is unequivocally induced by resistive coupling as the normal mode frequencies converge while the associated dampings diverge.

To exemplify the switching of capillary and dilational behaviour the calculated frequency and damping data are plotted as a function of ε_o/γ_o for each dilational viscosity value (see figure 8.4.11). At positive dilational viscosity values the two frequencies cross at $\varepsilon_o/\gamma_o = 0.27$, which is not within the range observed experimentally (0.13-0.21) and moreover the dampings retain their individual characteristics. The frequencies and damping of each mode begin to exhibit signs of switching in behaviour when the dilational viscosity is zero. Mode mixing is however observed when the dilational viscosity becomes negative (figure 8.4.11c). In this case the frequencies converge and become equal when ε_o/γ_o is close to the resonance condition. Under these conditions the behaviour of each mode is interchanged as the capillary mode takes on dilational behaviour and vice versa. This splitting is also observed in the damping as indicated in figure 8.4.11c by the dashed line.

a) Frequency
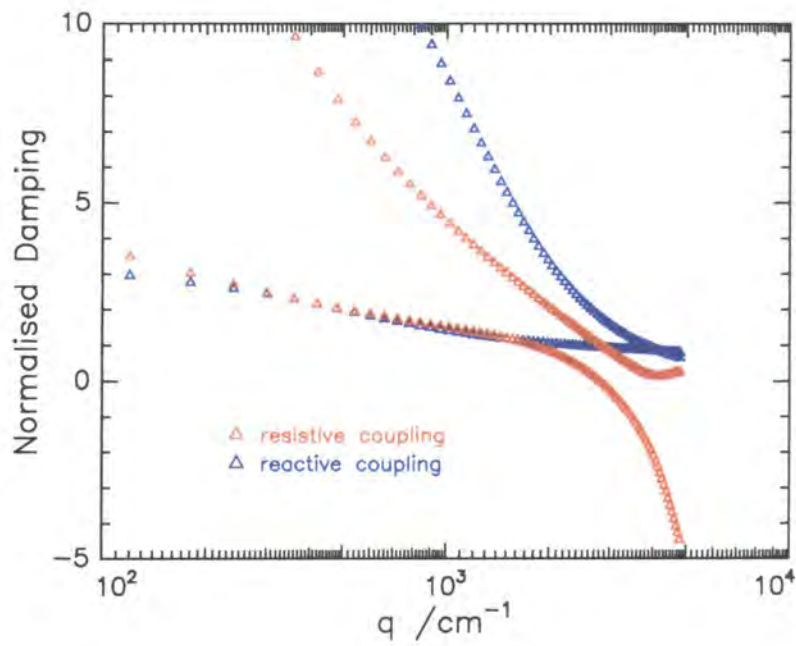
b) Damping

Figure 8.4.10. Comparison of normalised a) frequency and b) damping for reactive and resistive coupling inducing mode mixing.
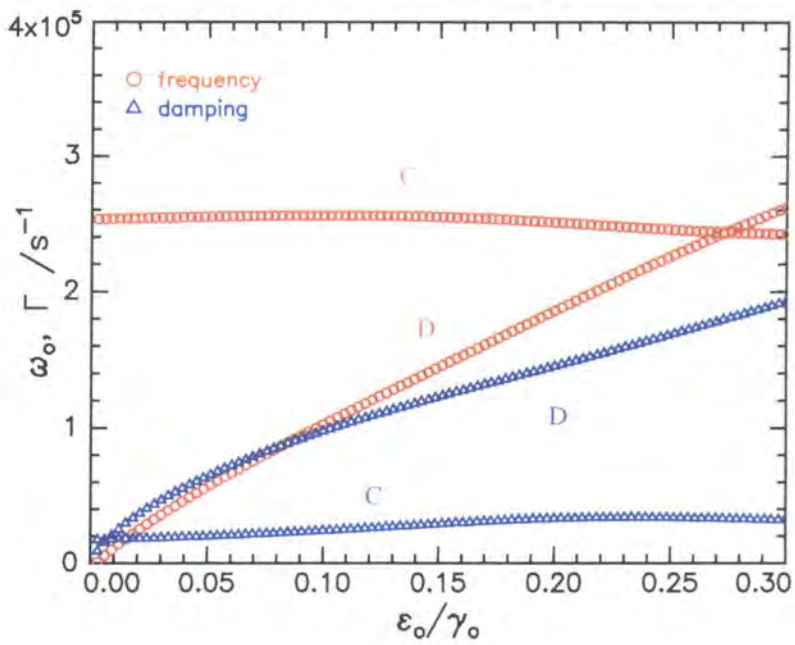
a) $\varepsilon' = 1 \times 10^{-5}$
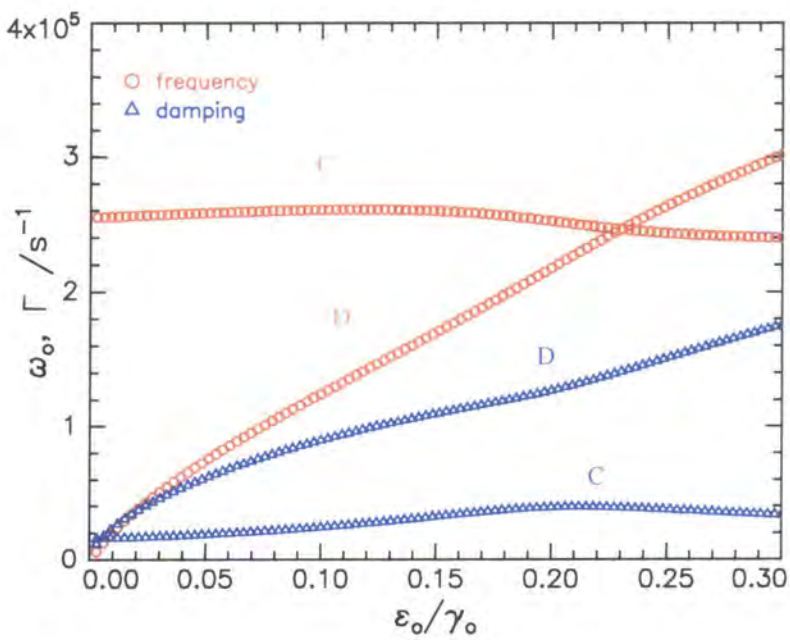
b) $\varepsilon' = 0$
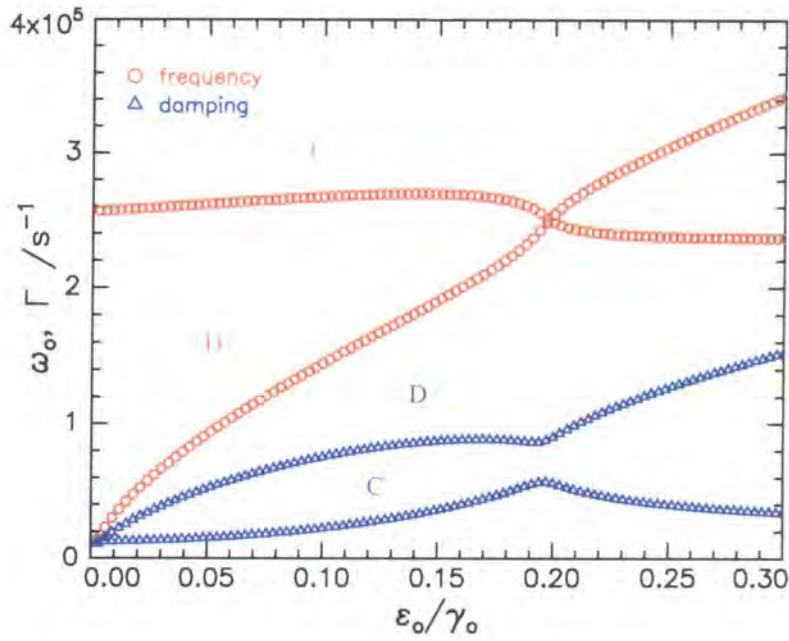
c) $\varepsilon' = -1 \times 10^{-5}$

Figure 8.4.11. Frequency and damping of capillary (C) and dilational (D) modes calculated as a function of ε_o / γ_o for $\gamma_o = 66$ mN m^{-1}, $\varepsilon_o = 8$ mN m^{-1} and a) $\varepsilon' = 1 \times 10^{-5}$ mN m^{-1}, b) $\varepsilon'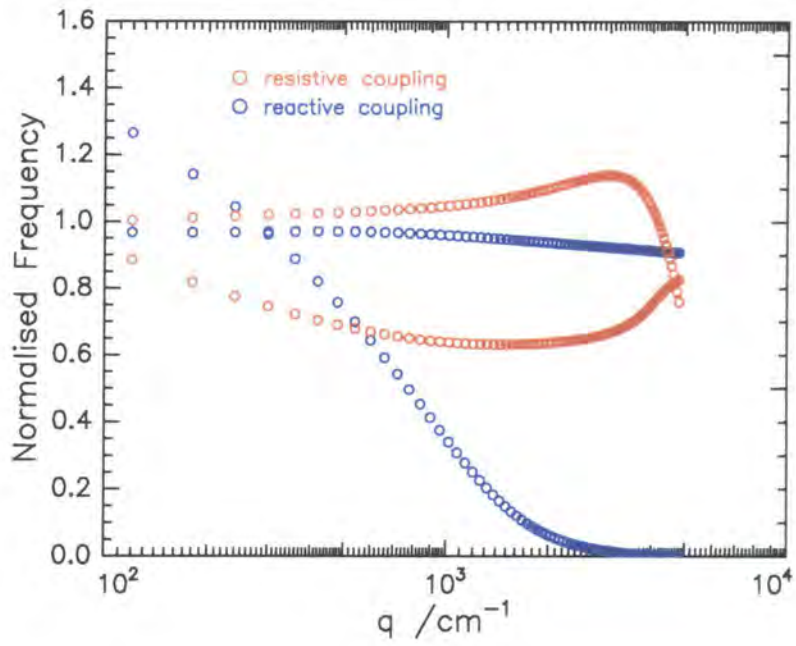 = 0$ and c) $\varepsilon' = -1 \times 10^{-5}$ mN m^{-1}. The dashed lines represent the crossover between capillary and dilational mode and vice versa.

A more explicit illustration of the mode 'flipping' is observed if the simulated data are presented in a dispersion plot as in figure 8.4.12. When ε' is positive both capillary and dilational modes retain their individual characteristics as the dilational mode sweeps down from right to left while the capillary mode forms a semi-circular arc moving from left to right starting at co-ordinates (1, 4). Decreasing to $\varepsilon' = 0$ appears to have no significant effect on the dispersion behaviour except the data are shifted slightly to higher normalised frequencies. When $\varepsilon' = -1 \times 10^{-5}$ mN m^{-1} however distinct characteristics are exhibited. At low q the dilational mode behaves as expected and begins to sweep down from right to left, but at a critical q value, the data take on capillary behaviour and curl with a semi-circle form. Meanwhile the capillary mode at

low q increases and forms a sweeping arc of increased diameter and at the co-ordinate (1.02, 2) behaviour switches and assumes dilational characteristics.
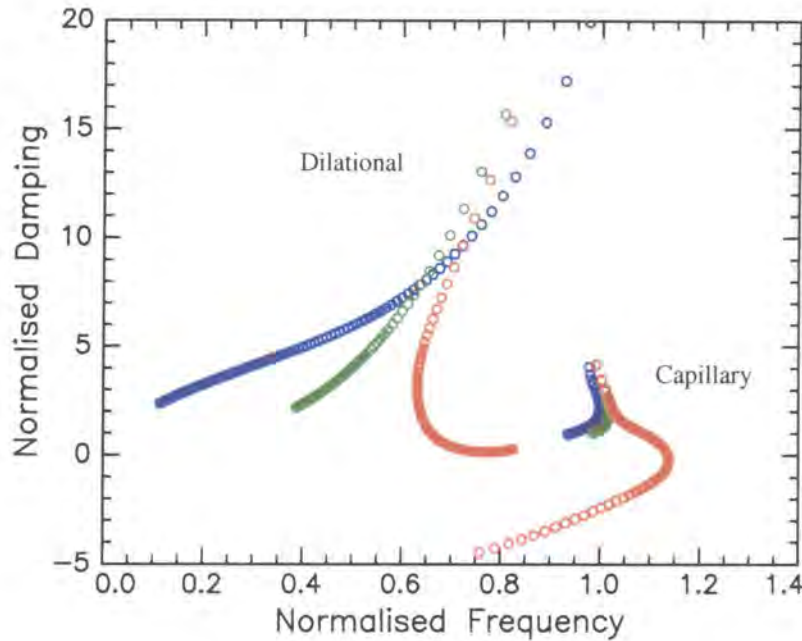
Figure 8.4.12. Generated data from the dispersion equation plotted in the complex plane where the surface tension and dilational modulus are constant at 66 mN m^{-1} and 8 mN m^{-1} and the different behaviour observed is due to variations in the dilational viscosity ε'; $\varepsilon' = 1 \times 10^{-5}$ mN m^{-1} (blue); $\varepsilon' = 0$ (green) and $\varepsilon' = -1 \times 10^{-5}$ mN m^{-1} (red).

Relating this plot to the experimental system we anticipate observation of a jump from one mode to another with no change in magnitude at circa 1000 cm^{-1}, as this q value is associated with the discontinuity in damping data given in figure 8.4.2 and figure 8.4.8. The experimental data for *n25* is plotted in the complex plane in figure 8.4.13 where the numbers indicate the q values associated with the data points. It is immediately obvious that the data is highly scattered as expected as the physical systems will not be as well-behaved as the simulated data. Nonetheless there is a distinct change in behaviour as the wavenumber increases. Initially the normalised damping decreases linearly from left to right and as it approaches a q value of 1000 cm^{-1} the trend changes as the normalised damping increases with increasing normalised frequency. This suggests that at low wavenumbers the capillary mode is dominating the damping of the surface waves until the critical q value, where the dilational

characteristics disappear suddenly and the dilational mode takes over and dominates the surface waves.
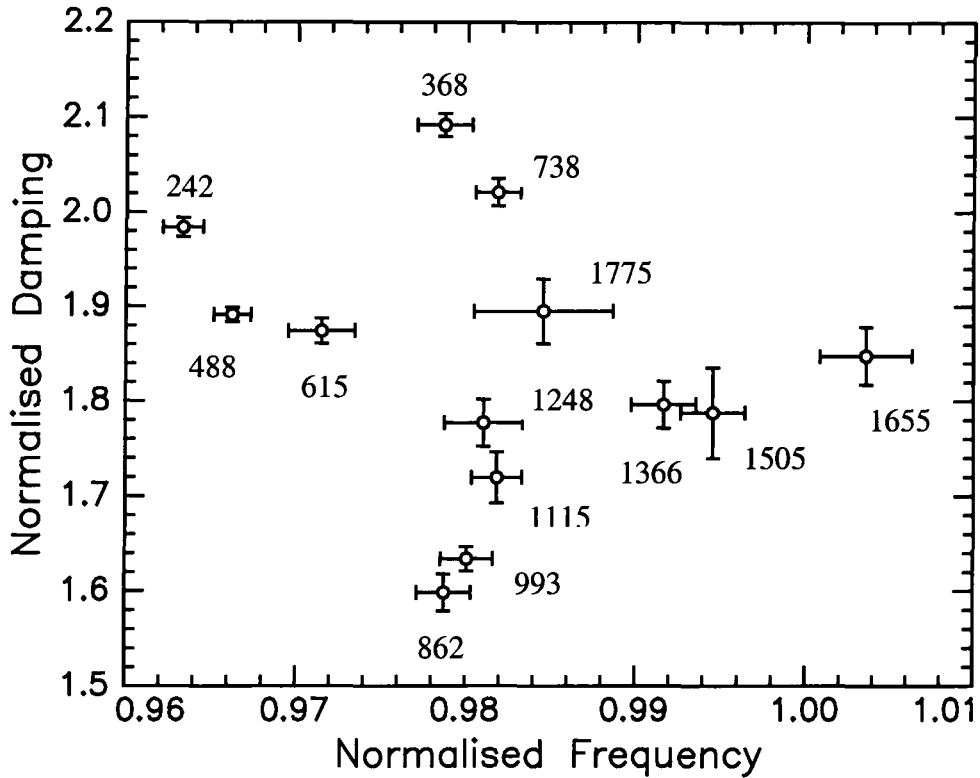
Figure 8.4.13. Normalised frequency and damping behaviour for *n25* plotted in the complex plane. The numbers are the associated q values for each data point.

The dispersion behaviour of all three copolymers are compared in figure 8.4.14 where the symbols represent the experimental data points and the solid lines guide the eye and highlight the average transition from capillary to dilational characteristics in each system. It is clear from this diagram that the behaviour of all three copolymers are indistinguishable as all copolymer films exhibit mode mixing, where the surface characteristics change from being predominantly dilational to capillary. These results confirm that the discontinuity observed in the damping data is indicative of the modes becoming mixed and interestingly the switch in behaviour occurs when the dilational viscosity switches from positive to negative values. Mode mixing is therefore induced in resistive coupling as in the reactive case[27] when the dilational viscosity assumes

negative values. Therefore mode mixing is induced by a reduction in the dilational damping while that for the capillary mode increases. This agrees well with the switching of the dominating mode: from capillary to dilational mode as q increases.

The physical interpretation of negative viscosities was discussed in the previous section (see section 8.3) and unfortunately the significance of these values remains elusive for this system where the copolymer forms an insoluble film. Phenomenologically such negative viscosities are effective parameters and account for energy being gained by one of the other surface modes, not accounted for in the dispersion equation hence it is incomplete. If the dispersion equation were to describe fully the surface dynamics then all five surface modes would need to be incorporated. This would be an extremely difficult task and also would be difficult to relate to experimental results as only the dilational and capillary modes experimentally contribute to the scattering of light.
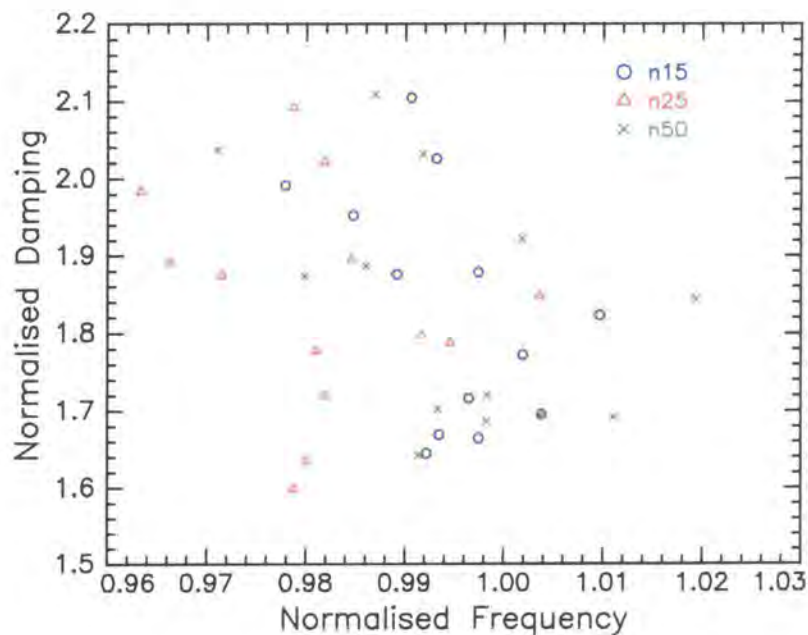
Figure 8.4.14. Normalised frequency and damping behaviour for each graft copolymer plotted in the complex plane.

Section 8.5   Conclusions

The surface viscoelastic behaviour of the series of graft copolymers has been examined using SQELS as a function of time, surface concentration and surface frequency.

Time dependence studies were undertaken to examine the homogeneity of the graft copolymer films. It was found that the spread film was patchy and formed islands only at extremely low surface concentrations i.e. $\Gamma_s \leq 0.1$ mg m^{-2}, which concurs with the theoretical surface concentration of 0.11 mg m^{-2} where PEO grafts are predicted to overlap in 2-dimensions. As the spread monolayer was compressed further a uniform film was obtained giving complete coverage of the surface. Identical behaviour was detected even for the high surface concentrations, $\Gamma_s \geq 2.0$ mg m^{-2}, suggesting that no aggregates or bi-layers form.

Surface concentration studies have revealed that the architecture of the graft copolymer distinctly influences the capillary and dilational modes. There is no apparent dependence on graft length as each system exhibits a resonance between the capillary and dilational modes at 0.4 mg m^{-2}, and this concentration has been linked to the sharp structural transition within the monolayer observed by NR. The behaviour of the dilational modulus and its associated viscosity close to the resonance concentration is influenced by the high percentage of PEO and displays Kramers-Kronig-types characteristics. These changes are attributed to changes of the in-plane mechanical properties of the film. At the resonance concentration all materials exhibit an abrupt change in dilational viscosity as values jump from positive to negative magnitude. The negative values are interpreted as effective parameters where energy is transferred, possibly from one of the other surface modes not accessible by light scattering.

Frequency dependence studies undertaken at the resonance concentration revealed intriguing behaviour. The frequency followed the theoretical dependency with q for a capillary wave but a discontinuity was observed in the damping data, where the dependence at low q followed capillary damping but the high q data revealed a stronger dependence. This effect was investigated by generating data using the dispersion equation and it was concluded that the behaviour observed experimentally is due to resistive coupling between the modes. It is thought that at low q the capillary mode

dominates behaviour but at intermediate q a switch in behaviour occurs and the viscoelastic behaviour is influenced predominantly by the dilational mode.

Minimal dependencies of long wave surface dynamics are observed with PEO graft length. These changes occur at higher surface concentrations and correlate with those observed in surface pressure isotherm studies. No dependence on copolymer architecture was noted in the frequency dependent studies, which is not surprising as the monolayer organisation of all copolymers are identical at the resonance concentration.

Section 8.6   References

1)   Earnshaw, J. C.; McGivern, R. C. *J. Colloid Interface Sci.*, **1988**, *123*, 36.

2)   Earnshaw, J. C.; McGivern, R. C.; McLaughlin, A. C.; Winch, P. J. *Langmuir*, **1990**, *6*, 650.

3)   Buzza, D. M. A.; Jones, J. L.; McLeish, T. C. B.; Richards, R. W.; *J. Chem. Phys.*, **1998**, *109*, 5008.

4)   Lucassen-Reynders, E. H.; Lucassen, J. *Adv. Colloid Interface Sci.*, **1969**,*2*, 347.

5)   Richards, R. W.; Taylor, M. R. *J. Chem. Soc., Faraday Trans.*, **1996**, *92*, 601.

6)   Richards, R. W.; Rochford, B. R.; Taylor, M. R. *Macromolecules*, **1996**, *29*, 1980.

7)   Milling, A. J.; Richards, R. W.; Hiorns, R. C.; Jones, R. G. *Macromolecules*, **2000**, *33*, 2651.

8)   Peace, S. K.; Richards, R. W. *Langmuir*, **1998**, *14*, 667.

9)   Pippard, A. B. *The Physics of Vibration*, Cambridge University Press, Cambridge, UK, **1989**.

10)   Ferry, J. D. *Viscoelastic Properties of Polymers*, John Wiley & Sonds, New York, USA, **1970**.

11)   Earnshaw, J. C.; McLaughlan, A. C. *Proc. R. Soc. Lond. A*, **1993**, *440*, 519.

12)   Earnshaw, J. C.; Sharpe, D. J. *J. Chem. Soc. Faraday, Trans.* **1996**, *92*, 611.

13)   Earnshaw, J. C.; McCoo, E. *Langmuir*, **1995**, *11*, 1087.

14)   Richards, R. W.; Taylor, M. R. *Macromolecules*, **1997**, *30*, 3892.

15)   Sharpe, D.; Eastoe, J. *Langmuir*, **1995**, *11*, 4636.

16)   Booth, C.; Richards, R. W.; Taylor, M. R.; Yu, G. E.; *J. Phys.Chem. B*, **1998**, *102*, 209.

17)   Van Der Tempel, M.; Lucassen-Reynders, E. H.; *Adv. Colloid Interface Sci.* **1993**, *18*, 281.

18)   Hennenberg, M.; Chu, X. L.; Sanfeld, A.; Velarde, M. G. *J. Colloid Interface Sci.*, **1992**, *150*, 7.

19)   Kazhdan, D.; Shtilman, L.; Colovin, A. A.; Pisman, L. M. *Phys. Fluids*, **1995**, *7*, 2679.

20)   Langevin, D. (ed.) *Light Scattering By Liquid Surfaces and Complimentary Techniques*, Marcel Dekker, Inc., New York, USA, 1992.

21)   Kramer, L. *J. Chem. Phys.* **1971**, *55* 2097.

22) Brown, A. S.; Richards, R. W.; Buzza, D. M. A.; McLeish, T. C. B. *Faraday Discuss.,* **1999,** *112,* 1.

23) Peace, S. K. *Ph.D. Thesis,* **1996,** *Durham University.*

24) Levich, V. G. *Physicochemical Hydrodynamics,* Prentice-Hall, **1962.**

25) Pippard, A. B. *Response and Stability,* Cambridge University Press, Cambridge, UK, **1988.**

26) Earnshaw, J. C.; McLaughlin, A. C. *Proc. R. Soc. Lond. A.,* **1991,** *433,* 663.

27) Earnshaw, J. C.; McLaughlin, A. C. *Proc. R. Soc. Lond. A.,* **1993,** *440,* 519.

Chapter Nine

Conclusions and Further Work

Section 9.1   Conclusions

The organisation and surface wave dynamics of a series of well-defined graft copolymers spread at the air-water interface have been investigated. There were four major aspects to this work. Initially a series of well-defined graft copolymers were synthesised. They were and subsequently spread to form thin films at the air-water interface before their surface pressure isotherms were recorded and analysed. The technique of neutron reflectometry was applied to determine the organisation of the copolymers on a molecular level as a function of surface concentration and graft length. Finally surface quasi-elastic light scattering was applied to investigate into the influence of the presence of the graft copolymer thin films on the long wavelength dynamics and viscoelasticity of the surface of an air-water interface and also the monolayer viscoelasticity.

A series of novel well-defined polynorbornene-g-poly(ethylene oxide) copolymers were prepared by combining anionic and ring opening metathesis polymerisation (ROMP) techniques (Chapter Four). This synthetic pathway combined two living polymerisation steps hence the procedure provided control over not only the degree of polymerisation and the molecular weight distribution of the graft and backbone chains, but also of the grafting density. The hydrophobic backbone length was kept constant at 50 norbornene units while the degree of polymerisation of the hydrophilic graft was varied from 15, 25 to 50 ethylene oxide units. Graft chains with a degree of polymerisation greater than 50 were not polymerisable due to steric hindrance and the poor reactivity of the Grubbs initiator used for ROMP (section 4.4). Longer length graft chains are highly desirable as their behaviour is expected to be more akin to polymer brushes allowing polymer brush theory to be tested rigorously. Future synthesis could focus on applying different, more reactive initiators for example the new ruthenium complex where both the phosphine ligands of the Grubbs initiator (see figure 2.1.8) are replaced with imidazolinylidene ligands. Alternative methods could be applied to remove the residual water from the PEO grafts, for example freeze drying, to prevent deactivation of the Schrock initiator. It is expected that higher degrees of polymerisation of PEO macromonomers will ROMP due to the increased reactivity of the molybdenum initiator. Various amphiphilic copolymer molecules could be prepared,

for example polyelectrolyte materials, which could be quarternertised in attempt to stretch the chains even further. The industrial application of such molecules could be optimised if their structure-property relationship was well understood.

All graft copolymers were spread at the air - water and air - PEO solution (0.1, 1.0, 2.0 and 5.0%) interface and formed stable thin films. Surface pressure isotherm studies (Chapter Five) revealed that monolayer behaviour was highly dependent on both the graft length of the spread copolymer and on the chemical composition of the subphase. The monolayer characteristics of each graft copolymer spread at low surface concentrations at the air - water interface (section 5.4) (< 0.7 mg m^{-2}) were similar to those observed for homoPEO and were independent of the backbone. At higher surface concentrations (> 0.7 mg m^{-2}) the isotherm behaviour of each copolymer began to diverge from each of other and different equilibrium surface pressures were observed depending on the graft length. As the degree of polymerisation of the graft length increased the equilibrium surface pressure decreased suggesting that the longer length grafts adopted a more coiled conformation. As homoPEO was introduced into the subphase (section 5.5) the surface tension decreased as expected as PEO molecules were adsorbed at the surface in preference to water molecules. This adsorption increased with increasing percentage of homoPEO in the subphase. The surface pressure data recorded for the graft copolymer with n_{EO} = 25 revealed that the quantity of homoPEO present also influenced monolayer characteristics. All isotherms recorded exhibited similar shaped curves, the only difference between them was the magnitude of the surface pressure over the entire surface concentration range since the value increased with increasing mobile PEO present in the subphase. This behaviour was expected as the hydrophobicity of the near surface layer increased with increasing PEO content as a greater number of PEO molecules adsorbed at the surface displacing water molecules, thus reducing the number of favourable EO/water interactions.

The interfacial organisation of each copolymer film spread at the air - water interface and the distribution of water in the near surface region was elucidated using neutron reflectometry. Three methods were adopted to analyse the data collected including the optical matrix approach and the kinematic approximation both of which are model dependent. The third method was the model independent Bayesian analysis and was used to verify the models applied to describe the interfacial organisation. The

kinematic approximation provided detailed information regarding the distribution of the PEO component but did not satisfactorily describe the distribution of water components due to an error in instrumental set-up. The optical matrix analysis method predicted the arrangement of both the main and graft chains successfully and it was apparent that the results obtained were in good agreement with those predicted from the independent Bayesian analysis. This reveals that accurate segmental concentration profiles can be obtained from neutron reflectometry data provided the models adopted are carefully selected and all data sets are rigorously analysed. In all cases experimental studies it was found that the hydrophobic backbone constitutes the majority of the uppermost layer, the minority component being air with some evidence of a very small amount of PEO also being present. This latter component is thought to arise from a combination of the cis/trans stereochemistry of the backbone and the strong affinity for the subphase of the PEO grafts resulting in some of the grafts bending over the backbone before being immersed in the aqueous subphase. As the monolayer was compressed the PEO grafts explored greater depths in the subphase. The organisation of the PEO grafts was described by combining two layers: uniform (upper layer) with parabolic decay (lower layer). Currently theory predicts that molecules behaving as ideal brushes at an interface

stretch according to the relationship: $h \propto N\sigma^{1/3}$, where h is the brush thickness and σ is the grafting density (section 6.3.). Since the PEO chains resemble end tethered polymers therefore their stretching behaviour was analysed as a function of both surface concentration and graft length. Examination of the data as a function of surface concentration revealed that a distinct phase change was present at circa 1.0 mg m^{-2}, which marked a change in the response of the copolymer organisation monolayer compression. The gradients of the slopes at low surface concentrations were extracted for each copolymer but they do not correspond to the theoretical value proposed ($\frac{1}{3}$),

but instead were found to be 1.32 for *n15* and circa $\frac{2}{3}$ for both the *n25* and *n50* copolymers. The stronger rate of increase in penetration depth observed has been attributed to the modest molecular weight of the chains and their 2-dimensional mobility at the interface. The phase transition observed at 1.0 mg m^{-2} is characteristic of a change in molecular organisation where the chains move from having a predominantly pseudo 2-dimensional packing to only 3-dimensional stretching normal to the surface. At the high surface concentrations all copolymers behaved in a similar manner and an

exponent of 0.35 was extracted, indicating that the PEO chains stretch into the subphase in accordance with theoretical polymer brushes.

The knowledge of the graft copolymer system could be extended by studying the organisation of the middle copolymer at the air-PEO solution interfaces using neutron reflectometry. The organisation at four subphase concentrations would be probed (0.1, 1.0, 2.0 and 5.0 %) to match the surface pressure isotherm work presented here (section 5.5).

Monte Carlo methods were used to investigate the spatial organisation of an amphiphilic graft copolymer (polynorbornene-g-poly(ethylene oxide) when present as a free molecule at a hydrophobic/hydrophilic interface when its energy has been minimised (Chapter Seven). The effect of monolayer compression on molecular orientation was also explored simply by confining the molecule laterally. At low surface concentrations the simulation model predicted surface arrangements that were in good agreement with the organisations observed experimentally. Similar trends in the physical properties of the simulated and experimental model were observed when the molecules were confined laterally due to monolayer compression. Precise agreement was not obtained however and evidence suggested this was due to the limitations of the current simulation model (section 7.4). To overcome such deficiencies a sophisticated model has been proposed where the simulation system has been modified to include ten amphiphilic molecules. It is thought that this will include the physical effect of intermolecular interactions which will hopefully lead to an increase in polymer-polymer entanglements therefore a higher concentration will be required before stretching comparable to that observed experimentally will be achieved.

Following the determination of the organisation of the polymer at the air-liquid interface, attention was then turned to the long wavelength dynamics of each copolymer film at the air-water interface (Chapter Eight) and were probed using surface quasi-elastic light scattering. The surface viscoelasticity of the monolayers were also examined as a function of time, surface concentration and surface frequency. Such time dependent studies (section 8.2) revealed that all films where $\Gamma_s \geq 0.08$mg m^{-2} were homogeneous and stable to periods in excess of 10 hours. Surface concentration studies (section 8.3) revealed that the graft copolymer system distinctly influenced the capillary

and dilational modes that there was no obvious dependence on graft length. A resonance was observed between the two surface modes at 0.4 mg m^{-2} for all copolymers, and has been linked to the distinct structural transition within the monolayer. The variation of the dilational modulus and the associated viscosity displayed Kramers-Kronig type behaviour, which was attributed to changes within the mechanical properties of the spread film as it was compressed. At the resonance concentration the dilational viscosity changed abruptly from positive to negative magnitude for all copolymer films. Such negative values have been interpreted as **effective** parameters and possibly arose from the exchange of energy from one of the other surface modes not accessible by light scattering. The results obtained from frequency studies were intriguing (section 8.4). At low wavenumbers the frequency of the capillary wave followed the dependence predicted theoretically, but a discontinuity was observed at intermediate wavenumber, and thereafter the data revealed a stronger dependence. This behaviour was attributed to the capillary and dilational modes coupling resistively, thus inducing mode mixing. It was predicted that at low wavenumbers the capillary mode dominated the surface behaviour and at the discontinuity the behaviour switched and surface viscoelasticity was influenced predominantly by the dilational mode.

The next logical step for SQELS is to attempt to address the ambiguity of negative dilational viscosities. The observation of such negative values implies that the dispersion equation used to describe the polymers at the air-liquid interface is not correct and would therefore benefit from further development. Numerous amphiphilic graft copolymers could be studied to determine if the unusual behaviour observed in this study is characteristic of either the copolymer topology or the high grafting density of PEO. If the synthetic strategy employed to prepare copolymers with longer grafts is successful then the influence of graft length could be extended to investigate for possible influence on properties. Furthermore the influence of thin films of graft copolymer on the dynamic properties of at the air-PEO solution interface would complement surface pressure isotherm work (section 5.5) and would allow extension of previous studies of surface excess layers of homoPEO by surface quasi elastic light scattering. Understanding such systems would be beneficial and could be extended to liquid - liquid interfaces, which may have direct application in practical situations, for

example polymeric stabilisers or compatibilisers where a variety of components could be present.

Appendix A

Additional Data

Section A **Additional Results**

Γ_s /mg m^{-2}	Layer	d /Å	ϕ_{NB}	ϕ_W	ϕ_{EO}	ϕ_{AIR}	n_{NB} /10^{-3} Å^{-3}	n_{EO} /10^{-3} Å^{-3}
4.0	1	4 ± 2	0.37	0	0.03	0.60	1.85	0.41
	2	19 ± 1	0	0.02	0.98	0	0	13.54
	3	10 ± 2	0	0.15	0.85	0	0	11.75
	4	10 ± 2	0	0.90	0.10	0	0	1.38
3.5	1	4 ± 2	0.34	0	0.08	0.58	1.70	1.10
	2	18 ± 2	0	0.02	0.98	0	0	13.54
	3	6 ± 1	0	0.62	0.58	0	0	8.02
	4	12 ± 1	0	0.92	0.08	0	0	1.11
3.0	1	5 ± 2	0.28	0	0.06	0.66	1.40	0.83
	2	19 ± 1	0	0.03	0.97	0	0	13.41
	3	15 ± 2	0	0.91	0.09	0	0	1.24
2.5	1	4 ± 1	0.55	0	0.05	0.40	2.75	0.07
	2	15 ± 1	0	0.02	0.98	0	0	13.54
	3	17 ± 1	0	0.85	0.15	0	0	2.07
2.0	1	8 ± 1	0.47	0	0.06	0.47	2.35	0.03
	2	17 ± 1	0	0.12	0.88	0	0	12.16
	3	9 ± 1	0	0.95	0.05	0	0	0.69
1.5	1	7 ± 1	0.71	0	0.02	0.27	3.55	0
	2	14 ± 2	0	0.22	0.78	0	0	10.78
	3	8 ± 1	0	0.94	0.06	0	0	0.83
1.0	1	5 ± 2	0.92	0	0	0.08	4.60	0
	2	9 ± 1	0	0.19	0.81	0	0	11.19
	3	6 ± 1	0	0.92	0.08	0	0	1.11
0.7	1	3 ± 1	0.49	0	0	0.51	2.45	0
	2	7 ± 1	0	0.25	0.75	0	0	10.36
	3	5 ± 1	0	0.91	0.09	0	0	1.24
0.5	1	4 ± 1	0.35	0	0	0.65	1.75	0
	2	5 ± 1	0	0.40	0.60	0	0	8.29
	3	7 ± 1	0	0.91	0.09	0	0	1.24
0.4	1	5 ± 1	0.70	0	0	0.30	3.50	0
	2	6 ± 1	0	0.45	0.55	0	0	7.60
	3	4 ± 1	0	0.96	0.04	0	0	0.55
0.3	1	3 ± 1	0.35	0	0	0.65	1.75	0
	2	3 ± 1	0	0.36	0.64	0	0	8.85
	3	3 ± 1	0	0.81	0.19	0	0	2.63

Table A.1   Layer thicknesses, volume fraction compositions and number densities of the individual components from three/four uniform layers for *n15* from optical matrix analysis.

353

Γ_s /mg m^{-2}	Layer	d /Å	ϕ_{NB}	ϕ_W	ϕ_{EO}	ϕ_{AIR}	n_{NB} /10^{-3} Å^{-3}	n_{EO} /10^{-3} Å^{-3}
4.0	1	5±2	0.60	0	0.07	0.33	5.10	1.00
	2	20±1	0	0.01	0.99	0	0	13.68
	3	16±2	0	0.20	0.80	0	0	11.06
	4	27±3	0	0.97	0.03	0	0	0.42
3.5	1	5±1	0.30	0	0.07	0.63	2.55	1.00
	2	21±2	0	0.01	0.99	0	0	13.68
	3	14±1	0	0.86	0.25	0	0	3.46
	4	26±1	0	0.94	0.06	0	0	0.83
3.0	1	5±1	0.30	0	0.06	0.64	2.55	0.83
	2	21±4	0	0.06	0.94	0	0	12.99
	3	41±1	0	0.95	0.05	0	0	0.69
2.5	1	5±2	0.39	0	0.11	0.61	3.32	1.52
	2	19±1	0	0.07	0.93	0	0	12.85
	3	40±2	0	0.97	0.03	0	0	0.42
2.0	1	3±1	0.39	0	0	0.61	3.32	0
	2	17±1	0	0.10	0.90	0	0	12.44
	3	36±2	0	0.98	0.02	0	0	0.28
1.5	1	3±1	0.46	0	0	0.54	3.91	0
	2	17±2	0	0.33	0.67	0	0	9.26
	3	25±1	0	0.96	0.04	0	0	0.55
1.0	1	3±1	0.48	0	0	0.52	4.08	0
	2	10±2	0	0.25	0.75	0	0	10.36
	3	21±1	0	0.97	0.03	0	0	0.41
0.7	1	4±1	0.46	0	0	0.54	3.91	0
	2	7±1	0	0.22	0.78	0	0	10.78
	3	14±1	0	0.98	0.02	0	0	0.28
0.5	1	4±1	0.53	0	0	0.47	4.51	0
	2	7±1	0	0.19	0.66	0	0	9.12
	3	11±1	0	0.99	0.06	0	0	0.83
0.4	1	5±1	0.51	0	0	0.49	4.34	0
	2	3±1	0	0.19	0.81	0	0	11.19
	3	10±1	0	0.94	0.06	0	0	0.83
0.3	1	4±1	0.42	0	0	0.58	3.57	0
	2	3±1	0	0.28	0.65	0	0	8.98
	3	11±1	0	0.94	0.05	0	0	0.69

Table A.2   Layer thicknesses, volume fraction compositions and number densities of the individual components from three/four uniform layers for *n50* from optical matrix analysis.

$\Gamma_{sTOTAL}/mg\ m^{-2}$	$\Gamma_{sEO}/mg\ m^{-2}$	$\Gamma_{sEO\ cal}/mg\ m^{-2}$	$\Gamma_{sEO}/\Gamma_{sEO\ cal}$
4.0	3.44	3.21 ± 0.32	0.93
3.5	3.01	2.58 ± 0.29	0.86
3.0	2.58	2.18 ± 0.13	0.85
2.5	2.15	1.94 ± 0.13	0.90
2.0	1.72	1.70 ± 0.11	0.99
1.5	1.29	1.25 ± 0.18	0.97
1.0	0.86	0.85 ± 0.04	0.99
0.7	0.60	0.58 ± 0.04	0.97
0.5	0.43	0.40 ± 0.08	0.93
0.4	0.35	0.35 ± 0.03	1.0
0.3	0.26	0.26 ± 0.03	1.0

Table A.3 Calculated surface concentrations of PEO from three/four uniform layers for *n15* from optical matrix analysis.

$\Gamma_{sTOTAL}/mg\ m^{-2}$	$\Gamma_{sEO}/mg\ m^{-2}$	$\Gamma_{sEO\ cal}/mg\ m^{-2}$	$\Gamma_{sEO}/\Gamma_{sEO\ cal}$
4.0	3.80	3.79 ± 0.22	0.99
3.5	3.33	3.00 ± 0.27	0.89
3.0	2.85	2.54 ± 0.42	0.88
2.5	2.38	2.19 ± 0.16	0.90
2.0	1.90	1.75 ± 0.06	0.92
1.5	1.42	1.33 ± 0.11	0.94
1.0	0.95	0.86 ± 0.12	0.91
0.7	0.66	0.63 ± 0.04	0.96
0.5	0.48	0.46 ± 0.05	0.96
0.4	0.38	0.35 ± 0.04	0.92
0.3	0.28	0.27 ± 0.05	0.97

Table A.4 Calculated surface concentrations of PEO from three/four uniform layers for *n50* from optical matrix analysis.

Γ_s /mg m^{-2}	d_1 /Å^{-1}	ϕ_1	d_2 /Å^{-1}	ϕ_2	n_1 /10^{-3} Å^{-3}	n_2 /10^{-3} Å^{-3}
4.0	29±2	0.83	23±1	0.27	11.47	4.04
3.5	22±1	0.89	30±2	0.25	12.30	3.45
3.0	18±2	0.89	27±2	0.26	12.30	3.56
2.5	15±1	0.91	25±2	0.23	12.58	3.15
2.0	12±1	0.79	30±2	0.19	10.92	2.59
1.5	8±2	0.70	28±4	0.19	9.67	2.65
1.0	9±2	0.54	23±7	0.10	7.46	1.35
0.7	4±1	0.94	13±1	0.13	12.99	1.76
0.5	4±1	0.49	7±3	0.25	6.77	3.44
0.4	3±1	0.37	7±2	0.23	5.11	3.16
0.3	3±1	0.40	3±1	0.28	5.53	3.85

Table A.5 Layer thicknesses, volume fractions and calculated number densities for *n15* from optical matrix calculations with a uniform layer plus parabolic decay model. The subscripts 1 and 2 denote the uniform and parabolic layer respectively.

Γ_{sTOTAL} /mg m^{-2}	Γ_{sEO} /mg m^{-2}	$\Gamma_{sEO\ calc.}$ /mg m^{-2}	$\Gamma_{sEO}/\Gamma_{sEO\ calc.}$
4.0	3.44	3.33±0.16	0.97
3.5	3.01	2.97±0.11	0.99
3.0	2.58	2.55±0.25	0.99
2.5	2.15	2.10±0.14	0.98
2.0	1.72	1.70±0.13	0.99
1.5	1.29	1.28±0.24	0.99
1.0	0.86	0.80±0.21	0.93
0.7	0.60	0.60±0.12	1.00
0.5	0.43	0.43±0.14	1.00
0.4	0.35	0.33±0.03	0.94
0.3	0.26	0.24±0.04	0.92

Figure A.6 Calculated surface concentrations of PEO for *n15* from optical matrix calculations using a uniform layer with parabolic decay model.

Γ_s /mg m^{-2}	d_1 /Å^{-1}	ϕ_1	d_2 /Å^{-1}	ϕ_2	n_1 /10^{-3} Å^{-3}	n_2 /10^{-3} Å^{-3}
4.0	37 ± 2	0.85	23 ± 2	0.15	11.75	2.07
3.5	33 ± 1	0.78	29 ± 1	0.17	10.78	2.35
3.0	32 ± 1	0.68	28 ± 2	0.18	9.40	2.48
2.5	26 ± 2	0.59	30 ± 2	0.16	8.15	2.21
2.0	19 ± 1	0.74	35 ± 3	0.11	10.23	1.52
1.5	14 ± 1	0.78	26 ± 4	0.11	10.78	1.38
1.0	5 ± 1	0.69	27 ± 2	0.26	9.54	2.21
0.7	11 ± 2	0.49	19 ± 4	0.04	6.77	0.55
0.5	5 ± 1	0.63	11 ± 3	0.10	8.71	1.38
0.4	5 ± 1	0.56	13 ± 5	0.06	7.74	0.83
0.3	3 ± 1	0.47	10 ± 3	0.17	6.50	1.35

Table A.7   Layer thicknesses, volume fractions and calculated number densities for *n50* from optical matrix calculations with a uniform layer plus parabolic decay model. The subscripts 1 and 2 denote the uniform and parabolic layer respectively.

Γ_{sTOTAL} /mg m^{-2}	Γ_{sEO} /mg m^{-2}	$\Gamma_{sEO\ calc.}$ /mg m^{-2}	$\Gamma_{sEO}/\Gamma_{sEO\ calc.}$
4.0	3.80	3.57 ± 0.22	0.94
3.5	3.33	3.26 ± 0.10	0.98
3.0	2.85	2.84 ± 0.11	0.99
2.5	2.38	2.20 ± 0.16	0.92
2.0	1.90	1.89 ± 0.11	0.99
1.5	1.42	1.42 ± 0.12	1.00
1.0	0.95	0.93 ± 0.12	0.98
0.7	0.66	0.64 ± 0.12	0.97
0.5	0.48	0.47 ± 0.11	0.99
0.4	0.38	0.37 ± 0.08	0.97
0.3	0.28	0.27 ± 0.09	0.99

Figure A.8   Calculated surface concentrations of PEO for *n50* from optical matrix calculations using a uniform layer with parabolic decay model.

Γ_{sTOTAL} /mg m^{-2}	Γ_{sEO} /mg m^{-2}	d_1 /Å^{-1}	n_1 /10^{-3} Å^{-3}	d_2 /Å^{-1}	n_2 /10^{-3} Å^{-3}	$\Gamma_{sEO\ calc.}$ /mg m^{-2}	$\Gamma_{sEO}/\Gamma_{sEO\ calc.}$
4.0	3.44	29 ± 2	3.30 ± 0.41	24 ± 3	4.69 ± 0.50	2.22 ± 0.02	0.67
3.5	3.01	23 ± 2	5.11 ± 0.55	25 ± 2	4.12 ± 0.43	1.86 ± 0.02	0.62
3.0	2.58	24 ± 3	5.39 ± 0.75	22 ± 4	3.75 ± 0.12	0.81 ± 0.03	0.67
2.5	2.15	20 ± 3	5.35 ± 0.16	22 ± 2	3.41 ± 0.16	1.51 ± 0.01	0.80
2.0	1.72	16 ± 2	4.43 ± 0.24	26 ± 3	2.74 ± 0.24	1.21 ± 0.01	0.70
1.5	1.29	17 ± 2	4.61 ± 0.54	17 ± 2	2.61 ± 0.31	1.00 ± 0.02	0.78
1.0	0.86	16 ± 1	4.39 ± 0.28	15 ± 1	2.04 ± 0.16	0.80 ± 0.01	0.93
0.7	0.60	10 ± 1	3.59 ± 0.16	7 ± 1	2.84 ± 0.43	0.46 ± 0.01	0.77
0.5	0.43	6 ± 1	3.32 ± 0.32	6 ± 1	2.41 ± 0.23	0.31 ± 0.01	0.72
0.4	0.35	4 ± 1	3.59 ± 0.64	6 ± 1	2.45 ± 0.13	0.25 ± 0.01	0.71

Table A.9   Number densities, layer thicknesses and calculated surface concentrations from the PEO kinematic approximation for *n15* using the uniform layer with half-parabola decay model.

Γ_{sTOTAL} /mg m^{-2}	Γ_{sEO} /mg m^{-2}	d_1 /Å^{-1}	n_1 /10^{-3} Å^{-3}	d_2 /Å^{-1}	n_2 /10^{-3} Å^{-3}	$\Gamma_{sEO\,calc.}$ /mg m^{-2}	$\Gamma_{sEO}/\Gamma_{sEO\,calc.}$
4.0	3.80	21 ± 2	7.20 ± 1.60	46 ± 3	3.87 ± 0.12	2.83 ± 0.03	0.75
3.5	3.33	25 ± 1	6.83 ± 0.81	40 ± 3	3.54 ± 0.18	2.62 ± 0.03	0.79
3.0	2.85	19 ± 2	6.22 ± 0.61	38 ± 1	2.82 ± 0.21	1.90 ± 0.02	0.67
2.5	2.38	11 ± 1	6.12 ± 0.87	39 ± 2	2.25 ± 0.16	1.34 ± 0.03	0.56
2.0	1.90	20 ± 1	5.97 ± 0.70	37 ± 2	1.67 ± 0.09	1.47 ± 0.02	0.77
1.5	1.42	19 ± 2	5.87 ± 0.54	25 ± 4	1.70 ± 0.28	1.22 ± 0.02	0.86
1.0	0.95	10 ± 1	5.29 ± 0.41	21 ± 2	1.56 ± 0.13	0.70 ± 0.02	0.74
0.7	0.66	7 ± 1	5.35 ± 0.48	18 ± 1	2.22 ± 0.12	0.65 ± 0.02	0.98
0.5	0.48	6 ± 1	5.21 ± 0.47	14 ± 1	1.09 ± 0.11	0.38 ± 0.02	0.79
0.4	0.38	4 ± 1	4.72 ± 0.27	15 ± 2	1.38 ± 0.08	0.34 ± 0.01	0.89

Table A.10 Number densities, layer thicknesses and calculated surface concentrations from the PEO kinematic approximation for *n50* using the uniform layer with half-parabola decay model.

Appendix B

Additional Equations

Section B.1   PEO self-partial structure factors
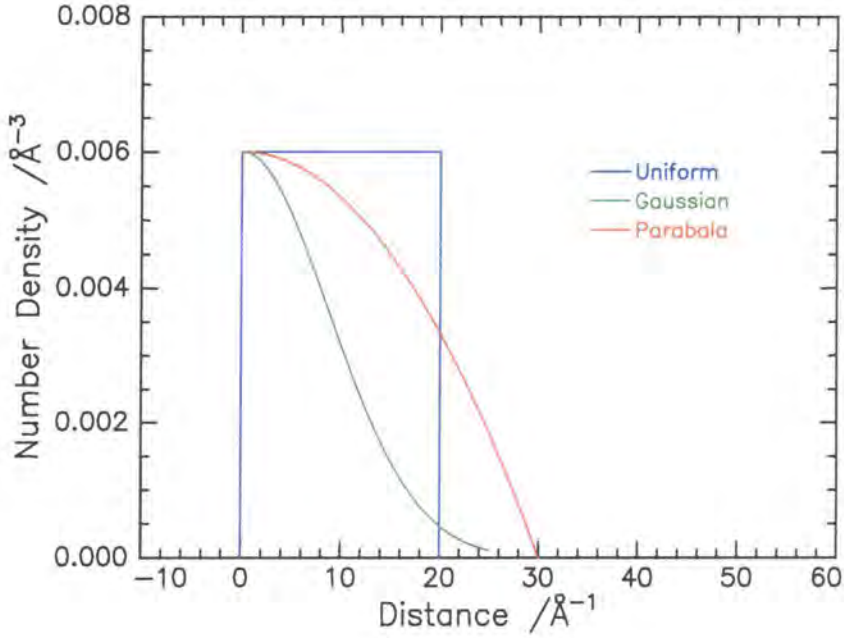
Figure B.1   Schematic sketch of an uniform layer, a parabolic and gaussian distribution of segments (uniform layer model has $d_1=20$ Å, $n_1=0.006$ Å^{-3}; the Gaussian distribution has $d_1=25$ Å, $n_1=0.006$ Å^{-3} and the parabolic distribution has $d_1=30$ Å, $n_1=0.006$ Å^{-3}).

Single Uniform Layer

The real space distribution for species i;

$$n_i(z) = n_{i1}$$

Equation B.1

and the partial structure factor is given by;

$$Q^2 h_{ii}(Q) = 4n_{i1}^2 \sin^2\left(\frac{Q\sigma}{2}\right)$$

Equation B.2

where n_i is the number density of i segments at the air-water interface (in this study i equates to EO) and σ is the standard deviation of the uniform layer.

Single Half-Gaussian Distribution

Real space distribution for species i is;

$$n_i(z) = n_{i1} \exp\left(\frac{-4z^2}{\sigma^2}\right)$$

Equation B.3

and the partial structure factor is given by;

$$Q^2 h_{ii}(Q) = \left(n_i^2\right)\left(\frac{\pi\sigma^2}{4}\right)\exp\left(\frac{-Q^2\sigma^2}{8}\right)$$

Equation B.4

where σ is the standard deviation of the half Gaussian layer.

Single Half-Parabola

The real space distribution is;

$$n_i(z) = n_{i1}\left(1 - \frac{z^2}{\sigma^2}\right)$$

Equation B.5

and the partial structure factor is;

$$Q^2 h_{ii}(Q) = \frac{16 n_{i1}^2}{Q^4 \sigma^4}\left(\sin(Q\sigma) - Q\sigma\cos(Q\sigma)\right)^2$$

Equation B.6

Sketches of the distribution of the composite models (double uniform and uniform plus parabolic decay) are given in figure B.2.
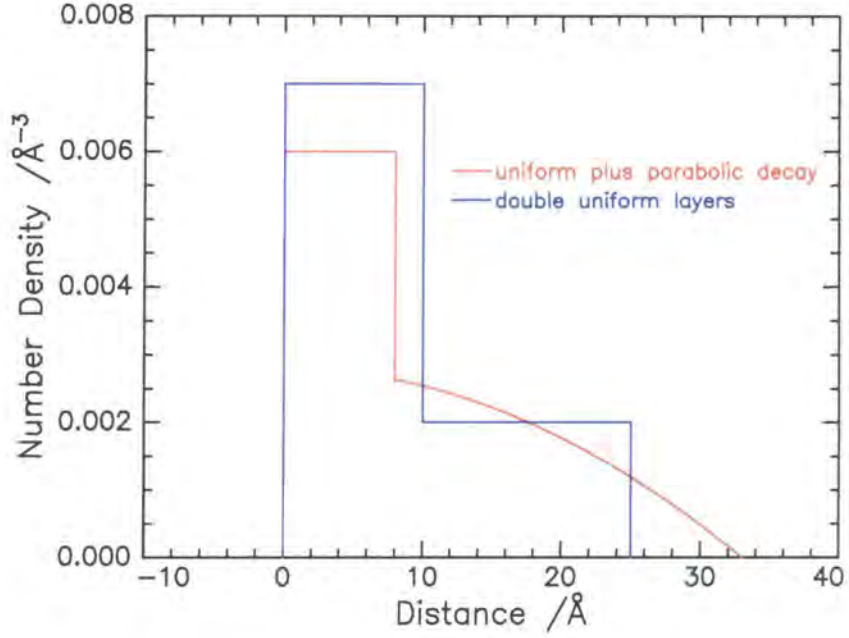
Figure B.2   Schematic sketch of a double uniform layer and a uniform layer plus parabolic decay distribution of segments (double uniform layer model has $d_1=10$ Å, $n_1=0.07$ Å^{-3}, $d_2=15$ Å and $n_2=0.02$ Å^{-3}, whereas the parabolic model has $d_1=8$ Å, $n_1=0.06$ Å^{-3}, $d_2=25$ Å and $n_2=0.03$ Å^{-3}).

Double Uniform Layers

The density profile for the double uniform layer model is given by;

$$n_i(z) = 0 \qquad z < \sigma + \tau$$

$$n_i(z) = n_{i1} \qquad 0 < z < \sigma$$

$$n_i(z) = n_{i2} \qquad \sigma < z < \sigma + \tau$$

$$n_i(z) = 0 \qquad z > \sigma + \tau$$

$$n_i(Q) = \frac{2n_i}{Q}\left(\sin\left(\frac{Q\sigma}{2}\right)\right) + \frac{2n_{i2}}{Q}\sin\left(\frac{Q\tau}{2}\right)\exp(\pm iQ\delta)$$

Equation B.7

where σ and τ are the lengths of the upper (1) and lower (2) layers respectively. The corresponding partial structure factor is;

$$Q^2h_{ii}(Q) = 4n_{ni1}^2\sin^2\left(\frac{Q\sigma}{2}\right) + 4n_{i2}^2\sin^2\left(\frac{Q\tau}{2}\right) + 8n_{i1}n_{i2}\sin\left(\frac{Q\sigma}{2}\right)\sin\left(\frac{Q\tau}{2}\right)\cos(Q\delta)$$

Equation B.8

Uniform Layer with Parabolic Decay

The distribution of the uniform/parabolic decay model is given by;

$$n_i(z) = 0 \qquad\qquad z \le -\sigma - \varepsilon$$

$$n_i(z) = n_{i2}\left(1 - \frac{(z+\sigma)^2}{\varepsilon^2}\right) \qquad -\sigma \le z \le 0$$

$$n_i(z) = n_{i1} \qquad\qquad -\sigma \le z \le 0 \qquad\text{**Equation B.9**}$$

where σ and ε are the lengths corresponding to the uniform and parabolic layers respectively.

The partial structure factor expression is;

$$h_{ii} = 2n_{i1}^2 + n_{i2}^2 - 2n_{i1}n_{i2} + 2n_{i1}\cos(Q\sigma)[n_{i2} - n_{i1}] +$$

$$\frac{1}{Q^2\varepsilon^4}\left\{\begin{array}{l}8n_{i2}^2[1+Q^2\varepsilon^2] + [\cos(Q\varepsilon)+Q\varepsilon\sin(Q\varepsilon)][4n_{i1}n_{i2}Q^2\varepsilon^2 - 4n_{i2}^2Q^2\varepsilon^2 - 8n_{i2}^2] + \\ 4n_{i1}n_{i2}Q^2\varepsilon^2[\cos(Q\sigma)-\cos(Q(\sigma+\varepsilon))-Q\varepsilon\ \sin(Q(\sigma+\varepsilon))-1]\end{array}\right\}$$

Equation B.10

Calculation of Surface Concentrations

Single uniform layer

$$\Gamma_s = \frac{n_i dm_i}{N_A} \times 10^{23} \ \text{m gm}^{-2}$$

Equation B.11

Single half-Gaussian layer

$$\Gamma_s = \frac{n_i \sqrt{\pi} dm_i}{2N_A} \times 10^{23} \ \text{m gm}^{-2}$$

Equation B.12

Single half-parabola layer

$$\Gamma_s = \frac{4 n_i dm_i}{3N_A} \times 10^{23} \ \text{m gm}^{-2}$$

Equation B.13

Double uniform layers

$$\Gamma_s = \left(n_{i1} d_1 + n_{i2} d_2 \right) \frac{m_i}{N_A} \times 10^{23} \ \text{m gm}^{-2}$$

Equation B.14

Uniform with parabolic decay

$$\Gamma_s = \left(n_{i1} d_1 + \frac{4}{3} n_{i2} d_2 \right) \frac{m_i}{N_A} \times 10^{23} \ \text{m gm}^{-2}$$

Equation B.15

where m_i is the molecular weight of species i (in this study i represents EO monomer: deuterated EO=48 g mol^{-1}) and n_i and d_i are the number density and the thickness of species *i* respectively.

Section B.2   Water self-partial structure factors

Uniform Water Layer

The number density of a uniform water layer is given by;

$$n_s(z) = 0 \qquad\qquad z < -\sigma/2$$
$$n_s(z) = n_{s1} \qquad\qquad -\sigma/2 < z < \sigma/2$$
$$n_s(z) = n_{s0} \qquad\qquad z < \sigma/2$$

Equation B.16

where σ is the thickness of the water layer and n_{s1} and n_{s0} are the number density of water in the polymer containing layer and in the bulk respectively. The expression for the self-partial structure factor is;

$$Q^2 h_{ss}(Q) = n_{s0}^2 + 4n_{s1}(n_{s1} - n_{s0}) \sin^2\left(\frac{Q\sigma}{2}\right) \qquad \textbf{Equation B.17}$$

where σ is the thickness of the layer.

Tanh Water Layer

The second model, hyperbolic tangent (tanh), provides a more physically realistic smooth transition from the number density to the bulk subphase. The number density distribution of the tanh profile is given by;

$$n_s(z) = n_{s0}\left(0.5 + 0.5\tanh\left(\frac{z}{\sigma}\right)\right) \qquad \textbf{Equation B.18}$$

and the self-partial structure factor expression is given by;

$$Q^2 h_{ss}(Q) = n_{s0}^2 \left(\frac{\sigma\pi Q}{2}\right)^2 \text{cosech}^2\left(\frac{\sigma\pi Q}{2}\right)$$

Equation B.19

Double Uniform Water Layer

The number density of such a double layer model is given by;

$$
\begin{aligned}
n_s(z) &= 0 & z &< -d_{s1}/2 \\
n_s(z) &= n_{s1} & -d_{s1}/2 &< z < d_{s1}/2 \\
n_s(z) &= n_{s2} & d_{w1}/2 &< z < d_{s2} + d_{s1}/2 \\
n_s(z) &= n_{s0} & z &> d_{s2} + d_{s1}/2
\end{aligned}
$$

Equation B.20

which leads to a self partial structure factor of;

$$Q^2 h_{ss} = n_{s1}^2 + (n_{s1} - n_{s2})^2 + (n_{s2} - n_{s0})^2 + 2n_{s1}(n_{s2} - n_{s1})\cos(Qd_{s1})$$

$$+ 2(n_{s1} - n_{s2})(n_{s2} - n_{s0})\cos(Qd_{n2}) + 2n_{s1}(n_{s0} - n_{s2})\cos(Q(d_{s2} + d_{s1}))$$

Equation B.21

Appendix C

Lectures and Conferences Attended and Publications

Section C.1   Lectures Attended

C.1.1   Academic Year 1997/1998

October 8   Professor E Atkins, Department of Physics, University of Bristol
             Advances in the control of architecture for polyamides: from nylons to
             genetically engineered silks to monodisperse oligoamides

October 15   Dr R M Ormerod, Department of Chemistry, Keele University
             Studying catalysts in action

October 21   Professor A F Johnson, IRC, Leeds
             Reactive processing of polymers: science and technology

October 23   Professor M R Bryce, University of Durham, Inaugural Lecture
             New Tetrathiafulvalene Derivatives in Molecular, Supramolecular and
             Macromolecular Chemistry: controlling the electronic properties of
             organic solids

October 28   Professor A P de Silva, The Queen's University, Belfast
             Luminescent signalling systems"

November 11 Professor V Gibson, Imperial College, London
             Metallocene polymerisation

November 12 Dr J Frey, Department of Chemistry, Southampton University
             Spectroscopy of liquid interfaces: from bio-organic chemistry to
             atmospheric chemistry

November 19 Dr G Morris, Department of Chemistry, Manchester Univ.
             Pulsed field gradient NMR techniques: Good news for the Lazy and
             DOSY

November 26 Professor R W Richards, University of Durham, Inaugural Lecture
             A random walk in polymer science

December 2   Dr C J Ludman, University of Durham
             Explosions

January 27   Professor R Jordan, Dept. of Chemistry, Univ. of Iowa, USA.
             Cationic transition metal and main group metal alkyl complexes in olefin
             polymerisation

January 28   Dr S Rannard, Courtaulds Coatings (Coventry)
             The synthesis of dendrimers using highly selective chemical reactions

February 3   Dr J Beacham, ICI Technology
             The chemical industry in the 21st century

February 18   Professor G Hancock, Oxford University
Surprises in the photochemistry of tropospheric ozone

February 24   Professor R Ramage, University of Edinburgh
The synthesis and folding of proteins

March 4   Professor T C B McLeish, IRC of Polymer Science Technology, Leeds
University
The polymer physics of pyjama bottoms (or the novel rheological
characterisation of long branching in entangled macromolecules)

March 11   Professor M J Cook, Dept of Chemistry, UEA
How to make phthalocyanine films and what to do with them.

March 18   Dr J Evans, Oxford University
Materials which contract on heating (from shrinking ceramics to bullet
proof vests

C.1.2   Academic Year 1998/1999

October 7   Dr S Rimmer, Ctr Polymer, University of Lancaster
New Polymer Colloids

October 21   Professor P Unwin, Department of Chemistry, Warwick University
Dynamic Electrochemistry: Small is Beautiful

October 27   Professor A Unsworth, University of Durham
What's a joint like this doing in a nice girl like you?
In association with The North East Polymer Association

October 28   Professor J P S Badyal, Department of Chemistry, University of Durham
Tailoring Solid Surfaces, Inaugural Lecture

November 10 Dr J S O Evans, Chemistry Department, University of Durham
Shrinking Materials

November 17 Dr J McFarlane
Nothing but Sex and Sudden Death!

November 18 Dr R Cameron, Department of Materials Science & Metallurgy,
Cambridge University
Biodegradable Polymers

December 1   Professor N Billingham, University of Sussex
Plastics in the Environment - Boon or Bane
In association with The North East Polymer Association.

January 20   Dr A Jones, Department of Chemistry, University of Edinburgh
              Luminescence of Large Molecules: from Conducting Polymers to Coral
              Reefs

February 10   Dr C Bain, University of Oxford
              Surfactant Adsorption and Marangoni Flow at Expanding Liquid
              Surfaces

February 17   Dr B Horrocks, Department of Chemistry, Newcastle University
              Microelectrode techniques for the Study of Enzymes and Nucleic Acids
              at Interfaces

March 9   Dr Michael Warhurst, Chemical Policy issues, Friends of the Earth
              Is the Chemical Industry Sustainable?

March 10   Dr A Harrison, Department of Chemistry, The University of Edinburgh
              Designing model magnetic materials

May 12   Dr Duncan Bruce, Exeter University
              The Synthesis and Characterisation of Liquid-Crystalline Transition
              Metal Complexes

C 1.3   Academic Year 1999/2000

October 12   Dr. S. Beckett (Nestle)
              Chocolate for the next Millennium

October 25   Professor S. Collins, University of Waterloo, Canada
              Methacrylate Polymerization Using Zirconium Enolate Initiators:
              Polymerization Mechanisms and Control of Polymer Tacticity

November 10   Dr. I. Samuel, Department of Physics, University of Durham
              Improving Organic Light Emitting Diodes by Molecular, Optical and
              Device Design

November 16   Professor A. Holmes
              Conjugated Polymers for the Market Place

November 23   Professor B. Caddy
              Trace evidence - a challenge for the forensic scientist

November 24   Professor T. Jones, Imperial College
              Atomic and Molecular Control of Inorganic and Organic Semiconductor
              Thin Films

November 30   Rev. R. Lancaster
              Principles and Practice

January 12   Professor D. Haddleton, Department of Chemistry, University of
Warwick
Atom Transfer Polymerisation - What's all the Hype About?

January 19   Dr. P.R. Fielden, UMIST
Miniaturised Chemical Analysis (Lab-on-a-Chip): Functional or Merely
Fashionable?

January 25   Professor B. Meijer
From Supramolecular Architecture Towards Functional Materials

February 2   Chick Wilson, Head of Crytallography, ISIS, Rutherford Appleton Lab
Protons in motion? Neutron diffraction studies of hydrogen atoms in
organic crystal structures.

February 9   Dr. S. Moratti, University of Cambridge
Shape and Stereoselectivity in Polymer

February 15   Professor D. Phillips
A Little Light Relief

February 23   Dr. N. Clarke, UMIST
The Flow of Polymer Blends

March 1   Professor D. Tildsley, Unilever (Head of Research)
Computer Simulation of Interfaces: Fact and Friction

March 21   Professor E. Rizzardo, CSIRO Mol. Sci. Victoria, Australia
Designed Polymers by Free Radical Addition-Fragmentation Processes

Section C.2   Conferences Attended

January 1998	IRC Polymer Engineering Course, University of Bradford
January 1998	IRC Polymer Physics Course, University of Leeds
April 1998*	RSC National Congress and Young Researchers' Meeting, University of Durham
September 1998*	New Perspectives in Neutron and Muon Science: A meeting for Young Researchers, Cosener's House, Abingdon
September 1998*	Neutron and Muon Beam Users' Meeting, Rutherford Appleton Laboratory, Oxfordshire
March 1999**	Scattering Techniques in Colloid and Surface Systems SCI Colloid and Surface Chemistry Group, Belgrave Square, London
April 1999*	RSC Faraday Discussion No. 112: Physical Chemistry in the Mesoscopic Regime, The Queen Hotel, Chester
August 1999**	218th American Chemical Society National Meeting, New Orleans
September 1999*	Neutron and Muon Beam Users' Meeting, Rutherford Appleton Laboratory, Oxfordshire
September 1999**	IRC Industrial Club Meeting, The Museum of Film, and Television, Bradford
April 2000**	Adsorption to Interfaces, Colloid and Interface Science Group RSC, University of Surrey
April 2000**	The Age of the Molecule, RSC Annual Conference, UMIST, Manchester
September 2000**	NATO Advanced Study Institute, Ring Opening Metathesis Polymerisation and Related Chemisty, Wroclaw, Poland

* indicates a poster presentation by the author

** indicates an oral presentation by the author

Section C 3   Publications

A.F. Miller, R.W. Richards and J.R.P. Webster, accepted by Macrmolecules.

A.F. Miller, R.W. Richards and J.R.P. Webster, Abstracts of American Chemical Society 218, Part 2, August, 1999.